University of Strathclyde Glasgow

DEPARTMENT OF CHEMICAL AND PROCESS ENGINEERING

UNIVERSITY OF STRATHCLYDE

Response Surface Methodology for Chemical Activation of Peanut Shells: Synthesis and Application of Activated Carbon for Wastewater Treatment

Oluwagbemi Victor Aladeokin

Thesis submitted for the degree of Doctor of Philosophy

2023

Declaration of Authenticity and Author's Rights

This thesis is the result of the author's original research. It has been composed by the author and has not been previously submitted for examination which has led to the award of a degree.

Oluwagbemi Victor Aladeokin

December 2023

Acknowledgements

This thesis would not have been possible without the support and guidance of many people who have contributed to my PhD journey. I would like to express my deepest appreciation and gratitude to them.

First and foremost, I would like to acknowledge the invaluable supervision and mentorship of Prof Ashleigh, who has been a constant source of inspiration, encouragement, and feedback throughout this research project. She has provided me with excellent guidance and advice, both academically and personally, and has helped me to develop my skills and confidence as a researcher. She has also facilitated my access to various facilities and resources within and outside the university, which have been crucial for the success of my work. I am truly fortunate and honoured to have her as my primary supervisor.

I would also like to thank the other members of Ashleigh's research group for their collegiality and collaboration. They have always been ready to help me with suggestions, constructive criticism, and fruitful discussions. I have learned from their expertise and experience, and I have enjoyed working with them.

My sincere gratitude goes to my second supervisor, Dr Tosin Somorin, for her support and assistance throughout my PhD program. She has been very helpful and has helped me to improve my work and enhance my professional skills.

I am grateful to the laboratory technicians for their assistance and expertise in the use of equipment and other practical work, especially Ian Airdrie for his eagerness and readiness to always assist. They have been very patient and cooperative with me, and I have acquired a lot of practical skills and techniques from them.

I owe a special thanks to my brother, Adewale Aladeokin, who has supported me emotionally and financially throughout my PhD program. He has played a major role in my personal and professional growth, and he has always been there for me as a brother, as well as a father figure since I lost my dad. He is a rare gem, and I will always be grateful for everything he has done. I am most blessed to have him as my brother.

Finally, I owe a special debt of gratitude to my parents, who have always been there for me with their unconditional love and support. They have instilled in me the values of hard work, perseverance, resilience, and honesty. Although my dad is no longer with us, he was always a loving and caring father, and I miss him dearly.

Abstract

Modern society has undergone rapid industrialization, which has led to various environmental and health challenges on a global level. Some of the main contributors to these challenges are the industrial discharge of organic dyes, oils, solvents, metal ions etc. and this situation constitutes a serious global concern. Industrial and agricultural effluents are abundant and feasible sources of water; however, these require treatment to protect the ecosystem and enable their reuse. Among various methods employed in the treatment of wastewater, adsorption is one of the most feasible and effective methods. Adsorption processes employ solid materials, known as adsorbents, to facilitate the removal of contaminants from water. Activated carbon (AC) is a widely used adsorbent that has high porosity and adsorption capacity for various contaminants. However, the production of commercial AC faces the challenges of high cost and scarcity of raw materials, due to the high demand of commercial ACs for multiple purposes. Therefore, there is a need to develop low-cost and alternative AC materials by exploring the use of renewable and abundant resources, such as biomass.

This work aims to synthesise AC materials from peanut shells, which are an agricultural by-product with high carbon content and potential as a low-cost and renewable precursor for AC production, and to optimise the activation variables (temperature, hold-time, and impregnation ratio, i.e., activating agent weight / precursor weight), to obtain AC materials with high surface areas and yields. Previous studies on peanut shells have lacked a focus in identifying the controlling activation variables to enhance the properties of peanut derived carbon materials. To bridge this gap, the current work employs a single stage chemical activation process, using $ZnCl_2$ as an activating agent, and investigates the effects of activation variables on the

properties of AC derived from peanut shells. A design of experiment (DoE) is used to generate a set of experimental design points and obtain a response surface of the results, to visualise the relationship between the responses (surface area and yield) and the independent variables, demonstrating how to model the synthesis of AC from biomass.

The work characterises the AC materials synthesised from peanut shells using various techniques, such as Brunauer-Emmett-Teller (BET) analysis of nitrogen adsorption data, Fourier transform infrared spectroscopy (FTIR), X-ray photoelectron spectroscopy (XPS), and scanning electron microscopy (SEM). Textural analysis revealed that the synthesised AC materials have relatively high surface areas and porosities, indicating the effectiveness of the chemical activation method, using $ZnCl_2$ as an activating agent. Response surface analysis revealed that temperature and impregnation ratio were the most significant variables in determining the characteristics of the AC materials derived from peanut shells. As revealed, by both textural and surface chemistry analyses, the synthesised AC materials show heterogeneous characteristics.

Furthermore, the work provided a screening analysis to select the most effective candidate among the synthesised AC materials, allowing its performance for the removal of ionic dyes (methyl orange, MO and methylene blue, MB) from water to be evaluated. The most effective candidate, denoted as PNTS2-600-15, was obtained under the following activated conditions: temperature of 600 °C, hold time of 15 min and an impregnation ratio of 2. PNTS2-600-15 showed low moisture and ash contents, indicating the high quality of the sample. The adsorption performance of PNTS2-600-15 for MO and MB dyes was investigated by varying the contact time, solution pH, and initial dye concentration. The experimental data were fitted using a number of kinetic and isotherm models to elucidate the adsorption mechanism, and capacity of the carbon material. The results indicate that a pseudo-second-order kinetic model,

and the Freundlich and Sips isotherm models, provided the best fit for the adsorption data of both dyes. The Sips model estimated the maximum adsorption capacities of PNTS2-600-15 for MO and MB to be 4584 mg g^{-1} and 1769 mg g^{-1}, respectively. These show outstanding capacities in comparison with other AC materials reported in the literature.

Finally, the mechanism of adsorption involved in the adsorption processes for MO and MB dyes on PNTS2-600-15 was further investigated, using several experimental techniques, such as post-adsorption characterisation of the textural and surface properties of the carbon material, and desorption studies of the adsorbed dyes. The adsorption mechanism was mainly attributed to π–π interactions, n–π electron donor-acceptor (EDA) interactions, and pore filling. The AC material exhibited good reusability and stability, achieving over 90% dye removal, after five cycles of regeneration.

This work demonstrates that peanut shells can be used as a low-cost and effective precursor for AC production, and that the properties and performance of the AC materials can be tuned and tailored by manipulating the activation variables. The work contributes to the development of sustainable and alternative AC materials for water remediation applications.

Table of Contents

List of Abbreviations

AC – activated carbon

ANOVA – analysis of variance

BBD – Box-Behnken design

BET – Brunauer-Emmett-Teller

BJH – Barrett-Joyner-Halenda

CCC – circumscribed central composite design

CCD – central composite designs

CCF – face-centred central composite design

CCI – inscribed central composite design

C_e – equilibrium concentration

C_0 – initial concentration

C.V. – coefficient of variation

DoE – design of experiment

EDA – electron donor-acceptor

FTIR – Fourier transform infrared spectroscopy

IPD – intraparticle diffusion

I.R. – impregnation ratio

IUPAC – International Union of Pure and Applied Chemistry

k_1 – PFO rate constant

k_2 – PSO rate constant

K_F – Freundlich constant

k_{int} – IPD rate constant

K_S – Sips equilibrium constant

K_L – Langmuir equilibrium constant

MB – methylene blue

MO – methyl orange

n_S – Sips model exponent

p/p^0 – relative pressure

PFO – pseudo-first order

pH – power of hydrogen

PNTS – peanut shells

PSD – pore size distribution

PSO – pseudo-second order

PZC – point of zero charge

q_e – adsorbate uptake at equilibrium

$q_{e,exp}$ – adsorbate uptake at equilibrium (experimental)

$q_{e,cal}$ – adsorbate uptake at equilibrium (calculated)

Q_m – maximum adsorption capacity

Q_S – Sips adsorption capacity

q_t – adsorbate uptake at time t

R.R. – reagent recovery

RMSE – root mean square error

RSM – response surface methodology

S – surface area

SEM – scanning electron microscope

$S(BET)$ – BET surface area

SSE – sum of squared error

S_{Micro} – micropore area

S_{Meso} – mesopore area

TPV – total pore volume

V_{mic} – micropore volume

XPS – X-ray photoelectron spectroscopy

1/n – Freundlich parameter

Chapter 1: Introduction

1.1 Water pollution and industrialization

Water pollution is a serious environmental problem that affects the health and well-being of humans, animals, and plants. One of the major sources of water pollution is the rapid industrialization of the modern world, which has resulted in numerous environmental and health challenges, on a global scale. Industrial and agricultural activities generate wastewater effluents that contain harmful substances, such as organic dyes, oil and solvents, metal ions, pesticides, etc. [1, 2]. These substances contaminate water sources and make them unfit for use or damage the natural ecosystems. Water pollution can have various effects, such as reducing the availability and quality of freshwater, causing diseases and deaths, disrupting food chains and biodiversity, and contributing to climate change. The United Nations World Water Development Report 2017 estimated that more than 80% of global wastewater was discharged into the environment without adequate treatment, with approximately 38% and 16% being industrial and agricultural wastewater, respectively [3]. This situation has become a pressing global issue that requires treatment to protect the ecosystem and facilitate the reuse of water sources. Organic pollutants, which are broad carbon-containing compounds derived from natural or synthetic sources, have been the focus of considerable scientific literature due to their environmental persistence, potential bioaccumulation and toxicity effects, etc. [4-6]. Therefore, it is important to understand the causes and effects of water pollution and to take action to prevent and control it.

1.1.1 Organic pollutants in wastewater and treatment techniques

The release of diverse classes of organic compounds, including dyes, phenols, and nitroaromatics, into aquatic ecosystems without adequate treatment poses significant

threats to environmental and human health [4, 5]. They can enter the aquatic environment through various pathways, such as domestic sewage, industrial effluents, agricultural runoff, oil spills, etc. [7, 8]. A variety of organic pollutants exist, but the main categories of organics are illustrated in Figure 1.1

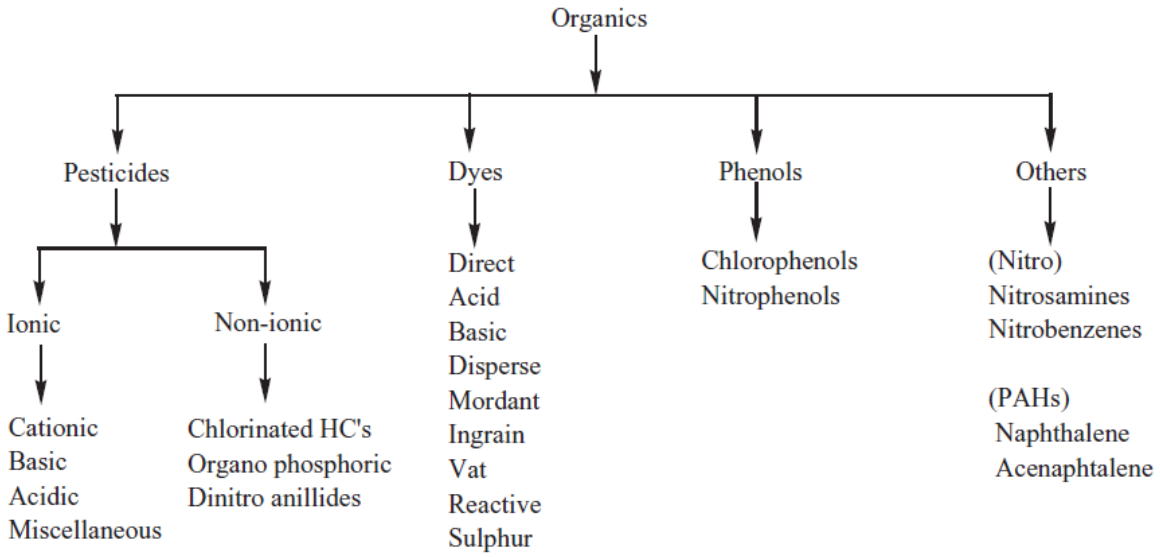

Figure 1.1. Main categories of organic pollutants [4]

Organic pollutants can have various effects on the environment and water quality, depending on their properties, concentrations, and interactions with other substances and organisms. Some of the effects are [7, 9, 10]:

- **Reduction of dissolved oxygen:** Organic pollutants can be degraded by microorganisms that use oxygen as an electron acceptor. This process consumes oxygen from the water and lowers the dissolved oxygen concentration, which can affect the survival and growth of aquatic life. The degree of oxygen depletion depends on the amount and type of organic pollutants, the temperature, the flow rate, and the availability of oxygen in the water.
- **Toxicity and bioaccumulation:** Organic pollutants can be toxic to aquatic organisms, causing acute or chronic effects, such as mortality, reduced growth,

impaired reproduction, altered behaviour, etc. Some organic pollutants can also bioaccumulate in the tissues of aquatic organisms, especially in fatty tissues, and biomagnify along the food chain, reaching higher concentrations in top predators. This can pose a risk to the health of wildlife and humans that consume contaminated fish or shellfish.

- **Endocrine disruption:** Some organic pollutants can interfere with the normal functioning of the endocrine system, which regulates the hormones and physiological processes of organisms. These pollutants are called endocrine disruptors and can mimic or block the action of natural hormones, such as estrogen, testosterone, thyroid hormones, etc. This can result in adverse effects on the development, growth, reproduction, metabolism, and behaviour of aquatic organisms, as well as humans.
- **Alteration of water quality parameters:** Organic pollutants can affect the physical and chemical properties of water, such as colour, odour, taste, pH, turbidity, conductivity, etc. These changes can reduce the aesthetic and potable value of water and increase the cost and difficulty of water treatment. For example, organic pollutants can react with chlorine or other disinfectants and form disinfection by-products, such as trihalomethanes, which are carcinogenic and mutagenic.

A wide variety of techniques are used to remove organic pollutants from wastewater: the common techniques include coagulation–flocculation, ozonation, ion exchange, reverse osmosis, advanced oxidation processes and adsorption [11-18].

Coagulation-flocculation: This technique involves adding chemicals to the wastewater to form clumps of particles that can be easily separated from the water. The chemicals, called coagulants and flocculants, help to bind the organic contaminants and other suspended solids together. The clumps, called flocs, can then be removed by sedimentation, flotation, or filtration.

Ozonation: This technique involves injecting ozone gas into the wastewater to oxidize the organic contaminants. Ozone is a powerful oxidant that can break down the molecular bonds of organic compounds and convert them into harmless substances, such as carbon dioxide and water. Ozonation can also disinfect the wastewater by killing bacteria and viruses.

Ion exchange: This technique involves exchanging the ions of the organic contaminants with the ions of a resin or a membrane. The resin or membrane called an ion exchanger, can be cationic, anionic, or mixed. Ion exchange can remove organic pollutants that have ionic properties, such as metal ions, nitrate, phosphate, etc.

Reverse osmosis: This technique involves applying high pressure to the wastewater to force it through a semi-permeable membrane that can filter out the organic contaminants and other dissolved solids. The membrane, called reverse osmosis membrane, can be made of polyamide, cellulose acetate, or other materials. Reverse osmosis can produce high-quality water that can be reused or discharged.

Advanced oxidation processes: These processes involve generating highly reactive species, such as hydroxyl radicals, to degrade the organic contaminants in the wastewater. The reactive species can be generated by various methods, such as ultraviolet light, hydrogen peroxide, ozone, etc. Advanced oxidation processes can remove persistent and toxic organic pollutants, such as Polycyclic aromatic hydrocarbons (PAHs), Polychlorinated biphenyls (PCBs), etc.

Biological treatment: This process uses microorganisms, such as bacteria, algae, or fungi, to break down organic pollutants in wastewater. Biological treatment can be aerobic, requiring oxygen, or anaerobic, not requiring oxygen. It can remove organic matter, nutrients, pathogens, and some metals from wastewater. This technique is often used as a secondary treatment method, following the removal of solids and oil by primary treatment methods, such as sedimentation or dissolved air flotation.

Biological treatment can improve the quality of wastewater before it is discharged into the environment or reused for other purposes.

Adsorption: This technique involves passing the wastewater through, or mixing with, a bed of porous material that can attract and retain the organic pollutants on its surface. Adsorption is a simple and versatile process that can remove a wide range of organic pollutants, including recalcitrant and persistent ones, such as dyes, phenols, pesticides, etc.

Table 1.1 below shows the merits and demerits of the treatment techniques discussed above.

Table 1.1. The merits and demerits of common treatment techniques employed in the removal of organic contaminants from wastewater.

Technique	Merits	Demerits
Coagulation–flocculation	Effective for removing turbidity and suspended solids. Relatively low investment cost. It can reduce the formation of disinfection by-products, such as trihalomethane (THM) and haloacetic acids, by removing precursors of these compounds. Removes a wide range of organic pollutants.	High operational cost due to chemical consumption. Less effective in removing organic pollutants that have low molecular weight, high solubility, or strong polarity. It may be influenced by various factors, such as pH, temperature, water quality, and coagulant type, that need to be controlled to achieve the desired removal efficiency. May generates a large amount of sludge.
Ozonation	Highly efficient at killing bacteria, viruses, and protozoa. Oxidizes inorganic and organic impurities, such as iron, manganese, sulphur, dyes, phenols, pesticides, etc. Produces less THM disinfection by-products than chlorination.	Toxic and requires consistent monitoring and safety measures. Expensive and requires high automation and reliability. It can form bromate, a carcinogenic by-product, if bromine is present in the water. It may not achieve complete mineralization of the organic pollutants, leaving behind some residual compounds that may require further treatment.
Ion exchange	Removes a wide range of organic contaminants natural organic matter, heavy metal ions, anions, boron, etc. Low running cost and energy consumption. Can handle shock loadings and operate over a wide range of temperatures.	Easily fouled by organic matter, iron, or calcium sulphate. High initial investment and frequent regeneration or replacement of the resin to maintain its performance. It may generate secondary pollutants, such as brine or spent regenerant, that require further treatment or disposal.

Table 1.1. The merits and demerits of common treatment techniques employed in the removal of organic contaminants from wastewater (continued).

Technique	Merits	Demerits
		It may have limited capacity and selectivity for some organic contaminants, especially those with low molecular weight or low charge.
Reverse osmosis	High removal efficiency- can remove up to 99% of organic contaminants, as well as other pollutants such as salts, metals, and microorganisms. Low chemical usage. Compact design.	High energy consumption. Membrane fouling, leading to frequent cleaning and replacement. Produces a concentrated stream of pollutants, which can pose challenges for disposal or further treatment due to its high salinity, toxicity, and volume. High initial investment and maintenance cost. Removes beneficial minerals from water.
Advanced oxidation processes	High removal efficiency. Rapid and non-selective degradation of persistent and toxic organic pollutants, such as PAHs, PCBs, etc. Small footprint and low retention time. Low chemical usage.	Requires high energy input and produces heat. Expensive and complex to operate and monitor. It can form bromate or other by-products if bromine or chlorine is present in the water. It may not achieve complete mineralization of the organic pollutants, leaving behind some residual compounds that may require further treatment.
Biological treatments	Environmentally friendly. Cost-effective and can handle a wide range of pollutants. Can produce valuable products, such as biogas, biomass, or fertilizers.	Sensitive to environmental conditions, such as temperature, pH, dissolved oxygen, etc. Can generate an excess amount of sludge. Slow process, as they depend on the growth and activity of microorganisms.
Adsorption	A simple and versatile method for removing a variety of organic and inorganic pollutants, including persistent ones. High removal efficiency. Environmentally friendly and cost-effective. Can use various natural and/or synthetic adsorbents, such as activated carbon, zeolite, clay, etc. Can be combined with other advanced oxidation processes to enhance the removal efficiency and regenerate used adsorbents.	May depend on pH. Limited by the adsorption capacity and selectivity of the adsorbent. Has a limited adsorbent life. It may generate secondary pollutants, such as spent adsorbents or desorption effluents, that need further treatment or disposal.

Due to the economic and environmental challenges, most of these conventional methods for treating wastewater containing organic pollutants have not been

extensively implemented on a large scale [19, 20]. Among these techniques, adsorption is one of the most widely used techniques for the treatment of wastewater [4, 5]. Adsorption processes have several advantages over other technologies, such as simplicity of design and operation, high removal efficiency, applicability in batch and continuous modes, tolerance to toxic substances, low cost and potential for regeneration and reuse [21-24].

The application of adsorption technology to wastewater treatment necessitates the choice of a proper media to accomplish the separation, or purification objectives. Various materials, with distinct structure and texture, are employed as media in adsorption processes, depending on their specific application. Solid materials that can adsorb species from gaseous or liquid phases are termed adsorbents. Silica gel, polymers, activated alumina, zeolites, ion exchange resin, and activated carbons are some of the several adsorbents available for commercial use, which are discussed below.

- **Silica gel:** This is a synthetic material made from silica, which is a form of silicon dioxide. It has a high porosity and can adsorb water and other polar molecules. It is commonly used as a desiccant, a catalyst support, and a chromatographic medium [25, 26].
- **Polymers:** These are synthetic or natural materials made from long chains of repeating units, called monomers. They have various properties and applications, depending on their chemical structure and composition. Some polymers can act as adsorbents, such as polyacrylamide, polyvinyl alcohol, and chitosan. They can adsorb organic pollutants, such as dyes, phenols, and pharmaceuticals, as well as metal ions [26, 27].
- **Activated alumina:** This is a porous material made from aluminum oxide. It has a high surface area and can adsorb water, fluoride, arsenic, and other contaminants. It is mainly used for water treatment, catalyst support, and gas drying [28].

- **Zeolites:** These are natural or synthetic materials made from aluminosilicates. They have a crystalline structure with regular pores and cavities. They can adsorb molecules based on their size, shape, and polarity. They are used for gas separation, water softening, ion exchange, and catalysis [27].
- **Ion exchange resin:** This is a type of material that can exchange ions with a solution. It is usually made of organic polymers that have ion exchange sites, where different types of ions are attached. These ions can be replaced by other ions in the solution, depending on their charge and size. Ion exchange resin is used for various purposes, such as water softening, water purification, and biodiesel filtration [27].
- **Activated carbons (AC):** These are porous materials made from carbonaceous sources, such as coal, wood, or coconut shells. They have a large surface area and can adsorb a wide range of organic and inorganic pollutants, such as dyes, pesticides, metals, and gases. They are widely used for water and air purification, gas separation, and solvent recovery [29].

As a porous solid media, AC offers high porosities that facilitate its application as an adsorbent for diverse industrial purposes in the contemporary era [30]. According to Yurtay *et al*. [31], the global AC market was valued at USD 5.75 billion in 2020 and is projected to reach USD 8.61 billion by 2025. The market report indicates the extensive utilization of AC in various applications. Most of the carbon-based materials, including commercial AC, are conventionally derived from non-renewable fossil-based precursors [31, 32]. The high demand for commercial AC for several applications has resulted in the high cost and scarcity of raw materials for AC production. Therefore, many researchers have explored renewable precursors from agricultural/food waste sources, such as nut shells, cotton stalks, rice husk, coconut shells, and papaya seeds [26, 33-38], to reduce the production cost of AC and enhance

the sustainability and circular economy [31, 39]. Directive 2009/28/EC, also, recommends the utilization of renewable sources such as biomass, which is defined as any biological material derived from plant or animal sources as well as any kind of biodegradable waste from agricultural, industrial, and municipal activities, for energy and value-added products production [40, 41].

Agricultural crop residues, which are the leftover parts of crops after harvesting or processing, are a major source of biomass. Peanuts are one such crop that produces peanut shells (husk) as residues after processing. The peanut (*Arachis hypogaea*), also called groundnut, goober, or monkey nut, is a leguminous crop that is widely cultivated mainly for its edible seeds; it can be grown in tropical and subtropical regions, as well as in warmer temperate zones, and undercover in cooler climates [40, 42]. The global production of peanuts has increased in the last decade, owing to their perceived health benefits, reaching a total of ~41.4 MMT in 2019/2020 [43]. Peanuts and other nut shells, which are often regarded as waste and utilised for their fuel value in different parts of the world [40], can be converted into more valuable products, such as AC [32, 44]. Previous studies have reported the use of peanut shells as a precursor for AC production [22, 44-48], achieving surface areas up to 1200 m^2/g; however, these studies have lacked a focus on identifying the controlling variables to enhance the carbon properties, which is investigated within this study – more details of this gap will be presented in subsequent sections.

1.2 History of AC

ACs have a long history, dating back to 1600 B.C. when Egyptians used wood chars for medical applications [29, 49]. Around 400 B.C., ancient Hindus and Phoenicians discovered the healing properties of AC and started to use it for water purification. In the 1700s – 1900s, carbon was used for various applications such as eliminating odours, decolourizing in sugar refining, purifying water and providing medical treatment. In the 20th century, during the World Wars, carbon was employed in gas

masks to filter out lethal gases; the production and use of AC increased after the World Wars, resulting in the development of modern AC air and water filters [29, 50]. AC has a large surface area, which can vary depending on the source material and activation method, but it typically ranges from 500 to 1500 m^2/g for commercial AC and is used for various applications such as water treatment, air and gas purification, metal recovery, food and beverage processing, and medical purposes, nowadays [51, 52].

1.3 Synthesis of AC

Activated carbon and activated charcoal are two terms that are used interchangeably. Activated charcoal is made from charcoal (char), which is a form of carbon that is made from organic materials, such as wood, through a process called pyrolysis. Pyrolysis is the thermal decomposition (300 – 500 °C) of biomass in the absence of oxygen, which prevents combustion and produces a mixture of carbon-rich solids (charcoals), and gases (syngas) [1]. The surface area of charcoal may range from 400 – 800 m^2/g [53, 54], which can be further enhanced by various activation techniques to create AC with high adsorption capacity.

A general overview of AC preparation reveals two main approaches: physical and chemical methods. The physical method involves carbonising carbonaceous materials (usually biomass with carbon content > 45% [55]) under inert conditions, as discussed above, followed by partial gasification of the char with oxidising gases such as carbon dioxide, steam, air, or their mixtures at high temperatures, between 700 – 1000 °C, to improve the pore structure. Physical activation processes have the advantage of being low-cost, due to the lack of chemicals and post-washing [9, 31, 32].

In contrast, chemical methods, which are performed at lower temperatures, below 700 °C, involve the addition of dehydrating agents, such as $ZnCl_2$, phosphoric acid, KOH, etc, to influence the carbonisation and prevent the formation of tar, thus increasing the carbon yield [56]. Chemical activation methods, where inorganic salts,

such as $ZnCl_2$, act as activating agents, allow the recovery and reuse of the salt for the same purpose. Previous studies [57-62] have employed different activating chemical agents, such as $ZnCl_2$, $CaCl_2$, KOH, etc., on various biomass to synthesise AC, and they have demonstrated that $ZnCl_2$ was more effective in creating high-quality carbon materials. An effective activating agent is a crucial factor in the production cost of AC [33]. Among other activating agents, $ZnCl_2$ is widely recognised for its effectiveness in enhancing the porosity of porous carbonaceous materials, through the initial breakdown of the biomass structure, followed by dehydration during the carbonisation step that results in char formation, creation of aromatic graphitic compounds and pore structure [56, 63, 64].

Chemical activation typically produces higher surface area and yield. The yield from physical activation is often lower due to the two-step process (carbonisation and activation) that operates at high temperatures. In chemical activation, a template of micropore is formed when carbonisation takes place around fine crystals of inorganic salt, and the removal of the salt by acid washing after carbonisation results in micropores with larger diameters than those formed by physical activation [29, 55]. By applying this method, one can synthesise carbon materials that possess larger micropores for the adsorption of larger molecular species, which would benefit their performance in liquid-phase applications. Overall, chemical activation is advantageous over physical activation in that it enhances the process yield and produces carbon materials with better surface chemistry and textural properties [55].

According to Saleem *et al*. [65], the overall chemical activation method can be carried out in one, two or three stage(s). In the one-stage process, the precursor material and the activating chemical are mixed and then heated in a furnace to the predetermined activation temperature in a single cycle. The two-stage process consists of two steps: first, the precursor material is charred at a temperature between 400 and 550 °C; second, the char is mixed with the activating chemical and then activated in the

furnace in the second step. The three-stage process differs from the two-stage process only in the addition of a preliminary stage one pretreatment step, which could involve, for instance, the solvent extraction of some impurities in the precursor.

The literature has reported on the impact of various activation parameters, such as impregnation ratio, temperature, time, and particle size, on the carbon yield and properties, using different precursors [59, 61, 63, 66]. Among these parameters, impregnation ratio and temperature were reported to be the most influential factors for the carbonisation process. However, the significance of activation time has also been investigated by some studies [58, 67], which revealed that carbon pore structure could be altered by the sintering effect and the yield could reduce at extended activation time. In light of these previous studies, the current study has chosen to focus on the following activation parameters: temperature, impregnation ratio, and hold time.

The production of AC involves two key factors: yield and surface area. The former reflects the economic viability of the process, while the latter indicates the adsorption potential of the product [41]. These two responses are often inversely related, and thus, it is essential to optimise the production process for large-scale applications. To achieve this goal, a conventional approach which involves changing one experimental factor at a time can be employed. However, this usually results in a large number of experimental runs. Alternatively, Design of Experiments (DoE) is a more efficient method that can simultaneously examine the interactions between experimental factors and reduce the number of experimental runs [68]. Response surface methodology or modelling (RSM) is a valuable technique within DoE that facilitates the optimisation of parameters by studying their combined effects [69, 70]. Chapter 4 provides a comprehensive overview of DoE and its applications.

Other relevant factors in the production of AC, that are examined in this study include pore size distribution (PSD), density and reagent recovery. PSD affects the adsorption

capacity and rate capability of AC. Different adsorbates require different pore configurations for optimal adsorption. Small, low-volume pores increase the surface area available for adsorption. The density of AC contributes to its overall mass and volume, which are important for practical applications like water purification and gas storage. A higher density can indicate a higher proportion of carbon content, which may enhance the adsorption performance for certain applications. [52, 71, 72]. Recovering and reusing chemical reagents can significantly reduce the production costs. The use of chemical activators can lead to environmental concerns. By recovering these chemicals, the overall environmental footprint of the production process is reduced [33].

1.4 Characterisation and features of AC

The properties and performance of porous carbon materials, which have diverse applications in environmental remediation, energy storage, catalysis, gas purification, chemical storage and purification, and electrode materials, can be assessed by characterisation [73]. The interaction and efficacy of AC with various substances for contaminant removal or energy storage depend on its characterisation parameters, such as surface area, pore size distribution, surface chemistry, thermal stability, and adsorption capacity [74, 75]. Moreover, the characterisation of AC facilitates the optimisation of the synthesis process and the selection of the appropriate precursor and activating agent for specific applications [76].

AC, a form of graphite composed of pure carbon, exhibits an amorphous and porous morphology. AC is used in various applications, and its application in adsorption processes depends on the following main features [23, 65].

- high surface area
- porosity
- surface functional groups

Adsorption capacity is proportional to the surface area of an adsorbent; hence a higher surface area is desirable for this process. Another relevant characteristic of AC for adsorption is porosity, which refers to the ratio of the total pore volume to the volume of the particles. The porosity of a material depends on the size, shape and distribution of the particles that constitute the material. AC materials contain pores of various sizes, which are categorised by IUPAC as micropore, mesopore and/or macropore. These pore types have distinct effects on the porosity and performance of AC. Micropores are in the form of 2D spaces between two graphitic walls, where the majority of adsorption occurs [29]. Micropore volume contributes immensely to the surface area of ACs, whereas the larger pores facilitate the diffusion of adsorbate molecules, which is essential for the kinetics and design of adsorption processes, especially in a liquid phase. The majority of ACs possess surface oxygen functional groups, which may originate from the precursor material, the activation process, or the storage conditions. These groups confer polar characteristics, such as hydrophilicity, to the AC surface [29, 77]. Surface oxygen functional groups can be present on AC as acidic surface oxides, such as carboxylic, phenolic, or carbonyl groups, or as basic surface oxides, such as cyclic ether groups. These groups endow the surface of AC with the ability to attract some target species. In addition, ash content is another important feature of AC. The percentage of ash in AC may vary between 1 and 12. A lower proportion of ash indicates a higher quality of carbon material, which enhances the potential of AC to remove organic contaminants from an aqueous phase owing to their hydrophobic characteristics [29, 78].

1.5 Forms of AC and their applications

The main forms of AC in commercial applications are powdered ACs (PAC) and granular ACs (GAC). Wood-derived sawdust is the common precursor for PAC, with an average size of 15 – 25 μm [79]. The PAC adsorption process typically involves mixing the PAC with liquid and then separating them, as the particle size may cause

a high pressure drop in column designs. PAC is widely used for decolourization in food processes, such as wine production, sugar refining, oil production, and water treatment. GACs have larger particle sizes than PACs and are in the form of crushed or pelletised granules that are derived from PAC through a process of granulation with binders such as coal tar pitch. GACs have applications in both gas and liquid phases. In the gas phase, GACs are used in air and gas purification, solvent recovery, etc. In the liquid phase, GACs are used in wastewater treatment, colour removal from food products, improving the odour and taste of water, and providing other benefits. GACs have operational advantages over PACs, such as ease of handling and low pressure drop in adsorption columns. Furthermore, most spent GACs can be regenerated and reused for multiple adsorption cycles [23, 29, 79].

1.6 An overview of AC applications

Given the characteristics of ACs elucidated in the preceding section, they have a wide range of applications in various domains. One of the main applications of ACs is the removal of pollutants from liquid and gaseous phases, such as wastewater treatment and gas purification. Another important application of ACs is the storage of energy in devices such as supercapacitors, hydrogen storage systems, and batteries, which benefit from the high surface area of ACs. ACs also have medicinal applications, such as detoxification, adsorption of toxins and drugs, and wound healing. In the agricultural sector, ACs can improve the quality of animal feed, decolourize white grape extract, and eliminate pesticides and herbicides from soil and water. Moreover, ACs can be used as food additives, improving the taste, odour and shelf-life properties of food products. They can also improve the quality of alcoholic beverages by removing undesirable compounds and improving clarity and flavour. Additionally, ACs have cosmetic applications, such as exfoliating, cleansing and moisturizing the skin. Finally, ACs have industrial applications, such as mercury scrubbing from flue

gas emissions and metal polishing by removing impurities from electroplating solutions [52, 73].

In the present study, peanut shells were selected as a precursor for AC synthesis. Previous research on peanut shells [44, 46] followed a two-stage process to produce carbon materials: precursor charring and chemical activation. However, these studies lacked adequate details on the effects of the activation variables, such as precursor to chemical agent ratio, activation temperature and time, on the final characteristics of the resulting carbons and the optimisation of the activation variables. The optimal ratio of precursor to chemical agent, which ensures high yield and surface area of the AC, and the optimal activation temperature and time, which prevent incomplete carbonization, are critical factors for large-scale production of AC. The performance of the ACs synthesised from peanut shells in this study is evaluated using methyl orange (MO) and methylene blue (MB). MB and MO are cationic and anionic organic dyes, respectively, that are commonly employed in various industries and pose serious threats to living organisms and the entire ecosystem if discharged into the environment without treatment. These organic dyes have high resistance to natural degradation [80, 81]. They are large heterocyclic aromatic compounds that are commonly used to assess the structure and adsorption capacity of ACs, as the accessible surface of an adsorbent for a large molecule is restricted by the molecular sieving effect [81, 82]. The high surface areas generated by the micropores and mesopores in the synthesised ACs were anticipated to offer sites for dye adsorption, and the larger mesopores and macropores should facilitate dye diffusion [83, 84]. The application of the synthesised ACs in this study is not limited to MB and MO, other pollutants such as phenol are proposed to be examined in future studies.

References

[1] Sabzehmeidani, M. M., Mahnaee, S., Ghaedi, M., Heidari, H. and Roy, V. A. (2021). Carbon based materials: A review of adsorbents for inorganic and organic compounds. Mat. Adv. 2**:** 598-627. https://doi.org/10.1039/D0MA00087F

[2] Edebali, S. (2019). *Advanced sorption process applications*, BoD–Books on Demand.

[3] U.N.E.S.C.O, W. W. a. P. (2017). *Wastewater: the untapped resource; facts and figures* [Online]. Available: https://unesdoc.unesco.org/ark:/48223/pf0000247553 [Accessed 14 August 2023].

[4] Kushwaha, S., Soni, H., Ageetha, V. and Padmaja, P. (2013). An Insight Into the Production, Characterization, and Mechanisms of Action of Low-Cost Adsorbents for Removal of Organics From Aqueous Solution. Critical Reviews in Environmental Science and Technology 43**:** 443-549. 10.1080/10643389.2011.604263

[5] Yu, Y., Qiao, N., Wang, D., Zhu, Q., Fu, F., Cao, R., Wang, R., Liu, W. and Xu, B. (2019). Fluffy honeycomb-like activated carbon from popcorn with high surface area and well-developed porosity for ultra-high efficiency adsorption of organic dyes. Bioresour Technol 285**:** 121340. https://doi.org/10.1016/j.biortech.2019.121340

[6] Arman, N. Z., Salmiati, S., Aris, A., Salim, M. R., Nazifa, T. H., Muhamad, M. S. and Marpongahtun, M. (2021). A review on emerging pollutants in the water environment: Existences, health effects and treatment processes. Water 13**:** 3258

[7] Bakiu, R., Roncarati, A. and Kamberi, E. (2023). Inorganic and organic pollutants in marine and coastal environments. Frontiers in Marine Science 10**:** 1245833

[8] Dheenadayalan, G. and Thiruvengadathan, R. (2021). Remediation of Organic Pollutants in Water. Water Pollution and Remediation: Organic Pollutants**:** 501-517

[9] Ruziwa, D. T., Rutsito, D. D. and Chaukura, N. (2022). Environmental Pollutants: Organic and Emerging Contaminants. *Biotechnology for Environmental Protection.* Springer

[10] Wts. *Biological Wastewater Treatment* [Online]. Available: https://watertreatmentservices.co.uk/biological-wastewater-treatment-how-does-it-work/ [Accessed 14 August 2023].

[11] Zolezzi, C., Ihle, C. F., Angulo, C., Palma, P. and Palza, H. (2018). Effect of the oxidation degree of graphene oxides on their adsorption, flocculation, and antibacterial behavior. Industrial & Engineering Chemistry Research 57**:** 15722-15730

[12] Li, R., Gao, B., Guo, K., Yue, Q., Zheng, H. and Wang, Y. (2017). Effects of papermaking sludge-based polymer on coagulation behavior in the disperse and reactive dyes wastewater treatment. Bioresource Technology 240**:** 59-67

[13] Mashtalir, O., Cook, K. M., Mochalin, V. N., Crowe, M., Barsoum, M. W. and Gogotsi, Y. (2014). Dye adsorption and decomposition on two-dimensional titanium carbide in aqueous media. Journal of Materials Chemistry A 2**:** 14334-14338

[14] Danwittayakul, S., Jaisai, M. and Dutta, J. (2015). Efficient solar photocatalytic degradation of textile wastewater using ZnO/ZTO composites. Applied Catalysis B: Environmental 163**:** 1-8

[15] Omi, F. R., Choudhury, M. R., Anwar, N., Bakr, A. R. and Rahaman, M. S. (2017). Highly conductive ultrafiltration membrane via vacuum filtration assisted layer-by-layer deposition of functionalized carbon nanotubes. Industrial & Engineering Chemistry Research 56**:** 8474-8484

[16] Kalyani, D., Telke, A., Dhanve, R. and Jadhav, J. (2009). Ecofriendly biodegradation and detoxification of Reactive Red 2 textile dye by newly isolated Pseudomonas sp. SUK1. Journal of hazardous materials 163**:** 735-742

[17] Shen, Y., Fang, Q. and Chen, B. (2015). Environmental applications of three-dimensional graphene-based macrostructures: adsorption, transformation, and detection. Environmental Science & Technology 49**:** 67-84

[18] Rashed, M. N. (2013). Adsorption technique for the removal of organic pollutants from water and wastewater. Organic pollutants-monitoring, risk and treatment 7**:** 167-194
[19] Sangamnere, R., Misra, T., Bherwani, H., Kapley, A. and Kumar, R. (2023). A critical review of conventional and emerging wastewater treatment technologies. Sustainable Water Resources Management 9**:** 58
[20] Teh, C. Y., Budiman, P. M., Shak, K. P. Y. and Wu, T. Y. (2016). Recent advancement of coagulation–flocculation and its application in wastewater treatment. Industrial & Engineering Chemistry Research 55**:** 4363-4389
[21] Rathi, B. S. and Kumar, P. S. (2021). Application of adsorption process for effective removal of emerging contaminants from water and wastewater. Environ. Pollut. 280**:** 116995. https://doi.org/10.1016/j.envpol.2021.116995
[22] Ahmad, M. A., Yusop, M. F. M., Zakaria, R., Karim, J., Yahaya, N. K. E., Yusoff, M. a. M., Hashim, N. H. F. and Abdullah, N. S. (2021). Adsorption of methylene blue from aqueous solution by peanut shell based activated carbon. Mater Today Proc 47**:** 1246-1251. https://doi.org/10.1016/j.matpr.2021.02.789
[23] Nazal, M. K. (2020). An overview of carbon-based materials for the removal of pharmaceutical active compounds. Carbon-Based Material for Environmental Protection and Remediation
[24] Arshadi, M., Mousavinia, F., Amiri, M. and Faraji, A. (2016). Adsorption of methyl orange and salicylic acid on a nano-transition metal composite: Kinetics, thermodynamic and electrochemical studies. Journal of colloid and interface science 483**:** 118-131
[25] Ali, M., Hoque, M., Safdar Hossain, S. and Biswas, M. (2020). Nanoadsorbents for wastewater treatment: next generation biotechnological solution. International Journal of Environmental Science and Technology 17**:** 4095-4132
[26] Seader, J., Henley, E. J. and Roper, D. K. (2016). *Separation process principles: With applications using process simulators*, John Wiley & Sons.
[27] Alan Gabelman, P. E. (2017). *Adsorption Basics* [Online]. Available: https://www.aiche.org/resources/publications/cep/2017/august/adsorption-basics-part-2 [Accessed 14 August 2023].
[28] Seader, J., Henley, E. and Roper, D. 2006. Separation Process Principles, 3rd. Edition.
[29] Suzuki, M. and Suzuki, M. (1990). *Adsorption engineering*, Kodansha Tokyo.
[30] Sricharoenchaikul, V., Pechyen, C., Aht-Ong, D. and Atong, D. (2008). Preparation and characterization of activated carbon from the pyrolysis of physic nut (Jatropha curcas L.) waste. Energy Fuels 22**:** 31-37. https://doi.org/10.1021/ef700285u
[31] Yurtay, A. and Kılıç, M. (2022). Fast and effective production of industrial grade activated carbon. Journal of Porous Materials**:** 1-14
[32] Titirici, M.-M., White, R. J., Brun, N., Budarin, V. L., Su, D. S., Del Monte, F., Clark, J. H. and Maclachlan, M. J. (2015). Sustainable carbon materials. Chem Soc Rev 44**:** 250-290. https://doi.org/10.1039/C4CS00232F
[33] Heidarinejad, Z., Dehghani, M. H., Heidari, M., Javedan, G., Ali, I. and Sillanpää, M. (2020). Methods for preparation and activation of activated carbon: a review. Environ Chem Lett 18**:** 393-415. https://doi.org/10.1007/s10311-019-00955-0
[34] Hu, B. (2010). K., Wang, L. Wu, S.-H. Yu, M. Antonietti, M.-M. Titirici. Adv. Mater 22**:** 813
[35] Deng, H., Li, G., Yang, H., Tang, J. and Tang, J. (2010). Preparation of activated carbons from cotton stalk by microwave assisted KOH and K2CO3 activation. Chemical Engineering Journal 163**:** 373-381
[36] Shen, Y. and Fu, Y. (2018). KOH-activated rice husk char via CO2 pyrolysis for phenol adsorption. Materials today energy 9**:** 397-405

[37] Chomiak, K., Gryglewicz, S., Kierzek, K. and Machnikowski, J. (2017). Optimizing the properties of granular walnut-shell based KOH activated carbons for carbon dioxide adsorption. Journal of CO2 Utilization 21**:** 436-443
[38] Trisunaryanti, W., Wijaya, K., Triyono, T., Wahyuningtyas, N., Utami, S. P. and Larasati, S. (2022). Characteristics of coconut shell-based activated carbon as Ni and Pt catalyst supports for hydrotreating Calophyllum inophyllum oil into hydrocarbon-based biofuel. Journal of Environmental Chemical Engineering 10**:** 108209
[39] Abuelnoor, N., Alhajaj, A., Khaleel, M., Vega, L. F. and Abu-Zahra, M. R. (2021). Activated carbons from biomass-based sources for CO2 capture applications. Chemosphere 282**:** 131111
[40] Perea-Moreno, M.-A., Manzano-Agugliaro, F., Hernandez-Escobedo, Q. and Perea-Moreno, A.-J. (2018). Peanut shell for energy: properties and its potential to respect the environment. Sustainability 10**:** 3254. https://doi.org/10.3390/su10093254
[41] Ec. Renewable energy directive. Available: https://energy.ec.europa.eu/topics/renewable-energy/renewable-energy-directive-targets-and-rules/renewable-energy-directive_en [Accessed 13 June 2023].
[42] Yu, J. ((2023)). Stability of Peanuts. *In:* Ferranti, P. (ed.) *Sustainable Food Science - A Comprehensive Approach.* Elsevier. doi.org/10.1016/B978-0-12-823960-5.00017-2
[43] Inc. (2020). Nuts and dried fruits statistical yearbook 2019/2020. Interntional Nut and Dried Fruit Council Spain.
[44] Malik, R., Ramteke, D. and Wate, S. (2006). Physico-chemical and surface characterization of adsorbent prepared from groundnut shell by ZnCl 2 activation and its ability to adsorb colour. Indian J. Chem. Technol. 13. http://nopr.niscpr.res.in/handle/123456789/7048
[45] Kumari, G., Soni, B. and Karmee, S. K. (2020). Synthesis of activated carbon from groundnut shell via chemical activation. J Inst Eng India Ser E**:** 1-8. https://doi.org/10.1007/s40034-020-00176-z
[46] Kamaraj, M. and Umamaheswari, P. (2017). Preparation and characterization of Groundnut shell activated carbon as an efficient adsorbent for the removal of Methylene blue dye from aqueous solution with microbiostatic activity. Journal Mater Environ Sci 8**:** 2019-2025
[47] Garg, D., Kumar, S., Sharma, K. and Majumder, C. (2019). Application of waste peanut shells to form activated carbon and its utilization for the removal of Acid Yellow 36 from wastewater. Groundw Sustain Dev 8**:** 512-519. https://doi.org/10.1016/j.gsd.2019.01.010
[48] Malik, R., Ramteke, D. S. and Wate, S. R. (2007). Adsorption of malachite green on groundnut shell waste based powdered activated carbon. Waste Manag 27**:** 1129-1138. https://doi.org/10.1016/j.wasman.2006.06.009
[49] Seader, J. D., Henley, E. J. and Roper, D. K. (2010). *Separation Process Principles, 3rd Edition*, John Wiley Incorporated.
[50] Camfil. (2020). Historic Journey of Activated Carbon and Breakthroughs. Available: https://www.camfil.com/en/insights/innovation-technology-and-research/journey-of-activated-carbon [Accessed 14 April 2023].
[51] Sharma, A., Jindal, J., Mittal, A., Kumari, K., Maken, S. and Kumar, N. (2021). Carbon materials as CO 2 adsorbents: A review. Environmental Chemistry Letters 19**:** 875-910
[52] Ganjoo, R., Sharma, S., Kumar, A. and Daouda, M. (2023). Activated Carbon: Fundamentals, Classification, and Properties.
[53] Liu, E. (2016). *Activated Charcoal* [Online]. Available: https://www.discovermagazine.com/the-sciences/activated-charcoal [Accessed 22 August 2023].
[54] Cooney, D. O. (1995). *Activated charcoal in medical applications*, CRC Press.
[55] Hock, P. E. and Zaini, M. a. A. (2018). Activated carbons by zinc chloride activation for dye removal – a commentary. Acta Chimica Slovaca 11**:** 99-106. https://doi.org/10.2478/acs-2018-0015
[56] Smíšek, M. and Černý, S. (1970). *Active carbon: manufacture, properties and applications*, Elsevier Publishing Company.

[57] Huang, Y. and Zhao, G. (2016). Preparation and characterization of activated carbon fibers from liquefied wood by KOH activation. Holzforschung 70**:** 195-202
[58] Mohanty, K., Jha, M., Meikap, B. and Biswas, M. (2005). Preparation and characterization of activated carbons from Terminalia arjuna nut with zinc chloride activation for the removal of phenol from wastewater. Industrial & engineering chemistry research 44**:** 4128-4138
[59] Zhang, H., Yan, Y. and Yang, L. (2010). Preparation of activated carbon from sawdust by zinc chloride activation. Adsorption 16**:** 161-166. https://doi.org/10.1007/s10450-010-9214-5
[60] Angin, D. (2014). Production and characterization of activated carbon from sour cherry stones by zinc chloride. Fuel 115**:** 804-811
[61] Ahmadpour, A. and Do, D. (1997). The preparation of activated carbon from macadamia nutshell by chemical activation. Carbon 35**:** 1723-1732. https://doi.org/10.1016/S0008-6223(97)00127-9
[62] Mondal, P., Balo Majumder, C. and Mohanty, B. (2007). Removal of trivalent arsenic (As (III)) from contaminated water by calcium chloride (CaCl2)-impregnated rice husk carbon. Industrial & engineering chemistry research 46**:** 2550-2557
[63] Caturla, F., Molina-Sabio, M. and Rodriguez-Reinoso, F. (1991). Preparation of activated carbon by chemical activation with ZnCl2. Carbon 29**:** 999-1007. https://doi.org/10.1016/0008-6223(91)90179-M
[64] Anisuzzaman, S., Joseph, C. G., Krishnaiah, D., Bono, A., Suali, E., Abang, S. and Fai, L. (2016). Removal of chlorinated phenol from aqueous media by guava seed (Psidium guajava) tailored activated carbon. Water Resour Ind 16**:** 29-36. https://doi.org/10.1016/j.wri.2016.10.001
[65] Saleem, J., Shahid, U. B., Hijab, M., Mackey, H. and Mckay, G. (2019). Production and applications of activated carbons as adsorbents from olive stones. Biomass Conversion and Biorefinery 9**:** 775-802
[66] Ruiz Bevia, F., Prats Rico, D. and Marcilla Gomis, A. (1984). Activated carbon from almond shells. Chemical activation. 1. Activating reagent selection and variables influence. Ind Eng Chem Prod Res Dev 23**:** 266-269
[67] Makeswari, M. and Santhi, T. (2013). Optimization of preparation of activated carbon from Ricinus communis leaves by microwave-assisted zinc chloride chemical activation: Competitive adsorption of Ni 2+ ions from aqueous solution. Journal of chemistry 2013
[68] Jawad, A. H., Alkarkhi, A. F. and Mubarak, N. S. A. (2015). Photocatalytic decolorization of methylene blue by an immobilized TiO2 film under visible light irradiation: optimization using response surface methodology (RSM). Desalin Water Treat 56**:** 161-172. https://doi.org/10.1080/19443994.2014.934736
[69] Mehmood, T., Ahmed, A., Ahmad, A., Ahmad, M. S. and Sandhu, M. A. (2018). Optimization of mixed surfactants-based β-carotene nanoemulsions using response surface methodology: an ultrasonic homogenization approach. Food Chem 253**:** 179-184. https://doi.org/10.1016/j.foodchem.2018.01.136
[70] Sulaiman, N. S., Hashim, R., Amini, M. H. M., Danish, M. and Sulaiman, O. (2018). Optimization of activated carbon preparation from cassava stem using response surface methodology on surface area and yield. Journal of Cleaner Production 198**:** 1422-1430
[71] Li, L., Sun, F., Gao, J., Wang, L., Pi, X. and Zhao, G. (2018). Broadening the pore size of coal-based activated carbon via a washing-free chem-physical activation method for high-capacity dye adsorption. RSC advances 8**:** 14488-14499
[72] Phothong, K., Tangsathitkulchai, C. and Lawtae, P. (2021). The analysis of pore development and formation of surface functional groups in bamboo-based activated carbon during CO2 activation. Molecules 26**:** 5641
[73] Sinha, P., Banerjee, S. and Kar, K. K. (2020). Characteristics of activated carbon. Handbook of Nanocomposite Supercapacitor Materials I: Characteristics**:** 125-154. https://doi.org/10.1007/978-3-030-43009-2_4

[74] Bedia, J., Peñas-Garzón, M., Gómez-Avilés, A., Rodriguez, J. J. and Belver, C. (2020). Review on activated carbons by chemical activation with FeCl3. C 6**:** 21
[75] Sütcü, H. (2011). Characterization of activated carbons produced from oleaster stones. *Progress in Biomass and Bioenergy Production.* IntechOpen
[76] Mkungunugwa, T., Manhokwe, S., Chawafambira, A. and Shumba, M. (2021). Synthesis and characterisation of activated carbon obtained from Marula (Sclerocarya birrea) nutshell. Journal of Chemistry 2021**:** 1-9
[77] Fletcher, A. J., Uygur, Y. and Thomas, K. M. (2007). Role of surface functional groups in the adsorption kinetics of water vapor on microporous activated carbons. The Journal of Physical Chemistry C 111**:** 8349-8359
[78] Zuim, D. R., Carpiné, D., Distler, G. a. R., De Paula Scheer, A., Igarashi-Mafra, L. and Mafra, M. R. (2011). Adsorption of two coffee aromas from synthetic aqueous solution onto granular activated carbon derived from coconut husks. J. Food Eng. 104**:** 284-292. https://doi.org/10.1016/j.jfoodeng.2010.12.019
[79] El Gamal, M., Mousa, H. A., El-Naas, M. H., Zacharia, R. and Judd, S. (2018). Bio-regeneration of activated carbon: A comprehensive review. Separation and Purification Technology 197**:** 345-359
[80] Islam, M. T., Saenz-Arana, R., Hernandez, C., Guinto, T., Ahsan, M. A., Bragg, D. T., Wang, H., Alvarado-Tenorio, B. and Noveron, J. C. (2018). Conversion of waste tire rubber into a high-capacity adsorbent for the removal of methylene blue, methyl orange, and tetracycline from water. J. Environ. Chem. Eng. 6**:** 3070-3082. https://doi.org/10.1016/j.jece.2018.04.058
[81] Li, H., Budarin, V. L., Clark, J. H., North, M. and Wu, X. (2022). Rapid and efficient adsorption of methylene blue dye from aqueous solution by hierarchically porous, activated starbons®: Mechanism and porosity dependence. J. Hazard. Mater. 436**:** 129174. https://doi.org/10.1016/j.jhazmat.2022.129174
[82] Barton, S. S. (1987). The adsorption of methylene blue by active carbon. Carbon 25**:** 343-350
[83] Chen, L., Ji, T., Mu, L., Shi, Y., Wang, H. and Zhu, J. (2017). Pore size dependent molecular adsorption of cationic dye in biomass derived hierarchically porous carbon. Journal of environmental management 196**:** 168-177
[84] Albadarin, A. B., Collins, M. N., Naushad, M., Shirazian, S., Walker, G. and Mangwandi, C. (2017). Activated lignin-chitosan extruded blends for efficient adsorption of methylene blue. Chemical Engineering Journal 307**:** 264-272

Chapter 2: Aim and Objectives

Chapter 1 provided background information on the problem and the proposed solution that this work addresses. It was highlighted that industrial and agricultural effluents are the most abundant and feasible sources of water, which require treatment to protect the ecosystem and enable their reuse. *Adsorption* is proposed as an effective and sustainable method for water remediation, which employs solid materials called *adsorbents* to remove *contaminants* from water. The advantages and applications of *activated carbon* (AC) as an adsorbent, which has high porosity and adsorption capacity for various contaminants were discussed, and *peanut shells* were identified as a potential precursor to synthesise AC, with gaps in previous studies that utilised the same biomass highlighted within the chapter. $ZnCl_2$ was identified as a suitable chemical activating agent, while the limitations and challenges of commercial AC production, which is affected by the high cost and scarcity of the raw materials, due to the high demand of commercial ACs for multiple purposes were acknowledged.

Consequently, this work aims to develop a low-cost and effective AC material that can serve as an alternative to commercial-grade adsorbents for water remediation applications.

The objectives of this work are:

1. To analyse the physical and chemical properties of the peanut shell, which is selected as a precursor to synthesise peanut shell based ACs in this study. Peanut shell is an abundant agricultural by-product that has high carbon content, making it potentially suitable as a precursor for AC production.
2. To employ design of experiments (DoE) to investigate the main and interacting effects of activation variables (factors) on the final properties of AC synthesised from peanut shells in a single stage chemical activation process – this allows the

exploration of the possibility of tuning/tailoring the final properties of the AC materials for specific applications by manipulating the activation variables. The activation variables examined in this work are:

- Temperature
- Hold time
- Impregnation ratio (chemical agent weight/ precursor weight)

3. To determine the optimal combination of the activation variables, as highlighted above, that maximizes the final properties of the AC derived from peanut shells.
4. To characterise the AC materials synthesised from peanut shells, performing a screening analysis to select the most effective candidate, and evaluate its performance for the removal of ionic dyes (methyl orange and methylene blue) from water; finally, comparing the performance of the optimised sample with several ACs reported in the literature.

Chapter 3: Characterisation Techniques and Background Theory

This chapter provides an overview of the characterisation techniques employed in this study and their underlying theories. These techniques assess the textural properties (e.g., BET specific surface area, pore volume and pore size), surface chemistry, and adsorption properties of the prepared adsorbents, within this context. Adsorption processes, and the use of gas adsorption (N_2 adsorption) for the characterisation of the texture of porous materials, and isotherms will be explored. More so, liquid adsorption methods are used to determine the adsorption properties of adsorbents are also detailed in this chapter.

3.1 Textural analysis

The textural properties (e.g., BET specific surface area, pore volume and pore size) of an adsorbent are crucial in determining its performance in various processes, and thus require careful examination and analysis. According to Seader *et al.* [1], a sorbent with a high capacity can enhance the system efficiency and feasibility, which is a desirable property for commercial applications. The surface area of an adsorbent relates to its capacity and can be assessed by gas adsorption techniques – these are well-established and the most widely used technique. Other techniques, such as mercury porosimetry [2], are also available for evaluating the internal surface area of porous solids, however, these were not employed here and are not discussed further.

3.1.1 Adsorption processes

Adsorption processes can be classified into two categories: physical adsorption (physisorption), which involves weak intermolecular forces, known as van der Waals forces, between the adsorbate molecules and the adsorbent surface, and chemisorption, which involves chemical bond formation between the adsorbate

molecules and the adsorbent surface [3]. Physisorption is exothermic in nature i.e., it involves the liberation of heat. It occurs rapidly, and can be unimolecular, or multimolecular, i.e., several layer(s) thick. It is a reversible process and hysteresis (discussed later in this chapter) may occur if the adsorption is multimolecular, such that capillary pores are filled [4]. Chemisorption, on the other hand, liberates larger heat energies. It is a slow process and can only be unimolecular. Chemisorption processes involve strong bonds between the adsorbate and the surface, which make desorption challenging, and often necessitate high temperatures to overcome the binding energies. The next section will explore further the process and the application of physisorption at the gas–solid interface in characterising solid porous materials.

3.1.2 Physisorption of gases

Typically, physical adsorption methods are employed to determine the textural properties of porous materials in commercial applications. Various fluids, such as N_2 at -195.8 °C, Ar at -186 °C, and CO_2 at 0 °C, have been used in the characterisation of porous materials. N_2, at -195.8 °C, is the most prevalent adsorptive for characterising porous solids, yet it presents some drawbacks, such as the potential blockage of narrow micropores by its molecules and the specific interactions with diverse surface functional groups. The characterisation of a porous material by adsorption involves introducing a known quantity of pure gas into a closed system at a constant temperature; the gas pressure decreases, as adsorption occurs, until a dynamic equilibrium is established. This can be expressed in terms of the relative pressure (p/p^0) of the gas and the amount of gas adsorbed in moles, mass, or volume, per unit mass of the solid material. The data is taken within the relative pressure range of interest and a plot of the amount adsorbed versus the relative pressure (p/p^0) yields an adsorption *isotherm*. Different adsorption mechanisms have been proposed by several people such as Langmuir [5], Freundlich [6], and Brunauer *et al*. [7], which will be discussed in the following section.

3.1.2.1 Physisorption isotherms

Material properties and measurement conditions determine the isotherm shape, which is the basis for isotherm classification. According to the IUPAC report on physisorption data for gas/solid systems published in 1985, the majority of the physisorption isotherms were grouped into six types [8]. However, due to developments, over the last three decades, the 1985 physisorption isotherm types were, in 2015, extended to eight types, as shown in Figure 3.1.

Type I isotherms exhibit a concave shape to the relative pressure (p/p^0) axis. Isotherms in this class are characterised by high uptake at low p/p^0. As reported by Thommes *et al*. [9], using N_2 at -195.8 °C or Ar at -186 °C as adsorptive, microporous materials with predominantly narrow micropores exhibit Type I(a) isotherms; Type I(b) isotherms are given by materials characterised by supermicropores (wider micropores, in the range 1.4 – 3.2 nm [10]). Type II isotherms are obtained with microporous or non-porous solid materials. Depending on the shape of the knee at point B (as shown in Figure 3.1), the transition from unimolecular to multimolecular adsorption may be clearly observed – a sharp knee – indicates a clear distinction between the two regimes. Types I & II are desirable isotherms – they indicate strong adsorption.

In contrast to Type I isotherms, Type III isotherm exhibits a convex shape to the relative pressure (p/p^0) axis. This type of isotherm indicates a low adsorption capacity, except at high relative pressures, implying a weak adsorbate – surface interaction. This is unfavourable for adsorption processes, e.g., adsorption of iodine vapour on silica gel [11].

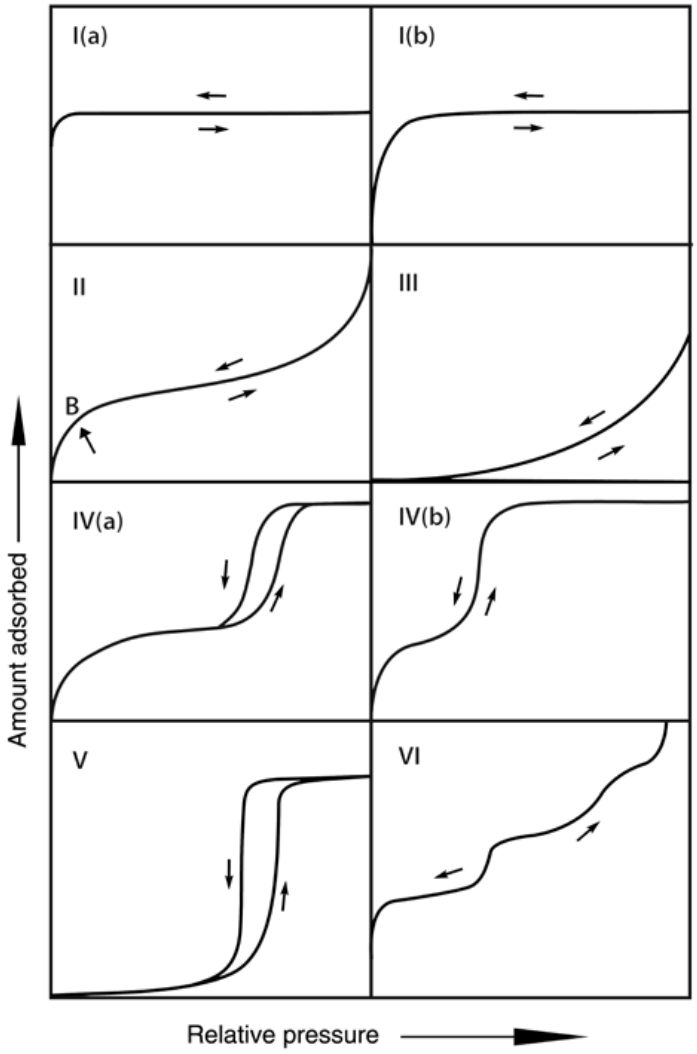

Figure 3.1. Types of physisorption isotherms [9]

Type IV isotherms are obtained with materials characterised by mesopores. The initial pore filling, showing the transition from unimolecular to multimolecular adsorption, is like the Type II isotherm, which is then followed by pore condensation, i.e., gas condensing to liquid-like phase. Type IV(a) isotherms are found with materials having wider mesopores. In this type of surface-adsorbate interaction, hysteresis occurs in the multilayer adsorption region. The upward adsorption curve of the hysteresis loop can be associated with multimolecular adsorption and pore condensation happening simultaneously, while the downward desorption curve is

due to pore condensation. Type IV(b) isotherms are found with materials characterised by smaller mesopores. Type IV isotherms are common within industrial mesoporous materials [8].

The Type V isotherm represents a case of a Type III isotherm where pore condensation occurs. These isotherms are not common and can be found within porous materials that exhibit weak interactions with adsorbates, such as adsorption of water on hydrophobic porous materials. Finally in this section, Type VI isotherms are associated with uniform non-porous materials. The stepwise pattern of this isotherm is influenced by the characteristics of the system and the temperature at which adsorption takes place. The height of the step corresponds to the monolayer capacity for each step.

3.1.2.2 Adsorption hysteresis

As discussed in the previous section, hysteresis may occur in the multilayer adsorption region for some adsorbate-surface interactions, as indicated by Types IV and V of the physisorption isotherm classification system. Hysteresis loops imply that the amount adsorbed is different when increasing the pressure than decreasing the pressure – this usually occurs when there is capillary condensation (i.e., gas condensing to liquid-like phase). The shapes exhibited by the hysteresis loops can also give insight into the type of pore shapes within the material investigated. The IUPAC classification of 1985 identified four types of hysteresis loops. However, due to the emergence of new types of isotherms over the last three decades, the hysteresis types were, in 2015, extended to six types, as shown in Figure 3.2.

Type H1 loops have an upward adsorption curve almost parallel to the downward desorption curve. Porous materials with cylindrical or ink-bottle pores typically exhibit this kind of hysteresis loop – this is a common feature of mesoporous solid materials [12].

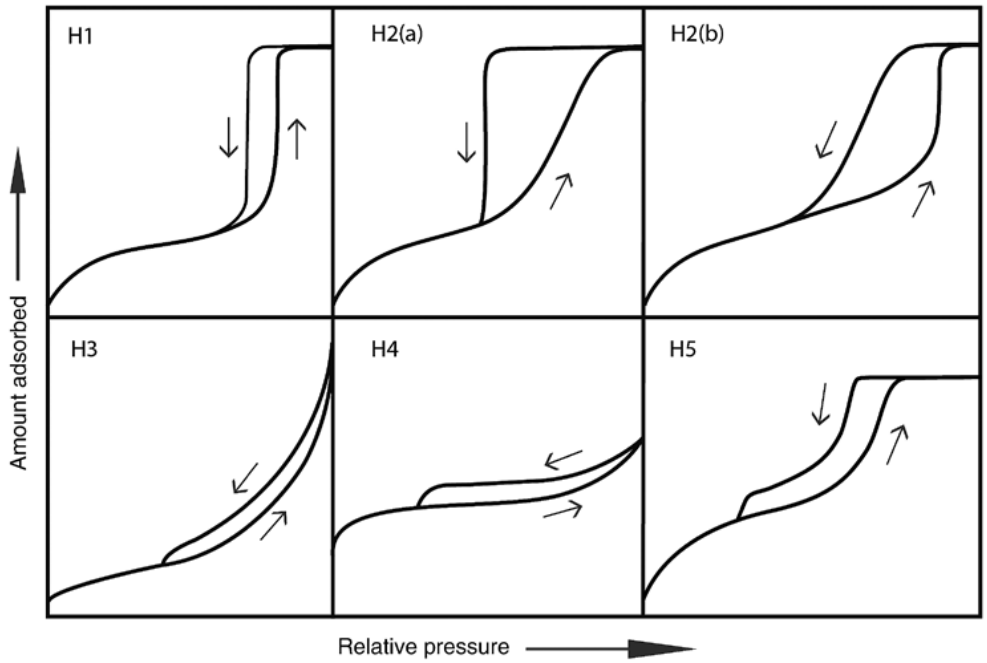

Figure 3.2. Classification of hysteresis loops[9].

Unlike Type H1, having cylindrical pores with open ends, Type H2 loops correspond to pores with a branched and interconnected network structure that have dead ends. Type H2(a) is a variant of Type H2, that is characterised by a steep desorption curve, resulting from pore blocking/transport of adsorptive through narrow pore necks or from evaporation processes occurring in the pores. Type H2(b) is characterised by a gradual decrease in its desorption curve, and can also be attributed to pore blocking – in this case, the pore necks are wider [13].

The upward adsorption curve of Type H3 loops is like a Type II isotherm curve, which does not show adsorption saturation at high relative pressure. This type of loop is observed with non-rigid aggregates of plate-like particles and could also result from incomplete filling of macropores with pore condensate. Type H4 is almost similar to H3, however, the adsorption curve has a combination of Type I and II isotherms – this shows that materials within this category possess some degree of microporosity, such as micro-mesoporous carbons, and some mesoporous zeolites.

The Type H5 loop, a rare phenomenon, has a unique shape that corresponds to some pore structures with open and partially blocked mesopores (e.g. silica inserted into a hexagonal template) [8, 9].

As discussed in Section 3.1.2, adsorption isotherms are essential for the characterisation of porous materials. They describe the equilibrium relationship between the amount of adsorbate on the adsorbent surface and the concentration or pressure of the adsorbate in the bulk phase. They provide insights into the adsorbent-adsorbate interactions and the factors influencing the adsorption behaviour. They also enable the comparison of the adsorption performance of different adsorbents and the design and optimisation of adsorption systems for various purposes [14]. Various adsorption isotherms that are frequently applied are discussed in the following sections.

3.1.2.3 Langmuir equation

The Langmuir model is one of the most widely used in analysing adsorption isotherms. The mechanism of gas adsorption proposed by Langmuir accounts for the equilibrium between gas phase molecules and adsorbed molecules. The derivation of the Langmuir equation is based on mass-action kinetics; it can be derived by considering the rates of adsorption and desorption of the gas molecules [15]. Langmuir made three fundamental assumptions [16, 17] that are outlined below:

1. All binding sites are energetically identical.
2. The absorbed layer is limited to a monolayer formation and each binding site can only hold one adsorbed molecule.
3. Intermolecular interactions do not occur.

Applying the above assumptions, assume

N = total number of surface sites

n = number of occupied sites by adsorbed molecules

The fraction of the occupied sites, surface coverage $\theta = \frac{n}{N}$

The fraction of vacant sites = 1 – θ

The rate of adsorption α the pressure of the gas, P, and 1 – θ.

$r_{ads} = k_a P(1 - \theta)$ (Equation 3.1)

where k_a is the rate constant for adsorption.

The rate of desorption α θ

$r_{des} = k_d \theta$ (Equation 3.2)

where k_d is the rate constant for desorption.

At equilibrium, $r_{ads} = r_{des}$ and,

$\theta = \frac{KP}{1+KP}$ (Equation 3.3)

where $K = k_a/k_d$ and $\theta = \frac{n_a}{n_m}$

Equation 3.3 can be written as:

$n_a = \frac{Kn_m P}{1+KP}$ (Equation 3.4)

where n_a is the specific amount of gas adsorbed at equilibrium pressure P and n_m is the monolayer capacity. These two parameters can be expressed in $cm^3 g^{-1}, mg g^{-1}$ or $mmol g^{-1}$.

Equation 3.4 gives the Langmuir equation, and the linear form can be expressed as

$\frac{P}{n_a} = \frac{1}{Kn_m} + \frac{P}{n_m}$ (Equation 3.5)

The Langmuir equation can be applied to determine the surface area of a material by plotting $\frac{P}{n_a}$ versus P, to obtain the line of best fit. The plot yields a regression equation, from which the values of n_m and K can be obtained, from the slope and the intercept

of the equation, respectively. The value of n_m can then be used in Equation 3.6 to calculate the surface area of the material ($m^2\ g^{-1}$) – the units of n_m must be converted appropriately.

$$S = n_m A_m N_A \qquad \text{(Equation 3.6)}$$

where A_m is the area occupied by one gas molecule ($m^2 molec^{-1}$), N_A is Avogadro's number (6.022×10^{23} molec mol^{-1}).

The calculation of Langmuir separation factor is necessary to characterise the features of the Langmuir isotherm model when the experimental equilibrium data fit well with the model. Hall *et al.* [18] classified adsorption systems into four types of idealized equilibrium behaviour, which are:

1. favourable equilibrium
2. unfavourable equilibrium
3. linear equilibrium
4. irreversible equilibrium

The adsorption systems were described using the separation factor, R_L (Equation 3.7) based on the shape of the isotherm.

$$R_L = \frac{1}{1+KC_0} \qquad \text{(Equation 3.7)}$$

where R_L is the separation factor (dimensionless equilibrium parameter) of a solid-liquid adsorption system, K is the Langmuir equilibrium constant, and C_0 is the initial adsorbate concentration.

The adsorption system is favourable if $0 < R_L < 1$, unfavorable $R_L > 1$, linear $R_L = 1$ and irreversible if $R_L = 0$ [19].

3.1.2.4 Brunauer–Emmett–Teller (BET) equation

The BET equation, the most prevalent multilayer adsorption model for evaluating the surface area of a material, was derived by Brunauer *et al*. [7] in 1938, based on the Langmuir mechanism. The three additional assumptions underpinning the derivation of the BET equation (Equation 3.8) are highlighted below:

1. The physical adsorption of gas molecules on a solid surface is not restricted to monolayer formation – unlimited multilayer formation is possible.
2. The adsorption energy for the first monolayer formation is unique, whereas the successive layers have the same as energy of liquefaction [20].
3. Each molecule adsorbed in a layer is a potential binding site for subsequent layers [21].

$$\frac{p/p^0}{n(1-p/p^0)} = \frac{1}{n_m C} + \frac{C-1}{n_m C}(p/p^0) \qquad \text{(Equation 3.8)}$$

Where n is the amount of gas adsorbed at p/p^0, n_m is the monolayer capacity, and C is a constant related to the exponential of the heat of adsorption.

$$C = \exp\left(\frac{|\Delta H_A| - |\Delta H_L|}{RT}\right) \qquad \text{(Equation 3.9)}$$

To apply the above linear BET equation, the experimental data for n and p/p^0 are plotted in the form of $\frac{p/p^0}{n(1-p/p^0)}$ versus p/p^0, from which the values of n_m and C are determined from the slope and intercept of the best linear regression (the linear region is often within ~0.05 – 0.35 relative pressure).

The n_m can then be used to compute the BET specific surface area using Equation 3.10.

$$S(BET) = n_m A_m N_A \qquad \text{(Equation 3.10)}$$

where A_m is the area per adsorbate molecule and N_A is Avogadro's number

The BET method is widely used, however its inherent limitations for determining the surface area of microporous materials have been discussed by many authors [22]. For

instance, with microporous materials it may be difficult to determine the linear region of the BET plot, which means the monolayer capacity, n_m, may not be correctly evaluated. To overcome this difficulty, Rouquerol *et al*. [23] recommended a procedure as follows:

1. The BET equation should only be applied to the range where the plot of $n(1 - p/p^0)$ increases with p/p^0.
2. The chosen range should yield a linear BET plot with a positive intercept on the vertical axis, resulting in a valid value of C.
3. The selected BET range should include the p/p^0 value that corresponds to nm.

3.1.2.5 Freundlich equation

Freundlich (1906) proposed an empirical equation (Equation 3.11) to describe the characteristics of gas adsorption on a heterogeneous adsorbent [6, 24]. The Freundlich equation is based on exponential distribution of site energies, and the adsorption capacity increases with the increase of the adsorbate concentration or pressure, but at a decreasing rate. The equation has been frequently used to model adsorption of organic compounds from aqueous solution [25]. In the case of liquid phase applications, the pressure term is replaced by the adsorbate concentration.

$$q_e = K_F P_e^{1/n} \qquad \text{(Equation 3.11)}$$

where q_e is the adsorbate uptake at equilibrium, K_F is the Freundlich constant, and n is the Freundlich parameter, which indicates the magnitude of adsorbent heterogeneity.

The Freundlich equation does not describe the maximum capacity of an adsorbent – at high pressure or concentration, as the equation is unable to predict a limited surface coverage [26].

3.1.2.6 Sips equation

The Sips equation (Equation 3.12) is an empirical relationship, which combines features of the Langmuir and Freundlich models. It was proposed by Sips [27] in 1948 to describe the adsorption behaviour of heterogeneous systems and overcome the drawback of increasing adsorbate concentration that occurs in the Freundlich isotherm. The Sips isotherm model reduces to the Freundlich isotherm at low adsorbate concentrations, thus violating Henry's law. However, at high adsorbate concentrations, this model exhibits a monolayer adsorption capacity similar to the Langmuir isotherm [28].

$$q_e = \frac{Q_S K_S C_e^{n_S}}{1+K_S C_e^{n_S}} \qquad \text{(Equation 3.12)}$$

where Q_S (mg g^{-1}) is the Sips adsorption capacity of adsorbent, K_S (L $mg^{-1})^{n_s}$ is the Sips equilibrium constant and n_S (dimensionless) is the exponent of the Sips model.

The Sips isotherm model can be used to describe homogeneous or heterogenous processes [29]. The heterogeneity of the system is proportional to the n_S parameter, which is typically > 1. A value of 1 or close to 1 signifies an adsorbent with relatively uniform binding sites [28, 30].

3.1.3 Porosity

Porosity refers to the fraction of the total pore volume to the volume of the particle [9]. The porosity of a material is influenced by the size, shape and arrangement of the particles that make up the material. The pores contained within a solid material can be classified into "open" and "closed" types, as shown in Figure 3.3. Open pores are connected to the external surface – they allow the probe fluid (gas or liquid) to penetrate. Closed pores are isolated voids within a solid material that are not connected to the external surface – they are not accessible by the probe fluid. However, the accessibility of these pores also depends on their sizes [31]. Other types

of pores, such as transport pores and blind pores may also exist within solid materials. Transport pores link the external surface to the inner pores, while blind pores do not lead to other pores or surfaces.

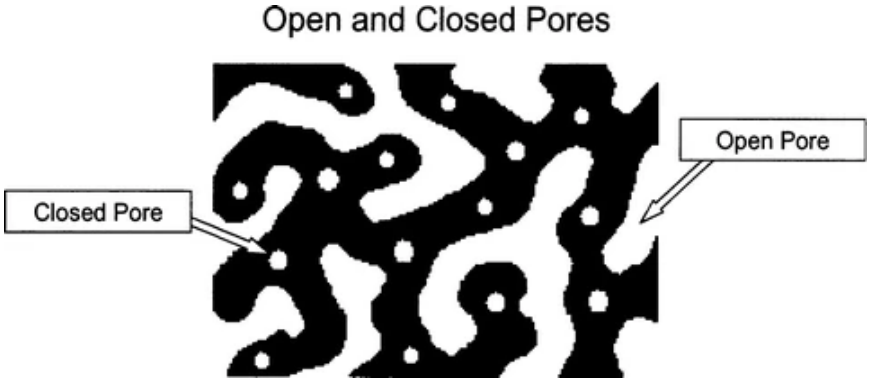

Figure 3.3. Illustration of open and closed pore types in a porous material [31].

According to the IUPAC classification [32], pore widths are classified as follows:

Micropore: pores of internal widths < 2 nm

Subdivided into

- Ultramicropores – internal widths < 0.7 nm
- Supermicropore – internal widths range from 0.7 – 2 nm.

Mesopores: internal widths range from 2 – 50 nm.

Macropores: internal widths > 50 nm.

3.1.3.1 Pore size and volume analyses

Various methods have been proposed for the evaluation of micro-and mesoporosity of porous materials, such as the application of the Gurvitsch rule, t-plot method, or Dubinin-Radushkevich (D-R) approach [33] for estimating pore volume. Other approaches such as Horvath and Kawazoe (HK), Saito and Foley (SF) and Cheng-Yang (CY) [34-36], allow determination of pore volume and pore size distribution. The limitations of these semi-empirical methods stem from neglecting the influence of pore size and shape on the molecular packing density in micropores [32]. The Barrett-

Joyner-Halenda (BJH) approach [37] is one of the most widely used methods for pore size analysis of mesoporous materials. This method, which is discussed in the next section, is based on the Kelvin equation; it also tends to underestimate the pore size by 20 – 30 % for pore size < 10 nm.

3.1.3.1.1 Barrett-Joyner-Halenda (BJH) method

The Barrett-Joyner-Halenda (BJH) approach is a common method for estimating the pore size distribution and volume of porous materials. The BJH approach is based on two assumptions: (1) all pores are cylindrical in shape and (2), at equilibrium, the adsorbate molecules are physically adsorbed to the walls of the pores and the capillary volume is filled with condensate [37]. First, the system is considered to have an open-ended cylindrical pore (Figure 3.4) with radius r_p. On the inside walls of the pore is an adsorbed layer of molecules of thickness t. When desorption occurs i.e., when the p/p^0 is lowered, the condensate within the inner capillary evaporates – the radius of the of the inner capillary is denoted r_k, as shown in Figure 3.4.

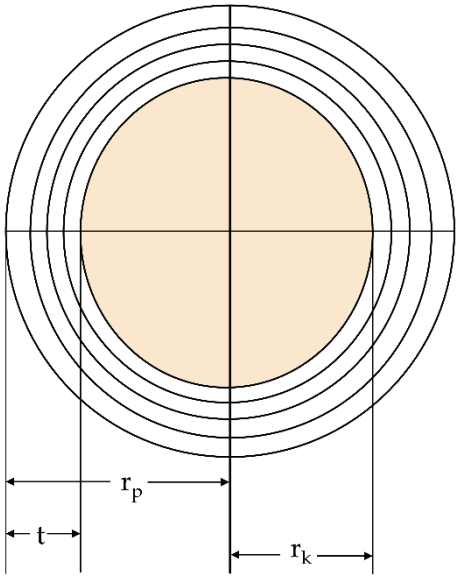

Figure 3.4. Schematic representation of the pore cross-section, showing the pore radius r_p, the thickness t, of the physically adsorbed layer, and the inner capillary radius r_k.

As stated under the assumptions, the equilibrium between the adsorbed phase and the gas phase involves two mechanisms – the physical adsorption on the pore walls and capillary condensation. This leads to Equation 3.13, which gives the relationship between the pore volume, V_p, and the inner capillary volume, V_k.

$$V_p = V_k \, r_p^2 / r_k^2 \qquad \text{(Equation 3.13)}$$

Equation 3.13 cannot be used to compute the pore volume, since the inner capillary volume is unknown. To address this issue and acquire more data to calculate V_p, the measurement of the gas volume desorbed, as the relative pressure decreases, is required. However, the process diminishes the thickness of the physically adsorbed layer, and this factor must be considered. As the relative pressure is lowered further, the evacuation of the next range of pores continues, leading to thinning of the physically adsorbed layers from the evacuated pores. The process continues all to the n^{th} desorption. It is obvious that this process involves a large number of pores, hence an average area of the pores from which the gas is desorbed is required. The above considerations led to the development of Equation 3.14, which is used for computing pore volume distributions with pore widths.

$$V_{pn} = R_n \Delta V_n - R_n \Delta t_n \sum_{j=1}^{n-1} c_j A_{pj} \qquad \text{(Equation 3.14)}$$

where $R_n = \overline{r_p^2}/(\bar{r}_k + \Delta t)^2$, ΔV_n= the change in volume corresponding to the decrease in p/p^0, Δt_n= the change in thickness corresponding to the decrease in p/p^0; this can be obtained by subtracting the value of t from the successive t, as p/p^0 changes, $area\ of\ each\ pore, A_p = 2V_p/r_p$, and $c = (\bar{r_p} - \bar{t_r})/\bar{r_p}$, where $\bar{t_r}$ is the thickness of the physically adsorbed layer corresponding to p/p^0; this can be obtained by subtracting Δt from the value of t.

BJH method applies the Kelvin equation (Equation 3.15) to obtain a relationship between p/p^0 and inner capillary radius, r_k, which could be used to determine r_p, using the relation, $r_p = r_k + t$.

$$\log (p/p^0) = -2\gamma V_m/RTr_k \quad \text{(Equation 3.15)}$$

where γ = surface tension of liquid nitrogen, V_m= molar volume of nitrogen, R = gas constant, and T = temperature.

The values of t can be obtained using Equation 3.16 [38]

$$t = \sqrt{\frac{13.99}{0.034 - logp/p^0}} \quad \text{(Equation 3.16)}$$

The unit of t is in Angstrom (Å)

The values of r_p from $r_p = r_k + t$ can now be used to compute the values of R in $R_n = \overline{r_p^2}/(\bar{r}_k + \Delta t)^2$ in which $\bar{r}_p$ is the average of the radius of the pore at a given p/p^0, and the successive pore, p/p^0 is increased.

The BJH method involves a number of iterations, and this could be practically achieved by employing a computing machine with Equation 3.14.

3.1.3.1.2 t-plot method

The t-plot method is another approach that enables the evaluation of microporosity and surface area of porous materials, as proposed by Lippens and de Boer [39]. To apply this method, one must first determine the average thickness of adsorbed layers for a reference material that has no micro- or mesoporosity. The reference material must possess the same surface chemistry as the porous material under investigation. Then, the t-curve for the porous material is obtained by plotting the amount adsorbed, n, against the thickness, t, from the reference material corresponding to each p/p^0. Equation 3.16 is applicable to carbon blacks [38, 39], and it is employed in this research work to plot the t-curve.

To estimate the surface area of a mesoporous material, the amount adsorbed, n, obtained from the isotherm of the material, is plotted as a function of the thickness, t, producing the t-curve for the material. Any part of the t-curve, that is different from

the shape of the material's isotherm, suggests the non-linear region. Usually, the curve yields two straight lines. The first straight line, at low p/p^0, passes through the origin, and the slope is used to estimate the total surface area of the material using Equation 3.17.

$$S\ (m^2/g)\ = slope\ *\ (\rho_{N2\ gas}/\rho_{N2\ liq.}) \quad \text{(Equation 3.17)}$$

where $\rho_{N2\ gas}$ and $\rho_{N2\ liq.}$ are the densities of nitrogen in the gas and liquid phase, respectively.

Adsorption on the internal surface of the mesopores corresponds to the first straight line that passes through the origin. Following this process, capillary condensation occurs, resulting in adsorption on the external surface of the material. The latter yields the second straight line at high p/p^0 – the slope of this line is used to determine the external surface area.

$$V_{mic}\ = Intercept\ *\ (\rho_{N2\ gas}/\rho_{N2\ liq.}) \quad \text{(Equation 3.18)}$$

However, for microporous materials, the first straight line, at low p/p^0, does not usually pass through the origin or fits linearly[40].The intercept of the straight line on the vertical axis is usually taken to estimate the micropore volume, V_{mic} (Equation 3.18). To determine the micropore surface area, the second straight line is used to estimate the external surface area as described above, and this can be subtracted from S_{BET} to obtain the micropore surface area. The first linear line, if present, in microporous materials, is associated with micropore filling, hence it is not usually used to estimate the micropore surface area.

3.2 Surface chemistry analysis

Surface chemistry analysis of an adsorbent refers to the identification and analysis of the chemical species on its surface, and how they influence the interaction of the adsorbent with other atoms or molecules. The surface chemistry of an adsorbent plays

a crucial role in adsorption processes. Factors, such as the point of zero charge (PZC) or surface functional group determination, can provide both qualitative and quantitative information on the surface nature of adsorbents. Various methods, such as the salt addition method or Fourier transform infrared spectroscopy (FTIR), are employed to gain insight into the surface chemical properties of materials.

3.2.1 Point of zero charge

The point of zero charge (PZC) is the pH at which the net charge of the total particle surface (i.e., adsorbent's surface) is zero. Mular and Roberts [41] first proposed the salt addition method for determining PZC. Over the years, the method has been modified by various researchers [42]. The surface charge of solid materials can be determined by this method, which involves preparing solutions of equal ionic strength, at varying pH levels, using inert electrolytes such as NaCl, KNO_3, $NaNO_3$, etc. Equal mass of the solid material is added to the salt solutions at varying pH levels, and these mixtures are allowed to equilibrate. After equilibration, usually after 24 hrs, the final pH measurement is taken.

The final pH (pH_f) of the solution depends on the initial pH (pH_i) of the solution and the PZC of the solid material. When the pH_i of the solution is lower than PZC, protons are adsorbed on the surface of the material, increasing the pH_f of the solution. When the pH_i of the solution is higher than PZC, protons are released from the surface of the material, leaving the pH_f of the solution lower [43]. The pH difference, ΔpH (i.e., $pH_f - pH_i$) is plotted against the pH_i. The point of zero charge of the material corresponds to where $pH_f = pH_i$ (i.e., the point where the curve intersects the x-axis).

The PZC of an adsorbent is influenced by the chemical species on its surface, and the knowledge of this provides useful information for selecting an adsorbent for the removal of specific pollutants from water.

3.2.2 Fourier transform infrared spectroscopy

Infrared spectroscopy technique is used to study the interaction between molecules and infrared radiation – a form of electromagnetic radiation with longer wavelength than visible light. Depending on the energy of the light, molecules of a sample undergo vibrational motions along their bond length when they absorb light from a source. Figure 3.5 shows the schematic working of a Fourier transform infrared (FTIR) spectrometer.

The beam splitter splits the radiation emitted by the infrared source into two beams. One travels to the fixed mirror and the other beam travels to the moving mirror. The beams are reflected and recombined at the beam splitter, producing an interference pattern [44]. The sample absorbs some of the light energy, causing its molecules to vibrate along their bond length. The transmitted beam from the sample is detected by a detector and converted to an electrical signal. This signal is called an interferogram.

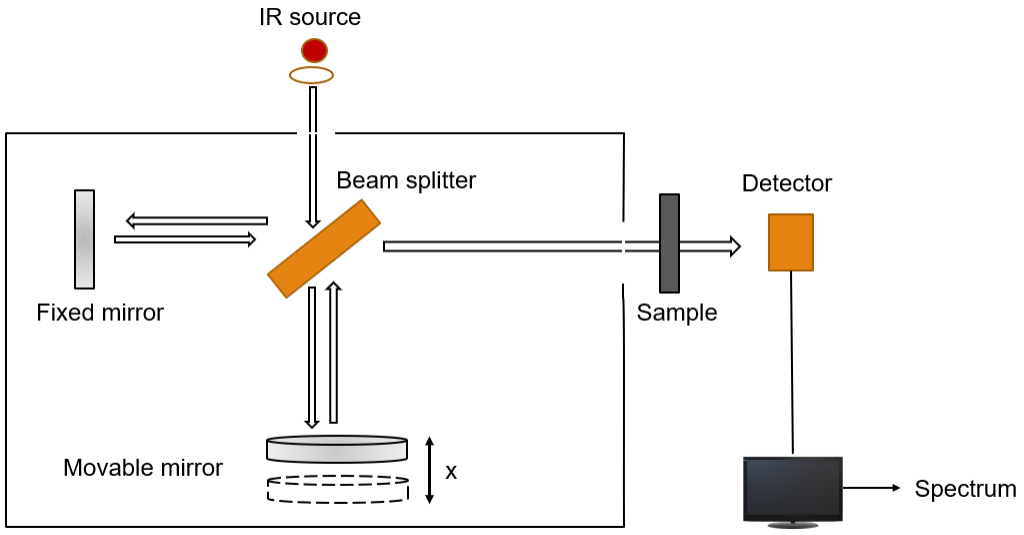

Figure 3.5. Schematic illustration of FTIR spectrometer

The interferogram, which is in the time domain, is transformed to the frequency domain by a Fourier transformation program within the system. The resulting spectrum is plotted as intensity versus wavenumber.

$$v = \sqrt{\frac{bond\ strength}{mass}} \qquad \text{(Equation 3.19)}$$

The factors that affect molecular bond vibration frequencies, v, are related by Equation 3.19. The stretching frequency is directly proportional to the bond strength. This allows differentiation between the carbon-carbon bonds within organic molecules. The order of their bond strength is as follows: C≡C > C=C > C–C. The other factor is the average of the atomic mass of the bonded atoms, which is inversely proportional to the stretching frequency e.g., a C-H bond will have a higher stretching frequency than a C-C or C-O bond [45].

This principle allows identification of various functional groups on the surface of carbon materials used within this study.

3.2.3 X-ray photoelectron spectroscopy

According to the photoelectric effect theory, proposed by Albert Einstein in 1905, light consists of discrete packets of energy called photons, which can eject electrons from atoms if their energy exceeds the minimum threshold required to remove an electron, as illustrated in Figure 3.6. X-ray photoelectron spectroscopy (XPS) is a technique that utilizes this principle to analyse the surface chemistry of a material. It can measure the elements, their chemical states, and their electronic structure on the top 1-10 nm of the material. XPS works by irradiating the material with X-rays and detecting the electrons that are ejected from the surface. The energy and intensity of these electrons can reveal information about the surface elements and their bonding. XPS is useful for studying materials such as metals, polymers, catalysts, coatings, and bio-materials [46, 47].

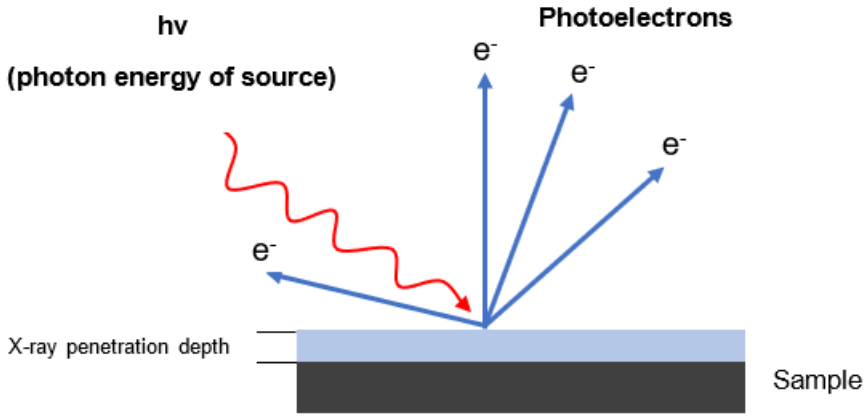

Figure 3.6. Schematic illustration of photoelectric effect.

The minimum energy required to eject an electron from a surface is known as the binding energy (BE). The kinetic energy (KE) of the emitted electron is determined by the difference between the energy of the incident photon and the binding energy, as expressed by Equation 3.20.

$$hv = BE + KE + \emptyset \qquad \text{(Equation 3.20)}$$

where hv = photon energy of source and $\emptyset$ = work function of instrument.

In an XPS instrument, an electron detector collects and counts the photoelectrons emitted by the sample. The spectrum of the sample is obtained by plotting the BE of the photoelectrons on the x-axis and their intensities (number of counts) on the y-axis. The spectrum can be analysed by fitting several peaks to the data, corresponding to the different chemical components of the material. A software, such as Fityk, can be used for this purpose, providing qualitative information on the elemental and chemical composition of the sample.

Additionally, the peak intensities can be used to perform quantitative analysis of the surface concentration of the material, expressed as atomic concentration. This requires three main steps: data acquisition, peak area extraction, and application of an equation

that accounts for various factors such as instrumental parameters, atomic sensitivity factors, and transmission function [48].

The relative atomic concentration of each element present in a sample can be calculated, using Equation 3.21.

$$C_X = \frac{\frac{I_i}{S_i}}{\sum_i \frac{I_i}{S_i}} \quad \text{(Equation 3.21)}$$

where C_X is the element concentration, I_i is the area of the peak for each element and S_i is the relative sensitivity factor of each element [48, 49].

3.3 Liquid adsorption method

Liquid adsorption is used to evaluate adsorption properties (e.g., iodine number, methylene blue number and molasses number) of an adsorbent, which are relevant for water/wastewater remediation. Unlike pure gas adsorption, where pressure change can be used to determine the amount of gas adsorbed, liquid adsorption does not involve pressure change, and no simple procedure has been developed. Liquid adsorption can be carried out using either batch or column (continuous) methods. For simplicity, the batch adsorption method is used within this study, and it is discussed in the following section.

3.3.1 Batch adsorption technique

This technique usually involves a reactor or tank (Figure 3.7), containing the liquid mixture and specific amount of adsorbent. The mixture is agitated under certain conditions until equilibrium is reached. After equilibration, the adsorbent is separated from the mixture, and the final concentration of the liquid is determined using a spectrophotometer.

The performance of an adsorbent can be expressed in terms of the amount of adsorbate adsorbed per unit mass of adsorbent at equilibrium, q_e (mg g^{-1}, mmol or meq g^{-1}) or percentage removal (%removal).

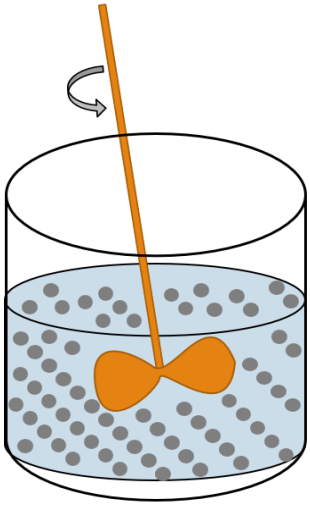

Figure 3.7. Schematic illustration of a liquid batch adsorption experiment

The equilibrium adsorption capacity, q_e, and the percentage removal, %removal, are calculated using Equations 3.22 and 3.23, respectively.

$$q_e = \frac{C_o - C_e}{m} * V \qquad \text{(Equation 3.22)}$$

$$\%removal = \frac{C_o - C_e}{C_o} * 100 \qquad \text{(Equation 3.23)}$$

The adsorption properties of the carbon materials developed in this study were evaluated using this technique.

3.3.2 Adsorption kinetics

Adsorption kinetics is an important parameter in adsorption systems – it describes the rate and mechanism of adsorption, relating to surface reactions, mass transfer, and the diffusion of adsorbate in the system [50]. The following steps are involved in adsorption kinetics [24]:

1. Adsorbate transport from the bulk phase to the adsorbent surface
2. Diffusion of adsorbate through the thin layer of liquid (liquid film)
3. Diffusion of adsorbate into the pores of the adsorbent
4. Equilibration of adsorption/desorption on the surface (active sites) of the pores

The overall rate of adsorption can be controlled by each, or a combination, of the above steps. Adsorption kinetics is influenced by adsorbent characteristics, system temperature, adsorbate concentration, and flow rate [51]. Adsorption kinetics can be evaluated using Pseudo-First Order (PFO), Pseudo-Second Order (PSO), and Intra-Particle Diffusion (IPD) models, which are discussed in the following sections.

3.3.2.1 Pseudo-first-order kinetic model

The first-order rate equation (Equation 3.24) was used by Lagergren (1898) to model the kinetics of adsorption of adsorbate onto a solid [52]. PFO and PSO kinetic models are classified under adsorption reaction models.

$$\frac{dq_t}{dt} = k_1(q_e - q_t) \qquad \text{(Equation 3.24)}$$

where q_t is the uptake (mg g^{-1}) at time t, q_e is the adsorption capacity (mg g^{-1}) at equilibrium and k_1 is the PFO rate constant (min^{-1}). Integrating Equation 3.24 from t = 0 to t = t and $q_t = 0$ to $q_t = q_t$, gives linear Equation 3.25.

$$ln(q_e - q_t) = lnq_e - k_1 t \qquad \text{(Equation 3.25)}$$

The value of k_1 for the linear form is obtained by plotting $ln(q_e - q_t)$ against time, t.

The non-linear form of the PFO kinetic model is written as follows.

$$q_t = q_e(1 - e^{-k_1 t}) \qquad \text{(Equation 3.26)}$$

Figure 3.8 shows a typical non-linear plot for a PFO kinetic model, which can be obtained using Equation 3.26.

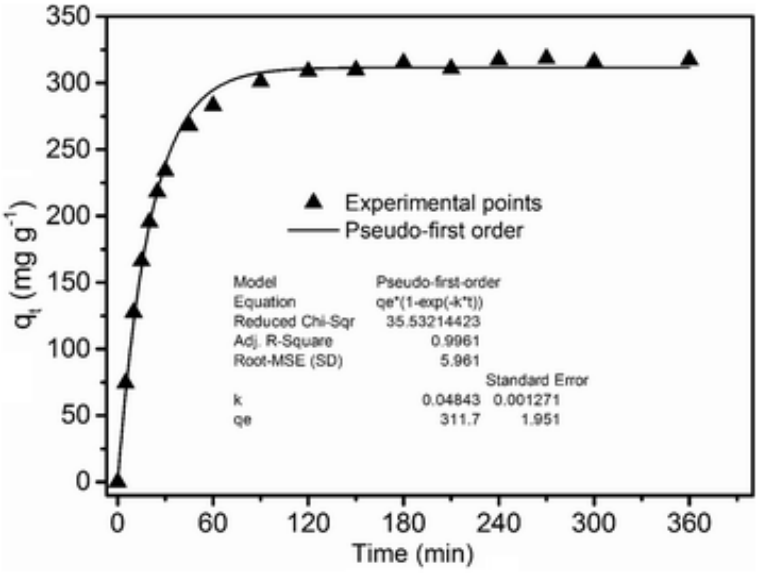

Figure 3.8. Pseudo-first-order kinetic adsorption model of Reactive Blue 4 dye using single-walled carbon nanotubes adsorbent [53].

3.3.2.2 Pseudo-second-order kinetic model

The PSO kinetic model was first proposed by Blanchard *et al*. [54] to evaluate the kinetics of ion exchange systems, and it was later developed by Ho *et al*. [55, 56] to describe adsorption kinetics of solid-liquid phase systems [24]. The PSO kinetic equation is mathematically described by Equation 3.27. The model assumes that the magnitude of the driving force, $(q_e - q_t)$, is determined by the available fraction of active sites on the adsorbent [51, 52].

$$\frac{dq_t}{dt} = k_2(q_e - q_t)^2 \qquad \text{(Equation 3.27)}$$

where k_2 is the PSO rate constant (g (mg·min)$^{-1}$). Integrating Equation 3.27 with boundary conditions: t (0, t) and q_t (0, q_t), yields Equation 3.28.

$$q_t = \frac{k_2 q_e^2 t}{1+k_2 q_e t} \qquad \text{(Equation 3.28)}$$

Equation 3.28 can be rearranged to give Equation 3.29.

$$\frac{t}{q_t} = \frac{1}{k_2 q_e^2} + \frac{t}{q_e} \qquad \text{(Equation 3.29)}$$

The values of q_e and k_2 can be obtained from slope and intercept of the linear plot of $\frac{t}{q_t}$ against t, which are equal $\frac{1}{q_e}$ and $\frac{1}{k_2 q_e^2}$, respectively.

Figure 3.9 shows a typical non-linear plot for a PSO kinetic model, which can be obtained using Equation 3.28.

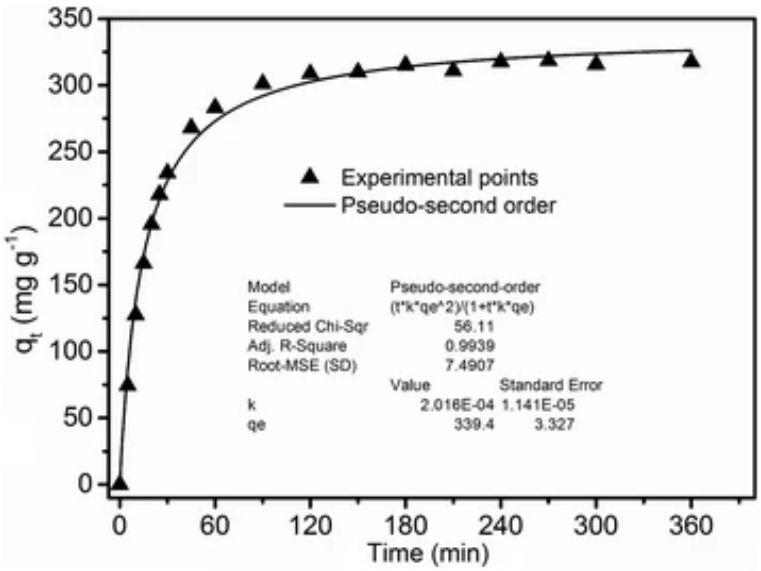

Figure 3.9. Pseudo-second-order kinetic adsorption model of Reactive Blue 4 dye using single-walled carbon nanotubes adsorbent [53].

3.3.2.3 Intraparticle diffusion model

In 1993, Weber and Morris found that in many adsorption systems, q_t varies almost directly with $\sqrt{t}$, as shown in Equation 3.30 [24, 52].

$$q_t = k_{int}\sqrt{t} + C \qquad \text{(Equation 3.30)}$$

where k_{int} is the intraparticle diffusion rate constant, and C is a constant indicating boundary layer thickness.

If the plot of q_t versus $\sqrt{t}$ yields a straight line that passes through the origin, the rate of adsorption is solely controlled by intraparticle diffusion. Oftentimes, the plot yields multiple linear sections, corresponding to film diffusion, pore diffusion and/or

adsorption/desorption equilibrium [51]. Figure 3.10 shows a typical Weber-Morris intraparticle kinetic plot, showing multiple linear sections.

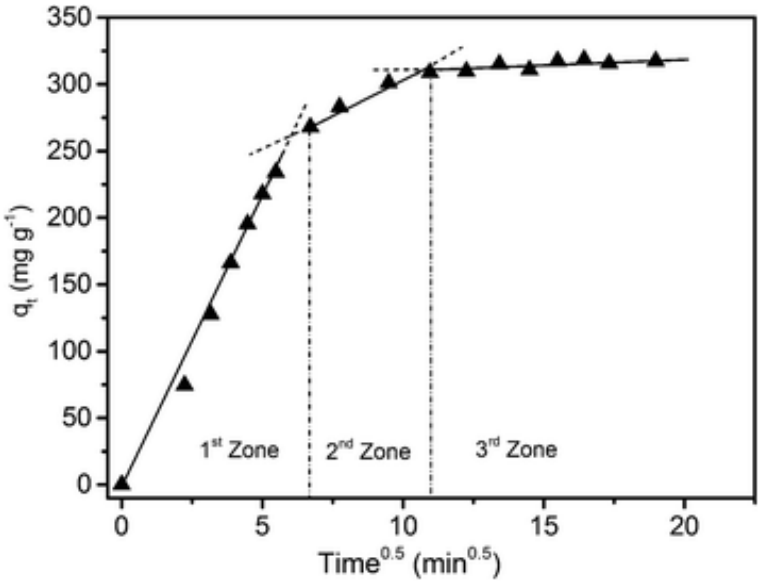

Figure 3.10. Weber-Morris intraparticle kinetic adsorption curve of Reactive Blue 4 dye using single-walled carbon nanotubes adsorbent [53].

References

[1] Seader, J. D., Henley, E. J. and Roper, D. K. (2010). *Separation Process Principles, 3rd Edition*, John Wiley Incorporated.

[2] Smithwick, R. (1982). A generalized analysis for mercury porosimetry. Powder Technology 33**:** 201-209

[3] Rahmani, K., Mahvi, A., Vaezi, F., Mesdaghinia, A., Nabizadeh, N. R. and Nazmara, S. (2009). Bioremoval of lead by use of waste activated sludge.

[4] Zeng, Y., Prasetyo, L., Tan, S. J., Fan, C., Do, D. and Nicholson, D. (2017). On the hysteresis of adsorption and desorption of simple gases in open end and closed end pores. Chemical Engineering Science 158**:** 462-479

[5] Langmuir, I. (1918). The adsorption of gases on plane surfaces of glass, mica and platinum. Journal of the American Chemical society 40**:** 1361-1403

[6] Freundlich, H. (1906). *Über die Adsorption in Lösungen. Habilitationsschrift durch welche... zu haltenden Probevorlesung" Kapillarchemie und Physiologie" einladet Dr. Herbert Freundlich*, W. Engelmann.

[7] Brunauer, S., Emmett, P. H. and Teller, E. (1938). Adsorption of gases in multimolecular layers. J. Am. Chem. Soc. 60**:** 309-319. https://doi.org/10.1021/ja01269a023

[8] Sing, K., Everett, D., Haul, R., Moscou, L. and Pierotti, R. (1985). Rouquerol j., Siemieniewska T., Reporting Physisorption Data for Gas/Solid systems with Special Reference to the Determination of Surface Area and Porosity(Recommendations 1984). Pure Appl. Chem 57**:** 603-619

[9] Thommes, M., Kaneko, K., Neimark, A. V., Olivier, J. P., Rodriguez-Reinoso, F., Rouquerol, J. and Sing, K. S. (2015). Physisorption of gases, with special reference to the evaluation of surface area and pore size distribution (IUPAC Technical Report). Pure Appl Chem 87**:** 1051-1069. https://doi.org/10.1515/pac-2014-1117

[10] Marsh, H. (1987). Adsorption methods to study microporosity in coals and carbons—a critique. Carbon 25**:** 49-58

[11] Seader, J., Henley, E. J. and Roper, D. K. (2016). *Separation process principles: With applications using process simulators*, John Wiley & Sons.

[12] Monson, P. A. (2012). Understanding adsorption/desorption hysteresis for fluids in mesoporous materials using simple molecular models and classical density functional theory. Microporous and Mesoporous Materials 160**:** 47-66

[13] Thommes, M. and Cychosz, K. A. (2014). Physical adsorption characterization of nanoporous materials: progress and challenges. Adsorption 20**:** 233-250

[14] Foo, K. Y. and Hameed, B. H. (2010). Insights into the modeling of adsorption isotherm systems. Chemical engineering journal 156**:** 2-10

[15] Sing, K. S., Rouquerol, F. and Rouquerol, J. (2013). Classical interpretation of physisorption isotherms at the gas-solid interface. Adsorption by Powders and Porous Solids: Principles, Methodology and Applications 2**:** 159-189

[16] Langmuir, I. (1916). The constitution and fundamental properties of solids and liquids. Part I. Solids. Journal of the American chemical society 38**:** 2221-2295

[17] Swenson, H. and Stadie, N. P. (2019). Langmuir's theory of adsorption: A centennial review. Langmuir 35**:** 5409-5426

[18] Hall, K. R., Eagleton, L. C., Acrivos, A. and Vermeulen, T. (1966). Pore-and solid-diffusion kinetics in fixed-bed adsorption under constant-pattern conditions. Industrial & engineering chemistry fundamentals 5**:** 212-223

[19] Tran, H. N., You, S.-J. and Chao, H.-P. (2017). Fast and efficient adsorption of methylene green 5 on activated carbon prepared from new chemical activation method. J. Environ. Manage. 188**:** 322-336. https://doi.org/10.1016/j.jenvman.2016.12.003

[20] Mcmillan, W. and Teller, E. (1951). The Assumptions of the BET Theory. The Journal of Physical Chemistry 55**:** 17-20
[21] Shimizu, S. and Matubayasi, N. (2022). Surface Area Estimation: Replacing the Brunauer–Emmett–Teller Model with the Statistical Thermodynamic Fluctuation Theory. Langmuir 38**:** 7989-8002
[22] Ambroz, F., Macdonald, T. J., Martis, V. and Parkin, I. P. (2018). Evaluation of the BET Theory for the Characterization of Meso and Microporous MOFs. Small methods 2**:** 1800173
[23] Rouquerol, J., Llewellyn, P. and Rouquerol, F. (2007). Is the BET equation applicable to microporous adsorbents. Stud. Surf. Sci. Catal 160**:** 49-56
[24] Azizian, S. and Eris, S. (2021). Adsorption isotherms and kinetics. *Interface science and technology*. Elsevier
[25] Ahmaruzzaman, M. (2008). Adsorption of phenolic compounds on low-cost adsorbents: a review. Advances in colloid and interface science 143**:** 48-67
[26] Tran, H. N., You, S.-J., Hosseini-Bandegharaei, A. and Chao, H.-P. (2017). Mistakes and inconsistencies regarding adsorption of contaminants from aqueous solutions: a critical review. Water Res. 120**:** 88-116. https://doi.org/10.1016/j.watres.2017.04.014
[27] Sips, R. (1948). On the structure of a catalyst surface. The journal of chemical physics 16**:** 490-495
[28] Saadi, R., Saadi, Z., Fazaeli, R. and Fard, N. E. (2015). Monolayer and multilayer adsorption isotherm models for sorption from aqueous media. Korean Journal of Chemical Engineering 32**:** 787-799
[29] Saleh, T. A. (2022). Isotherm models of adsorption processes on adsorbents and nanoadsorbents. *Interface Science and Technology*. Elsevier
[30] Varank, G., Demir, A., Yetilmezsoy, K., Top, S., Sekman, E. and Bilgili, M. S. (2012). Removal of 4-nitrophenol from aqueous solution by natural low-cost adsorbents.
[31] Nakanishi, K. (2016). Porosity Measurement. Handbook of Sol-Gel Science and Technology. Springer International Publishing AG**:** 1-11
[32] Thommes, M. (2010). Physical adsorption characterization of nanoporous materials. Chemie Ingenieur Technik 82**:** 1059-1073
[33] Hutson, N. D. and Yang, R. T. (1997). Theoretical basis for the Dubinin-Radushkevitch (DR) adsorption isotherm equation.
[34] Horváth, G. and Kawazoe, K. (1983). Method for the calculation of effective pore size distribution in molecular sieve carbon. Journal of Chemical Engineering of Japan 16**:** 470-475
[35] Saito, A. and Foley, H. (1991). Curvature and parametric sensitivity in models for adsorption in micropores. AIChE journal 37**:** 429-436
[36] Cheng, L. S. and Yang, R. T. (1995). Predicting isotherms in micropores for different molecules and temperatures from a known isotherm by improved Horvath-Kawazoe equations. Adsorption 1**:** 187-196
[37] Barrett, E. P., Joyner, L. G. and Halenda, P. P. (1951). The determination of pore volume and area distributions in porous substances. I. Computations from nitrogen isotherms. J Am Chem Soc 73**:** 373-380. https://doi.org/10.1021/ja01145a126
[38] Scherdel, C., Reichenauer, G. and Wiener, M. (2010). Relationship between pore volumes and surface areas derived from the evaluation of N2-sorption data by DR-, BET-and t-plot. Microporous and Mesoporous Materials 132**:** 572-575
[39] Lippens, B. C. and De Boer, J. (1965). Studies on pore systems in catalysts: V. The t method. Journal of Catalysis 4**:** 319-323
[40] Galarneau, A., Mehlhorn, D., Guenneau, F., Coasne, B., Villemot, F., Minoux, D., Aquino, C. and Dath, J.-P. (2018). Specific surface area determination for microporous/mesoporous materials: The case of mesoporous FAU-Y zeolites. Langmuir 34**:** 14134-14142

[41] Mular, A. and Roberts, R. (1966). A simplified method to determine isoelectric points of oxides. Canadian Mining and Metallurgical Bulletin 59**:** 1329
[42] Kosmulski, M. and Mączka, E. (2019). Surface charging and points of zero charge of less common oxides: Beryllium oxide. Colloids and Surfaces A: Physicochemical and Engineering Aspects 575**:** 140-143
[43] Cristiano, E., Hu, Y.-J., Siegfried, M., Kaplan, D. and Nitsche, H. (2011). A comparison of point of zero charge measurement methodology. Clays and Clay Minerals 59**:** 107-115
[44] Bialkowski, S. E., Astrath, N. G. and Proskurnin, M. A. (2019). *Photothermal spectroscopy methods*, John Wiley & Sons.
[45] Fleming, I., Williams, D., Fleming, I. and Williams, D. (2019). Infrared and raman spectra. Spectroscopic methods in organic chemistry**:** 85-121
[46] Easton, C. D., Kinnear, C., Mcarthur, S. L. and Gengenbach, T. R. (2020). Practical guides for x-ray photoelectron spectroscopy: Analysis of polymers. Journal of Vacuum Science & Technology A 38
[47] Laboratories, E. E. (2015). *X-ray Photoelectron Spectroscopy* [Online]. Available: https://www.eag.com/techniques/spectroscopy/x-ray-photoelectron-spectroscopy-xps-esca/ [Accessed 25 September 2023].
[48] Shard, A. G. (2020). Practical guides for x-ray photoelectron spectroscopy: Quantitative XPS. J. Vac. Sci. Technol. 38. https://doi.org/10.1116/1.5141395
[49] Qiu, Y., Wang, L., Leung, C.-F., Liu, G., Yang, S. and Lau, T.-C. (2011). Preparation of nitrogen doped K2Nb4O11 with high photocatalytic activity for degradation of organic pollutants. Appl. Catal. A-Gen. 402**:** 23-30. https://doi.org/10.1016/j.apcata.2011.04.015
[50] Krstić, V. (2020). Chapter 14: Role of zeolite adsorbent in water treatment. Handbook of nanomaterials for wastewater treatment: fundamentals and scale up issues. Elsevier Limited. Registered Office: The Boulevard, Langford Lane, Kidlington, Oxford, OX5 1GB, United Kingdom, Registration. https://doi.org/10.1016/B978-0-12-821496-1.00024-6
[51] Kajjumba, G. W., Emik, S., Öngen, A., Özcan, H. K. and Aydın, S. (2018). Modelling of adsorption kinetic processes—errors, theory and application. Advanced sorption process applications**:** 1-19
[52] Qiu, H., Lv, L., Pan, B.-C., Zhang, Q.-J., Zhang, W.-M. and Zhang, Q.-X. (2009). Critical review in adsorption kinetic models. Journal of Zhejiang University-SCIENCE A 10**:** 716-724. https://doi.org/10.1631/jzus.A0820524
[53] Lima, É. C., Adebayo, M. A. and Machado, F. M. (2015). Kinetic and equilibrium models of adsorption. Carbon nanomaterials as adsorbents for environmental and biological applications**:** 33-69. https://doi.org/10.1007/978-3-319-18875-1_3
[54] Blanchard, G., Maunaye, M. and Martin, G. (1984). Removal of heavy metals from waters by means of natural zeolites. Water research 18**:** 1501-1507
[55] Ho, Y.-S. and Mckay, G. (1999). Pseudo-second order model for sorption processes. Process biochemistry 34**:** 451-465
[56] Ho, Y. S., Ng, J. and Mckay, G. (2000). Kinetics of pollutant sorption by biosorbents. Separation and purification methods 29**:** 189-232

Chapter 4: Experimental Design

This chapter introduces the design of experiment principles and methods employed in this study and illustrates them with case studies, and a step-by-step guide on how to use Design Expert software for experimental design.

4.1 Principles of experimental design

Experimentation is the process of trying methods, activities, etc. to discover the effect that changes can have on the system under study. It is often used in scientific research to test hypotheses and identify causal relationships between variables, under controlled conditions. Experimentation enables us to acquire new knowledge, solve problems, enhance existing practices, or develop innovative products or services. A conventional approach to experimentation involves changing one experimental factor at a time, which may result in a large number of experimental runs. Alternatively, Design of Experiments (DoE) is a more efficient method that can simultaneously examine the interactions between factors and reduce the number of experimental runs [1]. DoE is a systematic way of conducting experiments to understand how multiple factors influence an outcome. DoE helps to optimize a process, system, or product by finding the best combination of factors [2]. There are three main principles of experimental design that help ensure valid and reliable results [2, 3]:

Randomisation: Randomisation is a fundamental principle that supports the use of statistical methods in experimental design. Randomisation implies that the assignment of the experimental units and the sequence of the experimental runs are determined by chance, i.e., it avoids the introduction of systematic and personal biases into the experiment by the experimenter. Randomised experimental runs ensure that the effects of uncontrolled or unknown sources of variation are minimized. To facilitate the selection and construction of experimental designs, experimenters often

employ computer software programs, such as Design Expert and Minitab. These programs generate a random order of the runs in the experimental design by using a random number generator.

Replication: To estimate the variability associated with the phenomenon under study, replication involves repeating an experimental condition or the entire experiment on different subjects or items. Replication differs from repeated measurements, which measure the same subject or item multiple times under the same experimental condition to assess the observational error. Replication accounts for sources of variability both within and between experimental runs, while repeated measurements only account for variability within a single run. Replication can enhance the significance, power, and replicability of the experimental results, whereas repeated measurements can decrease the observational error and increase the precision of the measurements. Replication requires proper sampling, and randomisation of subjects or items and treatments, whereas repeated measurements require careful control of measurement conditions and instruments.

Blocking: Blocking is a technique used in experimental design to reduce the effect of nuisance variables on the outcome of interest. Nuisance variables are factors that are not the focus of the experiment but may influence the response variable in some way. For instance, when preparing activated carbon from peanut shells, a nuisance variable could be the quality of the shells, which may vary depending on the region of cultivation, or other factors. Blocking involves grouping the experimental units (such as people, animals, or plants) into blocks that are similar in terms of the nuisance variable, and then randomly assigning treatments within each block. This way, the variation due to the nuisance variable is minimized within each block, and the effect of the treatment can be more clearly observed. Blocking can also improve the precision and power of statistical tests by reducing the error variance.

4.2 Designing experiments

The process of designing an experiment involves creating a set of systematic procedures to test a hypothesis or a research question. This requires careful planning and consideration, as it can be both challenging and time-consuming. A well-designed experiment can provide valid and reliable evidence to support or reject the hypothesis.

The following definitions are provided for the key terms used in experimental designs [4, 5]:

Factors: The term factors are also known as independent variables. Factors are the parameters or conditions that are manipulated or controlled in an experiment; they can be either *categorical* (e.g., gender, colour, etc.) or *numerical* (e.g., temperature, activation time, etc.).

Levels: These are different values or settings that are assigned to a factor, e.g., activation time could have levels of 0.5 h, 1 h and 2 h, whereas one could also have levels of yellow, red, green, etc.

Response variable: A response variable in DoE is the expected effect or outcome that is measured or observed in an experiment. It is also called a dependent variable or an output variable. The response variable is influenced by one, or more, independent variables or factors, which are the expected causes or inputs that are manipulated or controlled in an experiment.

Constant: as the name suggests, these factors do not vary across the experimental runs.

Nuisance variables: As previously defined, nuisance variables (or factors) are factors that are not the focus of the experiment but may influence the response variable in some way. Nuisance factors are classified into three categories: *uncontrolled factors*, which are environmental variables that cannot be easily manipulated (for example, ambient temperature and humidity); *controlled factors*, which are experimental

variables that can be set at different levels (for example, raw material batch); and *noise factors*, which are sources of variation that affect the measurement of the response (for example, instrument variation).

DoE is usually used to achieved one or a combination of the following objectives:

1. to screen the factors and interactions that have significant or negligible effects on the response, i.e., screening.
2. to optimize the experimental conditions that maximize or minimize the response, i.e., optimisation.
3. to evaluate the variability of the response under the selected experimental conditions, i.e., robustness.

Experimental design is a complex and meticulous process that requires careful planning. To ensure the validity and reliability of the data collected, many researchers follow a systematic procedure to design their experiments. This procedure consists of the following steps [4, 6]:

1. **Defining the experiment objectives**

   The first step of an experimental design is to formulate the research questions or problems that guide the investigation. This requires a thorough literature review or consultation with experts in the relevant field to define a clear and specific problem statement. A well-defined problem statement can enhance the understanding of the phenomenon under study and facilitate the solution of the problem. A useful technique is to list the specific questions or problems that the experiment aims to address. Using part of this study as a case study, previous studies have investigated the effects of various activation variables on the final properties of activated carbon using different precursors in a single stage chemical activation process. However, no sufficient information has been reported on the use of peanut shells as a precursor for this process. Furthermore, exploring the

effects of the activation variables can help to identify the optimal combination of these variables, which maximizes the final properties of the activated carbon produced. This experiment has two objectives: first, to examine the effects of activation variables on the final properties of activated carbon using peanut shells as a precursor in a single stage chemical activation process; and second, to determine the optimal combination of the activation variables that maximizes the final properties of the activated carbon derived from peanut shells.

2. **Selecting the response variables**

   The response variable should be chosen carefully to ensure that it reflects the relevant aspects of the process under investigation. It is possible to have more than one response variable for a given experiment. The measurement techniques for each response variable should be clearly defined and validated, and the calibration of the measurement system should be maintained throughout the experiment. If the measurement quality is low, the experimenter may opt to take multiple measurements for each experimental unit and use their mean as the observed response. Considering the peanut shell experiments described above, the response variables selected in the study are surface area and yield. These variables are commonly employed to evaluate activated carbon production process from an economic point of view.

3. **Selecting factors (variables) and levels**

   In this phase of an experimental design, it is important that the experimenter considers all sources of variation that may affect the process performance or outcome. The number of factors in an experiment may vary depending on the experiment and its objective. For screening experiments, the objective is to identify the most influential factors among many potential factors. Therefore, careful research is required to select the appropriate factors. The factors can be categorized into two types: design factors, which are the variables of interest to the

experimenter; and nuisance factors, which are the variables that are not of interest to the experimenter. The selected factors are varied within a range of values or quantities, which are called *levels*. The selection of levels requires proper research to ensure that they are sufficiently large to provide adequate information for the analysis of the study.

Continuing with the peanut shell experiments, the literature review informed the selection of factors for the experiments. The factors were temperature, hold time (residence time), and impregnation ratio (chemical weight/precursor weight). Previous studies, subject matter experts, and process considerations guided the choice of levels for these factors. Process considerations included the safety aspects of the materials, and the process involved.

4. **Selecting experimental design**

   Choosing an experimental design is the next step after completing the pre-experimental planning activities (steps 1 – 3). Applying the principles of experimental design, as discussed in Section 4.1, is essential for selecting an appropriate experimental design. Some designs may require one or more elements of these principles. Section 4.3 presents different types of experimental designs. Various statistical software/programs are now available to facilitate this step by suggesting a suitable design based on the input of factors, levels, and other relevant information. The objective of the experiment should always be considered; whether it is screening factors or optimising the process of choosing the design. For example, a response surface methodology (RSM) design is selected for the peanut experiment, because one of the objectives is to optimise the activation parameters – the details of this design type will be discussed later in this chapter.

5. **Conducting the experiment**

   When conducting the experiment, strict adherence to the planned procedure and close monitoring of the process is required. Any errors or inconsistencies in the

experimental execution could affect the experimental outcome and validity. According to Montgomery (2012) [2], conducting a few trial runs or pilot runs before the experiment can be beneficial. These runs can provide information on the consistency of the experimental material, the reliability of the measurement system, the estimation of the experimental error, and the practice of the experimental technique.

6. **Analysing the data**

After collecting data from the experiment, the next step is to statistically analyse the data. Statistical analysis of the data/results is the process of applying statistical methods to the data obtained from the experiment, in order to summarize, interpret, and draw conclusions from the data. Statistical analysis can help to achieve the following objectives:

- Describe the main features and patterns of the data, such as the mean, median, mode, standard deviation, range, frequency, etc.
- Test the hypotheses and assumptions that guided the design of the experiment, such as the significance, effect size, confidence interval, p-value, etc.
- Compare the results of different groups or treatments, such as using t-test, ANOVA, chi-square test, etc.
- Explore the relationships and associations between the variables, such as using correlation, regression, factor analysis, etc.
- Identify the sources of variation and error in the data, such as using error analysis, outlier detection, diagnostic plots, etc.

Statistical analysis of the results can be performed using various software tools, such as Design Expert, Minitab, Excel, etc. More details on statistical analysis of data will be covered later in this chapter.

7. **Conclusion**

   The analysis of the data leads to practical conclusions and recommendations based on the results. Verification runs are usually conducted to validate the conclusions. For example, if the experiment aimed to optimise the process, a verification run would confirm the optimal combination of variables (or factors) that maximises or minimises the dependent variable(s).

4.3 Factorial designs

4.3.1 Full factorial designs

These designs examine all possible combinations of factor levels and allow the estimation of all main effects and interactions, but they can be costly and time-consuming when the number of factors or levels is large. Full factorial designs are suitable for screening factors when the number of factors is low [7]. A common type of full factorial design is a 2-level design, where each factor has a low (-1 or -) and high (+1 or +) level. The factors are denoted by X_1, X_2, and X_3, the two levels assigned to each factor are given by (+), high, and (-), low, and y_1, y_2… are the responses. The total number of experiments in a full factorial design is $levels^k$ (where k = number of factors). So, for a 3 factor 2 level design, the total number of experiments is $2^k = 2^3 = 8$. Figure 4.1 shows the schematic illustration of a 2^3-full-factorial design, and Table 4.1 displays all the possible combinations of the factor levels.

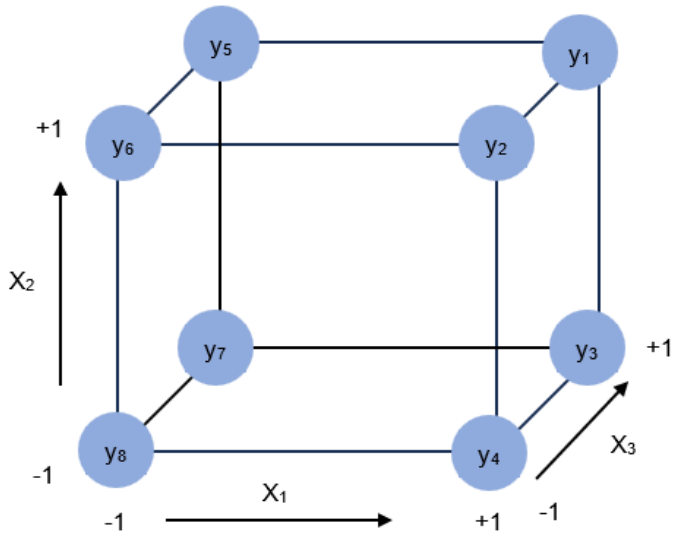

Figure 4.1. Schematic illustration of a 2^3-full-factorial design.

Table 4.1. Possible coded combinations of all the factor levels for a 2^3-full-factorial design.

Run	X_1	X_2	X_3	Response
1	+	+	+	y1
2	+	+	-	y2
3	+	-	+	y3
4	+	-	-	y4
5	-	+	+	y5
6	-	+	-	y6
7	-	-	+	y7
8	-	-	-	y8

$$\boldsymbol{y} = b_0 + b_1\boldsymbol{X_1} + b_2\boldsymbol{X_2} + b_3\boldsymbol{X_3} + b_{12}\boldsymbol{X_1X_2} + b_{13}\boldsymbol{X_1X_3} + \ldots$$

$$b_{23}\boldsymbol{X_2X_3} + b_{123}\boldsymbol{X_1X_2X_3} \qquad \text{(Equation 4.1)}$$

Equation 4.1 represents the model equation of the full factorial design experiment.

Where b_0 is the offset, b_1 is the coefficient for the effect of X_1, b_{12} is the coefficient for the interaction of X_1 and X_2, b_{123} is the coefficient for the interaction of X_1, X_2 and X_3 etc.

The main effect of each factor, or one factor effect on the response(s), can be estimated by comparing runs with replications. For example, runs 1 and 5 have the same levels for X_2 and X_3, but different levels for X_1. Therefore, the effect of X_1 on the response can be estimated by the difference between y_5 and y_1, i.e., $y_1 - y_5$. X_1 is + in runs 2, 3 and 4, similarly, we can compare runs 2 and 6, 3 and 7, and 4 and 8 to estimate the total effect of X_1 on the response. Therefore, the average of these effects can give us the effect of X_1 on the response, i.e.,

$$Effect\ of\ X_1 = \frac{(y_1 - y_5) + (y_2 - y_6) + (y_3 - y_7) + (y_4 - y_8)}{4} \quad \text{(Equation 4.2)}$$

$$= \frac{(y_1 + y_2 + y_3 + y_4 - y_5 - y_6 - y_7 - y_8)}{4} \quad \text{(Equation 4.3)}$$

The main effect of factors or one factor effect can be calculated using the following equation.

$$Effect = (\sum response\ at\ (+) - \sum response\ at\ (-))/2^{k-1} \quad \text{(Equation 4.4)}$$

Where k = no. of factors.

A similar approach can be applied to estimate the main effects of X_2 and X_3 as shown below.

$$Effect\ of\ X_2 = \frac{(y_1 + y_2 - y_3 - y_4 + y_5 + y_6 - y_7 - y_8)}{4} \quad \text{(Equation 4.5)}$$

$$Effectof\ X_3 = \frac{(y_1 - y_2 + y_3 - y_4 + y_5 - y_6 + y_7 - y_8)}{4} \quad \text{(Equation 4.6)}$$

The interaction effects of the factors can also be estimated by first expanding Table 4.1 as shown below.

Table 4.2. Possible coded combinations of all the factor levels and their interactions for a 2^3-full-factorial design.

Run	X_1	X_2	X_3	$X_1 X_2$	X_1X_3	$X_2 X_3$	$X_1 X_2X_3$	Response
1	+	+	+	+	+	+	+	y1
2	+	+	-	+	-	-	-	y2
3	+	-	+	-	+	-	-	y3
4	+	-	-	-	-	+	+	y4
5	-	+	+	-	-	+	-	y5
6	-	+	-	-	+	-	+	y6
7	-	-	+	+	-	-	+	y7
8	-	-	-	+	+	+	-	y8

The coded values for the interactions are calculated by multiplying the corresponding individual factors.

In a similar way, the interaction effects can be calculated using Equation 4.4. The interaction effects are estimated as follows.

$$Effectof\ X_1\ X_2\ = \frac{(y_1+y_2-y_3-y_4-y_5-y_6+y_7+y_8)}{4} \quad \text{(Equation 4.7)}$$

$$Effectof\ X_1\ X_3\ = \frac{(y_1-y_2+y_3-y_4-y_5+y_6-y_7+y_8)}{4} \quad \text{(Equation 4.8)}$$

$$Effectof\ X_2\ X_3\ = \frac{(y_1-y_2-y_3+y_4+y_5-y_6-y_7+y_8)}{4} \quad \text{(Equation 4.9)}$$

$$Effectof\ X_1\ X_2X_3\ = \frac{(y_1-y_2-y_3+y_4-y_5+y_6+y_7-y_8)}{4} \quad \text{(Equation 4.10)}$$

Utilizing contemporary computer software, such as Design Expert, Minitab, STAT/SAS, facilitates the efficient execution of the above calculations. These advanced tools offer a smooth approach to statistical analysis, allowing for a more effective interpretation of results.

4.3.2 Fractional factorial designs

A fractional factorial design is a type of experimental design that uses only a fraction of the possible combinations of factor levels that a full factorial design would use, i.e., 2^{k-1}. A fractional factorial design is useful when the number of factors is large or the resources are limited, as it reduces the number of runs and the cost of the experiment. For instance, a fractional factorial design for a 6-factor experiment (2^{6-1}) requires the same number of experimental runs as a full factorial design for a 5-factor experiment (2^5). However, a fractional factorial design also confounds some of the main effects and interactions, meaning that they cannot be estimated separately from each other. Therefore, a fractional factorial design requires some assumptions about the negligible effects and careful selection of the fraction to use [8].

The main effect of factors can be calculated using the following equation.

$$Effect = (\sum response\ at\ (+) - \sum response\ at\ (-))/2^{k-m-1} \qquad \text{(Equation 4.11)}$$

Where k = no. of factors, and m = 1 for half factorial design.

The interaction effects can be estimated, in a similar way, as that described in Equations 4.7 – 4.10.

4.4 Response surface methodology

Box and Wilson (1951) [9], introduced response surface methodology (RSM) as a statistical approach to facilitate the enhancement of manufacturing processes in the chemical industry. They proposed a method for designing experiments, fitting polynomial models, and optimising the response variable(s) by adjusting the independent variables. Their work was motivated by the need to improve the quality and efficiency of industrial production, especially in the context of complex chemical reactions. RSM has since been widely adopted and extended in various fields of science and engineering.

RSM is a useful tool for product design and process improvement, as it allows us to understand how the response depends on the independent variables, and how to adjust them to achieve our goals. RSM employs graphical techniques, such as contour plots, surface plots, interaction plots, etc., to visualize the shape and features of the response surface, which represents the relationship between the response and the independent variables. These graphical techniques can help us to identify the optimal settings of the independent variables that maximize or minimize the response, as well as to examine the effects of interactions and nonlinearities on the response [7, 10].

RSM enables a more thorough investigation of a response variable than a two-level factorial or fractional–factorial design. A centre point for each independent variable is included in its design, which adds a third level to each factor. This is called a three-level factorial design because of the third factor level [7].

The following sections describe the two main types of response surface designs: central composite designs and Box-Behnken designs.

4.4.1 Box-Behnken design

Box-Behnken design (BBD) is a type of experimental design for RSM. BBDs have the following characteristics [11, 12]:

- BBD only requires three levels of each factor, usually coded as -1, 0, +1, and the treatment combinations are at the midpoints of the edges and at the centre, as shown in Figure 4.2.
- The design is sufficient to fit a quadratic model, that is, one containing squared terms, products of two factors, linear terms and an intercept.
- The design does not include any points where all factors are at their extreme settings, such as all low or all high.

- The design is rotatable or near rotatable, which means that the estimation variance depends only on the distance from the centre and is more or less constant inside the experimental region.

BBDs are useful for optimising a response surface and avoiding levels that are extreme, i.e., corner points and the star points (axial points) which are extreme points in terms of region in which the experiment is being performed. They usually have fewer design points than central composite designs, making them less expensive to run. A typical BBD for 3 factors, with 1 replicate and 3 centre points is shown in Table 4.3.

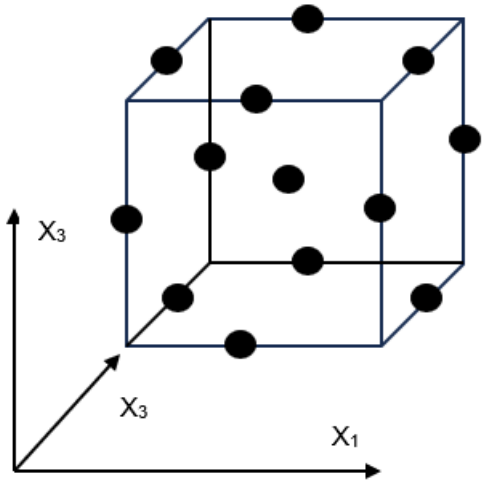

Figure 4.2. Schematic illustration of the Box-Behnken design for response surface methodology.

Table 4.3. A typical Box-Behnken design for 3 factors.

Run	X_1	X_2	X_3
1	-1	-1	0
2	+1	-1	0
3	-1	+1	0
4	+1	+1	0
5	-1	0	-1
6	+1	0	-1
7	-1	0	+1
8	+1	0	+1
9	0	-1	-1
10	0	+1	-1
11	0	-1	+1
12	0	+1	+1
13	0	0	0
14	0	0	0
15	0	0	0

4.4.2 Central composite design

Central composite designs (CCD) were first introduced by Box and Wilson in 1951, which have now become the most widely used second-order designs [12]. CCD are a type of factorial or fractional factorial design with centre points and axial points (also called star points) that allow for estimating curvature in the response surface. The factorial design has two levels for each factor, coded as -1 and +1, whereas the axial points add the third level per factor, denoted by $\pm\alpha$, where α is the distance between the axial and the centre points. The axial points represent new extreme values (high, +1 and low, -1) for each factor in the design domain. The value of α depends on the properties of the design, such as orthogonality or rotatability. CCD can fit a full quadratic model and are often used in sequential experimentation, as they can include

information from a prior factorial experiment. This feature makes them suitable also for screening variables. Three types of CCDs exist, which are described as follows [13].

- **Circumscribed central composite design (CCC)**

  This type of CCD has five levels for each factor, and the axial points are outside the factorial space, establishing new high and low ranges. This type of CCD explores the largest process space.

- **Inscribed central composite design (CCI)**

  This type of CCD has five levels for each factor, and the axial points are inside the factorial space, at the corners of the process space. This type of CCD explores the smallest process space.

- **Face-centred central composite design (CCF)**

  This type of CCD has three levels for each factor, and the axial points are at the centre of each face of the factorial space, i.e., $\alpha = \pm 1$. This type of CCD is not rotatable.

The location of the axial points for the three types of CCDs is illustrated in Figure 4.3.

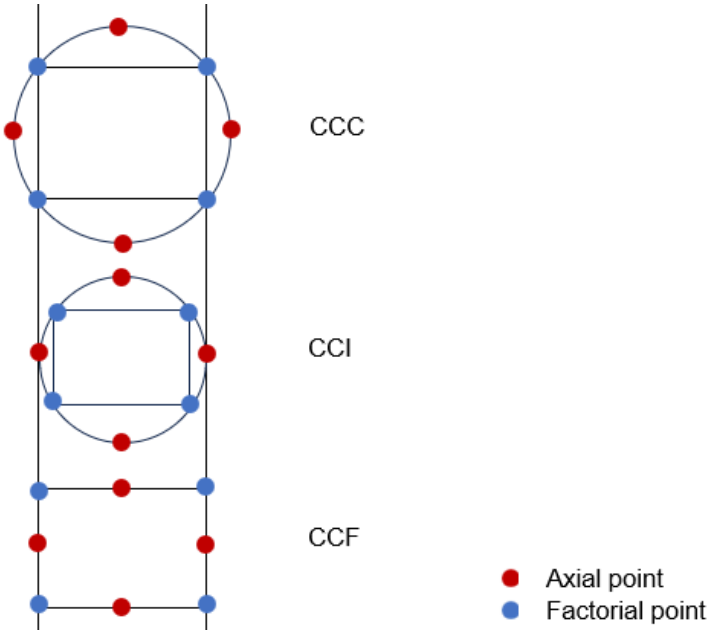

Figure 4.3. Schematic illustration of the position of axial points for the three types of central composite designs.

Note that Figure 4.3 is an illustration of a typical 2-factor CCD.

The value of α, which determines the location of the axial points, depends on the number of runs in the factorial part of the CCD, in order to maintain rotatability. Rotatability is a property of the design that ensures constant variance of the predicted response at a given distance from the centre point. The relation below can be used to determine the value of α.

$$\alpha = \sqrt[4]{2^k} \qquad \text{(Equation 4. 11)}$$

Where k is the number of factors and 2^k represents the factorial portion (full factorial) of the design. The factorial portion of the design can also be a fractional factorial design.

A comparative analysis of the main features of central composite designs and Box-Behnken designs is presented in Table 4.4. The choice of a design type depends on the experimental objectives and constraints, such as cost, time, flexibility of the equipment (in terms of variables adjustment), etc. Both CCD and BBD can achieve optimisation objectives, but CCD has some advantages over BBD. First, CCD can incorporate prior information from a factorial experiment, either full or fractional, and thus enable sequential experimentation. Second, CCD can explore the effects of the factors beyond or below the chosen levels, and thus provide more information about the response surface [4]. Therefore, this study employs CCD to investigate the effects of the activation parameters on the properties of activated carbon derived from peanut shells and to optimise the activation parameters.

Table 4.4. Comparison of the main features of central composite designs and Box-Behnken designs.

Feature	CCD	BBD
Number of levels per factor	3, 4, or 5	3
Number of runs	Depends on the type of CCD (circumscribed, inscribed, or faced) and the number of factors	Depends on the number of factors
Contains a factorial or fractional factorial design	Yes	No
Contains axial points (star points)	Yes	No
Contains corner points	Depends on the type of CCD	No
Contains centre points	Yes	Yes
Contains edge points	No	Yes
Rotatable or near rotatable	Yes	Yes
Orthogonal or near orthogonal	Depends on the type of CCD	Yes
Suitable for sequential experimentation	Yes	No
Suitable for estimating curvature	Yes	Yes
Suitable for estimating main effects and interactions	Yes	Yes
Robust to errors in the settings of input variables	No	Yes
Avoids extreme or undesirable values of the factors	No	Yes

As discussed in Section 4.4.2, the three types of CCD have different features in terms of design space exploration. The Circumscribed and Face-centred composite designs cover more design space than the Inscribed central composite design, but they also face more process constraints. For instance, the maximum temperature level was limited to 600 °C, which is lower than the boiling point of the activating agent (Zinc chloride; boiling point: 732 °C), to prevent the activating agent from escaping the

system and blocking the outlet tube of the tube furnace. Moreover, negative values arising from the axial points of the Circumscribed CCD (Figure 4.4), are not relevant to this design. Therefore, the Face-centred CCD (Figure 4.5) was chosen as a more suitable design considering the process constraints.

Std	Run	Factor 1 A:Temperature °C	Factor 2 B:Hold time min	Factor 3 C:Impregnation ratio (g/g)	Response 1 Surface area m2/g	Response 2 Yield %
3	1	300	120	0.25		
17	2	450	67.5	1.125		
10	3	662.132	67.5	1.125		
15	4	450	67.5	1.125		
11	5	450	-6.74621	1.125		
8	6	600	120	2		
2	7	600	15	0.25		
5	8	300	15	2		
1	9	300	15	0.25		
4	10	600	120	0.25		
9	11	237.868	67.5	1.125		
14	12	450	67.5	2.36244		
7	13	300	120	2		
13	14	450	67.5	-0.112437		
12	15	450	141.746	1.125		
18	16	450	67.5	1.125		
6	17	600	15	2		
16	18	450	67.5	1.125		

Figure 4.4. A typical Circumscribed central composite design using the factor levels selected in this study design.

Std	Run	Factor 1 A:Temperature °C	Factor 2 B:Hold time min	Factor 3 C:Impregnation ratio (g/g)	Response 1 Surface area m2/g	Response 2 Yield %
1	1	300	15	0.25		
10	2	600	67.5	1.125		
15	3	450	67.5	1.125		
8	4	600	120	2		
6	5	600	15	2		
4	6	600	120	0.25		
13	7	450	67.5	0.25		
5	8	300	15	2		
18	9	450	67.5	1.125		
9	10	300	67.5	1.125		
16	11	450	67.5	1.125		
17	12	450	67.5	1.125		
2	13	600	15	0.25		
11	14	450	15	1.125		
12	15	450	120	1.125		
14	16	450	67.5	2		
3	17	300	120	0.25		
7	18	300	120	2		

Figure 4.5. A typical Face-centred central composite design using the factor levels selected in this study design.

4.4.3 A step-by-step Face-centred CCD using Design Expert 13.1.0

Design Expert is a software developed by Stat-Ease Inc., Minneapolis, USA [14]. It facilitates the design, analysis, and optimisation of experiments using various statistical tools, such as factorial designs, response surface methods, etc. Design Expert enables the identification of significant factors that influence a process or product, the exploration of the effects of the factors on the response, and the determination of the optimal settings for the factors. Moreover, the software provides graphical tools to visualize results and numerical tools to optimise outcomes. A step-by-step guide using Design Expert for Face-centred CCD is provided in Appendix B. Note that this case study employs the chemical activation of peanut shells experiment conducted in this study.

References

[1] Jawad, A. H., Alkarkhi, A. F. and Mubarak, N. S. A. (2015). Photocatalytic decolorization of methylene blue by an immobilized TiO2 film under visible light irradiation: optimization using response surface methodology (RSM). Desalin Water Treat 56**:** 161-172. https://doi.org/10.1080/19443994.2014.934736

[2] Montgomery, C. (2012). Design and Analysis of Experiments. 8 edn. John Willey & Sons. Inc, New York

[3] Dean, A., Voss, D. and Draguljić, D. (2017). Principles and Techniques. *Design and Analysis of Experiments.* Springer, Cham. https://doi.org/10.1007/978-3-319-52250-0_1

[4] Ahmed, S. *Design of Experiments* [Online]. Available: https://www.theopeneducator.com/do [Accessed 14 March 2021].

[5] Hinkelmann, K. and Kempthorne, O. (2007). *Design and analysis of experiments, volume 1: Introduction to experimental design*, John Wiley & Sons.

[6] Dean, A., Voss, D., Draguljić, D., Dean, A., Voss, D. and Draguljić, D. (2017). Planning experiments. Design and analysis of experiments**:** 7-30

[7] John R. Wagner, E. M. M., Harold F. Giles (2014). Design of Experiments. *In:* John R. Wagner, E. M. M., Harold F. Giles (ed.) *Extrusion* Second Edition ed.: William Andrew Publishing. https://doi.org/10.1016/B978-1-4377-3481-2.00025-9

[8] Minitab. *Factorial and fractional factorial designs* [Online]. Available: https://support.minitab.com/en-us/minitab/21/help-and-how-to/statistical-modeling/doe/supporting-topics/factorial-and-screening-designs/factorial-and-fractional-factorial-designs/ [Accessed 25 June 2022].

[9] Box, G. and Wilson, K. (1951). On the experimental designs for exploring response surfaces. Ann Math Stat 13**:** 1-45

[10] Mehmood, T., Ahmed, A., Ahmad, A., Ahmad, M. S. and Sandhu, M. A. (2018). Optimization of mixed surfactants-based β-carotene nanoemulsions using response surface methodology: an ultrasonic homogenization approach. Food Chem 253**:** 179-184. https://doi.org/10.1016/j.foodchem.2018.01.136

[11] Bouzid Ait-Amir, P. P., Abdelkhalak El Hami (2015). Meta-Model Development. *In:* Abdelkhalak El Hami, P. P. (ed.) *Embedded Mechatronic Systems 2.* Elsevier. https://doi.org/10.1016/B978-1-78548-014-0.50006-2

[12] Dean, A., Voss, D., Draguljić, D., Dean, A., Voss, D. and Draguljić, D. (2017). Response surface methodology. Design and analysis of experiments**:** 565-614

[13] N.I.S.T. *Central composite designs* [Online]. Available: https://www.itl.nist.gov/div898/handbook/pri/section3/pri3361.htm [Accessed 22 June 2021].

[14] Statease. *DesignExpert* [Online]. Available: https://www.statease.com/software/design-expert/ [Accessed 14 April 2021].

Chapter 5: Synthesis of Activated Carbon from Peanut Shells by Chemical Activation: Optimisation and Characterisation

This chapter presents results and discussion from a systematic approach for the synthesis of activated carbons (ACs) from peanut shells (PNTS). It also includes experimental procedures for materials characterisation and selection, as well as analysis of the most effective candidate for removing methyl orange (MO) and Methylene Blue (MB) from aqueous solution.

5.1 Experimental procedures

This section aims to provide detailed experimental procedures for the synthesis, characterisation, and testing of activated carbons derived from peanut shells (PNTS). The underlying theories related to the methods examined in this section have been presented in Chapter 3 and are not repeated here. Moreso, the main factors that influenced the experimental outcome are highlighted under each sub-section.

5.1.1 Synthesis of activated carbon from peanut shells

Raw peanuts were purchased from a UK-based supplier. The shells of the peanuts were removed and washed with water to eliminate surface contaminants. The shells were subsequently oven-dried at 100 ± 2 °C for an overnight period. After drying, the shells were ground and sieved to obtain a 2 mm particle size. Each experimental run involved $ZnCl_2$ impregnation of 5 g (W1) of screened peanut shells (PNTS) at ratios of 0.25, 1.13 and 2, which represented the low, centre, and high levels of impregnation ratios ($ZnCl_2$ g/ precursor g), respectively – the full experimental design is presented in Chapter 4, as a case study. The precursor was thoroughly mixed with 25 mL of deionised water containing $ZnCl_2$ weights (W2) that varied according to the impregnation ratio in all experiments. The mixture was then allowed to equilibrate for approximately 24 h at room temperature. This is to note that the volume of water (25

mL) for impregnation, and the mass of the precursor (5 g) were kept constant in all experiments. The mixture underwent oven-drying at 100 ± 2 °C for an overnight period, after the impregnation process.

Carbonisation of the oven-dried sample occurred in a tube furnace under nitrogen flow (250 mL/min) at 300, 450 or 600 °C with a dwell/hold time of 15, 68 or 120 min, and a ramp-rate of 15 °C/min – the temperatures and hold times were varied according to the experimental design. The furnace yielded a carbonised product that was weighed (W3) and transferred into a jar with 200 mL of 0.1 M HCl. The jar was agitated for 1 h on a shaker to leach out any residual activating salt. After the acid wash, the liquid was separated by filtration and the product underwent boiling in 500 mL of hot deionised water for about 10 min and separated by filtration, before washing in room temperature deionised water to eliminate chloride ions and lower acidity – the washing was repeated 5 times with 500 mL of deionised water in each cycle. Finally, after washing, the product was dried in the oven at 100 ± 2 °C for approximately 24 h, weighed again after drying (W4) and stored for characterisation. Figure 5.1 shows the process cycle of the activated carbon developed from peanut shells. The samples were named for easy identification using the precursor initials (PNTS), impregnation ratio (I.R.), activation temperature and hold time.

The yield of the process, as a percentage, was calculated using the following equation:

$$Yield = \left(\frac{W4}{W1}\right) \times 100 \qquad \text{(Equation 5.1)}$$

The reagent recovery (R.R) from the process was estimated using the following equation:

$$R.R = \left(\frac{W3-W4}{W2}\right) \times 100 \qquad \text{(Equation 5.2)}$$

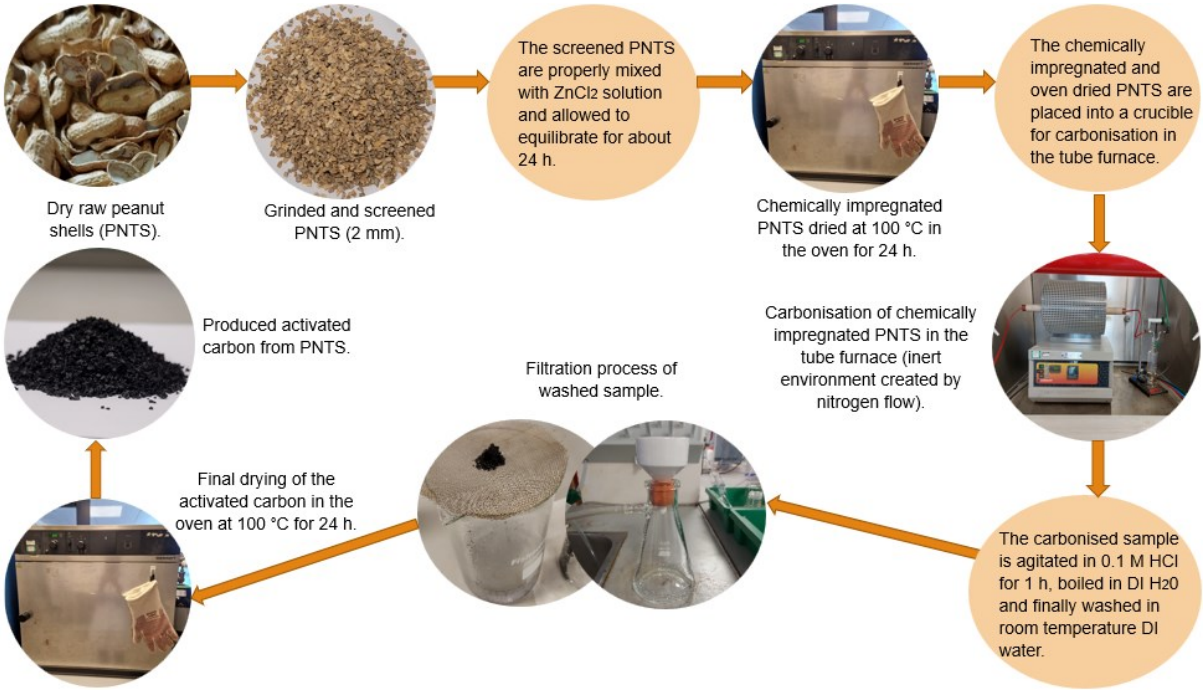

Figure 5.1. Activated carbon production process cycle from peanut shells.

5.1.2 Experimental design for the preparation of activated carbon

The experimental design examined the effects of three factors: temperature (A), hold time (B) and impregnation ratio (I.R.) (C), which were selected based on preliminary studies and previous reports [1-3]. The coded values for the activation variables were -1 for the minimum, 0 for the centre point and +1 for the maximum point, as shown in Table 5.1. Chapter 4 presents a case study of the procedures for creating a fully randomised experimental design, using the selected factors. Two properties were considered as the responses: yield (Y_1) and surface area (Y_2). The latter is an indication of potential adsorption capability. These properties determine the economic viability of the production process.

Table 5.1. Activation parameters and their coded values for the Face-centred central composite design used for the synthesis of PNTS-based activated carbons.

Variables (factors)	*Units*	*Variable levels*				
		Low (-1)	Mid (0)	High (1)	-α	+α
Temperature (A)	(°C)	300	450	600	300	600
Hold time (B)	(min)	15	68	120	15	120
Impregnation ratio, I.R.	(wt/wt)	0.25	1.13	2	0.25	2
Responses						
Yield (Y_1)	(%)					
Surface area (Y_2)	(m^2/g)					

5.1.3 Textural characterisation

The textural properties (e.g., BET specific surface area, pore volume and pore size) of the produced PNTS-based ACs were determined by the N_2 gas adsorption method, using the Brunauer–Emmett–Teller technique, as described in Chapter 3. This was achieved using a Micromeritics ASAP 2420 instrument that employs N_2 adsorption at -195.8 °C. First, the samples were outgassed to remove any physically adsorbed species accumulated during sample storage (e.g., H_2O, CO_2), and to ensure a reproducible initial state of the samples for the same application. Before outgassing, a clean sample tube and seal frit at room temperature were weighed as an empty tube set. Then, the sample was transferred into the empty tube using a funnel, and the mass of the sample plus tube set was measured. The mass of the sample was determined by difference and recorded. The optimal amount of sample required is best determined by experiment (i.e., this may require an initial trial). For nitrogen analysis, a sample mass providing, at least, a total surface area ranging from 40 to 120 m^2 is recommended. The sample tube plus sample was then connected to an outgas port of the instrument and surrounded by a heating mantle. Outgassing was performed, under vacuum, at 250 °C for 4 h, using a ramp rate of 10 °C/min.

After outgassing, the sample tube plus sample was weighed again to determine the mass of the sample post-outgas, for surface area analysis. The tube was inserted into

an open-ended cylindrical isothermal jacket and connected to an analysis port. Moreso, to increase the measurement accuracy, for samples with low surface area, a filler rod can be used to reduce the dead volume (volume of unoccupied space) within the sample tube. The system temperature was lowered to -195.8 °C by filling the analysis Dewar with liquid nitrogen. The adsorption process is usually performed by dosing the sample with nitrogen gas and allowing equilibration between two successive relative pressure readings – this process is automated within the system. The process continues with increasing pressure, up to the upper relative pressure boundary, usually between 0.99 and 0.995 [4]. After the adsorption process, the desorption process proceeds by lowering the pressure – this process is also automated within the system. The textural properties (surface area, pore volume, and pore size) of the sample were calculated from the gas adsorption isotherm using the theoretical analyses described in Chapter 3.

The total pore volume (TPV) was calculated using the equation below:

$$TPV = Q_{sat} * \left(\frac{\rho_{vap}}{\rho_{lig}}\right) \quad \text{(Equation 5.3)}$$

where Q_{sat} is maximum nitrogen adsorption (in cm^3/g, usually at relative pressure of 0.97 or above), ϱ_{vap} is density of N_2 vapour at standard temperature and pressure (STP, i.e., 0 °C and 1 atm) and ϱ_{liq} = density of liquid N_2 at its boiling point.

5.1.4 Surface chemistry characterisation

The determination of the points of zero charge (PZC) of the PNTS-based activated carbons (AC) was carried out using the salt addition technique described in Chapter 3. The pH values of 0.1 M $NaNO_3$ solutions (40 mL each) were adjusted from 3 to 11 using 0.1 M HNO_3 or 0.1 M NaOH solutions. AC sample (0.2 g) was added to each solution and shaken, at 150 rpm, for approximately 24 h, on a VWR STD 3500 shaker. After equilibration, the mixture was filtered, and the pH reading was recorded. The

pH difference, ΔpH between the initial (pH_i) and final (pH_f) pH values (i.e., $pH_f - pH_i$) was plotted against pH_i to determine the PZC.

Fourier transform infrared (FTIR) spectroscopy was used to gain insight into the various functional groups on the surface of the carbon materials. The measurement was achieved using a MB3000 FT-IR laboratory analyser. First, the sample platform of the analyser was cleaned with alcohol to eliminate any surface contaminants. Then, a background scan was performed to measure the air absorbance that had to be subtracted from the sample spectrum. The AC sample (approximately 0.02 g each) was ground and placed on the sample holder of the spectrometer. The sample was secured on the sample platform using the instrument's torque wrench. The samples were scanned over a range of 500 – 4000 $cm^{-1,}$ using the MB3000 FT-IR laboratory analyser with Horizon MB™ FTIR software. 449 scans were taken at a resolution of 8 cm^{-1}.

X-ray photoemission spectroscopy (XPS) analysis was conducted using a Thermo Scientific K-alpha X-ray Photoelectron Spectrometer (Thermo Scientific, East Grinstead, UK). The instrument was equipped with a monochromatic Al Kα X-ray source ($h\nu$ = 1486.6 eV), and a hemispherical electron analyser. The spectra were recorded at a pass energy of 40 eV with an energy step size of 0.05 eV. The high-resolution spectra of C1s, O1s, and N1s regions were obtained to identify the chemical states of these elements. The background subtraction was performed using the Shirley method [5]. The relative atomic concentration of each element was calculated using Equation 3.21 (Section 3.2).

5.1.5 True density measurement

The true densities of the PNTS-based AC samples, which is the mass of the adsorbent per volume occupied by the particle, excluding the volume of the pores, were determined using helium pycnometry (Micromeritics Accupyc II helium pycnometer with Accupyc II version 3.0 software). The mass of a clean pycnometer sample cup

and a small amount of AC sample in the cup were measured separately – the mass of the sample (W_s) was then determined by difference. The cup with the AC sample was placed and sealed within the pycnometer for analysis. The system was purged with helium gas (ten times) to eliminate any trapped gas molecules prior to analysis. Then, the pycnometer measurement process commenced, in which helium fills the chamber of known volume (V_1), and the system is allowed to reach a stable pressure (P_1). The gas is allowed to expand to a reference chamber and attain a stable pressure – this enables the calculation of change in pressure (ΔP) and volume (ΔV). Equations 5.3 and 5.4 are used to compute the sample volume (V_s) and density (ρ_s), respectively.

$$V_s = V_1 - (\frac{P_1}{\Delta P} - 1)\Delta V \quad \text{(Equation 5.4)}$$

$$\rho_s = W_s/V_s \quad \text{(Equation 5.5)}$$

5.1.6 Adsorption experiment

A batch adsorption experiment technique, as described in Chapter 3, was employed to evaluate the performance of the PNTS-based ACs for screening. This was achieved by agitating 0.05 g of AC sample with 50 mL of MO solution (100 mg/L initial concentration), in a 500 mL Erlenmeyer flask (several identical flasks were set up to allow the different time intervals to be probed). The mixtures were agitated on an orbital shaker, operated at 150 rpm, and at room temperature. At time intervals of 3 h, 5 h and 24 h, the mixtures were separated by centrifugation, and the residual concentrations (C_t) were measured at 465 nm, using a Varian CARY 5000 UV-VIS-NIR spectrophotometer.

5.1.7 Proximate and ultimate analysis

A thermogravimetric technique, based on British Standard BS1016, was used to perform proximate analysis of the precursor, and the PNTS-based activated carbon materials. The method followed a similar procedure to the one reported by Ottaway [6]. The proximate analysis of the AC sample was performed using a NETZSCH STA

449 F3 Jupiter system. A crucible containing 10 - 20 mg of the sample was weighed under a nitrogen gas flow of 50 mL/min and then heated to 100 °C at a rate of 10 °C/min. The sample was kept at this temperature for about 10 min until the mass stabilised, and the mass loss due to moisture content was recorded. The sample was further heated to 920 °C and maintained for 3 min, and the mass loss due to devolatilisation was recorded. The temperature was then lowered to 820 °C, and the gas flow was switched to 50 mL/min of pressurised air. The sample was kept under this condition for ~10 min until the mass stabilised. The gas flow was switched back to nitrogen and the furnace was cooled down to ambient temperature. The final mass of the sample was recorded, and the mass loss was due to oxidation. The ultimate analysis was carried out on an Exeter Analytical CE440 Elemental analyser.

5.1.8 Scanning electron microscopy

Using a JEOL JSM-IT100 scanning electron microscope (SEM) with an accelerating voltage of 20 kV, the surface morphology of both the raw precursor and the activated carbon was examined. Double sided carbon adhesive discs were used to mount the samples on aluminium SEM specimen stubs. Scanning was conducted at a magnification of 250x under high vacuum (HV) conditions.

5.2 Results and discussion

5.2.1 Fit summary of the experimental design for AC preparation

The dataset from the surface area analysis, yield of the process, and other dependent variables was analysed using Design Expert. Quadratic models for all the dependent variables were suggested by the sequential model sum of squares from the statistical software. Equations 5.5 and 5.6 show the regression equations obtained for the production process determining responses (Y_1: yield and Y_2: surface area).

$$Y_1 = +124.50 - 0.25A - 0.05B - 8.07C + 0.01AC - 0.01BC + 1.00C^2 \quad \text{(Equation 5.6)}$$

$$Y_2 = -6429.31 + 29.84A - 2.48B + 367.17C - 0.0039AB + 1.90AC - 0.15BC - 0.0313A^2 + 0.0346B^2 - 380.30C^2$$ (Equation 5.7)

The model and fit statistics for all analysed variables are summarised in Table 5.2. The parameters presented in the table were used to evaluate the quality of the model.

The coefficient of determination (R^2) was used to assess the fit of the regression model to the experimental data from this study. R^2 values obtained were 0.9932 and 0.9784 for yield and surface area, respectively. The R^2 values are close to 1, indicating a good fit of the regression models to the dataset i.e., the selected models can account for more than 97% of the variability observed in the responses.

Adjusted-R^2 is another useful model-based parameter for estimating the proportion of variance in the mean accounted for by the model, corrected for the number of model terms i.e., this parameter can be used to evaluate the effect of model reduction on the overall model performance. The adjusted R^2 value reduces with the increase of model terms if those terms do not add value to the model. The model summary statistics reveal slightly reduced adjusted R^2 values; this may suggest the existence of some model terms that do not add much value to the model.

Table 5.2. Model summary statistics for analysed variables obtained for the synthesis of PNTS-based activated carbons.

Response	*R^2*	*Adjusted R^2*	*Predicted R^2*	*Std. Dev.*	*Mean*	*C.V. %*	*Adeq. Precision*
Yield (%)	0.9932	0.9856	0.9360	0.83	51.26	1.61	33.55
Surface area (m^2/g)	0.9784	0.9541	0.8475	144.34	926.15	15.58	16.54
Reagent recovery (%)	0.9833	0.9645	0.7697	5.00	70.83	7.07	21.70
Micropore area (m^2/g)	0.9793	0.9561	0.8616	69.63	469.49	14.02	16.88
Mesopore area (m^2/g)	0.9694	0.9350	0.7634	99.35	429.82	23.11	15.77

The predicted R^2, of course, measures the amount of variation in new data (predictions), which can be explained by the model. The predicted R^2 values are in reasonable agreement with the adjusted R^2 values if they are within 0.2 of the adjusted R^2 values [7]. The adequate precision metric in the Design Expert software allows for

the estimation of the signal-to-noise ratio. A value above 4.0 for this parameter is preferable, which indicates adequate model discrimination [8, 9]. In this case, all adequate precision values, as shown in Table 5.2, are above 4. The reproducibility of a model can be measured using the coefficient of variation (C.V.) parameter, which is expressed as the ratio of standard deviation to the mean. A model is generally deemed reproducible if C.V. is less than 10% [10]. The C.V. values for surface area, micropore area, and mesopore area are above 10%. This can be attributed to errors in the measurement of these quantities. To enhance the reliability of the model, model reduction and transformation techniques are employed, as detailed in the subsequent sections.

The models were further evaluated using diagnostic plots, such as the normal plot, residual versus predicted response plot, and predicted versus actual plot. Figures 5.2 and 5.3 show the diagnostic plots for yield and surface area, respectively. The predicted versus actual plot for yield shows a high degree of correspondence between the predicted and the actual values, as evidenced by the points aligning with the 45-degree line and the high R^2 value. However, the surface area shows a lower degree of correspondence.

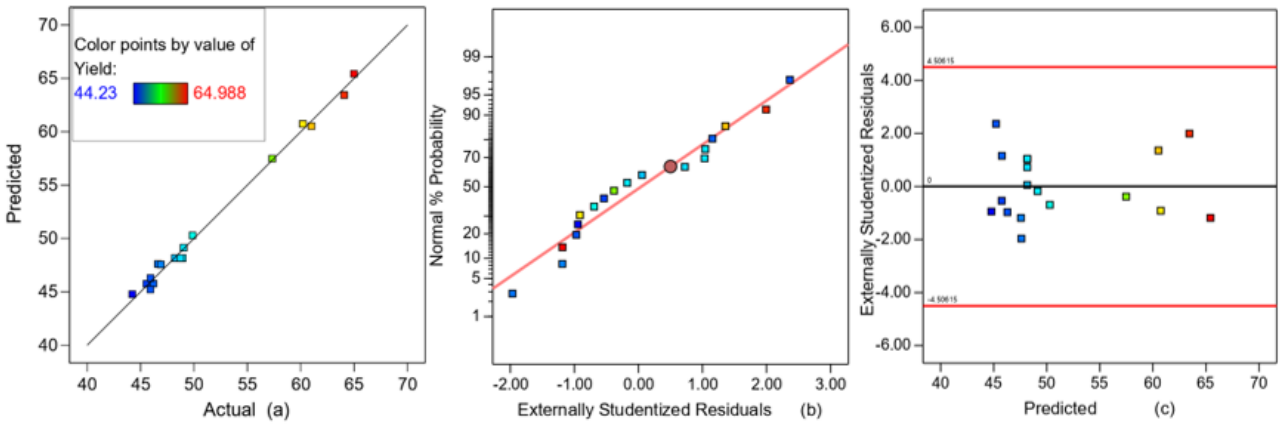

Figure 5.2. Diagnostic plots for yield: (a) predicted versus actual (b) normal plot and (c) residuals versus predicted in the synthesis of PNTS-based activated carbons.

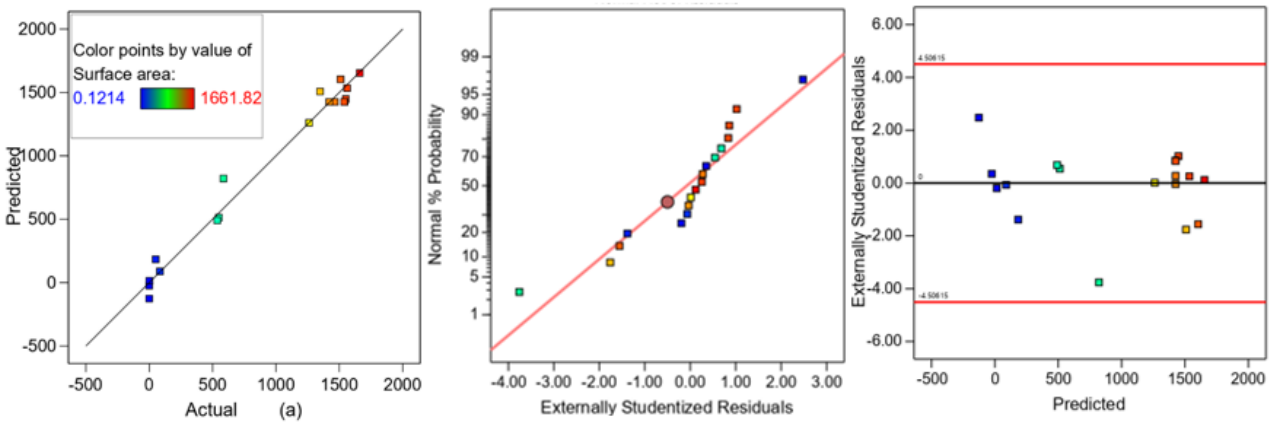

Figure 5.3. Diagnostic plots for surface area: (a) predicted versus actual (b) normal plot and (c) residuals versus predicted in the synthesis of PNTS-based activated carbons.

The normal probability plot assesses the normality of the residuals by comparing them to a straight line. Some deviation from the line is expected even with normal data. However, a clear pattern, such as an "S-shaped" curve, may indicate the need for transformation. The normal plot for yield shows that the residuals follow a normal distribution, as indicated by the points aligning with the straight line. While for surface area, some deviation from the line is observed – this may be an indication that a transformation may improve the model. To further investigate the normality of the residuals, the residual versus predicted values plot was examined. This plot displays the residuals against the ordered predicted response values. It tests the assumption of homoscedasticity (constant variance). The plot should show a random dispersion (constant variation of residuals along the graph) [11]. The residual versus predicted values plot for yield shows a random pattern of the residuals. However, the same plot for surface area reveals some heteroscedasticity, as the variance of the residuals expands from right to left. This may suggest that it is necessary to transform the response. None of the plots showed any outliers.

5.2.2 Model terms reduction

As indicated, by the adjusted-R^2 values for surface area, micro- and mesopore areas, this sub-section examines the impact of eliminating some terms, with low contributions, on the obtained models. Table 5.3 presents the analysis of variance (ANOVA) table before model terms reduction, which was used to test the average values of the variables. The p-value for each term was used to identify whether this was a term with a low contribution to the overall model. A suitable model will have high F-value, its p-value will be < 0.05 (significant), and the lack of fit will be non-significant ($p > 0.05$) [12]. The p-values of the quadratic models selected for yield and surface area are less than 0.05, as shown by the results of the analysis (Table 5.3). This implies that the models are statistically valid. However, some terms in the models have p-values > 0.05, e.g., the terms B, AB, BC, and B^2 show a smaller contribution to the surface area, while the terms AB, BC, B^2, and C^2 show less of a contribution to the yield.

Table 5.4 shows the model summary statistics after eliminating selected terms. The R^2 value for yield decreased after reducing the number of terms in the model, and ANOVA indicated a significant lack of fit (see Table A1 in Appendix A).

Table 5.3. Analysis of variance results for yield and surface area (before model reduction) of PNTS-based activated carbons.

Source	Sum of Squares	df	Mean Square	F-value	p-value
Yield					
Model	797.26	9	88.58	130.02	< 0.0001*
A-Temperature	636.26	1	636.26	933.85	< 0.0001*
B-Hold Time	5.84	1	5.84	8.58	0.0190*
C-Impregnation Ratio, I.R.	18.46	1	18.46	27.09	0.0008*
AB	1.94	1	1.94	2.85	0.1300
AC	14.68	1	14.68	21.54	0.0017*
BC	0.5597	1	0.5597	0.8215	0.3912
A^2	57.25	1	57.25	84.02	< 0.0001*
B^2	0.1210	1	0.1210	0.1776	0.6845
C^2	1.60	1	1.60	2.35	0.1640
Residual	5.45	8	0.6813		
Lack of Fit	5.09	5	1.02	8.37	0.0553
Pure Error	0.3647	3	0.1216		
Cor Total	802.72	17			
Surface area					
Model	7.54×10^6	9	8.38×10^5	40.24	< 0.0001*
A-Temperature	2.90×10^6	1	2.90×10^6	139.16	< 0.0001*
B-Hold Time	1743.69	1	1743.69	0.0837	0.7797
C-Impregnation Ratio, I.R.	9.83×10^5	1	9.83×10^5	47.20	0.0001*
AB	7666.01	1	7666.01	0.3680	0.5609
AC	5.00×10^5	1	5.00×10^5	24.00	0.0012*
BC	390.53	1	390.53	0.0187	0.8945
A^2	1.34×10^6	1	1.34×10^6	64.32	< 0.0001*
B^2	24686.20	1	24686.20	1.18	0.3081
C^2	2.30×10^5	1	2.30×10^5	11.03	0.0105*
Residual	1.67×10^5	8	20833.74		
Lack of Fit	1.56×10^5	5	31238.02	8.94	0.0505
Pure Error	10479.80	3	3493.27		
Cor Total	7.71×10^6	17			

*Significant at p-value < 0.05

Table 5.4. Model summary statistics for analysed variables (after model reduction) of PNTS-based activated carbons.

Response	*R^2*	*Adjusted R^2*	*Predicted R^2*	*Std. Dev.*	*Mean*	*C.V. %*	*Adeq. Precision*
Yield (%)	0.9872	0.9819	0.9624	0.93	51.26	1.81	37.81
Surface area (m^2/g)	0.9739	0.9630	0.9327	129.47	926.15	13.98	22.80
Reagent recovery (%)	0.9733	0.9587	0.8860	5.40	70.83	7.62	22.94
Micropore area (m^2/g)	0.9776	0.9707	0.9439	56.90	469.49	11.46	28.63
Mesopore area (m^2/g)	0.9538	0.9396	0.9184	95.79	429.82	22.28	21.62

This means that the data were not better fitted by the reduced model. The R^2 values for the other responses decreased, and the adjusted R^2 values increased slightly. The C.V. values for surface area, micropore area and mesopore area improved, but they were still higher than 10%. Moreover, the normal plot for surface area showed a greater degree of deviation and an outlier observed (see Figure A1 in Appendix A). The previous section suggested that reducing the number of terms in the models might improve the adjusted R^2, but this was not the case. The overall model did not improve significantly after term elimination, possibly because there were more significant terms than insignificant terms.

5.2.3 Model transformation

Model transformation was performed for the surface area response, including micro- and mesopore areas. The other responses did not show any indication that model transformation was required, on the basis of validation tools. Transformation of responses is a crucial aspect of any data analysis. It is required when the residuals (errors) depend on the magnitude of the predicted values [13]. Design Expert provides a range of transformations, such as square root, natural log, base 10 log, etc. The square root transformation, the simplest form, was suggested by the software to provide equal variance requirement. The model summary statistics, after model transformation, are presented in Table 5.5. The R^2 and adjusted R^2 values increased and the predicted R^2 remained reasonably consistent with the adjusted R^2. This implies

a better fit, minimizing the errors between the observed values and the predicted values.

Table 5.5. Model summary statistics for responses (after model transformation) of PNTS-based activated carbons.

Response	*R^2*	*Adjusted R^2*	*Predicted R^2*	*Std. Dev.*	*Mean*	*C.V. %*	*Adeq. Precision*
Surface area (m^2/g)	0.9937	0.9865	0.9112	1.82	26.34	6.91	30.99
Micropore area (m^2/g)	0.9950	0.9893	0.9158	1.15	19.47	5.92	34.45
Mesopore area (m^2/g)	0.9870	0.9724	0.8781	1.98	17.19	11.53	23.38

All adequate precision values are well over 4. The C.V. values improved considerably, with the C.V. value for mesopore area slightly exceeding 10%. Figure 5.4 presents the normal plots for the responses. The improvement of the models after transforming the responses is further confirmed by the increased alignment of the residuals on the normal plots, across all responses.

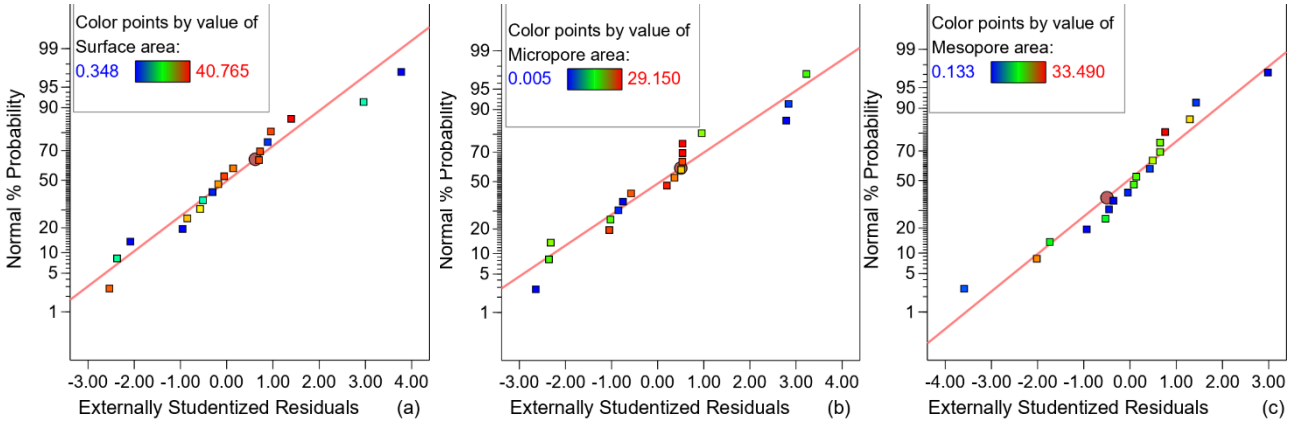

Figure 5.4. Normal plots for: (a) surface area (b) micropore area (c) mesopore area for PNTS-based activated carbons.

Table 5.6. Analysis of variance results for surface area (after model transformation) of PNTS-based activated carbons.

Source	Sum of Squares	df	Mean Square	F-value	p-value
Surface area					
Model	4156.24	9	461.80	139.50	< 0.0001*
A-Temperature	2065.61	1	2065.61	623.98	< 0.0001*
B-Hold Time	7.73	1	7.73	2.34	0.1650
C-Impregnation Ratio, I.R.	332.73	1	332.73	100.51	< 0.0001*
AB	13.39	1	13.39	4.04	0.0791
AC	69.09	1	69.09	20.87	0.0018*
BC	5.30	1	5.30	1.60	0.2415
A^2	701.69	1	701.69	211.97	< 0.0001*
B^2	1.32	1	1.32	0.3992	0.5451
C^2	85.81	1	85.81	25.92	0.0009*
Residual	26.48	8	3.31		
Lack of Fit	24.72	5	4.94	8.40	0.0550
Pure Error	1.77	3	0.5885		
Cor Total	4182.72	17			

*Significant at p-value < 0.05

Equation 5.8 shows the regression equation and Table 5.6 shows the ANOVA for surface area after transformation.

$$\sqrt{Y_2} = -158.93 + 0.73A + 0.037B + 11.86C - 0.00016AB + 0.022AC + 0.018BC - 0.00072A^2 + 0.00025B^2 - 7.35C^2 \quad \text{(Equation 5.8)}$$

5.2.4 Analysis of variance

The adequacy of the selected quadratic models was further assessed by using analysis of variance (ANOVA). This involved comparing the p-values and F-values from the ANOVA table (Tables 5.3 and 5.6). A suitable model will have a high F-value, a p-value less than 0.05 (significant), and a non-significant lack of fit ($p > 0.05$) [12].

The p-values of the quadratic models chosen for yield and surface area are less than 0.05, as shown by the analysis. This implies that the models are statistically valid. The

table (Table 5.3) shows that the p-values of model terms A, B, C, AC, and A^2 are less than 0.05 for yield, indicating that yield is significantly influenced by temperature, hold time, I.R., as well as the interaction of temperature and I.R. The F-value of 933.85 indicates that temperature is the most significant factor affecting yield. The lack of fit is not significant in this case because its p-value is greater than 0.05.

The ANOVA table (Table 5.6) reveals that the p-values of model terms A, C, AC, A^2, and C^2 are less than 0.05 for surface area, implying that surface area is significantly affected by temperature, I.R., and the interaction of temperature and I.R. The F-value of 623.98 shows that temperature is the most significant factor influencing surface area. The lack of fit for this model is not significant because its p-value is greater than 0.05. This implies that the models fit the dataset and can be used to navigate through the design space.

5.2.5 Influence of activation variables on responses

Figure 5.5 illustrates one factor effect on the yield of the process. The yield decreases with increasing temperature up to ~550 °C and then levels off slightly at higher temperatures. This can be attributed to the basic structure being already formed at ~500 °C, since the distillation of tar occurs at ~350 – 500 °C [14]. The hold time has a negligible effect on the yield of the process.

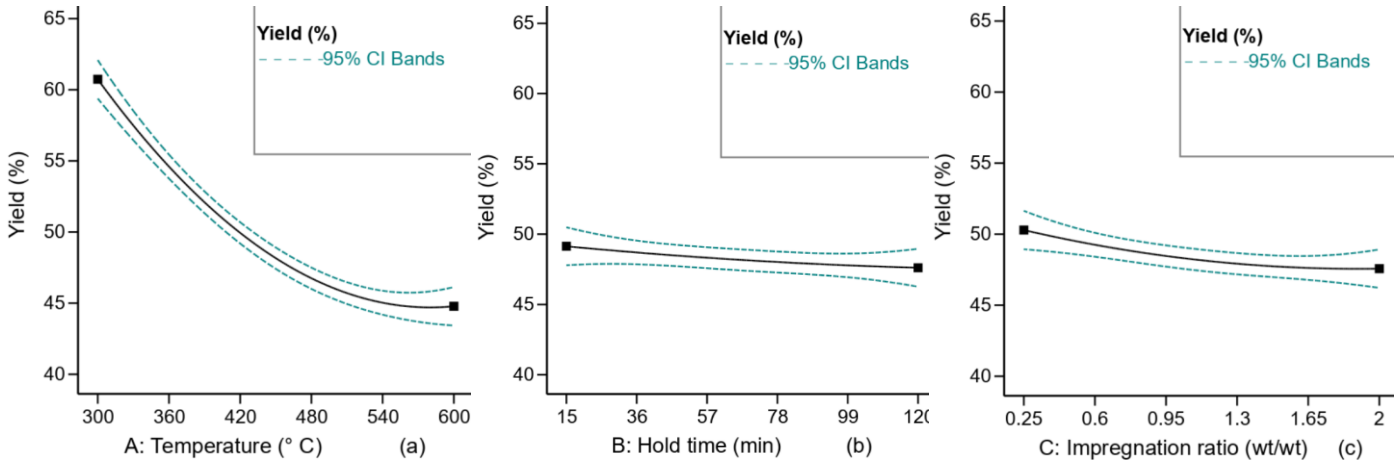

Figure 5.5. One factor effect on the process yield of PNTS-based activated carbons.

The yield decreases gradually with increasing I.R., showing minor changes for I.R. > 1.5. A higher amount of activating agent causes more volatile matter to evolve, which results in a lower yield [15]. Moreover, more cracks in the structure may occur, due to a higher amount of activating agent, which leads to deformation of micropores and reduced productivity [16].

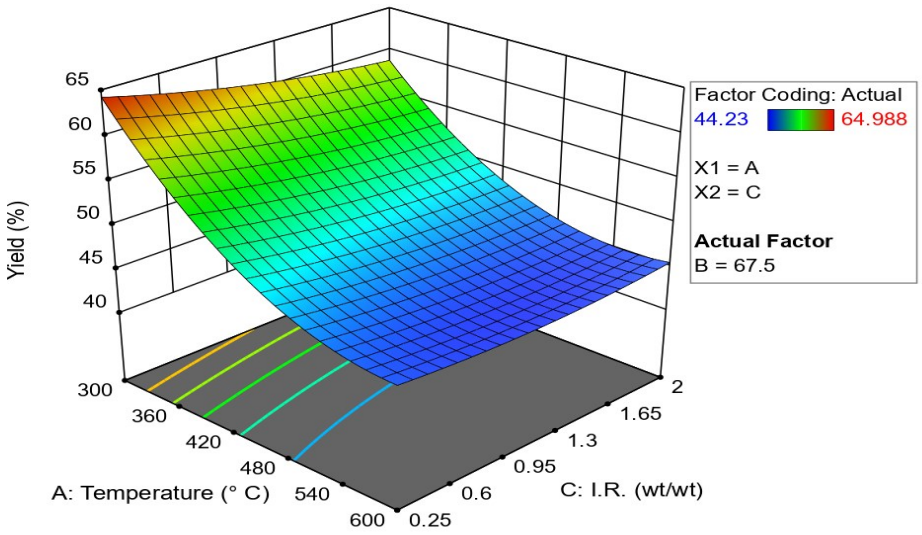

Figure 5.6. Interaction effects of temperature and impregnation ratio (I.R.) on process yield in the synthesis of PNTS-based activated carbons.

The yield of the process is also influenced by the interaction of I.R. and temperature. Figure 5.6 shows that the yield of the process is ≥ 60% when the temperature is below 350 °C and I.R. is below 1.5, but the surface area remains under 500 m^2/g (Figure 5.8). The yield stays between 50 and 55% when the temperature ranges from 350 to 455 °C, and is not significantly affected above 480 °C. The surface area also increases gradually, in this region, with increasing temperature, which shows the significance of temperature in developing the internal porous structure of the carbons.

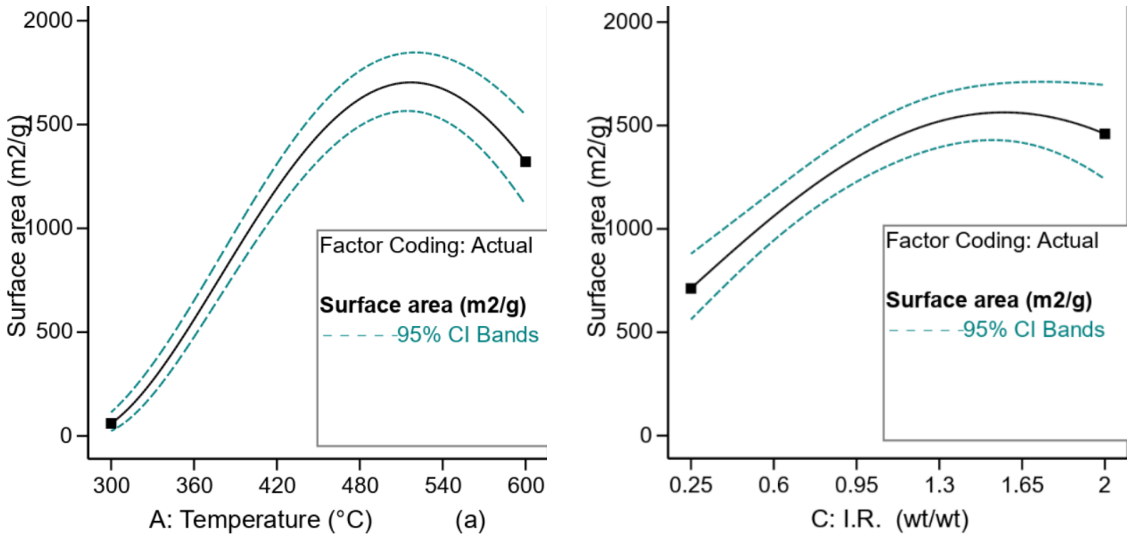

Figure 5.7. One factor effect on the surface area of PNTS-based activated carbons.

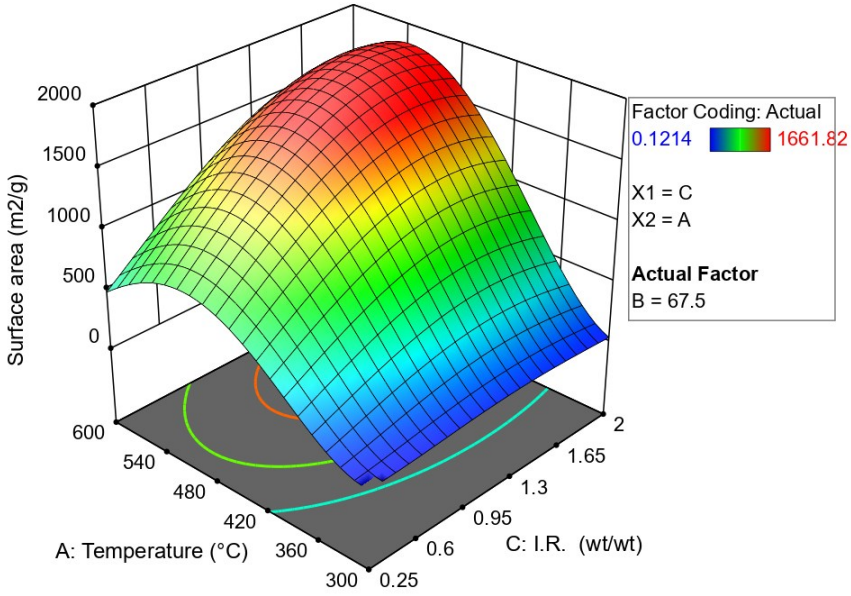

Figure 5.8. Interaction effects of temperature and impregnation ratio (I.R.) on surface area in the synthesis of PNTS-based activated carbons.

Figure 5.7 illustrates a one-factor effect on the surface area. The surface area increases significantly with increasing temperature up to ~520 °C, and microporosity decreases with further increase in temperature above 520 °C. Microporosity also decreases when I.R. is above 1. This is related to the enlargement of the pores with higher $ZnCl_2$ loading, which results in increased mesoporosity, as shown in Figures 5.9 and 5.10. The effect of the interaction of temperature and I.R. on porosity development is shown

in Figure 5.8. The surface area stays under 500 m^2/g when the carbonisation temperature is below 375 °C, for the selected range of I.R. However, at I.R. above 1 and carbonisation temperature above 420 °C, the surface area increases significantly over 500 m^2/g. The increase in porosity, with increasing I.R. and temperature, indicates that porosity is formed by the interstices left in the carbon material after washing and that volatile substances are removed from the surface of the carbon material during carbonisation at these temperatures.

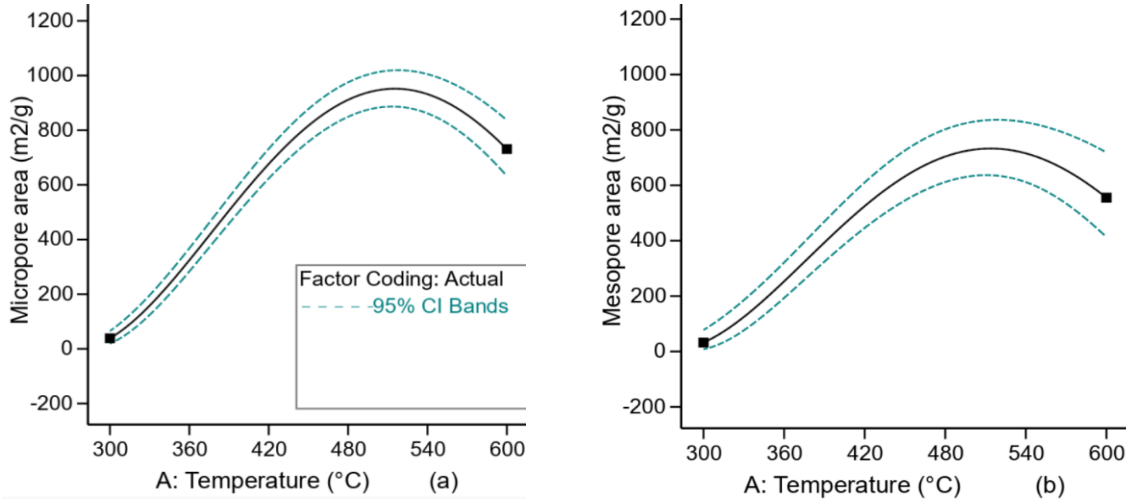

Figure 5.9. Temperature effects on (a) micropore and (b) mesopore development in the synthesis of PNTS-based activated carbons.

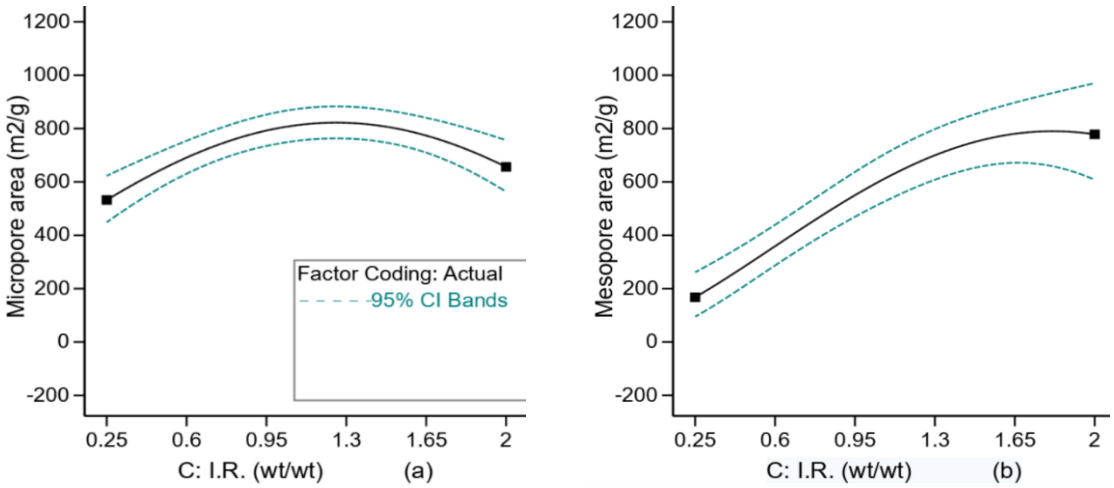

Figure 5.10. I.R. effects on (a) micropore and (b) mesopore development in the synthesis of PNTS-based activated carbons.

Reagent recovery (R.R.) from the activation process is mainly influenced by two factors: temperature and hold time. Figure 5.11 illustrates that the recovery rate declines significantly when the carbonisation temperature exceeds 500 °C. This can be attributed to the reagent evaporating from the carbon sample as the temperature rises. Moreover, the R.R. also decreases as the hold time at high temperatures increases, which implies that increased evaporation occurs when the activating agent remains at elevated temperatures for longer periods.

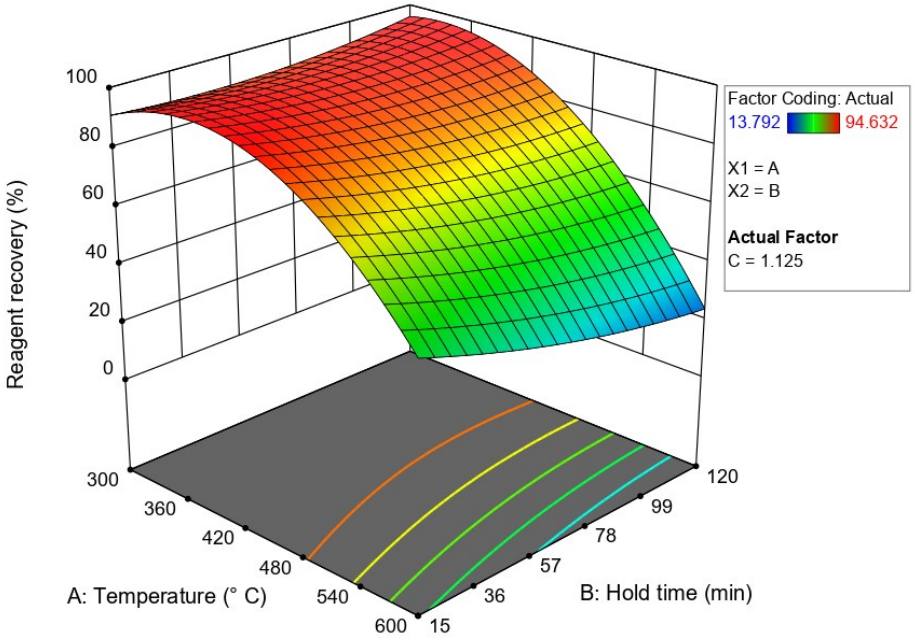

Figure 5.11. Interaction effects of temperature and hold time on reagent recovery in the synthesis of PNTS-based activated carbons.

As shown in Figure 5.12, the density of the samples increased as both temperature and I.R. increased. It can be observed (the gradient in Figure 5.12a) that temperature has a greater influence on the density of the samples. The effect of increased temperature and I.R. on the PNTS-based densities can also be visualised in the surface plot as shown in Figure 13. The higher density observed for samples with higher I.R. could be related to the inhibition of tar formation by $ZnCl_2$, due to condensation reactions

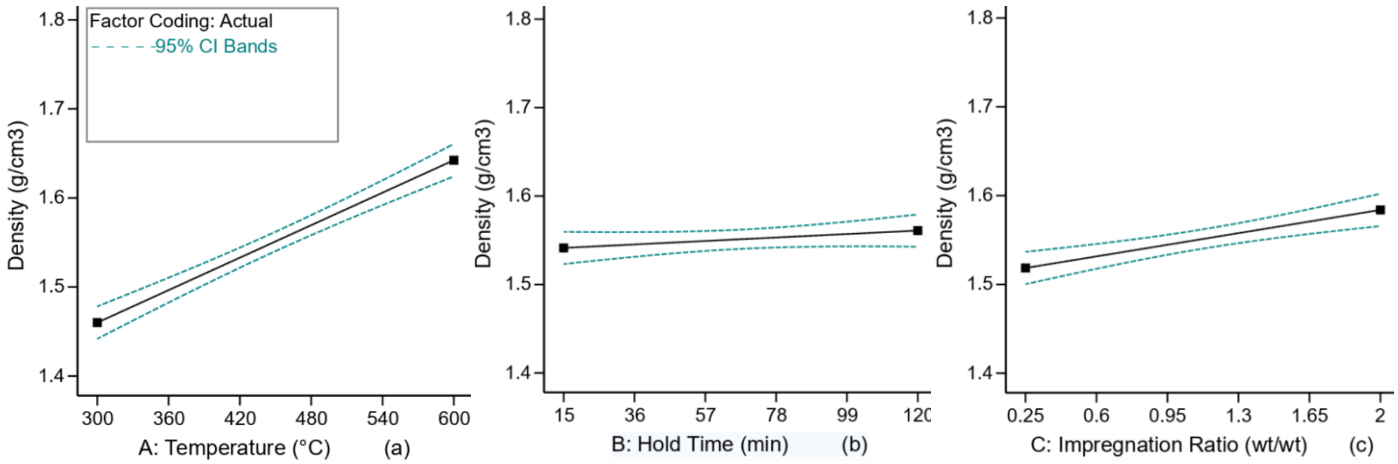

[2]. Figure 5.12b reveals that the hold time has no significant effect on density development.

Figure 5.12. One factor effect on the density of PNTS-based activated carbons.

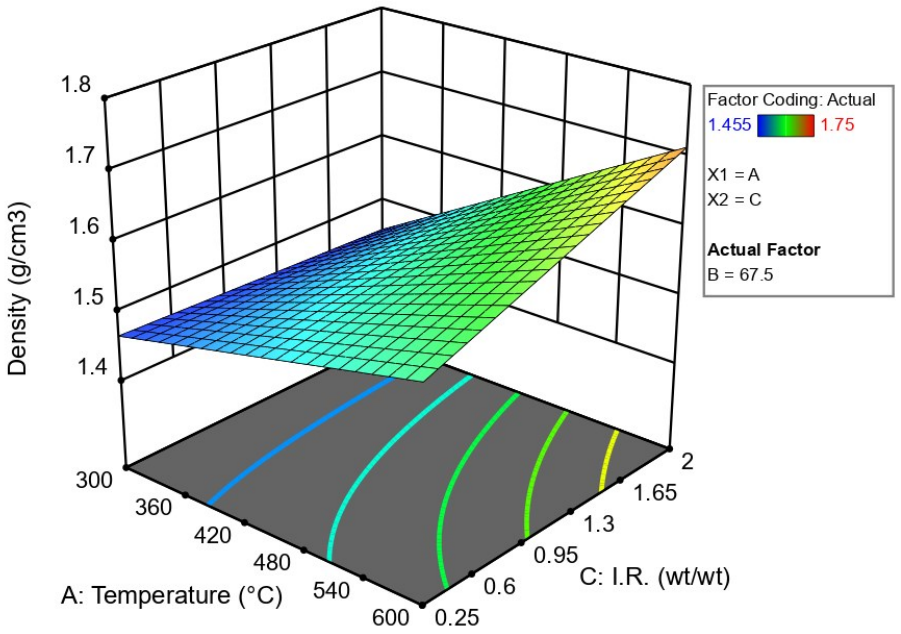

Figure 5.13. Interaction effects of temperature and impregnation ratio on the density of PNTS-based activated carbons.

5.2.6 Activation parameters optimisation

The design of experiment (DoE), which was the method used to map the activation process and simultaneously examine the interactions between the variables, results in different values of yield and surface area, which are shown in Table 5.7. It can be observed that the sample with the lowest surface area has the highest yield, indicating that there is a trade-off between these two responses. Using a performance criterion, surface area x yield [17], as discussed in Chapter 1, the design of experiment suggests the following optimal responses: a surface area of 1662 m^2/g and a yield of 45.93%, with the following activation parameters: a temperature of 600 °C, a hold time of 15 min, and an I.R. of 2. Since the developed models statistically represent the system and can be used to navigate the design space, there is a possibility of finding a region of optimal process parameters. Design Expert desirability function was employed to achieve this goal. In the optimisation process, the surface area was maximised while setting a target value for the yield. The constraints and the numerical optimisation solutions can be found in the Appendix A (see Tables A2 and A3). The solution obtained by RSM (Table 5.8) provides reduced energy input. The solution was verified by experiments, and the optimised run was performed in triplicate. The error percentage between the actual and predicted values for surface area varies from 1.83 – 2.61%, while the error for yield varies from -0.40 – 0.90 %. The minimal errors obtained between the actual and predicted values further validated the suitability of the models.

This is to note that the selection of optimisation criteria is contingent upon the desired outcomes of the process. For example, should mechanical strength be a requisite characteristic, preference may be given to an adsorbent that can withstand higher pressures or more rigorous conditions, even if it compromises a bit on yield.

Table 5.7. Textural characteristics of the PNTS-based activated carbons and experimental design with the response variables (yield and surface area).

		A	*B*	*C*				*dependent variables*	
Run	Sample name	Temp., ° C	Hold time, min.	I.R., wt/wt	Avg. Pore size, nm	Micropore vol., cm^3/g	Total pore vol., cm^3/g	Yield (Y_1), %	Surface area (Y_2), m^2/g
1	PNTS1.13-450-120	450	120	1.13	3	0.416	0.876	46.63	1562
2	PNTS1.13-300-68	300	68	1.13	6	0.006	0.006	60.20	51
3	PNTS1.13-450-68	450	68	1.13	3	0.431	0.810	48.94	1464
4	PNTS0.25-600-120	600	120	0.25	3	0.247	0.283	45.55	537
5	PNTS1.13-450-68	450	68	1.13	3	0.407	0.787	48.95	1420
6	PNTS0.25-300-120	300	120	0.25	43	-	0.006	64.07	-
7	PNTS2-300-15	300	15	2	8	-	0.001	61.01	1
8	PNTS0.25-300-15	300	15	0.25	25	-	-	64.99	-
9	PNTS1.13-450-68	450	68	1.13	3	0.429	0.857	48.73	1539
10	PNTS2-600-15	600	15	2	3	0.276	1.016	45.93	1662
11	PNTS0.25-450-68	450	68	0.25	3	0.224	0.274	49.87	586
12	PNTS0.25-600-15	600	15	0.25	3	0.248	0.290	46.20	550
13	PNTS1.13-450-15	450	15	1.13	3	0.416	0.746	49.03	1349
14	PNTS2-300-120	300	120	2	3	0.025	0.047	57.33	84
15	PNTS2-600-120	600	120	2	3	0.278	0.861	45.93	1510
16	PNTS1.13-450-68	450	68	1.13	3	0.443	0.854	48.21	1541
17	PNTS2-450-68	450	68	2	3	0.351	0.875	46.90	1551
18	PNTS1.13-600-68	600	68	1.13	2	0.391	0.687	44.23	1262
Opt.	PNTS1.7-485-15	485	15	1.7	3	0.387	0.940	47.41	1683

Note: Opt. = Optimised; - Negligible

Table 5.8. Optimal activation parameters to produce high carbon yield and surface area from PNTS, and experimental validation.

Source	Activation parameters			Responses		Desirability	Avg. Pore size, nm	Error, %	
	Temp., °C	Hold time, min.	I.R., wt/wt	Yield, %	Surface area, m^2/g			Yield	Surface area
RSM	485	15	1.7	47.22	1727	1	-		
Validation experiment 1	485	15	1.7	47.41	1683	-	3	-0.40	2.61
Validation experiment 2	485	15	1.7	46.88	1696	-	3	0.73	1.83
Validation experiment 3	485	15	1.7	46.80	1683	-	3	0.90	2.61

5.2.7 Characterisation analysis

The textural properties of all AC samples derived from PNTS were determined by N_2 adsorption and the results are shown in Tables 5.7 and 5.9. The total pore volume was calculated from the N_2 adsorption data, using Equation 5.3. The N_2 adsorption isotherm curves of the AC samples are shown in Figure 5.14 (eight samples with the largest surface area x yield are shown here). According to the IUPAC guidance on reporting physisorption data [18], clearly, all the isotherms belong to the Type I isotherm classification. It can be observed that some samples (runs 1, 10, 15, 16, 17, and optimised run) are characterised by a combination of micro- and mesopores (as shown by the opening of the knee of the isotherm).

Table 5.9. Experimental design showing the textural characteristics of the PNTS-based carbons and reagent recovery ratio.

	A	*B*	*C*			*dependent variables*	
Run	*Temp., ° C*	*Hold time, min.*	*Impregnation Ratio, I.R.*	*R.R, %*	*True density, g/cm³*	*Micropore area, m²/g*	*Mesopore area, m²/g*
1	450	120	1.13	85.23	1.540	797	765
2	300	68	1.13	92.33	1.455	29	22
3	450	68	1.13	82.87	1.529	828	636
4	600	120	0.25	23.63	1.576	478	59
5	450	68	1.13	87.90	1.540	779	641
6	300	120	0.25	75.51	1.474	-	-
7	300	15	2	94.63	1.465	-	1
8	300	15	0.25	76.37	1.467	-	-
9	450	68	1.13	86.60	1.550	825	714
10	600	15	2	58.29	1.673	541	1121
11	450	68	0.25	78.19	1.526	493	92
12	600	15	0.25	34.64	1.549	481	69
13	450	15	1.13	89.57	1.553	797	552
14	300	120	2	93.96	1.465	48	36
15	600	120	2	13.79	1.750	541	969
16	450	68	1.13	85.48	1.553	849	691
17	450	68	2	52.01	1.566	677	874
18	600	68	1.13	20.61	1.733	747	515
Opt.	485	15	1.7	80.12	1.605	744	939

Note: Opt. = Optimised; - Negligible

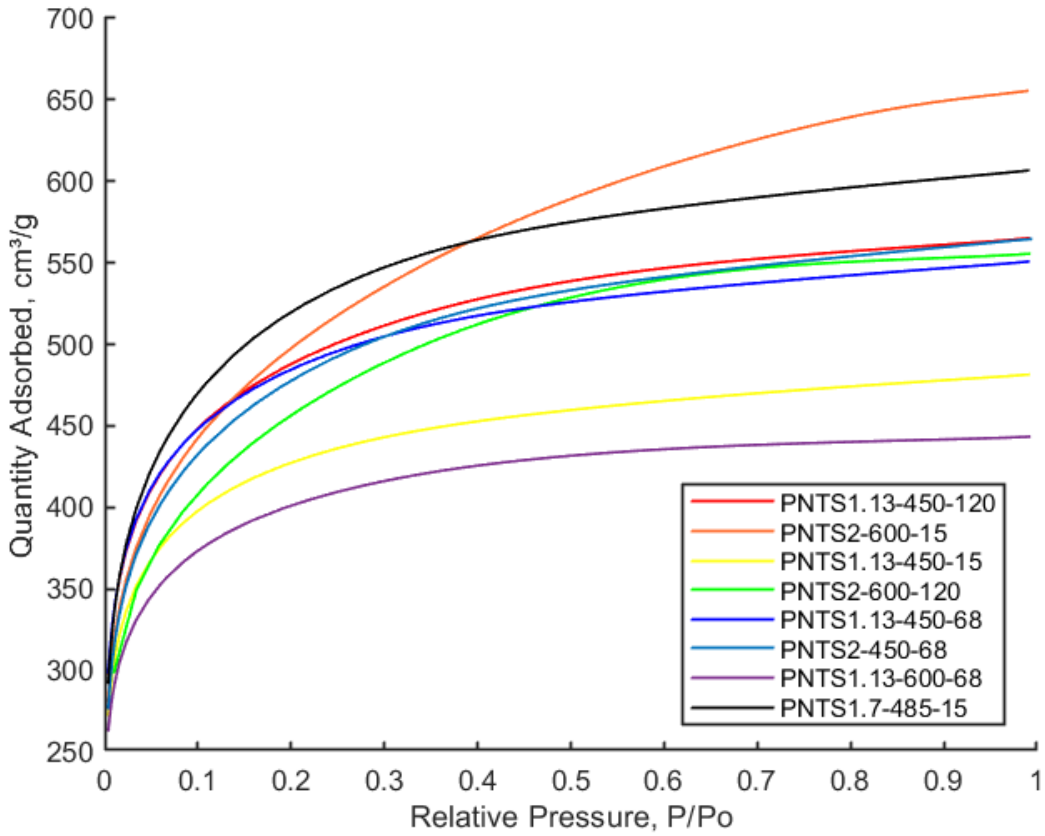

Figure 5.14. Nitrogen adsorption isotherms of PNTS-based activated carbons.

The presence of wider micropores can be observed in PNTS1.7-485-15 (the optimised run) and PNTS2-600-15. However, the isotherm of the optimised run approaches a horizontal plateau, which suggests the presence of uniform wider micropores; on the other hand, the plateau of PNTS2-600-15 extends at a high relative pressure (P/P^o), indicating higher mesopore volume and the presence of hysteresis. The pore size distributions (PSD) are shown in Figure 5.15. All samples are characterised by pore size < 50 nm. The PSD reveals that PNTS2-600-15 has a more heterogenous characteristic owing to the presence of various pore sizes. Furthermore, the extension of the distribution at larger pore widths for PNTS2-600-15 corroborates the presence of larger pores.

As discussed in Section 3.1.2.4, the monolayer capacity, which is used to calculate the BET surface area can be obtained from the linear region of the BET plot. For Type II and IVa isotherms, this region typically ranges from ~0.05 to 0.35 relative pressures. However, for microporous materials, the linear region of the BET plot may occur at relative pressures lower than those for non-microporous materials. Rouquerol *et al*. [19] proposed a method to identify the linear region of the BET plot for microporous materials, which was adopted by the IUPAC report on physisorption data for gas/solid systems in 2015 (Section 3.1.2.4). Comparing surface areas of carbon materials is critical in studying their performance characteristics. Several previous studies on microporous materials have failed to explicitly specify the application of the procedure proposed by Rouquerol *et al*. [19], thus limiting the comparability of their results with other carbon materials. However, this comparison will be more realistic in the actual application of the carbon materials, where the surface area available, denoted as "effective" surface area by Hadi *et al*. [20] will translate to the capacity for the target species.

To evaluate the error of the conventional BET method for estimating the surface areas, the Rouquerol procedure was applied. The results obtained (Table 5.10) show that the micropore areas were underestimated by ~17 – 40%. The mesopore areas were determined by the t-plot method, as discussed in Section 3.1.3.1.2; the micropore areas were computed by subtracting the mesopore areas from the corrected surface areas.

Table 5.9 shows that all activated carbon samples exhibit relatively high densities, ranging from 1.455 g/cm^3 to 1.750 g/cm^3. Higher densities offer an advantage, as they facilitate the reduction of adsorption column size during the design phase. As previously discussed in Section 5.2.5, the densities of the samples were mainly affected by increasing both temperature and I.R., with temperature having a greater effect. Table 5.9 shows that samples activated at elevated temperatures and greater I.R. exhibit higher densities.

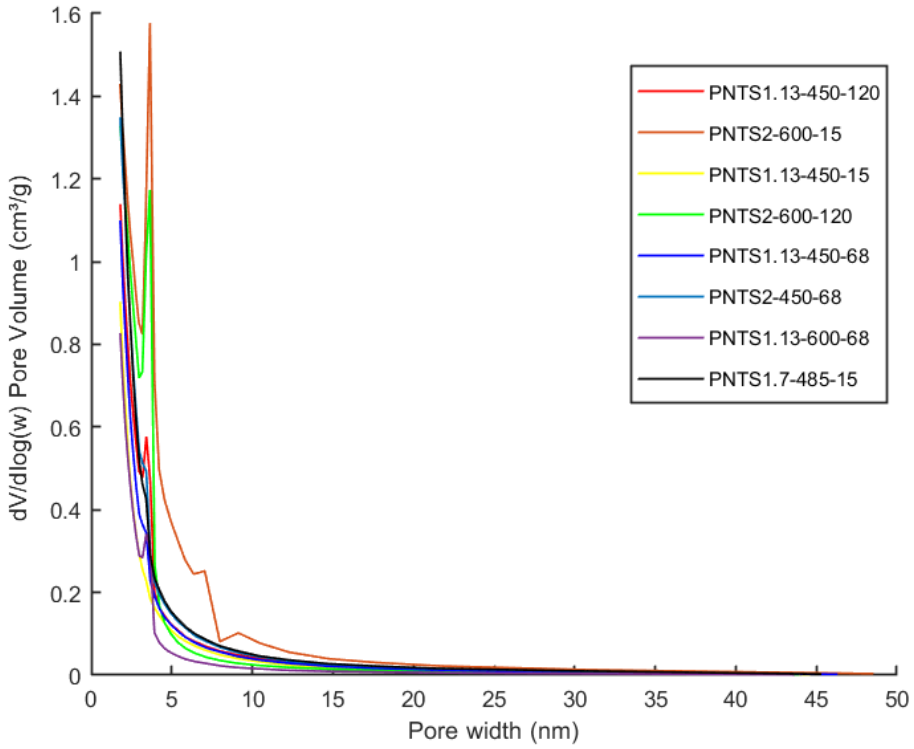

Figure 5.15. Barrett-Joyner-Halenda (BJH) pore size distribution of PNTS-based activated carbons.

Table 5.10. Corrected surface areas following Rouquerol procedure [19].

					Corrected surface areas	
Run	*Sample name*	*BET Surface area, m^2/g*	*Micropore area, m^2/g*	*Mesopore area, m^2/g*	*Surface area, m^2/g*	*Micropore area, m^2/g*
1	PNTS1.13-450-120	1562	797	765	1809	1045
2	PNTS1.13-300-68	51	29	22	62	40
3	PNTS1.13-450-68	1464	828	636	1738	1102
4	PNTS0.25-600-120	537	478	59	726	667
5	PNTS1.13-450-68	1420	779	641	1670	1029
6	PNTS0.25-300-120	-	-	-	1	-
7	PNTS2-300-15	1	-	1	1	-
8	PNTS0.25-300-15	-	-	-	1	-
9	PNTS1.13-450-68	1539	825	714	1809	1095
10	PNTS2-600-15	1662	541	1121	1807	686
11	PNTS0.25-450-68	586	493	92	670	578
12	PNTS0.25-600-15	550	481	69	702	633
13	PNTS1.13-450-15	1349	797	552	1609	1057
14	PNTS2-300-120	84	48	36	101	65
15	PNTS2-600-120	1510	541	969	1669	700
16	PNTS1.13-450-68	1541	849	691	1810	1119
17	PNTS2-450-68	1551	677	874	1735	861
18	PNTS1.13-600-68	1262	747	515	1498	983
Opt.	PNTS1.7-485-15	1683	744	939	1886	947

Note: Opt. = Optimised; - Negligible

The point of zero charge (PZC) values of the synthesised samples are displayed in Table 5.11, as determined from the plots shown in Figure 5.16. PZC plays a significant role in the selection of adsorbents for a range of adsorption systems. The surface of the adsorbent becomes positively charged due to protonation of the acidic groups on the surface when the pH of a solution ($pH_{solution}$) is lower than the PZC of an adsorbent, and negatively charged due to dissociation of the acidic oxygen groups present on the surface when $pH_{solution}$ is higher than the PZC of an adsorbent surface [21]. This influences the interaction between the adsorbent surface and charged species, such as ionic dyes.

Table 5.11. Point of Zero Charge (PZC) values of the synthesised PNTS-based activated carbons.

Run	*Sample name*	*PZC value*
1	PNTS1.13-450-120	4.35
10	PNTS2-600-15	5.80
13	PNTS1.13-450-15	4.00
15	PNTS2-600-120	6.55
16	PNTS1.13-450-68	4.20
17	PNTS2-450-68	4.48
18	PNTS1.13-600-68	5.85
Optimised	PNTS1.7-485-15	4.58

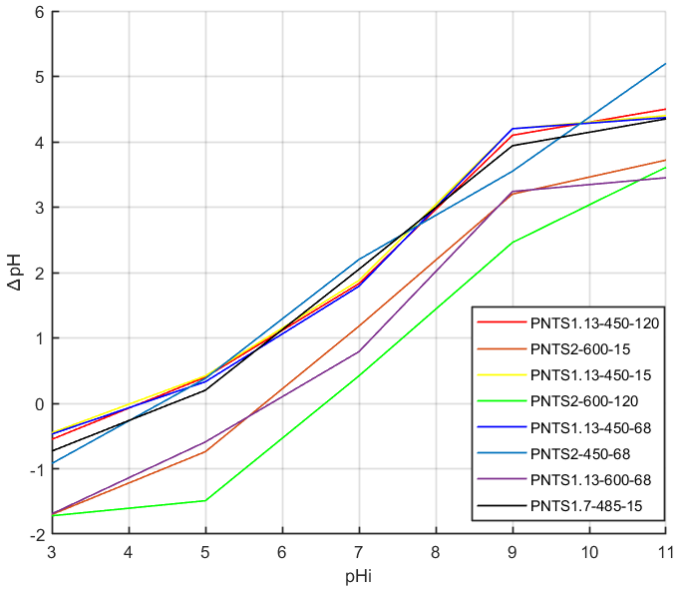

Figure 5.16. Point of Zero Charge (PZC) plots for PNTS-based activated carbons.

Fourier transformed infrared spectroscopy (FTIR) was used to investigate the surface chemistry of the precursor biomass, and PNTS-based activated carbons, in the wavenumber range 4000 – 500 cm^{-1}. The FTIR spectrum of the precursor (Figure 5.17) shows various peaks that indicate the presence of several functional groups in the raw peanut shell. The absorption peaks at 3332 cm^{-1} and 1249 cm^{-1} correspond to the O-H stretching vibrations (3600 – 3200 cm^{-1}) and bending frequency (1410 – 1260), respectively [22], and this could be linked to the presence of cellulose and water of crystallisation [1, 22]. It is observed that the O-H stretching disappeared in the activated samples, except for PNTS1.13-450-120 and PNTS1.13-450-15, which could be attributed to the dehydrating effects of $ZnCl_2$ and increased activation temperatures.

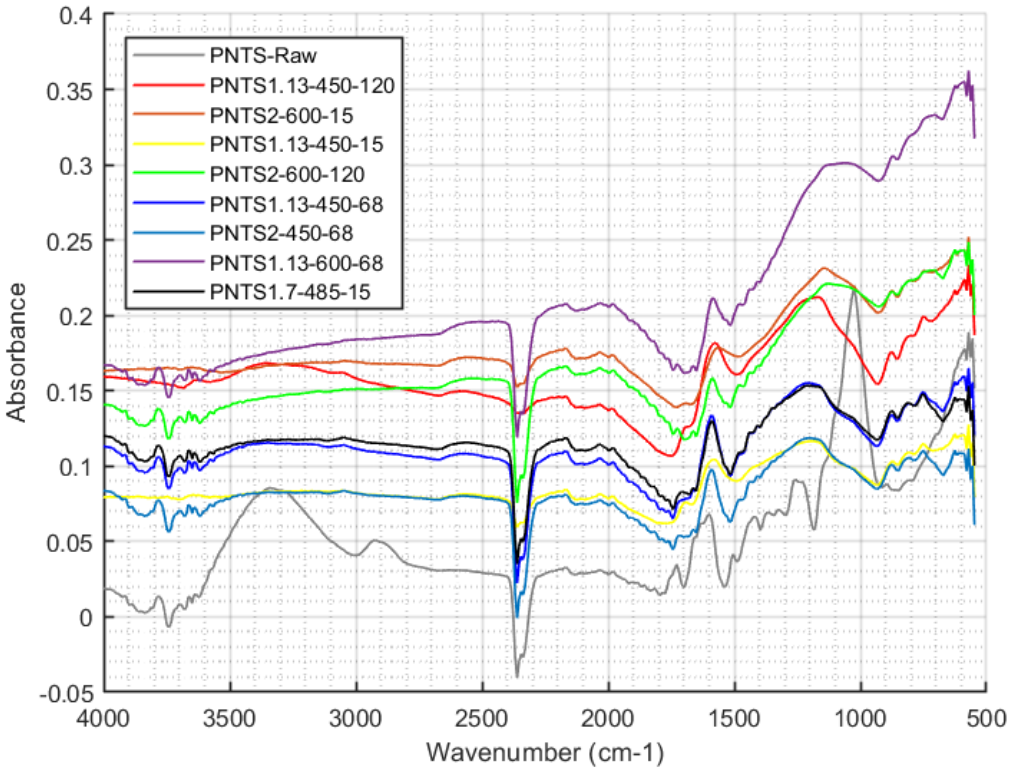

Figure 5.17. FTIR spectra of raw PNTS and PNTS-based activated carbons.

The absorption peaks found in the range 1770 – 1710 cm^{-1} for PNTS2-600-120, PNTS2-450-68, PNTS1.13-600-68, and PNTS1.7-485-15, corresponds to the presence of acid

anhydride groups or saturated ketones [23]. N-H bending (1650 – 1560 cm^{-1}), which can be attributed to amine functional groups and/or to the skeletal vibration of aromatic C═C bonds [24], is observed to be present in all samples. All samples show absorption peaks for ethers (1150 – 1070 or 1275 – 1200 cm^{-1}) and/or C-O stretching (1075 – 1020 cm^{-1}) [22, 25]. The FTIR analysis revealed that various oxygen complexes exist on the surface of the ACs. Activation at higher temperatures enhances the basic character of activated carbon, since surface acidity is reduced by CO_2 evolution as temperature increases [26]. It can be observed that the PZC values of the ACs increased with activation temperature, which agrees with the earlier statement.

Table 5.12. XPS analysis of the synthesised PTNS-based activated carbons.

Element (spectra lines)	C (1s)	C (1s)	C (1s)	C (1s)	O (1s)	O (1s)	O (1s)	N (1s)	N (1s)	N (1s)
Peak	1	2	3	4	1	2	3	1	2	3
Binding Energy (eV)	284.60 ± 0.15	285.75 ± 0.25	288.60 ± 0.20	284.43 ± 0.25	532.22 ± 0.15	533.30 ± 0.25	535.50 ± 0.20	398.45 ± 0.30	400.10 ± 0.15	402.00 ± 0.50
Functional groups	Graphitic, C–C/C═C	C in C–O/ C–N	C in ester (COOR, R = H or alkyl)	C–C	C═O	Ester (COOR, R = H or alkyl)	Linked to chemi-sorbed H_2O	Pyri-dinic-N	Graphi-tic-N	Oxi-dised-N
					Relative atomic concentration (%)					
PNTS1.13-450-120	34.34	24.61	13.63	1.28	1.79	0.38	0.02	5.86	14.30	3.78
PNTS2-600-15	42.57	22.24	11.77	1.05	0.70	6.34	0.32	3.70	9.47	1.85
PNTS1.13-450-15	40.92	8.27	15.03	4.16	12.69	0.54	0.00	8.07	7.66	2.65
PNTS2-600-120	35.84	23.69	13.29	3.07	3.23	0.16	0.12	4.02	14.45	2.14
PNTS1.13-450-68	40.00	14.48	13.35	2.46	10.76	1.05	0.00	5.79	10.80	1.30
PNTS2-450-68	41.81	9.70	19.32	1.45	8.09	0.56	0.55	5.74	11.14	1.65
PNTS1.13-600-68	29.75	22.54	13.74	1.48	7.41	1.40	0.00	4.43	17.13	2.13
PNTS1.7-485-15	31.75	23.27	12.36	1.04	7.17	2.36	0.03	6.66	13.59	1.78
References	**[27, 28]**	**[29, 30]**	**[30, 31]**	**[32]**	**[27]**	**[27, 31]**	**[33]**		**[27, 30, 32]**	

X-ray photoelectron spectroscopy (XPS) was used to further investigate the surface chemical composition of the synthesised PNTS-based activated carbons. The XPS spectra reveals three distinctive peaks, attributable to carbon (C1s), oxygen (O1s) and

nitrogen (N1s). The C1s peak was deconvoluted into four peaks, the O1s peak into three peaks, and the N1s peaks into three peaks, as shown in Table 5.12. Figure 5.18 shows the C1s, O1s and N1s spectra of PNTS2-600-15 and PNTS1.7-485-15, which have the highest surface areas among the samples. The spectra curves of the other samples are shown in Figure A2 (see Appendix A).

The C1s peaks were assigned to four groups: sp^2 graphitic hybridised carbon (C═C), sp^3 C–C, C–O/C–N and C in esters. These components were also confirmed by FTIR analysis. The O1s peak was deconvoluted into three groups: C═O, COOR and chemisorbed H_2O. The XPS analysis also detected nitrogen, which was consistent with the FTIR analysis that indicated the presence of nitrogen in the form of amide-N [34]. The N1s peaks were assigned to three functional groups: pyridinic-N, graphitic-N and oxidised-N, as summarised in Table 5.12.

The relative atomic concentrations were determined using the procedure outlined in Section 3.2. The analysis revealed that the C1s peak was the most dominant, accounting for 68 – 78% of the total signal, followed by the N1s peak with 15 – 24%, and the O1s peak with 2 – 13%. These values indicate that the samples had a high degree of carbonisation and nitrogen doping, as well as some oxygen-containing functional groups. The nitrogen content was likely introduced during the synthesis of the carbon material. Nitrogen can substitute carbon atoms (graphene-N) in the graphene lattice, creating active sites and increasing the surface area of the carbon material [32]. Previous studies have reported that nitrogen doping can induce mesopores in graphene, which can significantly contribute to its surface area [35, 36]. Moreover, heteroatoms such as oxygen, nitrogen and sulphur in the synthesised carbon can enhance its wettability, which is the ability of a liquid to maintain contact with a surface [37].

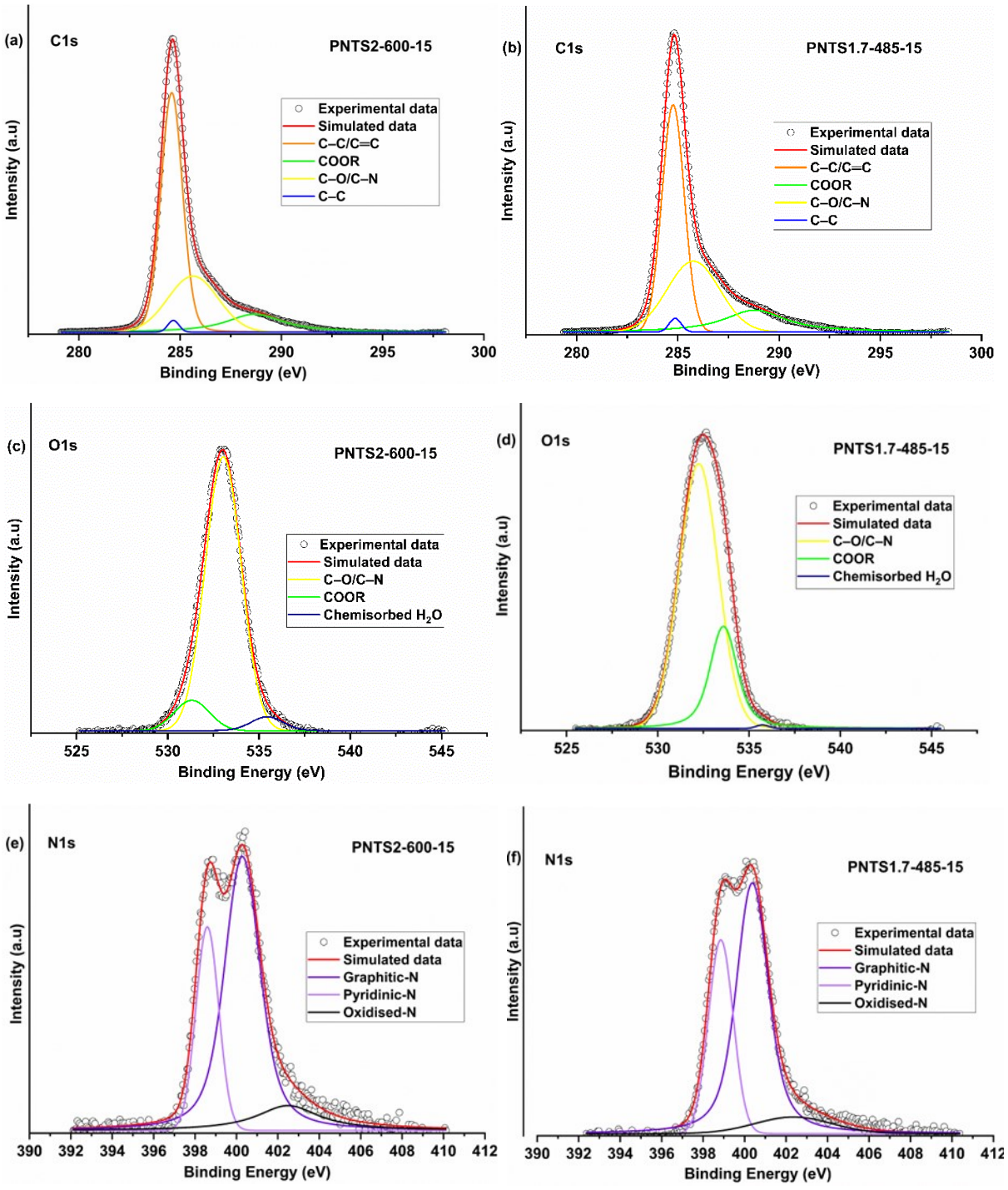

Figure 5.18. XPS spectra of PNTS2-600-15 (**a:** C1s, **c:** O1s and **e:** N1s) and PNTS1.7-485-15 (**b:** C1s, **d:** O1s and **f:** N1s).

The raw sample of the peanut shell (PNTS) and the two optimal samples (PNTS2-600-15 and PNTS1.7-485-15), as identified in Section 5.2.6, were examined under SEM to observe their surface morphology.

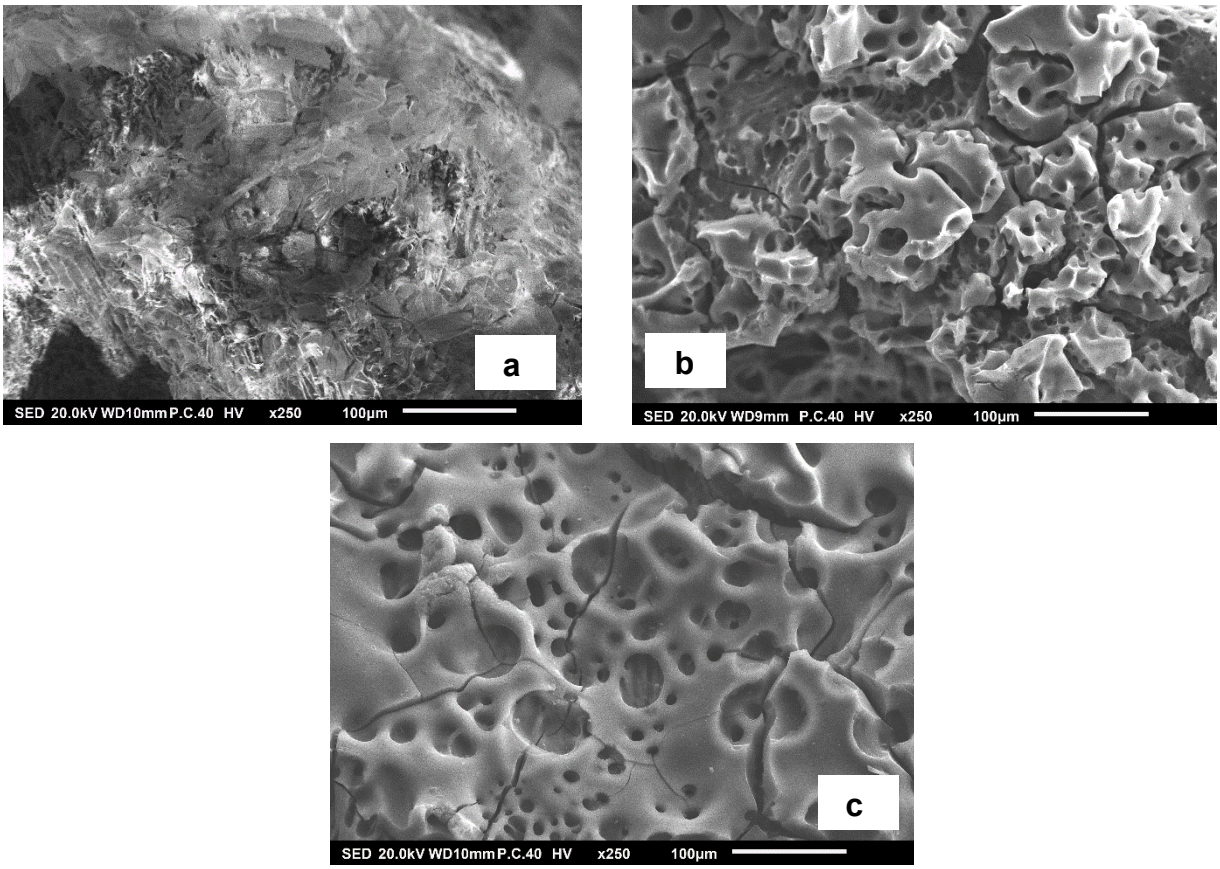

Figure 5.19. Scanning electron micrographs of (a) raw peanut shells (PNTS), and for chemically activated carbons derived from PNTS: (b) PNTS1.7-485-15 and (c) PNTS2-600-15.

Figure 5.19a shows the SEM image of the raw PNTS sample, which has a rough and irregular cellular structure with no apparent openings. However, after activation, the SEM images, at low magnification (250x), reveal the formation of channels within the structure, as shown in Figure 5.19b and 5.19c. The images also indicate the geometrical heterogeneity of the activated carbon materials. The optimised sample (PNTS1.7-485-15) has a relatively smooth surface and textural analysis (Table 5.7) confirms the presence of both micro- and mesopores within the carbon. On the other hand, run 10

(PNTS2-600-15) has a smoother surface but with larger channels, which can be attributed to the pore enlargement due to the increased $ZnCl_2$ loading, resulting in a higher mesopore area (Table 5.7).

Proximate analysis reveals the characteristics of the synthesised carbon samples in terms of their moisture, volatile, fixed carbon, and ash contents. Table 5.13 presents the data obtained for the raw PNTS and the optimal runs.

Table 5.13. Proximate and ultimate analyses of raw peanut shells, and for chemically activated carbons derived from peanut shells: PNTS2-600-15 and PNTS1.7-485-15.

	RAW PNTS	*PNTS2-600-15*	*PNTS1.7-485-15*
Proximate			
Volatile matter (%)	69.79	6.53	11.40
Fixed carbon (%)	27.53	91.19	86.42
Moisture content (%)	1.71	1.67	2.03
Ash (%)	0.97	0.61	0.15
Ultimate			
C (%)	48.61	89.32	80.7
H (%)	5.48	1.66	2.13
N (%)	0.86	1.87	1.69
O (%) [A]	44.08	6.54	15.33
H/C [B]	1.35	0.22	0.32
O/C [B]	0.68	0.05	0.14

[a] Calculated by difference; [b] Atomic ratio

The moisture and ash contents are below 3% and 1%, respectively, for all samples. The low moisture and ash contents of the synthesised samples indicate the high quality of the carbon materials [38]. This attribute enhances the hydrophobicity of carbon materials, which potentially makes them suitable for removing organic pollutants from aqueous phases [39]. The reduced ash content in the chemically activated samples may be attributed to the washing effect, which removed most of the ash components that were soluble in water and acid, during the production stage. The elemental composition of the raw PNTS and the optimal runs was determined by ultimate analysis, and is presented in Table 5.13. The degree of carbonisation and aromatisation can be inferred from the atomic H/C ratio, which reflects the amount of

plant organic matter in the sample, as reported by Chen *et al*. [40] and Tran *et al*. [38]. Similarly, the atomic O/C ratio can be used as an indicator of surface hydrophilicity, which is related to the content of polar groups, as reported by the same authors.

Compared with the precursor, the atomic H/C ratio of the chemically activated carbon materials decreased significantly, indicating a higher degree of carbonisation and aromatisation. The highest degree of carbonisation and aromatisation was achieved by PNTS2-600-15, which was consistent with XPS analysis. The atomic O/C ratio suggested that PNTS1.7-485-15 was the most hydrophilic among the chemically activated samples (Table 5.13). The nitrogen content of the samples increased after activation, which could be attributed to the effect of chemical activation and the nitrogen environment at different temperatures.

Table 5.14. Comparison of textural characteristics and activation conditions of ACs prepared from various precursors with $ZnCl_2$ and other activating agents.

Precursor	Activating agent	Activation condition			S_{BET}, m^2/g	Vt, cm^3/g	Yield, %	Ref.
		Temp., °C	Time, h	I.R, wt/wt				
Date stones	$ZnCl_2$	500	1.2	2	1045	0.641	40.5	[41]
Tea seed shells	$ZnCl_2$	500	1	1	1530	0.783	44.1	[42]
Safflower biochar	$ZnCl_2$	900	1	4	801	0.393	26	[43]
Vine shoots	$ZnCl_2$	700	2	1.3	1689	0.842	18.21	[44]
Palm kernel shell	$ZnCl_2$	550	1	1	1058	0.571	54	[45]
Pineapple waste	$ZnCl_2$	500	1	1	914	0.560	76	[46]
Rice husk	$ZnCl_2$	700	1	1	750	0.380	17.7	[47]
Tomato waste	$ZnCl_2$	600	1	6	1093	1.569	38.2	[1]
Rice straw	H_3PO_4	450	2	1	522	0.550	51.9	[48]
Date palm pits	H_3PO_4	400	1.2	3	952	1.380	41	[49]
Cotton cake	H_3PO_4	450	1.5	2	584	0.298	29.8	[50]
Mangosteen shell	K_2CO_3	900	2	1	1123	0.560	20.7	[51]
Pine	K_2CO_3	800	2	3	1509	0.66	35	[52]
Golden shower	K_2CO_3	800	4	1	1413	0.66	57.67	[38]
Macadamia nut shells	NaOH	700	1.5	3	1524	0.826	19.79	[53]
Plum kernels	NaOH	780	1	4	1887	1.049	37	[54]
Guava seeds	NaOH	750	1.5	3	2573	1.260	14.94	[55]
Maize stalks	KOH	700	1	0.75	1414	0.725	13.1	[56]
Rice straw	KOH	800	1	4	1554	0.930	13.5	[57]
Oil palm fruit	KOH	814	1.9	2.8	1141	0.600	17.96	[58]
Peanut shells	KOH	550	1	1	692	-	87	[59]
Peanut shells	$ZnCl_2$	600	15 min	2	1662	1.016	45.93	This work
Peanut shells	$ZnCl_2$	485	15 min	1.7	1683	0.940	47.41	This work

The carbon materials synthesised in this study were compared with AC materials from various precursors reported in the literature (Table 5.14). The comparison includes activation conditions, textural properties, and various activating agents. The synthesised AC materials demonstrated extraordinary characteristics under relatively low activation conditions (temperature and hold time), which reduced the energy input required.

5.3 Summary

The chemical method of activation employed in this investigation was suitable to produce PNTS-based activated carbons, as evidenced by the results presented in this chapter. A single stage chemical activation of peanut shells was investigated, using response surface methodology to examine the effects of the activation parameters (temperature, hold time and impregnation ratio) on the properties of the resulting activated carbons. Analysis revealed that temperature and impregnation ratio were the most significant factors in determining the characteristics of the activated carbons derived from peanut shells.

The heterogeneity of the activated carbon materials produced in this study was demonstrated by various characterisation techniques, which suggest that the carbon material has the potential to capture a variety of pollutants from water or gas streams. The carbon materials synthesised within this study exhibit extraordinary textural properties in comparison with activated carbons from various precursors in the literature.

References

[1] Sayğılı, H. and Güzel, F. (2016). High surface area mesoporous activated carbon from tomato processing solid waste by zinc chloride activation: process optimization, characterization and dyes adsorption. J Clean Prod 113**:** 995-1004. https://doi.org/10.1016/j.jclepro.2015.12.055

[2] Ahmadpour, A. and Do, D. (1997). The preparation of activated carbon from macadamia nutshell by chemical activation. Carbon 35**:** 1723-1732

[3] Ruiz Bevia, F., Prats Rico, D. and Marcilla Gomis, A. (1984). Activated carbon from almond shells. Chemical activation. 1. Activating reagent selection and variables influence. Ind Eng Chem Prod Res Dev 23**:** 266-269

[4] Rouquerol, J., Rouquerol, F., Llewellyn, P., Maurin, G. and Sing, K. S. (2013). *Adsorption by powders and porous solids: principles, methodology and applications*, Academic press.

[5] Shirley, D. A. (1972). High-resolution X-ray photoemission spectrum of the valence bands of gold. Phys. Rev. B 5**:** 4709. https://doi.org/10.1103/PhysRevB.5.4709

[6] Ottaway, M. (1982). Use of thermogravimetry for proximate analysis of coals and cokes. Fuel 61**:** 713-716. https://doi.org/10.1016/0016-2361(82)90244-7

[7] Ridge, E. and Kudenko, D. Sequential experiment designs for screening and tuning parameters of stochastic heuristics. Workshop on Empirical Methods for the Analysis of Algorithms at the Ninth International Conference on Parallel Problem Solving from Nature (PPSN), 2006. Citeseer, 27-34.

[8] Noordin, M. Y., Venkatesh, V., Sharif, S., Elting, S. and Abdullah, A. (2004). Application of response surface methodology in describing the performance of coated carbide tools when turning AISI 1045 steel. J Mater Process Technol 145**:** 46-58. https://doi.org/10.1016/S0924-0136(03)00861-6

[9] Danish, M., Hashim, R., Ibrahim, M. and Sulaiman, O. (2014). Response surface methodology approach for methyl orange dye removal using optimized Acacia mangium wood activated carbon. Wood science and technology 48**:** 1085-1105

[10] Ahmadi, M., Vahabzadeh, F., Bonakdarpour, B., Mofarrah, E. and Mehranian, M. (2005). Application of the central composite design and response surface methodology to the advanced treatment of olive oil processing wastewater using Fenton's peroxidation. J Hazad Mater 123**:** 187-195. https://doi.org/10.1016/j.jhazmat.2005.03.042

[11] Vining, G. (2010). Technical advice: residual plots to check assumptions. Qual Eng 23**:** 105-110. https://doi.org/10.1080/08982112.2011.535696

[12] El-Masry, E., Ibrahim, H., Moamen, O. A. and Zaher, W. (2022). Sorption of some rare earth elements from aqueous solutions using copolymer/activated carbon composite: Multivariate optimization approach. Adv Powder Technol 33**:** 103467. https://doi.org/10.1016/j.apt.2022.103467

[13] Miller, D. M. (1984). Reducing transformation bias in curve fitting. Am Stat 38**:** 124-126. https://doi.org/10.1080/00031305.1984.10483180

[14] Molina-Sabio, M. and Rodrıguez-Reinoso, F. (2004). Role of chemical activation in the development of carbon porosity. Colloids Surf A Physicochem Eng Asp 241**:** 15-25. https://doi.org/10.1016/j.colsurfa.2004.04.007

[15] Heidarinejad, Z., Dehghani, M. H., Heidari, M., Javedan, G., Ali, I. and Sillanpää, M. (2020). Methods for preparation and activation of activated carbon: a review. Environ Chem Lett 18**:** 393-415. https://doi.org/10.1007/s10311-019-00955-0

[16] Donald, J., Ohtsuka, Y. and Xu, C. C. (2011). Effects of activation agents and intrinsic minerals on pore development in activated carbons derived from a Canadian peat. Mater Lett 65**:** 744-747. https://doi.org/10.1016/j.matlet.2010.11.049

[17] Braghiroli, F. L., Fierro, V., Parmentier, J., Vidal, L., Gadonneix, P. and Celzard, A. (2015). Hydrothermal carbons produced from tannin by modification of the reaction medium: Addition of H+ and Ag+. Industrial Crops and Products 77**:** 364-374

[18] Thommes, M., Kaneko, K., Neimark, A. V., Olivier, J. P., Rodriguez-Reinoso, F., Rouquerol, J. and Sing, K. S. (2015). Physisorption of gases, with special reference to the evaluation of surface area

and pore size distribution (IUPAC Technical Report). Pure Appl Chem 87**:** 1051-1069. https://doi.org/10.1515/pac-2014-1117
[19] Rouquerol, J., Llewellyn, P. and Rouquerol, F. (2007). Is the BET equation applicable to microporous adsorbents. Stud. Surf. Sci. Catal 160**:** 49-56
[20] Hadi, P., Yeung, K. Y., Barford, J., An, K. J. and Mckay, G. (2015). Significance of "effective" surface area of activated carbons on elucidating the adsorption mechanism of large dye molecules. Journal of Environmental Chemical Engineering 3**:** 1029-1037
[21] Tran, H. N., You, S.-J. and Chao, H.-P. (2016). Effect of pyrolysis temperatures and times on the adsorption of cadmium onto orange peel derived biochar. Waste Manag Res 34**:** 129-138. https://doi.org/10.1177/0734242X15615698
[22] Fleming, I. and Williams, D. H. (1966). *Spectroscopic methods in organic chemistry*, Springer.
[23] (!!! INVALID CITATION !!! [1, 22, 23]).
[24] Tran, H. N., You, S.-J. and Chao, H.-P. (2017). Fast and efficient adsorption of methylene green 5 on activated carbon prepared from new chemical activation method. J. Environ. Manage. 188**:** 322-336. https://doi.org/10.1016/j.jenvman.2016.12.003
[25] Edebali, S. (2019). *Advanced sorption process applications*, BoD–Books on Demand.
[26] Suzuki, M. and Suzuki, M. (1990). *Adsorption engineering*, Kodansha Tokyo.
[27] Sinha, P., Banerjee, S. and Kar, K. K. (2020). Characteristics of activated carbon. Handbook of Nanocomposite Supercapacitor Materials I: Characteristics**:** 147-148. https://doi.org/10.1007/978-3-030-43009-2_4
[28] Li, H., Budarin, V. L., Clark, J. H., North, M. and Wu, X. (2022). Rapid and efficient adsorption of methylene blue dye from aqueous solution by hierarchically porous, activated starbons®: Mechanism and porosity dependence. J. Hazard. Mater. 436**:** 129174. https://doi.org/10.1016/j.jhazmat.2022.129174
[29] Chen, S., Huang, Y., Han, X., Wu, Z., Lai, C., Wang, J., Deng, Q., Zeng, Z. and Deng, S. (2018). Simultaneous and efficient removal of Cr (VI) and methyl orange on LDHs decorated porous carbons. Chemical Engineering Journal 352**:** 306-315. https://doi.org/10.1016/j.cej.2018.07.012
[30] Terzyk, A. P. (2001). The influence of activated carbon surface chemical composition on the adsorption of acetaminophen (paracetamol) in vitro: Part II. TG, FTIR, and XPS analysis of carbons and the temperature dependence of adsorption kinetics at the neutral pH. Colloids Surf. A Physicochem. Eng. Asp. 177**:** 23-45. https://doi.org/10.1016/S0927-7757(00)00594-X
[31] López, G. P., Castner, D. G. and Ratner, B. D. (1991). XPS O 1s binding energies for polymers containing hydroxyl, ether, ketone and ester groups. Surface and interface analysis 17**:** 267-272. https://doi.org/10.1002/sia.740170508
[32] Reddygunta, K. K. R., Callander, A., Šiller, L., Faulds, K., Berlouis, L. and Ivaturi, A. (2022). Sono-exfoliated graphene-like activated carbon from hazelnut shells for flexible supercapacitors. Int. J. Energy Res. 46**:** 16512-16537. https://doi.org/10.1002/er.8314
[33] Rivera-Utrilla, J. and Sánchez-Polo, M. (2002). The role of dispersive and electrostatic interactions in the aqueous phase adsorption of naphthalenesulphonic acids on ozone-treated activated carbons. Carbon 40**:** 2685-2691. https://doi.org/10.1016/S0008-6223(02)00182-3
[34] Leng, L., Xu, S., Liu, R., Yu, T., Zhuo, X., Leng, S., Xiong, Q. and Huang, H. (2020). Nitrogen containing functional groups of biochar: An overview. Bioresour. Technol. 298**:** 122286. https://doi.org/10.1016/j.biortech.2019.122286
[35] Deng, Y., Liu, K., Cao, H., Luo, M. and Yan, H. (2015). Synthesis of graphene with both high nitrogen content and high surface area by annealing composite of graphene oxide and gC 3 N 4. J. Iran. Chem. Soc. 12**:** 807-814. https://doi.org/10.1007/s13738-014-0543-2
[36] Wang, X., Sun, G., Routh, P., Kim, D.-H., Huang, W. and Chen, P. (2014). Heteroatom-doped graphene materials: syntheses, properties and applications. Chem. Soc. Rev. 43**:** 7067-7098. https://doi.org/10.1039/C4CS00141A

[37] Sinha, P., Banerjee, S. and Kar, K. K. (2020). Characteristics of activated carbon. Handbook of Nanocomposite Supercapacitor Materials I: Characteristics: 125-154. https://doi.org/10.1007/978-3-030-43009-2_4
[38] Tran, H. N., Chao, H.-P. and You, S.-J. (2018). Activated carbons from golden shower upon different chemical activation methods: synthesis and characterizations. Adsorp. Sci. Technol. 36: 95-113. https://doi.org/10.1177/0263617416684483
[39] Zuim, D. R., Carpiné, D., Distler, G. a. R., De Paula Scheer, A., Igarashi-Mafra, L. and Mafra, M. R. (2011). Adsorption of two coffee aromas from synthetic aqueous solution onto granular activated carbon derived from coconut husks. J. Food Eng. 104: 284-292. https://doi.org/10.1016/j.jfoodeng.2010.12.019
[40] Chen, X., Chen, G., Chen, L., Chen, Y., Lehmann, J., Mcbride, M. B. and Hay, A. G. (2011). Adsorption of copper and zinc by biochars produced from pyrolysis of hardwood and corn straw in aqueous solution. Bioresour. Technol. 102: 8877-8884. https://doi.org/10.1016/j.biortech.2011.06.078
[41] Ahmed, M. J. and Theydan, S. K. (2012). Physical and chemical characteristics of activated carbon prepared by pyrolysis of chemically treated date stones and its ability to adsorb organics. Powder Technology 229: 237-245
[42] Gao, J.-J., Qin, Y.-B., Zhou, T., Cao, D.-D., Xu, P., Hochstetter, D. and Wang, Y.-F. (2013). Adsorption of methylene blue onto activated carbon produced from tea (Camellia sinensis L.) seed shells: kinetics, equilibrium, and thermodynamics studies. Journal of Zhejiang University Science B 14: 650-658
[43] Angın, D., Altintig, E. and Köse, T. E. (2013). Influence of process parameters on the surface and chemical properties of activated carbon obtained from biochar by chemical activation. Bioresource Technology 148: 542-549
[44] Erdem, M., Orhan, R., Şahin, M. and Aydın, E. (2016). Preparation and characterization of a novel activated carbon from vine shoots by ZnCl 2 activation and investigation of its rifampicine removal capability. Water, Air, & Soil Pollution 227: 1-14
[45] García, J. R., Sedran, U., Zaini, M. a. A. and Zakaria, Z. A. (2018). Preparation, characterization, and dye removal study of activated carbon prepared from palm kernel shell. Environmental Science and Pollution Research 25: 5076-5085
[46] Mahamad, M. N., Zaini, M. a. A. and Zakaria, Z. A. (2015). Preparation and characterization of activated carbon from pineapple waste biomass for dye removal. International Biodeterioration & Biodegradation 102: 274-280
[47] Kalderis, D., Bethanis, S., Paraskeva, P. and Diamadopoulos, E. (2008). Production of activated carbon from bagasse and rice husk by a single-stage chemical activation method at low retention times. Bioresource technology 99: 6809-6816
[48] Fierro, V., Muñiz, G., Basta, A., El-Saied, H. and Celzard, A. (2010). Rice straw as precursor of activated carbons: Activation with ortho-phosphoric acid. Journal of hazardous materials 181: 27-34
[49] Reddy, K. S. K., Al Shoaibi, A. and Srinivasakannan, C. (2012). A comparison of microstructure and adsorption characteristics of activated carbons by CO2 and H3PO4 activation from date palm pits. New Carbon Materials 27: 344-351
[50] Ibrahim, T., Moctar, B. L., Tomkouani, K., Gbandi, D.-B., Victor, D. K. and Phinthè, N. (2014). Kinetics of the adsorption of anionic and cationic dyes in aqueous solution by low-cost activated carbons prepared from sea cake and cotton cake. Am. Chem. Sci. J 4: 38-57
[51] Chen, Y., Huang, B., Huang, M. and Cai, B. (2011). On the preparation and characterization of activated carbon from mangosteen shell. Journal of the Taiwan Institute of Chemical Engineers 42: 837-842
[52] Galhetas, M., Mestre, A. S., Pinto, M. L., Gulyurtlu, I., Lopes, H. and Carvalho, A. P. (2014). Chars from gasification of coal and pine activated with K2CO3: Acetaminophen and caffeine adsorption from aqueous solutions. Journal of Colloid and Interface Science 433: 94-103

[53] Martins, A. C., Pezoti, O., Cazetta, A. L., Bedin, K. C., Yamazaki, D. A., Bandoch, G. F., Asefa, T., Visentainer, J. V. and Almeida, V. C. (2015). Removal of tetracycline by NaOH-activated carbon produced from macadamia nut shells: kinetic and equilibrium studies. Chemical Engineering Journal 260**:** 291-299

[54] Tseng, R.-L. (2007). Physical and chemical properties and adsorption type of activated carbon prepared from plum kernels by NaOH activation. Journal of hazardous materials 147**:** 1020-1027

[55] Pezoti, O., Cazetta, A. L., Bedin, K. C., Souza, L. S., Martins, A. C., Silva, T. L., Júnior, O. O. S., Visentainer, J. V. and Almeida, V. C. (2016). NaOH-activated carbon of high surface area produced from guava seeds as a high-efficiency adsorbent for amoxicillin removal: Kinetic, isotherm and thermodynamic studies. Chemical Engineering Journal 288**:** 778-788

[56] El-Hendawy, A.-N. A. (2009). An insight into the KOH activation mechanism through the production of microporous activated carbon for the removal of Pb2+ cations. Applied Surface Science 255**:** 3723-3730

[57] Basta, A., Fierro, V., El-Saied, H. and Celzard, A. (2009). 2-Steps KOH activation of rice straw: an efficient method for preparing high-performance activated carbons. Bioresource technology 100**:** 3941-3947

[58] Hameed, B., Tan, I. and Ahmad, A. (2009). Preparation of oil palm empty fruit bunch-based activated carbon for removal of 2, 4, 6-trichlorophenol: Optimization using response surface methodology. Journal of Hazardous materials 164**:** 1316-1324

[59] Kumari, G., Soni, B. and Karmee, S. K. (2020). Synthesis of activated carbon from groundnut shell via chemical activation. J Inst Eng India Ser E**:** 1-8. https://doi.org/10.1007/s40034-020-00176-z

Chapter 6: A Comparative Study of PNTS-based Activated Carbon for the Removal of Anionic and Cationic Dyes from Water

This chapter presents the screening analysis results of eight samples (PNTS1.13-450-120, PNTS2-600-15, PNTS1.13-450-15, PNTS2-600-120, PNTS1.13-450-68, PNTS2-450-68, PNTS1.13-600-68 and PNTS1.7-485-15) that exhibited high surface area and yield from the outcome of DoE in Chapter 5 to identify the most effective PNTS-based carbon material for removing methyl orange (MO) and methylene blue (MB) from aqueous phase. It also presents the adsorption study results of the selected PNTS-based activated carbon sample, for the removal of MO (anionic) dye and MB (anionic) dye from the aqueous phase. The experimental procedures for the adsorption studies are described in detail. The results are discussed and compared with relevant published studies.

6.1 Materials and Experimental procedures

This section aims to provide detailed experimental procedures and the steps taken for the preparation of materials for the adsorption studies undertaken here. The underlying theories related to the methods examined in this section have been reviewed in Chapter 3 and are not repeated here.

6.1.1 Materials preparation

The PNTS-based activated carbon (AC) materials synthesised in Chapter 5, were sieved to obtain particle size in the range of 1.25 – 2 mm and stored in an airtight container for subsequent use. Methyl orange ($C_{14}H_{14}N_3NaO_3S$) with the molecular weight of 327.33 g/mol and methylene blue ($C_{16}H_{24}ClN_3O_3S$) with the molecular weight of 373.90 g/mol were purchased from Sigma – Aldrich, UK. All reagents used were of analytical grade and were used without further purification. The structures of methyl

orange (MO) and methylene blue (MB) are shown in Figure 6.1. In each case, stock solution (1000 mg/L) was prepared by dissolving an accurately weighed quantity of the selected dye in distilled water. The desired concentrations of the solutions were obtained by diluting the stock solution with distilled water.

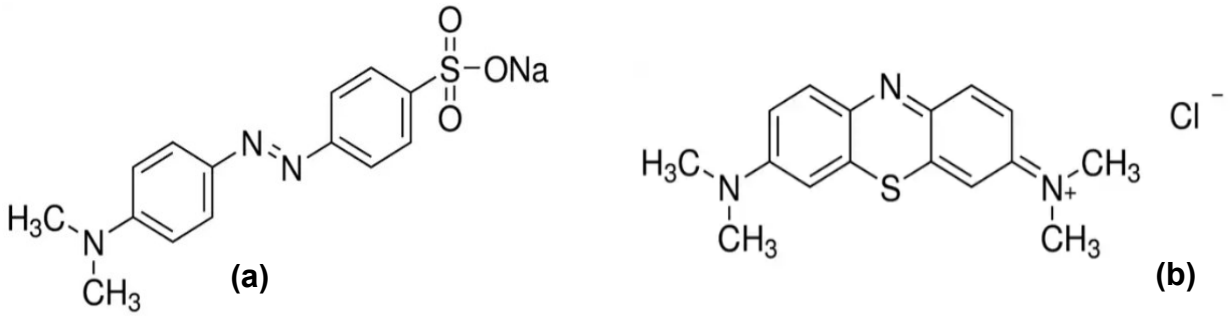

Figure 6.1. The molecular structure of: (a) methyl orange (b) methylene blue.

6.1.2 Adsorption experiment

The efficiency of the PNTS-based carbon materials to remove MO and MB from the aqueous phase was evaluated using batch adsorption experiments. The adsorption experiments were conducted in 500 mL Erlenmeyer flasks with a known mass of AC sample and dye solutions at specified concentrations and volumes. The mixtures were agitated on an orbital shaker, operated at 150 rpm, and desired temperatures using a temperature control chamber. At predetermined time intervals, the mixtures were separated by centrifugation, and the residual concentrations were measured at 465 nm and 664 nm for MO and MB, respectively, using a Varian CARY 5000 UV-VIS-NIR spectrophotometer. The calibration curves for MO and MB dyes (see Figures A3 and A4 in Appendix A) were obtained by plotting the absorbance values versus the corresponding concentrations of standard solutions (3 – 25 mg/L). This range was chosen to be within the detection limit of the measurement and the highest concentration of dye that can be accurately measured without saturation or non-

linearity. The residual concentrations of the analytes were determined by interpolating the absorbance values from the calibration curves. The adsorption of the dyes by the adsorbent was replicated with the average values recorded and this was investigated under various experimental conditions, such as adsorbent dosage, contact time, volume, pH, and initial concentration. The effects of these parameters on the adsorption efficiency and capacity were evaluated and discussed.

6.2 Results and discussion

6.2.1 Adsorbent screening for MO and MB removal

The choice of adsorbent for liquid phase adsorption depends on factors such as the surface area, pore size, surface chemistry of the adsorbent (i.e., the surface charge of the adsorbent, and the functional groups), etc. Eight samples (PNTS1.13-450-120, PNTS2-600-15, PNTS1.13-450-15, PNTS2-600-120, PNTS1.13-450-68, PNTS2-450-68, PNTS1.13-600-68 and PNTS1.7-485-15) that exhibited high surface area and yield, were selected from the DoE outcome for pore size distribution analysis. Small micropores are present in PNTS1.13-450-120, PNTS1.13-450-15, PNTS1.13-450-68, and PNTS1.13-600-68 (as shown in Table 5.7, Chapter 5), which could limit the diffusion rates of MO and MB within the pores. PNTS2-450-68 exhibits some wider pores, whereas PNTS2-600-15, PNTS2-600-120, and PNTS1.7-485-15 have wider micropores, which could facilitate water phase application. Therefore, on this basis, PNTS2-600-15, PNTS2-600-120, and PNTS1.7-485-15 could be potential candidates for liquid phase applications.

Owing to the complexity of liquid phase adsorption, pore size analysis alone is not adequate for screening the samples. Thus, the same samples were subjected to adsorption tests under the same operating conditions. The results of the screening test are shown in Figures 6.2 and 6.3.

All samples achieved more than 90% MO and MB removal after 24 h contact time. However, the uptake of both dyes occurs faster with PNTS2-600-15, PNTS2-600-120, and PNTS1.7-485-15 (the optimised run), corresponding to the expected outcome from the results of the earlier pore size analysis. Still, PNTS2-600-15 and PNTS2-600-120 showed better performance. These two samples were activated under similar conditions, except for the hold time of 2 h for PNTS2-600-120, and 15 min for PNTS2-600-15, resulting in similar textural characteristics. This supports the findings of this study, in Chapter 5, that hold time is an insignificant factor in determining the final textural characteristics of the produced ACs. Therefore, based on these analyses, PNTS2-600-15 was selected as the most effective candidate for further adsorption studies.

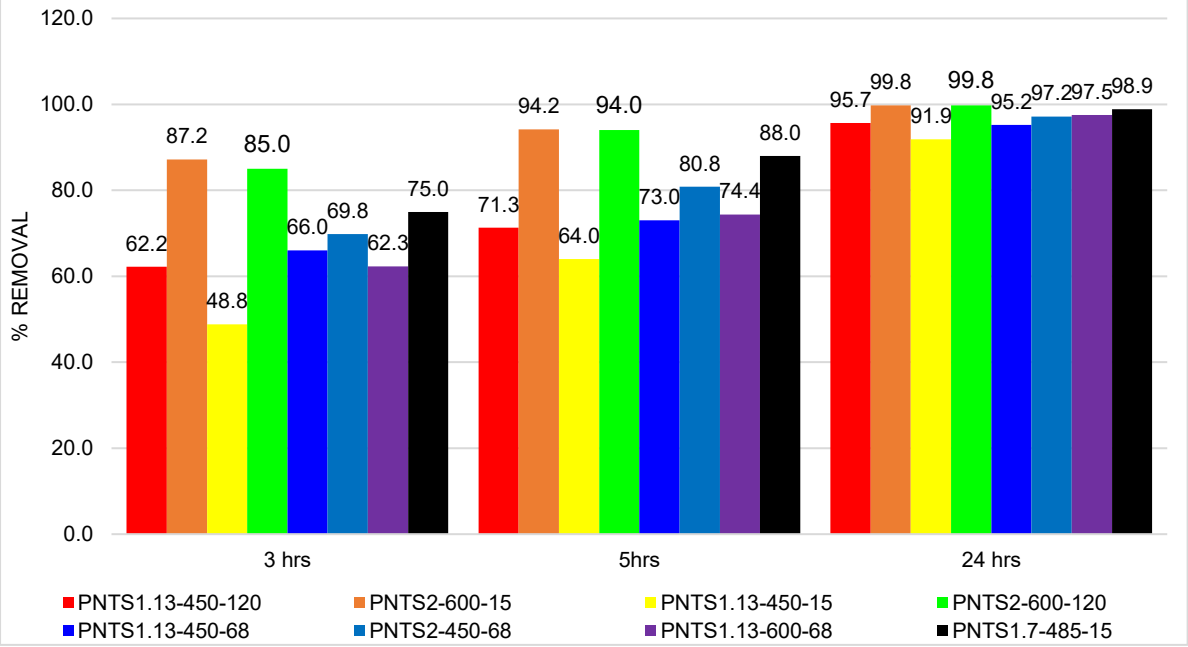

Figure 6.2. Methyl orange removal performance test with contact time (initial conc. = 100 ppm, pH = 5.5, dosage = 1 g/L) on activated carbons derived from peanut shells.

In addition to the textural characteristics, it is crucial to discuss the role of point of zero charge (PZC) in the performance test. The PZC values of the samples are displayed in Table 5.11 (Chapter 5). Although the wider pores may facilitate the diffusion of MO, it should be noted that, due to MO dissociating into negatively

charged ions, the samples with PZC values below the solution pH may experience repulsive forces. Hence, this suggests that the interaction favours samples with PZC values above 5.5 (solution pH). While for MB, the uptake with time was reduced, and this may be attributed to electrostatic repulsion experienced between the positively charged surface of the samples and positively charge ions of MB.

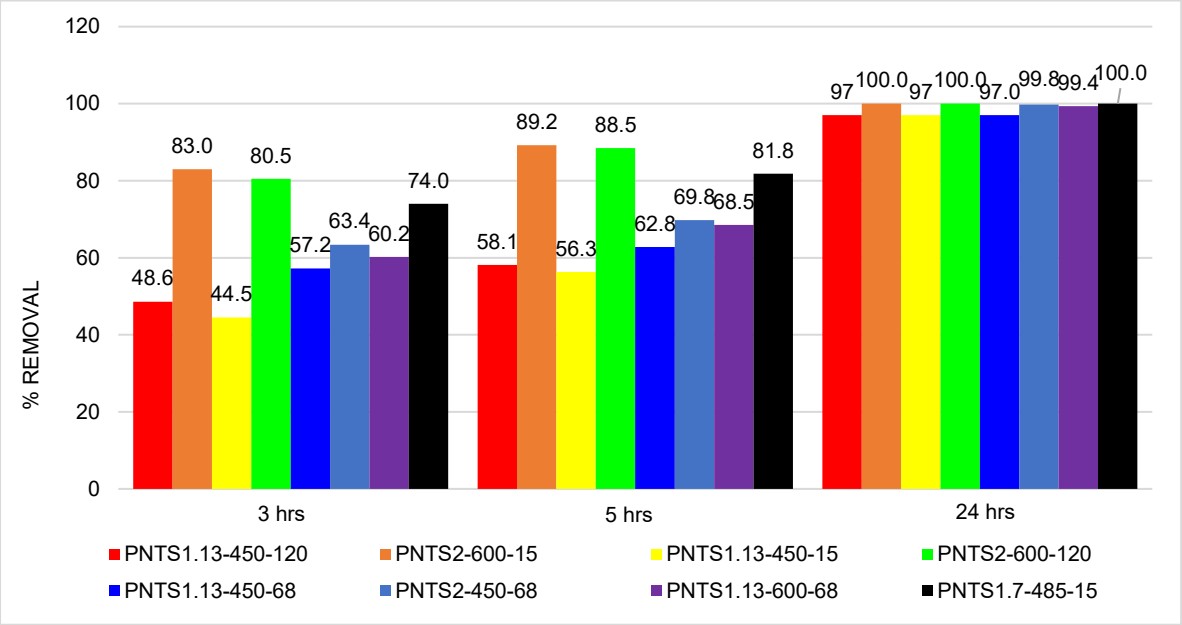

Figure 6.3. Methylene blue removal performance test with contact time (initial conc. = 100 ppm, pH = ~5.5, dosage = 1 g/L) on activated carbons derived from peanut shells.

6.2.2 Effect of adsorbent dose on MO adsorption

The effect of adsorbent dose on the removal of MO dye was investigated by varying the amount of adsorbent from 0.01 to 0.2 g in 50 mL of the dye solution with an initial concentration of 100 mg/L. Figure 6.4 shows that the percentage removal of dye increased from 29.5 – 100% with the increase of adsorbent dose from 0.01 – 0.2 g after 240 min of contact time. The amount adsorbed per unit mass of adsorbent (adsorption capacity) was calculated and plotted on the secondary y-axis (Figure 6.4).

The results indicate that the amount adsorbed per unit mass decreases with increasing adsorbent dose. This can be explained by the fact that the number of available

adsorption sites and the surface area of the adsorbent increase proportionally to the adsorbent dose, which results in an increase in the amount of dye adsorbed on the adsorbent surface [1]. The results show that the dye removal efficiency increased significantly, from 29.5 to 98%, as the adsorbent dose increased from 0.01 to 0.07 g, indicating that more dye molecules were adsorbed by the increased number of adsorption sites. However, on further increase of adsorbent dose, the dye removal efficiency reached a maximum of 100% at 0.1 g and remained constant thereafter with a decrease in adsorption capacity per unit mass of adsorbent at higher doses, which can be attributed to unsaturated adsorption sites within the adsorption process, as insufficient dye molecules are presented for saturation [1, 2].

Based on the results shown in Figure 6.4, the optimal adsorbent dose for achieving 100% dye removal efficiency was determined to be 0.1 g in 50 mL of solution. This was also confirmed by the visual observation of the colour change of the dye solution, as illustrated in Figure 6.5. Therefore, the adsorbent dose of 0.1 g, corresponding to 2 g/L, was selected as the optimum dose for the subsequent adsorption experiments.

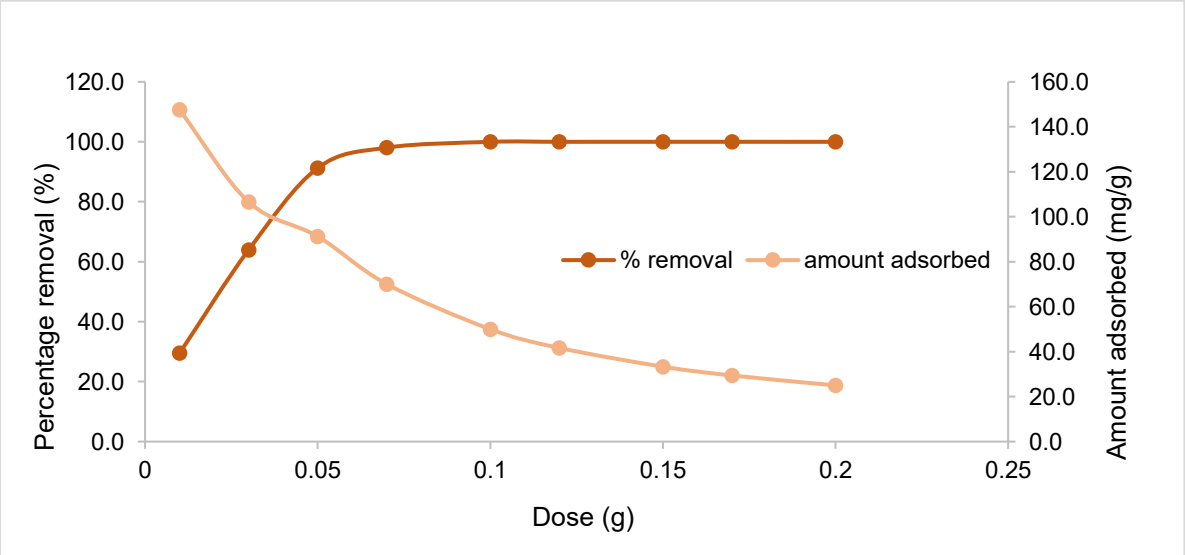

Figure 6.4. Effect of adsorbent dose on percentage methyl orange removal and quantity adsorbed on activated carbons derived from peanut shells (PNTS2-600-15).

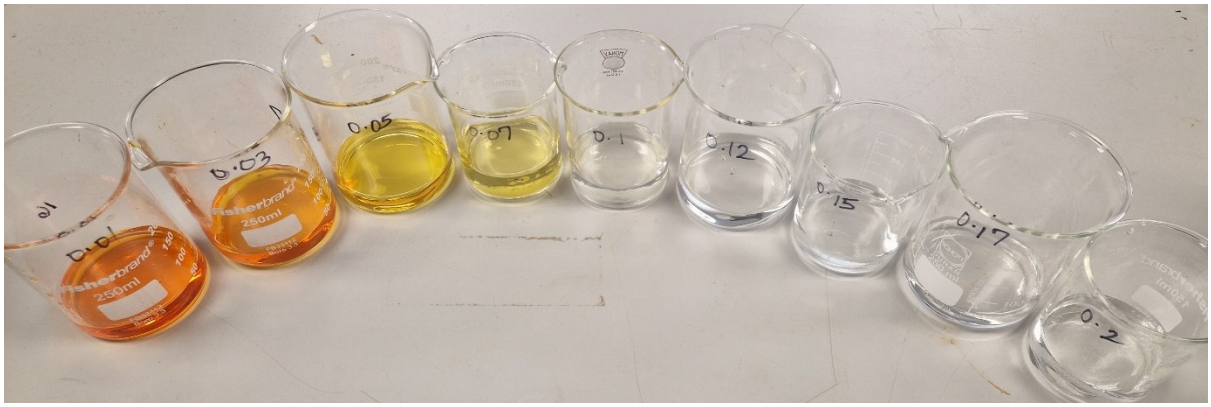

Figure 6.5. Image showing decolouration with varying adsorbent dose (0.01 – 0.2) in 50 mL of 100 mg/L methyl orange concentration using activated carbons derived from peanut shells (PNTS2-600-15).

6.2.3 Effect of contact time on MO and MB adsorption

Figure 6.6 presents the influence of contact time on the adsorption behaviour of MO and MB at 25 ± 1 °C, for 360 min. The figure shows that, while both systems adsorbed a similar final amount, MO adsorption was faster than MB, reaching approximately 80% removal within 20 min, while MB only attained 61% removal in the same duration. The adsorption rate for both dyes slowed down after 30 min and approached equilibrium. The initial rapid adsorption process may be due to the availability of active sites on the external surfaces of the adsorbent. After the saturation of these sites, the dyes penetrated the pores of the adsorbent at a slower rate until the equilibrium was achieved [3]. The faster adsorption process of MO may be attributed to the stronger affinity of the adsorbent towards MO molecules [4]. The equilibrium time for both dyes was established as 180 min, where MO and MB removal attained 100% and 99.80%, respectively. Beyond this time point, no significant increase in dye removal was observed. Therefore, 180 min was chosen as the equilibrium time for both dyes in subsequent experiments.

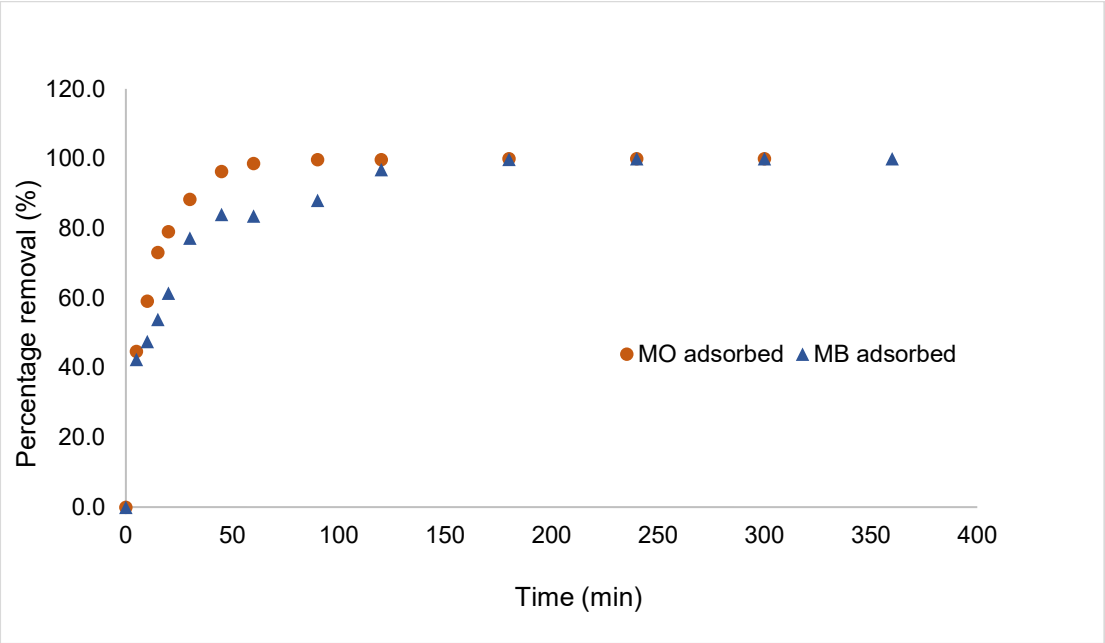

Figure 6.6. Effect of contact time on methyl orange and methylene blue adsorption on activated carbons derived from peanut shells (PNTS2-600-15).

6.2.4 Effect of volume on MO and MB adsorption

Adsorption process scale-up entails enhancing the size and performance of an adsorption system to satisfy a higher requirement or criterion. Scale-up necessitates accounting for both equilibrium and kinetic factors, as well as other parameters, such as pressure drop, heat transfer, dispersion, and regeneration. The volume of the fluid influences all of these parameters, and, hence, it is essential to consider it when designing and operating an adsorption system [5].

Figure 6.7 depicts the influence of varying the volume while maintaining the same dosage of 2 g/L. The volume ranged from 20 to 100 mL. At the equilibrium time of 180 min, each case exhibited approximately 100% removal, indicating that varying the volume of the adsorption system for both dyes does not affect the equilibrium time and removal efficiency of the system.

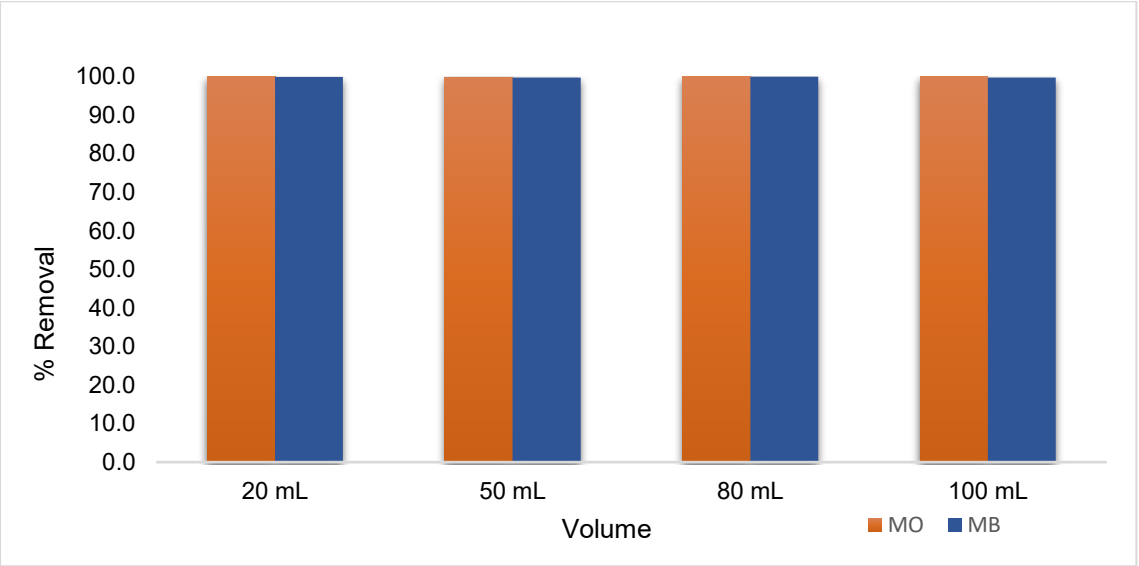

Figure 6.7. Effect of volume on methyl orange and methylene blue adsorption on activated carbons derived from peanut shells (PNTS2-600-15).

6.2.5 Effect of pH on MO and MB adsorption

Figure 6.8 illustrates the effect of pH on the adsorption of MO and MB dyes by PNTS2-600-15. The initial pH of the dye solution is a crucial factor, which affects the adsorption capacity by influencing the chemical properties of both the dye molecules and the adsorbent in the aqueous medium [6]. The adsorption capacity of PNTS2-600-15 exhibited a marginal increase at pH 3 for MO, and at pH 11 for MB. However, the overall effect of the dyes' solution pH on the adsorption capacity of the adsorbent was minimal. The adsorption mechanism would be expected to depend strongly on the solution pH, if electrostatic attraction was the dominant factor, which appears not to be the case for PNTS2-600-15.

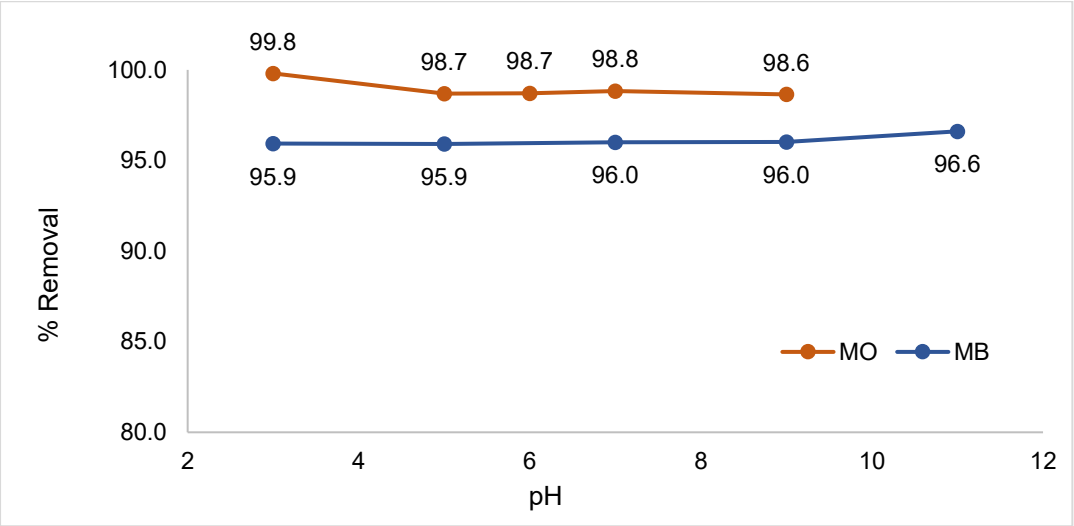

Figure 6.8. Effect of varied solution pH levels on methyl orange and methylene blue adsorption (C_0 = 250 mg/L, Temp. = 25 ± 1 °C) on activated carbons derived from peanut shells (PNTS2-600-15).

MO adsorption was still adequate in solutions of pH above the PZC of the AC despite a negative AC surface charge existing at these pH values. MB adsorption was also relatively high in solutions of pH below the PZC of the AC, despite a positive AC surface charge existing at these pH values, owing to the protonation of the acidic groups (i.e., -COOH and -OH) on the surface of the AC. This indicates that the adsorption mechanism of the dyes on PNTS2-600-15 is not strongly dependent on electrostatic attractions and must involve other interactions, such as pore filling, hydrogen bonding or π-π stacking. It is noteworthy that the adsorption capacity of the AC was relatively high at a pH of 7, suggesting that the AC could effectively remove the dyes from solution under neutral pH conditions.

6.2.6 Effect of initial concentration on MO and MB adsorption

Figure 6.9 demonstrates how the initial concentration influences the adsorption of MO and MB onto PNTS2-600-15. The adsorption experiments were performed at different initial dye concentrations ranging from 10 to 500 mg/L, while keeping the temperature at 25 ± 1 °C, and the contact time at 180 min.

As shown in the figure, the initial concentration has an inverse effect on the percentage removal and a direct effect on the amount of dye adsorbed.

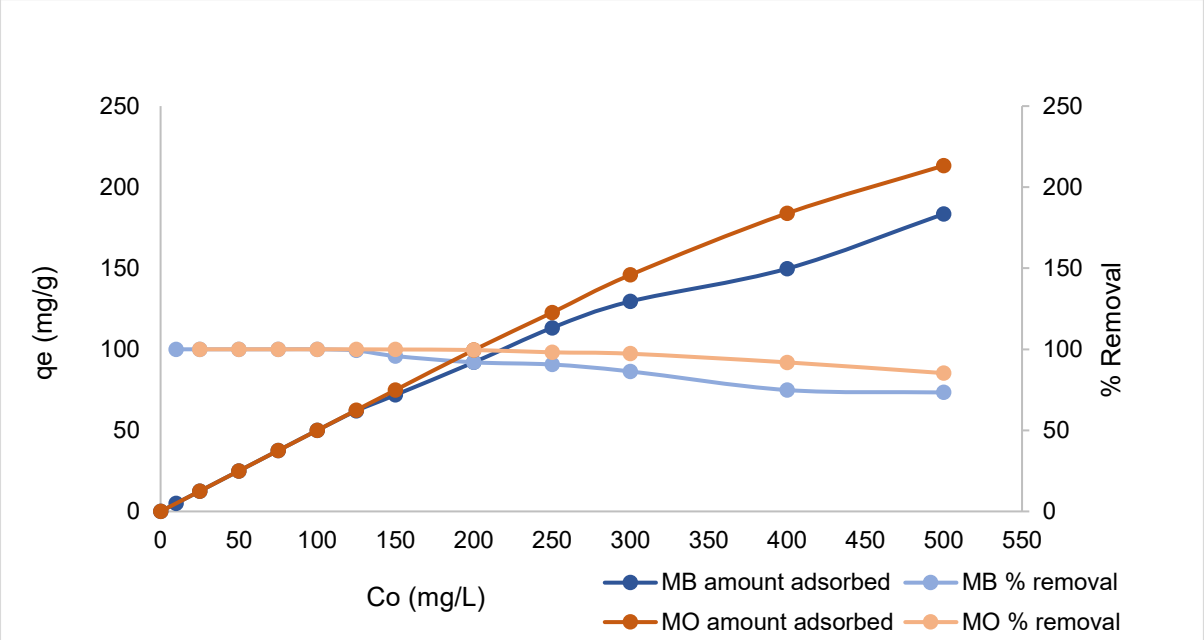

Figure 6.9. Effect of initial concentration on the adsorption of MO and MB on activated carbons synthesised in this study (PNTS2-600-15).

A higher initial concentration enhances the mass transfer gradient between the bulk solution and the adsorbent surface, resulting in more dye molecules being adsorbed. However, when the concentration increases beyond a certain point, the available adsorption sites become saturated, and the percentage removal declines [4, 6].

6.2.7 Adsorption kinetics

6.2.7.1 Pseudo-first order and second-order kinetic models

The rate and mechanism of adsorption, relating to surface reactions, mass transfer, and the diffusion of adsorbate in the adsorption system were investigated using pseudo-first order (PFO), pseudo-second order (PSO) and intraparticle diffusion models (IPD). As discussed in Chapter 3, the non-linear form of PFO and PSO are expressed in Equations (3.26) and (3.28), respectively, and Figures 6.10 and 6.11 show

the plots for PFO and PSO models, respectively. The calculated values of the models' parameters and the determination coefficients, i.e. R^2, are presented in Table 6.2.

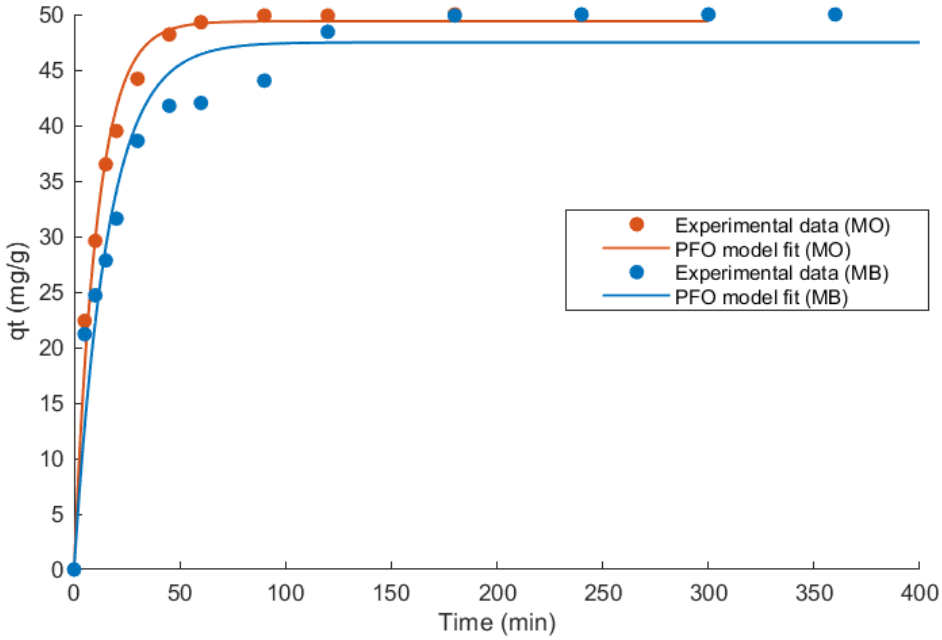

Figure 6.10. Pseudo-first-order kinetic fitting curve for the adsorption of methyl orange and methylene blue on activated carbon PNTS2-600-15.

The determination coefficients (R^2) of the PFO and PSO models for the adsorption kinetics of MO onto PNTS2-600-15 are presented in Table 6.2. Both models show high R^2 values of 0.9896 and 0.9928, respectively, indicating a good fit to the experimental data. Moreover, the calculated equilibrium adsorption capacities, $q_{e,cal}$, from both models are in close agreement with the experimental value, $q_{e,exp}$. Therefore, it can be said that both models are suitable for describing the adsorption process of MO onto PNTS2-600-15.

The R^2 values of the PFO and PSO models for the adsorption kinetics of MB onto PNTS2-600-15 are 0.9460 and 0.9848, respectively, as shown in Table 6.2.

Table 6.2. Kinetic models parameters and determination coefficients for adsorption of methyl orange and methylene blue on activated carbon PNTS2-600-15.

		Pseudo-first-order kinetic model			*Pseudo-second-order kinetic model*		
	$q_{e,exp}$ *(mg/g)*	$q_{e,cal}$ *(mg/g)*	k_1 *(min^{-1})*	R^2	$q_{e,cal}$ *(mg/g)*	k_2 *g/(mg·min)*	R^2
MO	50	49.38	0.0922	0.9896	51.37	0.0023	0.9928
MB	50	47.49	0.0632	0.9460	51.41	0.0018	0.9848

Intraparticle diffusion model

	$k_{int,1}$	$k_{int,2}$	$k_{int,3}$	R^2_1	R^2_2	R^2_3	C_1	C_2	C_3
		($mg/g.min^{1/2}$)						*(mg/g)*	
MO	7.9131	2.2846	0.0264	0.9903	0.9336	0.8976	4.80	32.03	49.61
MB	5.3667	1.5478	0.0168	0.9785	0.8859	0.6464	8.16	30.57	49.70

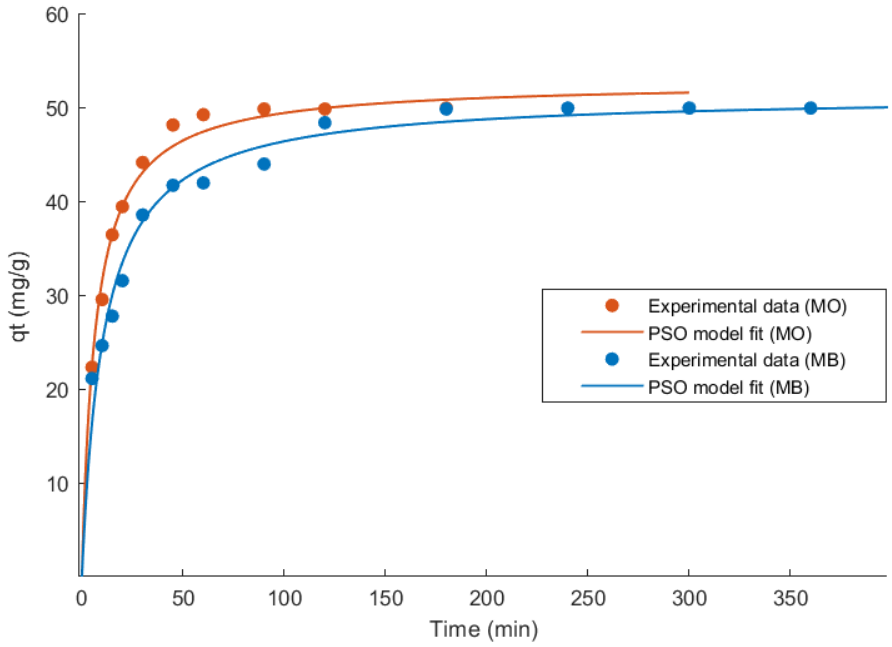

Figure 6.11. Pseudo-second-order kinetic fitting curve for the adsorption of methyl orange and methylene blue on activated carbon PNTS2-600-15.

The PSO model shows a higher R^2 value, indicating a better fit to the experimental data. Furthermore, the calculated equilibrium adsorption capacity, $q_{e,cal}$, from the PSO model is closer to the experimental value, $q_{e,exp}$, than that from the PSO model. Thus, the PSO model is more suitable for describing the adsorption process of MB onto PNTS2-600-15.

The PSO model is more applicable for both dyes, as indicated by the higher R^2 values and the closer agreement between $q_{e,cal}$ and $q_{e,exp}$. The pseudo-second order rate constant, k_2, for MO is higher than that for MB, implying a faster adsorption rate of MO onto PNTS2-600-15. This may be due to the stronger affinity of the adsorbent surface for MO. Moreover, the PSO model suggests that the adsorption mechanism may involve chemisorption, which is based on the formation of covalent bonds through electron sharing or exchange [7]. However, it has been argued and reported that the adsorption mechanism cannot be determined solely by the reaction kinetic models, and that other analytical techniques must be put into consideration [8-10].

6.2.7.2 Intraparticle diffusion model

Intraparticle diffusion was explored by using the intraparticle diffusion model as described in Equation 3.30 (Section 3.3.2.3). If the plot of q_t versus $\sqrt{t}$ yields a straight line that passes through the origin, the rate of adsorption is solely controlled by intraparticle diffusion [3, 11].

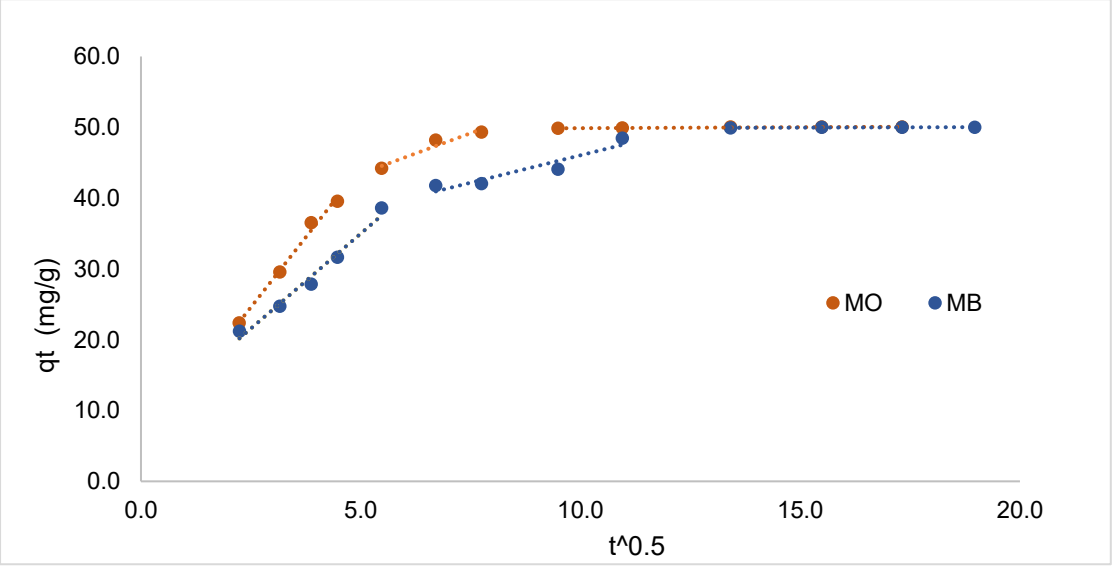

Figure 6.12. Intraparticle diffusion model plots for methyl orange and methylene blue adsorption on activated carbon PNTS2-600-15.

As shown in Figure 6.12, the intraparticle diffusion model plots for MO and MB adsorption onto PNTS2-600-15 yield multiple linear sections. This suggests that intraparticle diffusion was not the sole rate-limiting step of the adsorption process of MO and MB onto PNTS2-600-15. Rather, other mechanisms may also influence the adsorption rate, and they may operate concurrently [11-13].

The intraparticle diffusion model parameters and determination coefficients for the kinetic data of MO and MB are shown in Table 6.2. The first linear section of the plot (Figure 6.12) corresponds to the diffusion of dye molecules from the bulk solution across the liquid film to the external surface of the adsorbent. The first linear section of the plot also indicates a stronger attraction force between the adsorbent surface and MO molecules, as evidenced by the higher rate constant ($k_{int,1}$) value. The C values (Table 6.2) which represent the boundary layer effects, were positive in all cases, indicating the occurrence of an initial adsorption process [14, 15]. The second linear section corresponds to a slower process, as shown by the lower rate constant ($k_{int,2}$) values. This section represents the intraparticle diffusion of the dye molecules into the adsorbent particles, which occurs after the external surface of the adsorbent is saturated [16, 17]. The third section describes the final equilibrium stage for which the intraparticle diffusion starts to slow down due to the lower dye concentration [11].

6.2.8 Adsorption isotherms

Equilibrium adsorption data were obtained by varying the initial concentration of the selected dye in the aqueous phase, from 10 to 500 mg/L, while maintaining the temperature at 25 ± 1 °C, and the contact time at 180 min. The experiments were conducted without altering the pH of the dye solutions, which varied from 5.10 – 6.13. The data obtained represent the adsorption isotherm and were used to investigate the relationship between the dye concentration in aqueous phase and the adsorbent surface. The adsorption isotherm data were fitted to Langmuir, Freundlich, and Sips

isotherm models, as described in Chapter 3, to determine the most suitable model for describing the adsorption behaviour of MO and MB on PNTS2-600-15.

6.2.8.1 Langmuir isotherm model

The nonlinear form of the Langmuir isotherm model, as expressed in Equation 3.4 (Chapter 3), was used to fit the adsorption equilibrium data. Figure 6.13 shows the nonlinear fits of the Langmuir model to the adsorption isotherms obtained for MO and MB on AC PNTS2-600-15. The model parameters and error analysis, such as determination coefficients (R^2), sum of squared errors (SSE) and root mean square errors (RMSE), are given in Table 6.3. According to Ayawei *et al.* [18], the evaluation of the isotherm model fit should not rely solely on the R^2 values, but also consider other error analysis criteria. The low R^2 values, and high SSE and RMSE values, as shown in Table 6.3, suggest that the Langmuir model is not a suitable fit for the adsorption isotherms of either MO or MB.

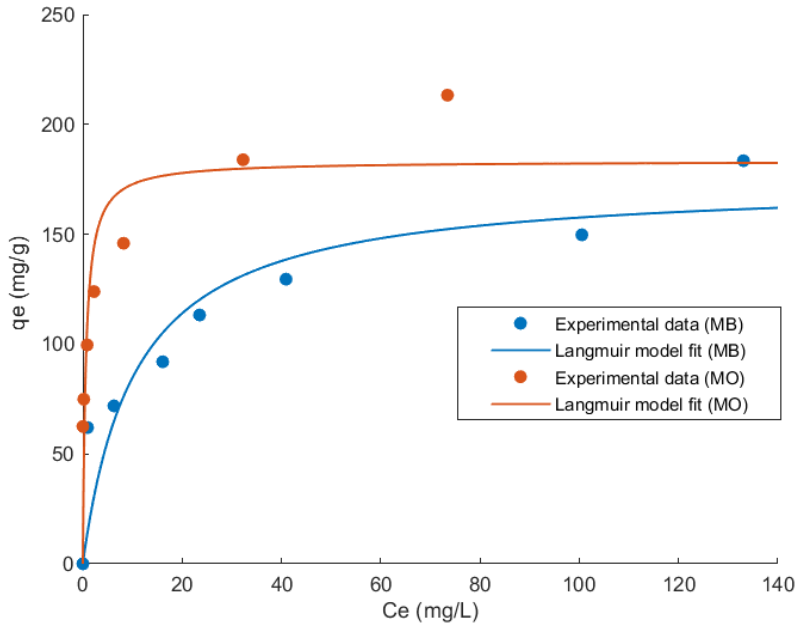

Figure 6.13. Nonlinear fits of Langmuir isotherm model to isotherms obtained for adsorption of methyl orange and methylene blue on activated carbon PNTS2-600-15.

As discussed in Chapter 3, the calculation of the separation factor is necessary to characterise the features of the Langmuir isotherm model when the experimental equilibrium data fit well with the model. However, since the Langmuir model is not a good fit for the adsorption equilibrium data of MO and MB, the separation factor was not considered.

Table 6.3. Isotherm parameters for methyl orange and methylene blue adsorption by activated carbon PNTS2-600-15, derived from Langmuir, Freundlich and Sips non-linear isotherm models.

Parameters	Unit	MO	MB
1. Langmuir isotherm model			
Q_m	mg/g	183.3	174.2
K_L	L/mg	1.639	0.0946
R^2	—	0.801	0.861
SSE	—	6622	3173
RMSE	—	33.2	23.0
2. Freundlich isotherm model			
K_F	$(mg/g)(L/mg)^{1/n}$	106.4	49.45
1/n	—	0.159	0.255
R^2	—	0.993	0.976
SSE	—	218.8	545.8
RMSE	—	6.0	9.5
3. Sips isotherm model			
Q_S	mg/g	4584	1769
K_S	$(L/mg)^{n_s}$	0.024	0.028
n_s	—	0.163	0.273
R^2	—	0.993	0.975
SSE	—	230.8	577.1
RMSE	—	6.2	10.7

6.2.8.2 Freundlich isotherm model

The nonlinear form of the Freundlich isotherm model, as expressed in Equation 3.11 (Chapter 3), was used to fit the adsorption equilibrium data. Figure 6.14 shows the nonlinear fits of Freundlich model to the adsorption isotherm of MO and MB. As shown in Table 6.3, the higher R^2 values and lower SSE and RMSE, relative to the values obtained for Langmuir model, suggest that the Freundlich model is more suitable to describe the adsorption equilibrium data of MO and MB on PNTS2-600-15. The suitability of the Freundlich model indicates that the adsorption was a multilayer process onto a heterogeneous surface, with an exponential distribution of energies [19]. The Freundlich parameter, 1/n (dimensionless), which reflects the adsorption intensity or surface heterogeneity, was calculated to be 0.159 and 0.255 for MO and MB, respectively. The 1/n values obtained, being between 0 and 1, indicate favourable adsorption of MO and MB [4, 11, 20]. The lower value of 1/n for MO implies a higher adsorption driving force between the MO molecules and the adsorbent surface [21].

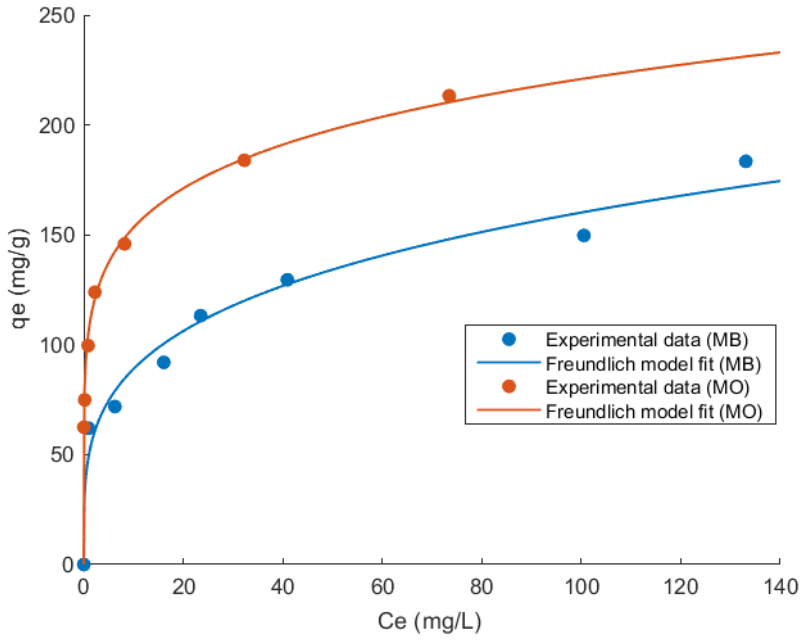

Figure 6.14. Nonlinear fits of Freundlich isotherm model to isotherms obtained for adsorption of methyl orange and methylene blue on activated carbon PNTS2-600-15.

6.2.7.3 Sips isotherm model

The nonlinear form of the Sips isotherm model, as expressed in Equation 3.12 (Chapter 3), was used to fit the adsorption equilibrium data. Figure 6.15 shows the nonlinear fits of the Sips model to the adsorption isotherms of MO and MB on PNTS2-600-15. As shown in Table 6.3, the R^2 values for the Sips model are higher than those for the Langmuir model, and comparable to those for the Freundlich model. Moreover, error analysis reveals that the SSE and RMSE values for the Sips model are only slightly different from those for the Freundlich model. Based on these results, both the Freundlich and Sips models can be said suitable to describe the adsorption isotherms obtained for MO and MB. Overall, the Freundlich model has a better fit to the adsorption data than the Sips model. According to Varank *et al.* [4], the Sips isotherm exponent, n_S, determines the degree of deviation from the Langmuir model, which is obtained when n_S = 1. The values of n_S (Table 6.3) obtained from fitting the experimental data to the Sips model are much lower than 1, indicating that the Freundlich model is more suitable to describe the experimental data.

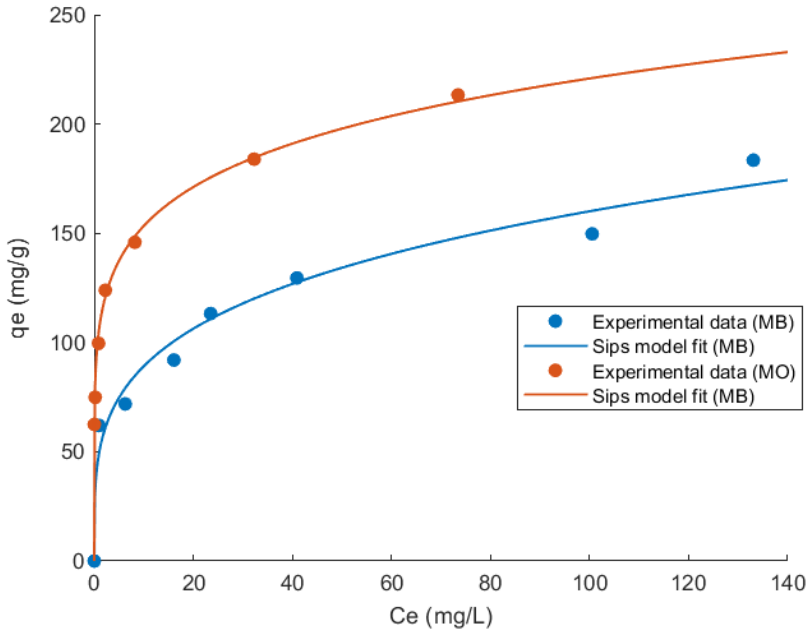

Figure 6.15. Nonlinear fits of Sips isotherm model to isotherms obtained for adsorption of methyl orange and methylene blue on activated carbon PNTS2-600-15.

6.2.8 Desorption studies

Desorption studies are, to some extent, essential for understanding the adsorption mechanism, and critical to predict the regeneration potential of adsorbents, which can enhance the economic feasibility of the treatment process, by enabling multiple cycles of adsorbent reuse [22]. To further investigate the effect of pH levels on the adsorption of MO and MB onto PNTS2-600-15, the desorption experiments of MO and MB were carried out using deionised (DI) water at pH 8 and pH 2 as desorbing agents.

According to the measurements reported earlier, the PZC of PNTS2-600-15 was approximately 6. Therefore, at pH values higher than the PZC, the surface of PNTS2-600-15 was expected to be negatively charged to facilitate the desorption of MO anions. Conversely, at pH values lower than the PZC, the surface of PNTS2-600-15 was expected to be positively charged to favour the desorption of MB cations. However, the results did not support this hypothesis, as no significant desorption was observed under these conditions (see Figure A5 in Appendix A for the visual images of this experiment), indicating that the adsorption was not strongly dependent on electrostatic attractions.

The effects of applying pure solvent (water) and/or heat as driving forces for desorption, to facilitate the release and removal of adsorbed material from the surface were also investigated. The percentages of MO and MB desorbed using DI water at ambient temperature and 80 ± 2 °C in a single wash are shown in Figure 6.16. The results indicate that the desorption percentages were minimal for both dyes at ambient temperature (note: after 1 h of agitation, the dye concentration in the solution reached a saturation point, and some of the desorbed dye molecules started to re-attach to the adsorbent surface, therefore, agitation time was limited to 20 min - see Figure A6 in Appendix A). However, when the temperature of the solvent was increased to 80 °C, a significant increase in the desorption percentages was noted for both dyes. This

suggests that the adsorption process was exothermic in nature and likely dominated by physical interactions.

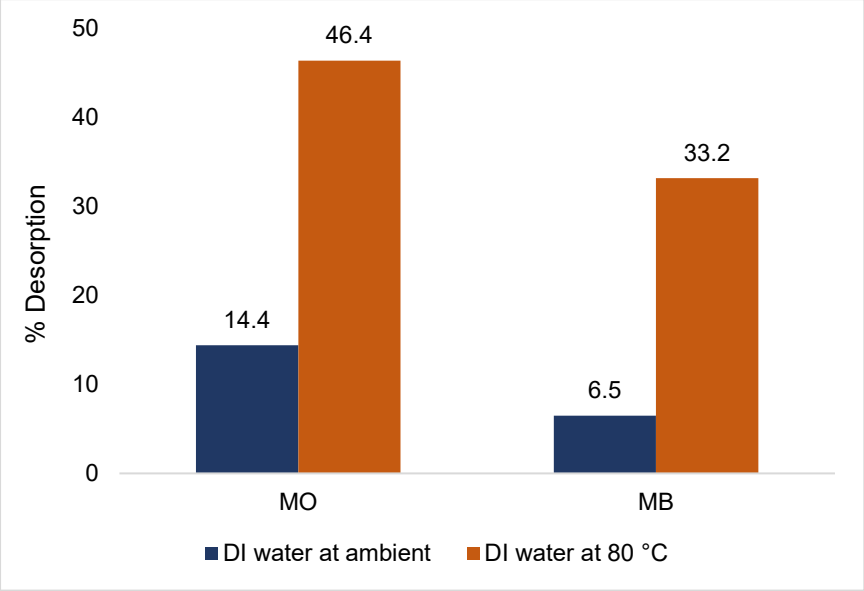

Figure 6.16. Percentage of methyl orange and methylene blue desorbed using deionised water at ambient temperature and 80 °C in a single wash (PNTS2-600-15).

Figure 6.17 shows the trend of MO and MB removal efficiencies of PNTS2-600-15 as a function of the desorption–adsorption cycle using DI water at 80 °C in a single wash. The adsorption capacity of the regenerated adsorbent, using hot water as a regenerant for both dyes, declined progressively with each cycle, as a fraction of dye molecules remained bound to the adsorbent surface irreversibly and reduced the available sites for adsorption. This suggests that there is a chemical interaction between a fraction of molecules and the surface, or that the temperature and/or contact time are not sufficient to achieve complete desorption, and the effect of this accumulates over time.

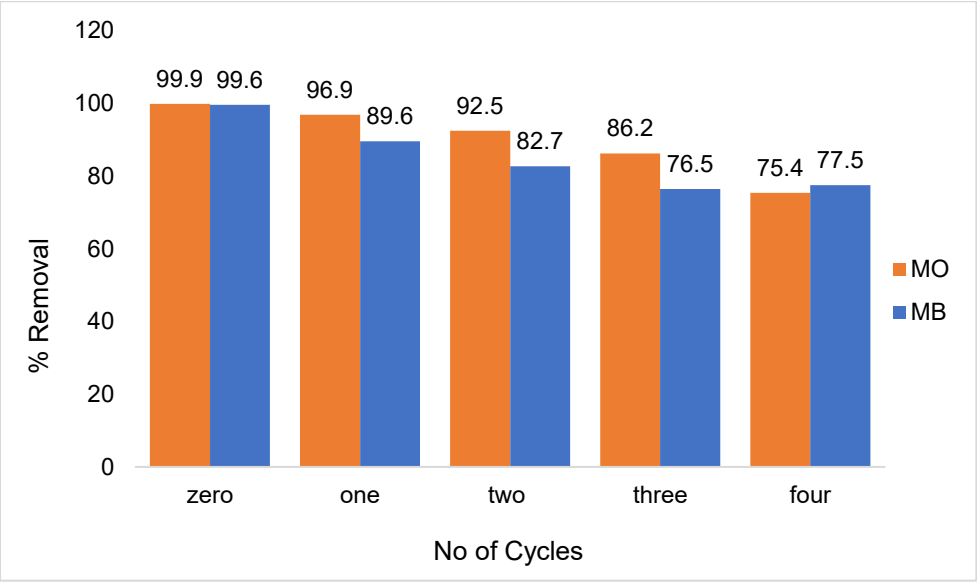

Figure 6.17. Variation of methyl orange and methylene blue removal efficiencies by activated carbon PNTS2-600-15, as a function of the adsorption–desorption cycle using deionised water at 80 °C in a single wash.

As a result of the desorption experiment at 80 °C, in a single wash, the temperature of the DI water was increased to 90 ± 2 °C and was used to rinse the spent adsorbent multiple times until further negligible desorption was observed. Figure 6.18 illustrates the variation of MO and MB removal efficiencies by PNTS2-600-15 in successive cycles, using DI water at 90 °C for multiple washes. As shown by the results, increasing the temperature and number of washes enhanced the desorption process. The adsorbent exhibited a high and stable removal efficiency, of over 99%, for MO dye throughout the repeated adsorption–desorption cycles. However, its removal efficiency for MB dye declined to 88% in the sixth cycle. This could be attributed to more MB dye molecules chemically bound with the adsorbent surface and remaining irreversible in the desorption process.

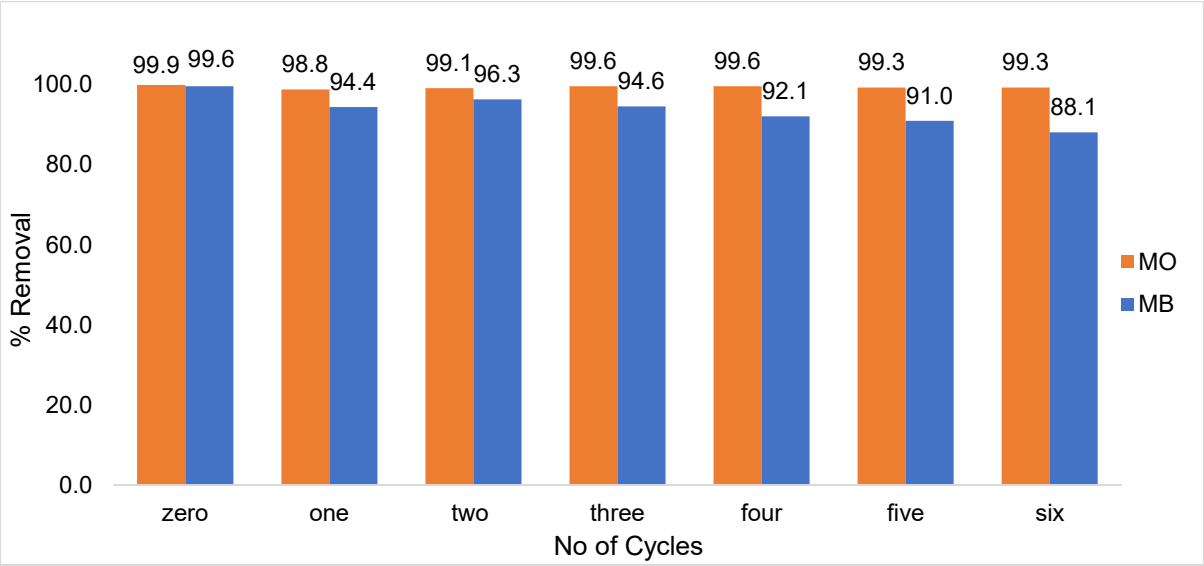

Figure 6.18. Variation of methyl orange and methylene blue removal efficiencies by activated carbon PNTS2-600-15, as a function of the adsorption–desorption cycle using deionised water at 90 °C in multiple washes.

6.2.9 Adsorption mechanism

Typically, both anionic and cationic dyes may undergo various modes of adsorption mechanism, such as electrostatic interaction, hydrogen bonding, π–π stacking, n–π interaction (which entails the transfer of lone pair electrons from oxygen, nitrogen, or sulphur atoms to π orbitals of C═O, C═N or aromatic groups) and pore filling [8, 23-25].

The effect of solution pH on the adsorption behaviour of MO and MB on PTNS2-600-15 was investigated and discussed in Section 6.2.5. The results suggested that the adsorption process was not strongly dependent on electrostatic attractions. As already discussed under desorption studies (Section 6.2.8), the desorption of both dyes was negligible in basic and acidic solutions, also, implying that electrostatic interactions did not play a significant role in the adsorption of MO and MB on PNTS2-600-15.

The surface hydrogens of the hydroxyl groups (H-donor) on the AC samples may form hydrogen bonds with the heteroatoms (such as oxygen, nitrogen, and halogens; H-acceptor) within the dye structure, which is a type of dipole-dipole H-bonding, or

with aromatic rings in the dye structure (this is known as Yoshida H–bonding interaction) [23, 24]. The surface chemistry of the synthesised ACs was examined by FTIR and XPS, which both indicated the existence of various oxygen complexes. XPS detected the presence of ester functionalities, COOR, on the surface of PNTS2-600-15, where R could be H or alkyl groups. If R = H, the hydrogen in –OH of the carboxyl group could participate in hydrogen bonding with the dyes, but FTIR analysis showed that –OH groups were absent or infinitesimal in PNTS2-600-15, after activation, which could be attributed to the dehydrating effects of $ZnCl_2$ and increased activation temperatures. Therefore, the role of hydrogen bonding interaction in the adsorption of MO and MB on PNTS2-600-15 was assumed to be minimal or negligible.

The potential n–π interaction was also explored. Both MO (polycyclic aromatic compound) and MB (heterocyclic aromatic compound) are aromatic in nature, which may enable n–π electron donor-acceptor (EDA) interactions. The C–O groups on PNTS2-600-15, as revealed by both FTIR and XPS analyses (Section 5.2.7), could serve as electron donors and the aromatic rings of the dyes as electron acceptors [26, 27].

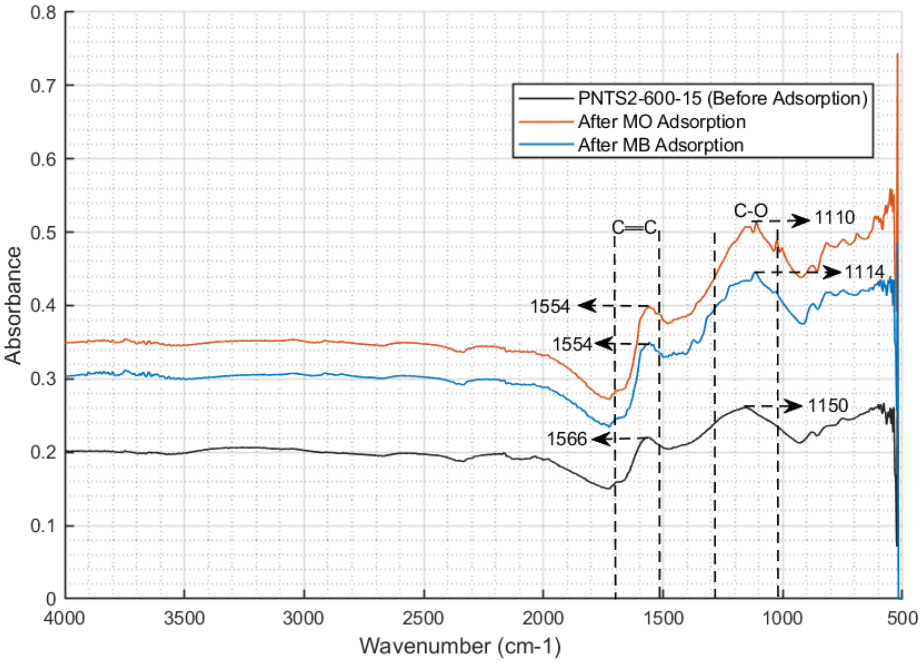

Figure 6.19. FTIR spectra of activated carbon PNTS2-600-15, before and after methyl orange and methylene blue adsorption.

The FTIR analysis of PNTS2-600-15 post-adsorption of each dye revealed changes and shifts in the peaks corresponding to the C–O groups on the adsorbent (Figure 6.19). The peak at 1150 cm^{-1}, attributed to the C–O groups on PNTS2-600-15, shifted to 1110 cm^{-1} and 1114 cm^{-1} after adsorption of MO and MB, respectively. These shifts indicate that some dye molecules were adsorbed at the sites of the C–O groups on the adsorbent, as suggested by Al-Ghouti *et al*. [28]. Therefore, it can be inferred that there was significant n–π electron donor-acceptor (EDA) interaction between the adsorbent and the dye molecules.

The kinetic studies, reported in Section 6.2.7, indicated that pore diffusion was involved in the adsorption of both MO and MB dyes on PNTS2-600-15. As the dye molecules diffuse into the adsorbent particles, due to the heterogeneous nature of PNTS2-600-15, as revealed by the characterisation analysis in Section 5.2.7 (Chapter 5), molecular sieving effects could facilitate pore filling by selectively adsorbing dye molecules that fit the pore size of the adsorbent.

Table 6.4. Textural characteristics of activated carbon PNTS2-600-15, methyl orange-loaded PNTS2-600-15, and methylene blue-loaded PNTS2-600-15.

	S_{BET} (m^2/g)	S_{Micro} (m^2/g)	S_{Meso} (m^2/g)	V_{Micro} (cm^3/g)	V_{Meso} (cm^3/g)	*TPV* (cm^3/g)	*Avg. pore size* (*nm*)
PNTS2-600-15	1711	399	1312	0.200	0.872	1.072	3
MO-loaded	1326	583	743	0.300	0.427	0.727	2
MB-loaded	1292	615	677	0.317	0.388	0.705	3

Pore filling was investigated by performing textural analysis on MO-and MB- loaded PNTS2-600-15, as shown in Table 6.4. The results revealed that the adsorption of the dye molecules affected the surface properties and the pore structure of the adsorbent. The surface area and the total pore volume decreased after the adsorption process, while the micropore volume increased. This can be attributed to the formation of dye

layers on the walls of the larger pores, reducing the external surface area and the mesopore volume. This process effectively narrows the pore size, leading to an increase in the micropore volume.

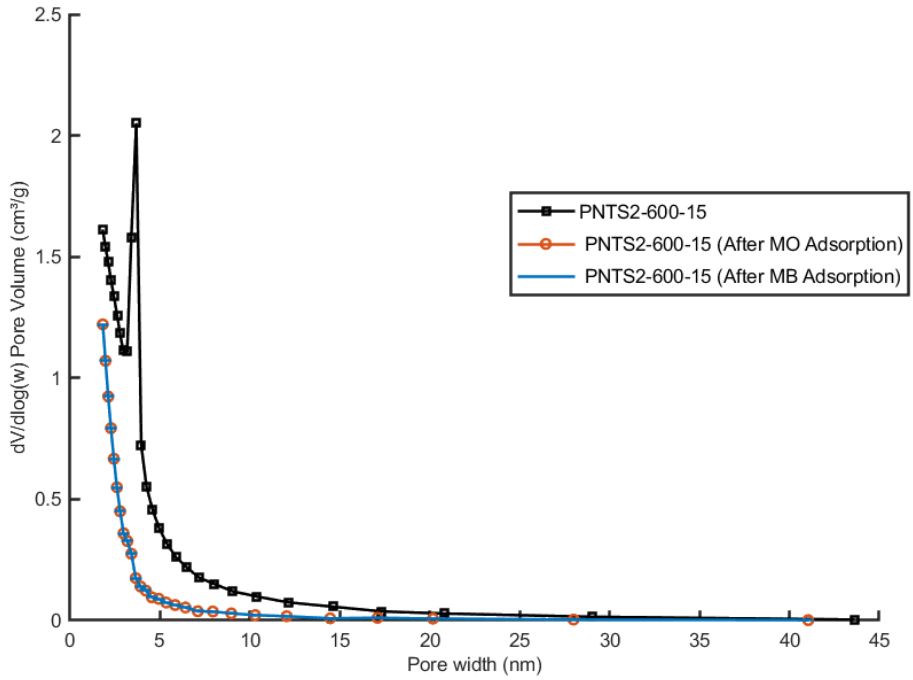

Figure 6.20. Pore size distribution of activated carbon PNTS2-600-15: before and after adsorption of methyl orange and methylene blue.

Pore size distribution curves, as shown in Figure 6.20, were also used to visualise this phenomenon; the curves of both MO- and MB-loaded samples shifted to the left, indicating a reduction in pore widths. The multilayer formation of the dye molecules is consistent with the Freundlich model, which fits the equilibrium data. Based on this analysis, it can be concluded that the adsorption process was influenced by a pore-filling mechanism, which is in agreement with previous studies [29, 30].

The π–π dispersion interaction between the dye molecules and the AC synthesised in this study was also investigated. The FTIR and XPS analyses (Section 5.2.7) revealed that all the AC materials synthesised in this work exhibited aromatic C=C bonds,

which indicates the presence of π electrons in the AC aromatic rings [22]. Among the ACs characterised, quantitative XPS analysis revealed that PNTS2-600-15 had the highest percentage of carbon-attached functional groups (approximately 78%), with aromatic C=C bonds constituting approximately 43% of these. This indicated a higher π electron density in the basal plane of PNTS2-600-15.

However, consideration must also be given to the electron-withdrawing groups present on the surface of the carbon material. Previous studies reported that an increase in the concentration of oxygenated groups, which are electron-withdrawing, reduces the basal plane electron density of the synthesised aromatic carbon [27, 31]. The XPS quantitative analysis showed that PNTS2-600-15 had roughly 7% of oxygenated groups. This analysis suggested that PNTS2-600-15 had a high π-electron density in its graphene layer that could interact with the aromatic rings of the dye molecules.

The FTIR analysis of PNTS2-600-15 after adsorption of both dyes revealed changes and shifts in the peaks corresponding to the aromatic C=C bonds on the adsorbent (Figure 6.19). The peak at 1566 cm^{-1}, attributed to the skeletal vibration of aromatic C=C bonds on PNTS2-600-15 shifted to 1554 cm^{-1} after adsorption of MO and MB. This shift indicates that some dye molecules interacted at the sites of the C=C bonds of the adsorbent, as suggested by Al-Ghouti *et al*. [28] and Tran *et al*. [32]. Therefore, it can be inferred that there were significant π–π dispersion interactions between the adsorbent and the dye molecules.

The adsorption of organic and aromatic compounds on carbon materials is governed by a complex interplay of electrostatic and dispersive interactions [27]. Previous studies have suggested that the adsorption of aromatic compounds involves the formation of donor-acceptor complexes between the carbonyl groups on the carbon surface and the organic molecules [33] or the π–π interactions between the aromatic rings [34]. Tran, et al. [23] reported that the adsorption of methylene green 5 on AC

was mainly driven by π–π interactions and pore filling. In this study, we propose that the adsorption mechanisms of MO and MB on the synthesised AC are similar and that they involve π–π interactions, n–π electron donor-acceptor (EDA) interactions and pore filling, based on the evidence from pH analysis, FTIR and XPS analyses, textural analysis, and desorption studies. Other mechanisms, such as electrostatic interactions and hydrogen bonding, may also play minor roles.

Tables 6.5 and 6.6 display a comparison of the maximum adsorption capacity of PNTS2-600-15 for MO and MB against other AC materials in the literature. According to the Sips model, the peanut shell-based AC material developed in this study exhibited outstanding adsorption performance for both dyes. The outstanding adsorption performance could be attributed to the following factors.

Surface Heterogeneity: The adsorption of both dyes (MO and MB) is well described by the Freundlich isotherm which assumes a heterogeneous surface.

Table 6.5. Comparison of adsorption capacities of activated carbons derived from various precursors for the removal of methyl orange.

			Experimental condition				
Adsorbent	Q_{max} (mg/g)	Method of Q_{max} determination	adsorbent dose (g/L)	pH	temp. (°C)	time (h)	Ref.
Methyl orange							
AC from popcorn	969	Experiment	0.25	-	25	12	[35]
AC from waste tire rubber	588	Langmuir	0.5	3.6	23	24	[36]
AC from coconut shell	3	Experiment	10	-	25	12 min	[37]
Mesoporous carbon from Sucrose	294.1	Langmuir	2.0	-	25	1	[38]
AC from boiler residue	161.8	Langmuir	1.0	5.0	25	50 min	[39]
AC/$NiFe_2O_4$	182.8	Langmuir	3.0	3.0	30	30 min	[40]
AC from date pits	434.0	Langmuir	4.0	3.5	25	4	[41]
AC from waste orange/lemon peels	33	Langmuir	4.0	2.0	25	1	[42]
Commercial AC	113.6	Langmuir	0.75	2.0	25	30 min	[43]
AC from aloe vera	196.1	Langmuir	1.0	3.0	25	1	[44]
PNTS2-600-15	4584	Sips	2.0	natural	25	3	This work

Table 6.6. Comparison of adsorption capacities of activated carbons derived from various precursors for the removal of methylene blue.

Adsorbent	Q_{max} (mg/g)	Method of Q_{max} determination	Experimental condition				Ref.
			adsorbent dose (g/L)	pH	temp. (°C)	time (h)	
Methylene blue							
AC from waste orange/lemon peels	38	Langmuir	4.0	6.0	25	1	[42]
AC from date pits	455	Langmuir	4.0	9.0	25	4	[41]
AC from orange peels	108.9	Langmuir	1.0	7.1	30	8	[45]
AC from coal	28.1	Langmuir	-	-	25	1	[46]
AC from Pistachio-nut shell	155.6	Experiment	1.0	8.0	20	80 min	[47]
AC from peanut shells	555.6	Langmuir	-	8.0	30	20	[48]
AC from waste tire rubber	833	Langmuir	0.5	10.0	23	24	[36]
AC from acacia wood	338.3	Langmuir	1.0	natural	30	24	[49]
AC from coffee husk	418.8	Langmuir	1.0	7.0	30	16	[50]
AC from sunflower seed husks	240	Langmuir	2.0	8.0	30	260 min	[51]
AC from coconut husk	418.2	Langmuir	1.0	-	30	-	[52]
PNTS2-600-15	1769	Sips	2.0	natural	25	3	This work

Comparative analysis, as shown in Tables 6.5 and 6.6, indicates that most of the adsorbents have been characterised using the Langmuir isotherm model, predicated on the assumption of a homogeneous surface. The heterogeneity associated with PNTS2-600-15 may confer an enhanced adsorption capacity, attributable to the facilitation of increased dye molecule adsorption at the available active sites.

Multilayer Adsorption: While the Langmuir isotherm assumes monolayer adsorption, the Freundlich isotherm can describe multilayer adsorption. This means that PNTS2-600-15 following the Freundlich isotherm can accumulate more adsorbate layers, leading to higher adsorption capacity.

Flexibility Over a Range of Concentrations: The Sips isotherm also describes the adsorption of MO and MB on PNTS2-600-15. The Sips isotherm is a hybrid model that combines the features of the Langmuir and Freundlich isotherms and is particularly effective at high adsorbate concentrations. It overcomes the limitations of the

Freundlich isotherm at higher concentrations, which can result in a better performance of the adsorbent.

Adsorbate-Adsorbent Interactions: The Sips isotherm also accounts for the interactions between adsorbate molecules and the adsorbent surface. These interactions can enhance the adsorption capacity, especially when specific interactions such as chemical bonding or strong physical forces are at play.

The combination of surface heterogeneity, the ability to support multilayer adsorption, effectiveness over a wide range of concentrations, specific adsorbate-adsorbent interactions, and broad energy distribution of adsorption sites all contribute to the superior performance of PNTS2-600-15 described by both Freundlich and Sips isotherms compared to the ones described solely by the Langmuir isotherm in the comparators (Tables 6.5 and 6.6).

6.3 Summary

The adsorption performance of the PNTS-based AC materials prepared in this study for the removal of MO and MB dyes from the aqueous phase was evaluated. Among the different PNTS-based AC materials, PNTS2-600-15 and PNTS2-600-120 exhibited the highest adsorption capacities and kinetics for both dyes. However, PNTS2-600-15 was selected as the optimal AC material due to its shorter activation time, compared to PNTS2-600-120.

The effects of various parameters, such as contact time, solution pH, and initial dye concentration, on the adsorption performance of PNTS2-600-15 for MO and MB dyes were investigated. The experimental data were analysed using different kinetic and isotherm models to elucidate the adsorption mechanism, and capacity of the carbon material. The results indicate that a pseudo-second-order kinetic model and the Freundlich and Sips isotherm models provided the best fit for the adsorption data of both dyes. The Sips model estimated the maximum adsorption capacities of PNTS2-

600-15 for MO and MB to be 4584 mg/g and 1769 mg/g, respectively. These show outstanding capacities in comparison with various AC materials reported in the literature.

To further elucidate the mechanisms involved in the adsorption process, several experimental techniques were employed, such as post-adsorption characterization of the textural and surface properties of the carbon material, and desorption studies of the adsorbed dyes. The adsorption mechanism was mainly attributed to π–π interactions, n–π electron donor-acceptor (EDA) interactions, and pore filling. The AC material exhibited good reusability and stability, achieving over 90% dye removal, after five cycles of regeneration.

References

[1] Malik, R., Ramteke, D. and Wate, S. (2006). Physico-chemical and surface characterization of adsorbent prepared from groundnut shell by ZnCl 2 activation and its ability to adsorb colour. Indian J. Chem. Technol. 13. http://nopr.niscpr.res.in/handle/123456789/7048

[2] Özacar, M. and Şengil, İ. A. (2005). A kinetic study of metal complex dye sorption onto pine sawdust. Process Biochem. 40**:** 565-572. https://doi.org/10.1016/j.procbio.2004.01.032

[3] El Maguana, Y., Elhadiri, N., Bouchdoug, M., Benchanaa, M. and Jaouad, A. (2019). Activated carbon from prickly pear seed cake: optimization of preparation conditions using experimental design and its application in dye removal. Int. J. Chem. Eng. 2019. https://doi.org/10.1155/2019/8621951

[4] Varank, G., Demir, A., Yetilmezsoy, K., Top, S., Sekman, E. and Bilgili, M. S. (2012). Removal of 4-nitrophenol from aqueous solution by natural low-cost adsorbents.

[5] Knaebel, K. S. (1990). A "How to" guide for adsorber design. Adsorption Research, Inc., Dublin, Ohio

[6] Kaur, S., Rani, S. and Mahajan, R. K. (2013). Adsorption kinetics for the removal of hazardous dye congo red by biowaste materials as adsorbents. J. Chem. 2013. https://doi.org/10.1155/2013/628582

[7] Qiu, H., Lv, L., Pan, B.-C., Zhang, Q.-J., Zhang, W.-M. and Zhang, Q.-X. (2009). Critical review in adsorption kinetic models. Journal of Zhejiang University-SCIENCE A 10**:** 716-724. https://doi.org/10.1631/jzus.A0820524

[8] Tran, H. N., You, S.-J., Hosseini-Bandegharaei, A. and Chao, H.-P. (2017). Mistakes and inconsistencies regarding adsorption of contaminants from aqueous solutions: a critical review. Water Res. 120**:** 88-116. https://doi.org/10.1016/j.watres.2017.04.014

[9] Lima, É. C., Adebayo, M. A. and Machado, F. M. (2015). Kinetic and equilibrium models of adsorption. Carbon nanomaterials as adsorbents for environmental and biological applications**:** 33-69. https://doi.org/10.1007/978-3-319-18875-1_3

[10] Lima, E. C., Cestari, A. R. and Adebayo, M. A. (2016). Comments on the paper: a critical review of the applicability of Avrami fractional kinetic equation in adsorption-based water treatment studies. Desalin. Water Treat. 57**:** 19566-19571. https://doi.org/10.1080/19443994.2015.1095129

[11] El Maguana, Y., Elhadiri, N., Benchanaa, M. and Chikri, R. (2020). Activated Carbon for Dyes Removal: Modeling and Understanding the Adsorption Process. J. Chem. 2020: 1-9. https://doi.org/10.1155/2020/2096834
[12] Foo, K. and Hameed, B. (2012). Mesoporous activated carbon from wood sawdust by K2CO3 activation using microwave heating. Bioresour. Technol. 111: 425-432. https://doi.org/10.1016/j.biortech.2012.01.141
[13] Gürses, A., Doğar, Ç., Yalçın, M., Açıkyıldız, M., Bayrak, R. and Karaca, S. (2006). The adsorption kinetics of the cationic dye, methylene blue, onto clay. J. Hazard. Mater. 131: 217-228. https://doi.org/10.1016/j.jhazmat.2005.09.036
[14] Wu, F.-C., Tseng, R.-L. and Juang, R.-S. (2009). Initial behavior of intraparticle diffusion model used in the description of adsorption kinetics. Chem. Eng. J. 153: 1-8. https://doi.org/10.1016/j.cej.2009.04.042
[15] Ofomaja, A. E., Naidoo, E. B. and Pholosi, A. (2020). Intraparticle diffusion of Cr (VI) through biomass and magnetite coated biomass: A comparative kinetic and diffusion study. S. Afr. J. Chem. Eng. 32: 39-55. https://doi.org/10.1016/j.sajce.2020.01.005
[16] El Maguana, Y., Elhadiri, N., Benchanaa, M. and Chikri, R. (2020). Adsorption thermodynamic and kinetic studies of methyl orange onto sugar scum powder as a low-cost inorganic adsorbent. J. Chem. 2020: 1-10. https://doi.org/10.1155/2020/9165874
[17] Sun, Q. and Yang, L. (2003). The adsorption of basic dyes from aqueous solution on modified peat–resin particle. Water Res. 37: 1535-1544. https://doi.org/10.1016/S0043-1354(02)00520-1
[18] Ayawei, N., Ebelegi, A. N. and Wankasi, D. (2017). Modelling and interpretation of adsorption isotherms. J. Chem. 2017. https://doi.org/10.1155/2017/3039817
[19] Levan, M. D. and Vermeulen, T. (1981). Binary Langmuir and Freundlich isotherms for ideal adsorbed solutions. The Journal of Physical Chemistry 85: 3247-3250
[20] Subbaiah, M. V. and Kim, D.-S. (2016). Adsorption of methyl orange from aqueous solution by aminated pumpkin seed powder: Kinetics, isotherms, and thermodynamic studies. Ecotoxicology and environmental safety 128: 109-117. https://doi.org/10.1016/j.ecoenv.2016.02.016
[21] Tan, I., Ahmad, A. and Hameed, B. (2009). Adsorption isotherms, kinetics, thermodynamics and desorption studies of 2, 4, 6-trichlorophenol on oil palm empty fruit bunch-based activated carbon. J. Hazard. Mater. 164: 473-482. https://doi.org/10.1016/j.jhazmat.2008.08.025
[22] Tran, H. N., You, S.-J. and Chao, H.-P. (2017). Insight into adsorption mechanism of cationic dye onto agricultural residues-derived hydrochars: negligible role of π-π interaction. Korean J. Chem. Eng. 34: 1708-1720. https://doi.org/10.1007/s11814-017-0056-7
[23] Tran, H. N., You, S.-J. and Chao, H.-P. (2017). Fast and efficient adsorption of methylene green 5 on activated carbon prepared from new chemical activation method. J. Environ. Manage. 188: 322-336. https://doi.org/10.1016/j.jenvman.2016.12.003
[24] Iwuozor, K. O., Ighalo, J. O., Emenike, E. C., Ogunfowora, L. A. and Igwegbe, C. A. (2021). Adsorption of methyl orange: A review on adsorbent performance. Curr. Res. Green Sustain. Chem. 4: 100179. https://doi.org/10.1016/j.crgsc.2021.100179
[25] Das, A. and Panwaria, P. (2022). Understanding the n→ π* non-covalent interaction using different experimental and theoretical approaches. Phys. Chem. Chem Phys. https://doi.org/10.1039/D2CP02070J
[26] Mattson, J. A., Mark Jr, H. B., Malbin, M. D., Weber Jr, W. J. and Crittenden, J. C. (1969). Surface chemistry of active carbon: specific adsorption of phenols. Journal of Colloid and Interface Science 31: 116-130
[27] Rivera-Utrilla, J. and Sánchez-Polo, M. (2002). The role of dispersive and electrostatic interactions in the aqueous phase adsorption of naphthalenesulphonic acids on ozone-treated activated carbons. Carbon 40: 2685-2691. https://doi.org/10.1016/S0008-6223(02)00182-3

[28] Al-Ghouti, M., Khraisheh, M., Allen, S. and Ahmad, M. (2003). The removal of dyes from textile wastewater: a study of the physical characteristics and adsorption mechanisms of diatomaceous earth. J. Environ. Manage. 69**:** 229-238. https://doi.org/10.1016/j.jenvman.2003.09.005
[29] Juang, L.-C., Wang, C.-C. and Lee, C.-K. (2006). Adsorption of basic dyes onto MCM-41. Chemosphere 64**:** 1920-1928. https://doi.org/10.1016/j.chemosphere.2006.01.024
[30] Lee, C.-K., Liu, S.-S., Juang, L.-C., Wang, C.-C., Lin, K.-S. and Lyu, M.-D. (2007). Application of MCM-41 for dyes removal from wastewater. J. Hazard. Mater. 147**:** 997-1005. https://doi.org/10.1016/j.jhazmat.2007.01.130
[31] Huff, M. D. and Lee, J. W. (2016). Biochar-surface oxygenation with hydrogen peroxide. J. Environ. Manage. 165**:** 17-21. https://doi.org/10.1016/j.jenvman.2015.08.046
[32] Tran, H. N., Wang, Y.-F., You, S.-J. and Chao, H.-P. (2017). Insights into the mechanism of cationic dye adsorption on activated charcoal: The importance of π–π interactions. Process Saf. Environ. 107**:** 168-180. https://doi.org/10.1016/j.psep.2017.02.010
[33] Mattson, J. A., Mark Jr, H. B., Malbin, M. D., Weber Jr, W. J. and Crittenden, J. C. (1969). Surface chemistry of active carbon: specific adsorption of phenols. J. Colloid Interface Sci. 31**:** 116-130. https://doi.org/10.1016/0021-9797(69)90089-7
[34] Coughlin, R. W. and Ezra, F. S. (1968). Role of surface acidity in the adsorption of organic pollutants on the surface of carbon. Environ. Sci. Technol. 2**:** 291-297. https://doi.org/10.1021/es60016a002
[35] Yu, Y., Qiao, N., Wang, D., Zhu, Q., Fu, F., Cao, R., Wang, R., Liu, W. and Xu, B. (2019). Fluffy honeycomb-like activated carbon from popcorn with high surface area and well-developed porosity for ultra-high efficiency adsorption of organic dyes. Bioresour Technol 285**:** 121340. https://doi.org/10.1016/j.biortech.2019.121340
[36] Islam, M. T., Saenz-Arana, R., Hernandez, C., Guinto, T., Ahsan, M. A., Bragg, D. T., Wang, H., Alvarado-Tenorio, B. and Noveron, J. C. (2018). Conversion of waste tire rubber into a high-capacity adsorbent for the removal of methylene blue, methyl orange, and tetracycline from water. J. Environ. Chem. Eng. 6**:** 3070-3082. https://doi.org/10.1016/j.jece.2018.04.058
[37] Islam, M. S., Ang, B. C., Gharehkhani, S. and Afifi, A. B. M. (2016). Adsorption capability of activated carbon synthesized from coconut shell. Carbon Lett. 20**:** 1-9. http://dx.doi.org/10.5714/CL.2016.20.001
[38] Mohammadi, N., Khani, H., Gupta, V. K., Amereh, E. and Agarwal, S. (2011). Adsorption process of methyl orange dye onto mesoporous carbon material–kinetic and thermodynamic studies. Journal Colloid Interf Sci 362**:** 457-462. https://doi.org/10.1016/j.jcis.2011.06.067
[39] Martini, B. K., Daniel, T. G., Corazza, M. Z. and De Carvalho, A. E. (2018). Methyl orange and tartrazine yellow adsorption on activated carbon prepared from boiler residue: Kinetics, isotherms, thermodynamics studies and material characterization. Journal of Environmental Chemical Engineering 6**:** 6669-6679
[40] Jiang, T., Liang, Y.-D., He, Y.-J. and Wang, Q. (2015). Activated carbon/NiFe2O4 magnetic composite: a magnetic adsorbent for the adsorption of methyl orange. J Environ Chem Eng 3**:** 1740-1751. https://doi.org/10.1016/j.jece.2015.06.020
[41] Mahmoudi, K., Hosni, K., Hamdi, N. and Srasra, E. (2015). Kinetics and equilibrium studies on removal of methylene blue and methyl orange by adsorption onto activated carbon prepared from date pits-A comparative study. Korean J. Chem. Eng. 32**:** 274-283. https://doi.org/10.1007/s11814-014-0216-y
[42] Ramutshatsha-Makhwedzha, D., Mavhungu, A., Moropeng, M. L. and Mbaya, R. (2022). Activated carbon derived from waste orange and lemon peels for the adsorption of methyl orange and methylene blue dyes from wastewater. Heliyon 8. https://doi.org/10.1016/j.heliyon.2022.e09930
[43] Khattabi, E. H. E., Rachdi, Y., Bassam, R., Mourid, E., Naimi, Y., Alouani, M. E. and Belaaouad, S. (2021). Enhanced elimination of methyl orange and recycling of an eco-friendly adsorbent activated

carbon from aqueous solution. Russ. J. Phys. Chem. B 15**:** S149-S159. https://doi.org/10.1134/S1990793122020063
[44] Khaniabadi, Y. O., Heydari, R., Nourmoradi, H., Basiri, H. and Basiri, H. (2016). Low-cost sorbent for the removal of aniline and methyl orange from liquid-phase: aloe vera leaves wastes. Journal of the Taiwan institute of chemical engineers 68**:** 90-98
[45] Gunay Gurer, A., Aktas, K., Ozkaleli Akcetin, M., Erdem Unsar, A. and Asilturk, M. (2021). Adsorption isotherms, thermodynamics, and kinetic modeling of methylene blue onto novel carbonaceous adsorbent derived from bitter orange peels. Water, Air, & Soil Pollution 232**:** 1-17
[46] Shokry, H., Elkady, M. and Hamad, H. (2019). Nano activated carbon from industrial mine coal as adsorbents for removal of dye from simulated textile wastewater: Operational parameters and mechanism study. J. Mater. Res. Technol. 8**:** 4477-4488. https://doi.org/10.1016/j.jmrt.2019.07.061
[47] Bazrafshan, E., Mohammadi, L., Kord Mostafapour, F. and Zazouli, M. A. (2013). Adsorption of methylene blue from aqueous solutions onto low-cost ZnCl2 treated pistachio-nut shell ash. Wulfenia 20**:** 149-163
[48] Ahmad, M. A., Yusop, M. F. M., Zakaria, R., Karim, J., Yahaya, N. K. E., Yusoff, M. a. M., Hashim, N. H. F. and Abdullah, N. S. (2021). Adsorption of methylene blue from aqueous solution by peanut shell based activated carbon. Mater Today Proc 47**:** 1246-1251. https://doi.org/10.1016/j.matpr.2021.02.789
[49] Yusop, M. F. M., Ahmad, M. A., Rosli, N. A. and Abd Manaf, M. E. (2021). Adsorption of cationic methylene blue dye using microwave-assisted activated carbon derived from acacia wood: optimization and batch studies. Arab. J. Chem. 14**:** 103122. https://doi.org/10.1016/j.arabjc.2021.103122
[50] Tran, T. H., Le, A. H., Pham, T. H., Nguyen, D. T., Chang, S. W., Chung, W. J. and Nguyen, D. D. (2020). Adsorption isotherms and kinetic modeling of methylene blue dye onto a carbonaceous hydrochar adsorbent derived from coffee husk waste. Science of the Total Environment 725**:** 138325
[51] Baytar, O., Şahin, Ö. and Saka, C. (2018). Sequential application of microwave and conventional heating methods for preparation of activated carbon from biomass and its methylene blue adsorption. Applied Thermal Engineering 138**:** 542-551
[52] Foo, K. and Hameed, B. (2012). Coconut husk derived activated carbon via microwave induced activation: effects of activation agents, preparation parameters and adsorption performance. Chemical Engineering Journal 184**:** 57-65

Chapter 7: Conclusions and Future Work

7.1 Conclusions

This research aimed to synthesise a cost-effective and efficient activated carbon (AC) material from peanut shells (PNTS) for water remediation applications. Various techniques, such as Brunauer-Emmett-Teller (BET) analysis of nitrogen adsorption data, Fourier transform infrared spectroscopy (FTIR), X-ray photoelectron spectroscopy (XPS), scanning electron microscopy (SEM) nitrogen adsorption-desorption isotherms, and thermogravimetric analysis (TGA), were employed to characterise the physical and chemical properties of the PNTS precursor and the PNTS-derived AC materials. Moreover, design of experiments (DoE) was applied to investigate the main and interactive effects of activation variables (temperature, hold time, and impregnation ratio) on the final properties of the PNTS-derived AC, such as yield, surface area, micropore area, mesopore area and density. The performance of the PNTS-based AC material for the removal of ionic dyes (methyl orange, MO and methylene blue, MB) from water was also evaluated.

The findings of this research revealed that the PNTS-based AC materials developed in this study possessed high yield, surface area, and pore volume, and they displayed a heterogeneous and porous structure with a mixture of micropores and mesopores. The PNTS-based AC material exhibited high adsorption capacity and efficiency for the removal of ionic dyes from water, and it outperformed several ACs reported in the literature, including previously reported work on PNTS. The implications of this research are that the PNTS-based AC material could be a viable alternative to commercial-grade adsorbents for water remediation applications, as it has comparable or superior properties and performance, and that the DoE approach could offer a valuable tool for optimising the activation variables and customising the final properties of the AC materials for specific applications. The PNTS-based AC material

could also contribute to environmental protection and sustainability, as it utilises a renewable and abundant agricultural by-product as a precursor; the AC was also able to treat water contaminated with dye, as demonstrated in this study. In addition, the value and utilisation of peanut shells, which are often considered waste or biomass, can be improved, and create new opportunities for income generation and resource management.

Previous studies have reported that peanut shells can be used as a precursor to synthesise PNTS-based AC with a surface area of up to 1200 m^2/g. However, these studies have lacked sufficient details on how the activation variables, such as the precursor to chemical agent ratio, activation temperature and time, affect the final characteristics of the resulting carbons and how the activation variables can be optimised. The optimal ratio of precursor to chemical agent, which ensures high yield and surface area of the AC, and the optimal activation temperature and time, which prevent incomplete carbonisation, are critical factors for large-scale production of AC (new set-ups or retrofits). In this study, the synthesised PNTS-based AC exhibited a surface area of ~1700 m^2/g, which was ~42% higher than the previously reported work, obtained using the optimal activation conditions of a temperature of 485 °C, hold time of 15 min and an impregnation ratio of 1.7. The PNTS-derived AC material showed a low ash content (below 1%) and a high fixed carbon content (above 86%), indicating the high quality of the synthesised carbons. Furthermore, response surface analysis showed that temperature and impregnation ratio were the most significant variables in influencing the characteristics of the AC materials derived from peanut shells, using $ZnCl_2$ as an activating agent.

The PNTS-based AC was evaluated for its adsorption performance using MO and MB dyes as the adsorbates. The experimental data were analysed using a number of kinetic and isotherm models to elucidate the adsorption mechanism, and capacity of the carbon material. The results suggest that the adsorption process of both dyes

followed a pseudo-second-order kinetic model, and that the Freundlich and Sips isotherm models were the most suitable for describing the adsorption equilibrium data. The Sips model estimated the maximum adsorption capacities of the PNTS-based AC for MO and MB to be 4584 mg g^{-1} and 1769 mg g^{-1}, respectively. These values indicate remarkable capacities compared with other AC materials reported in the literature. Furthermore, the adsorption mechanism of MO and MB dyes on the PNTS-based AC was further investigated using several experimental techniques, such as post-adsorption characterisation of the textural and surface properties of the carbon material, and desorption studies of the adsorbed dyes. The results revealed that the adsorption mechanism was predominantly governed by π–π interactions, n–π electron donor-acceptor (EDA) interactions, and pore filling, i.e., the adsorption mechanism was mainly driven by physical interactions. This is also a notable feature, as most commercial-grade ACs rely on physical adsorption to achieve separation, enabling regeneration and reusability of the AC materials. The PNTS-based AC material showed good reusability and stability, achieving over 90% dye removal, after five cycles of regeneration.

One of the limitations of the work presented in this thesis is that peanuts are typically cultivated in warm climates, making them very abundant and accessible in some regions of the world. However, peanut shells could be used as a low-cost and sustainable precursor to synthesise adsorbent material, providing a solution for wastewater treatment, especially in developing countries where peanut shells are readily available and accessible.

In conclusion, the outcomes of this work have:

- advanced the scientific knowledge and understanding of the synthesis and characterisation of activated carbon materials from biomass, and the factors that affect their properties.

- provided a novel and systematic approach to model and optimise the activation variables to synthesise AC materials from peanut shells, using a design of experiments and response surface analysis approach.
- demonstrated the potential and feasibility of using peanut shells as a low-cost and renewable precursor for AC synthesis and compared it with several other precursors reported in the literature.
- demonstrated that the AC material derived from peanut shells was suitable for the removal of ionic dyes from water, and elucidated the adsorption mechanism, which indicated that the adsorption was majorly driven by physical interactions, making it comparable with commercial-grade ACs.

7.2 Future work

This research has made a significant contribution to the scientific knowledge and understanding of the synthesis and characterisation of activated carbon materials derived from peanut shells, and their application for water remediation, implying that this work has the potential to contribute to environmental protection and sustainable development, as well as valorising agricultural wastes, and promoting waste management and a route towards a circular economy. However, further research is needed to facilitate the real-life implementation of this work.

Precursors such as peanut shells have a relatively low density, which requires chemical pretreatment to enhance the pore structure and the yield of the resulting AC materials. However, this may lead to the possible generation of secondary pollutants during the activation process. Therefore, a unit such as Soxhlet extraction can be incorporated into future work to recover and reuse the chemicals, such as $ZnCl_2$ and $CaCl_2$ salts that are easily recoverable.

The work presented in this thesis tested only two dyes, namely methyl orange (MO) and methylene blue (MB), which have different charges and molecular structures.

However, there are many other dyes with different properties that are widely used in various industries, such as textile, paper, leather, cosmetics, and food. Therefore, it would be interesting and useful to test the adsorption performance of the peanut shell based activated carbon (PNTS-based AC) for other dyes, such as Congo red, Rhodamine B, Malachite green etc., to evaluate the versatility and selectivity of the PNTS-based AC. Moreover, the adsorption mechanism and kinetics of these dyes on the PNTS-based AC could be further investigated using various experimental techniques and models.

Another limitation of this work is that it only used synthetic solutions with known concentrations of dyes. However, real wastewater samples have complex compositions and varying pH values, which may affect the adsorption process and the stability of the PNTS-based AC. Therefore, it would be important and relevant to test the PNTS-based AC with real wastewater samples, such as those collected from dyeing industries or municipal sewage plants, to assess the practical applicability and stability of the PNTS-based AC. Furthermore, the regeneration and reusability of the PNTS-based AC after multiple cycles of adsorption and desorption could be evaluated using real wastewater samples.

Finally, one other important aspect that can be explored for future work is scale up, which means both increasing the production of the PNTS-based AC and testing its performance for water remediation on a larger scale. This would require careful planning, preparation, and execution. Moreover, the present work employed a batch adsorption method, which has some limitations, such as handling small volumes of solution. Therefore, a column adsorption method could be adopted in the future to overcome these limitations and facilitate scale up of the system. A column adsorption method can provide continuous operation and easy regeneration of the PNTS-based AC, allowing simulation of the real industrial conditions.

Publications

This thesis has resulted in two research articles that contribute to the field of activated carbon production and application. The first article, titled "Production of High Surface Area Activated Carbon from Peanut Shell by Chemical Activation with Zinc Chloride: Optimisation and Characterization", has been published in the Journal of BioEnergy Research. The full article is provided in Appendix C. The second article, titled "A Novel Activated Carbon Material from Peanut Shells for the Removal of Methyl Orange and Methylene Blue Dyes from Wastewater: Kinetics, Isotherms, and Mechanism", has been accepted and to be published in the Journal of Adsorption Science and Technology.

Appendices

Appendix A

Table A1. Analysis of variance results for the reduced quadratic model.

Response 1: Yield

Source	Sum of Squares	df	Mean Square	F-value	p-value	
Model	792.44	5	158.49	185.07	< 0.0001	significant
A-Temperature	636.26	1	636.26	742.97	< 0.0001	
B-Hold Time	5.84	1	5.84	6.82	0.0227	
C-Impregnation Ratio	18.46	1	18.46	21.55	0.0006	
AC	14.68	1	14.68	17.14	0.0014	
A^2	117.20	1	117.20	136.85	< 0.0001	
Residual	10.28	12	0.8564			
Lack of Fit	9.91	9	1.10	9.06	0.0481	significant
Pure Error	0.3647	3	0.1216			
Cor Total	802.72	17				

Response 2: Surface area

Source	Sum of Squares	df	Mean Square	F-value	p-value	
Model	7.510E+06	5	1.502E+06	89.60	< 0.0001	significant
A-Temperature	2.899E+06	1	2.899E+06	172.95	< 0.0001	
C-Impregnation Ratio	9.833E+05	1	9.833E+05	58.66	< 0.0001	
AC	5.000E+05	1	5.000E+05	29.83	0.0001	
A^2	1.389E+06	1	1.389E+06	82.86	< 0.0001	
C^2	2.052E+05	1	2.052E+05	12.24	0.0044	
Residual	2.012E+05	12	16763.03			
Lack of Fit	1.907E+05	9	21186.28	6.06	0.0826	not significant
Pure Error	10479.80	3	3493.27			
Cor Total	7.711E+06	17				

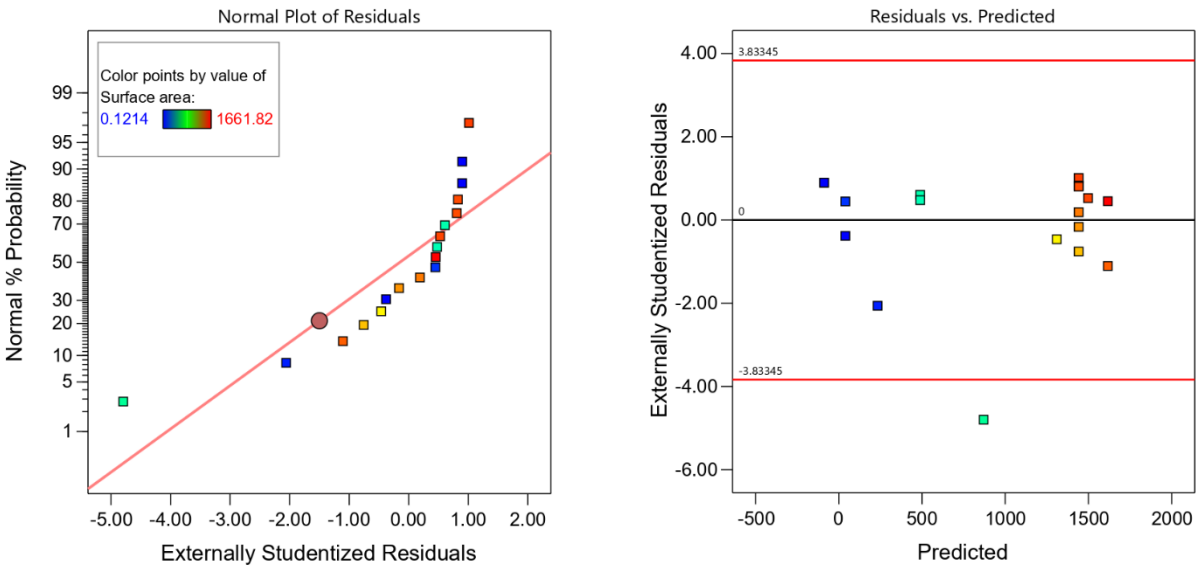

Figure A1. Diagnostic plots after model reduction for surface area.

Table A2. Constraints for optimisation of activation variables

Name	Goal	Lower Limit	Upper Limit
A: Temperature	is in range	300	600
B: Hold Time	is in range	15	120
C: Impregnation Ratio	is in range	0.25	2
Yield	is target = 47.22	44.23	64.988
Surface area	maximize	0.1214	1661.82

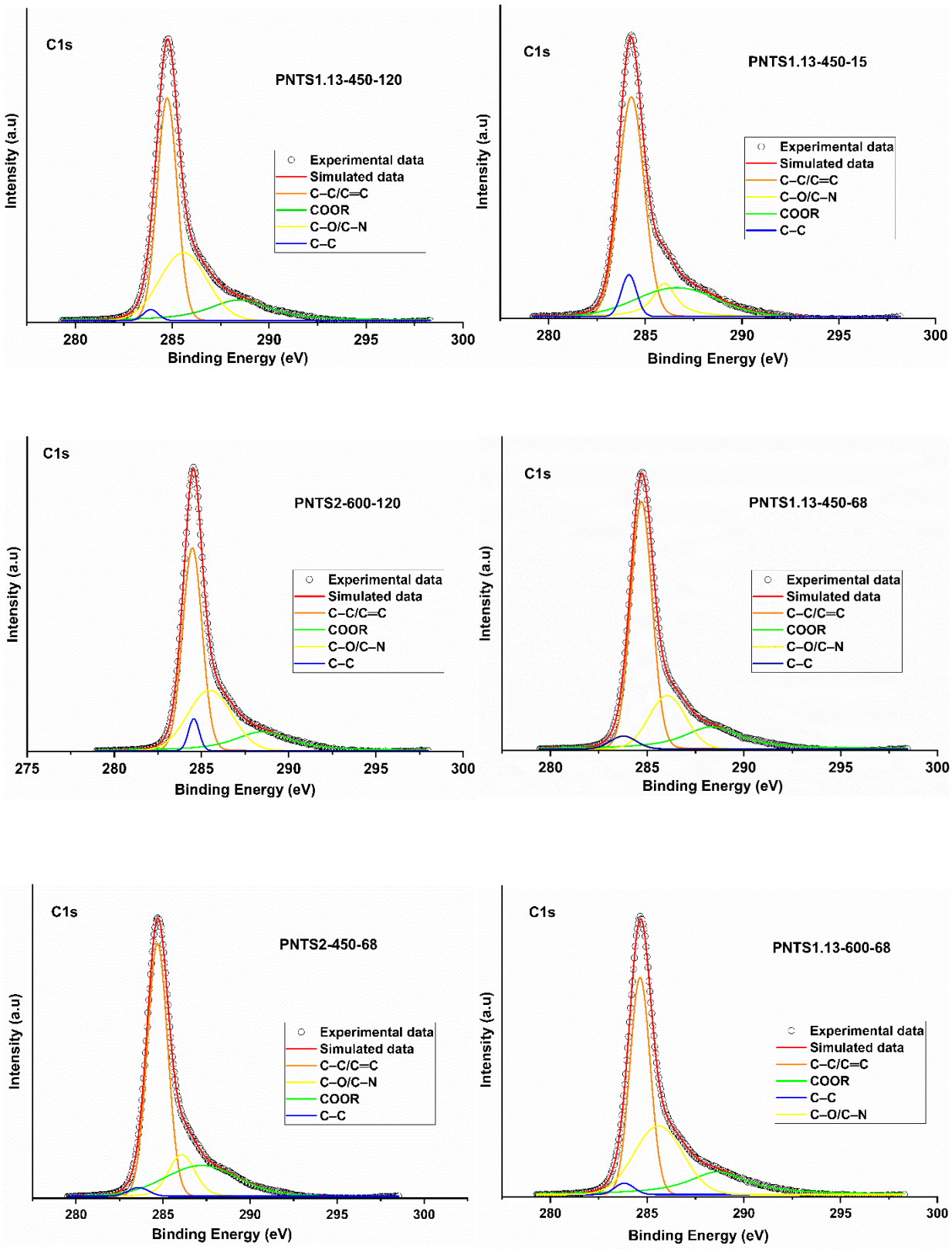

Figure A2a. C1s spectra curves obtained via XPS analysis for the as-synthesised peanut shell based ACs.

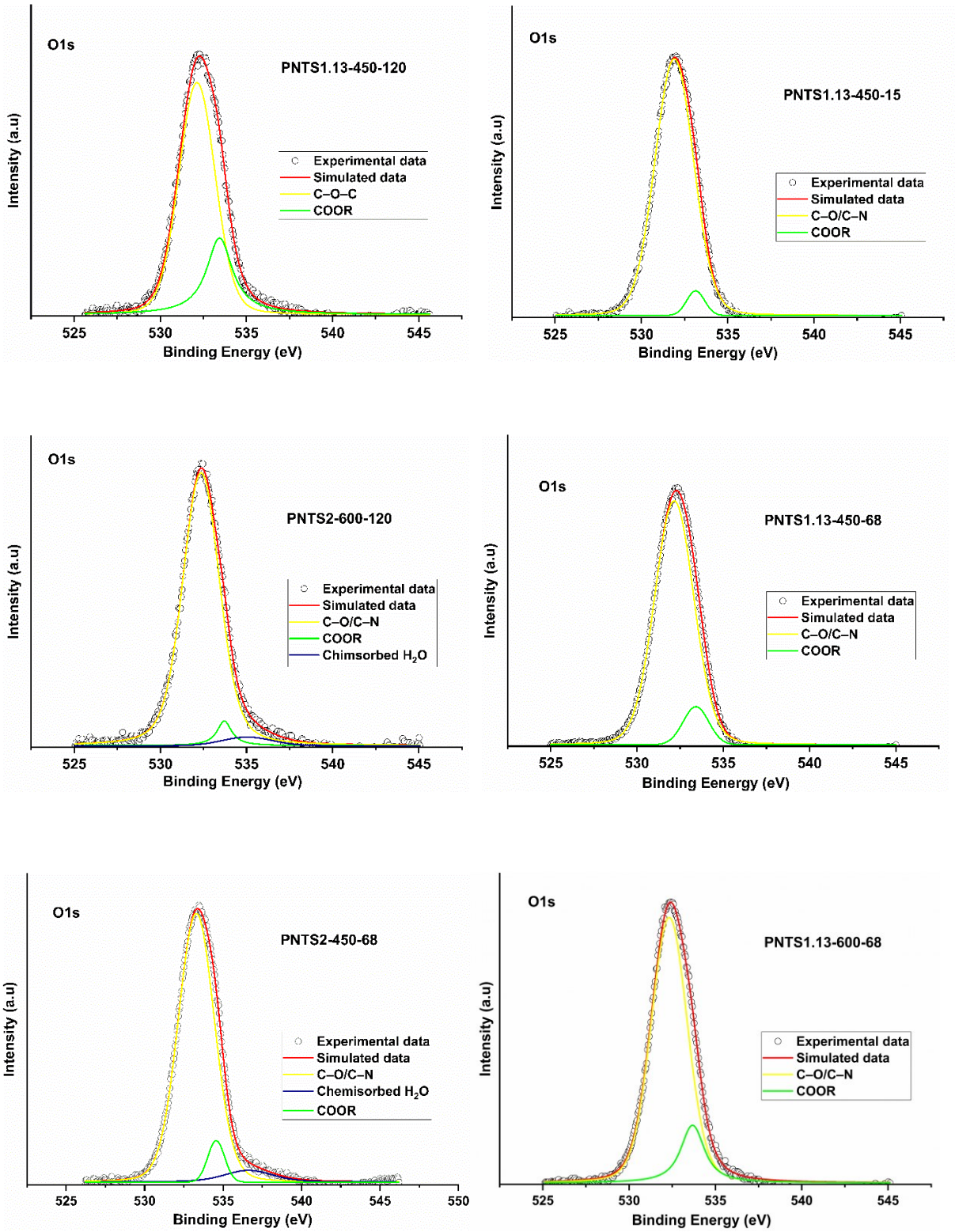

Figure A2b. O1s spectra curves obtained via XPS analysis for the as-synthesised peanut shell based ACs.

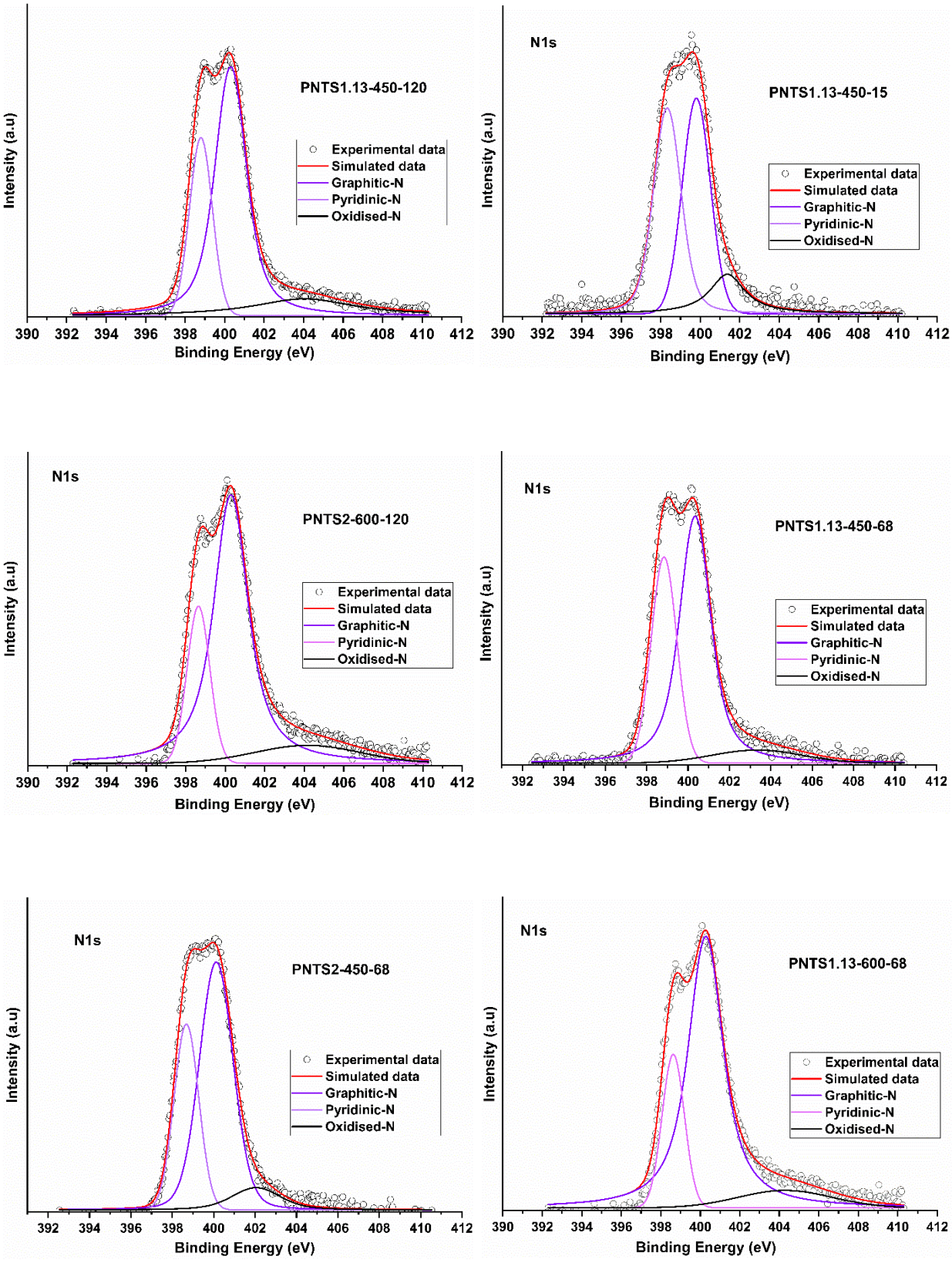

Figure A2c. O1s spectra curves obtained via XPS analysis for the as-synthesised peanut shell based ACs.

Note: The spectra curves illustrated here are for runs 1, 13, 15, 16, 17 and 18 accordingly.

Table A3. Numerical optimisation solutions from response surface methodology

15 Solutions found.

Number	Temperature	Hold Time	Impregnation Ratio	Yield	Surface area	Desirability	
1	**485.422**	**15.400**	**1.729**	**47.220**	**1727.290**	**1.000**	**Selected**
2	444.915	116.970	1.599	47.220	1670.972	1.000	
3	486.650	17.393	1.221	47.220	1703.005	1.000	
4	445.294	115.054	1.601	47.220	1666.382	1.000	
5	447.579	114.375	1.500	47.220	1673.884	1.000	
6	474.936	35.074	1.433	47.220	1696.420	1.000	
7	478.032	32.459	1.301	47.220	1681.241	1.000	
8	447.604	111.761	1.508	47.237	1665.154	1.000	
9	448.559	108.466	1.513	47.220	1661.452	0.999	
10	446.186	113.612	1.549	47.243	1665.149	0.999	
11	468.457	47.045	1.458	47.255	1665.148	0.999	
12	445.989	114.553	1.528	47.264	1665.121	0.999	
13	450.318	105.047	1.469	47.220	1656.693	0.999	
14	457.768	75.878	1.501	47.220	1637.703	0.996	
15	455.577	84.349	1.476	47.220	1637.602	0.996	

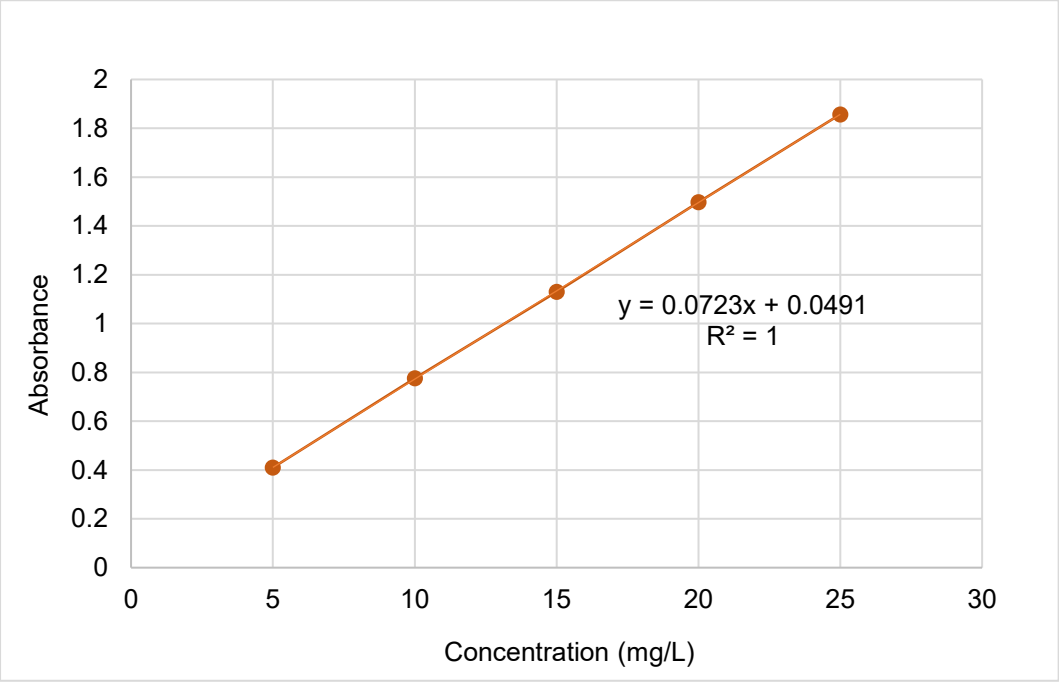

Figure A3. UV-vis calibration curve for methyl orange dye, measured at 465 nm.

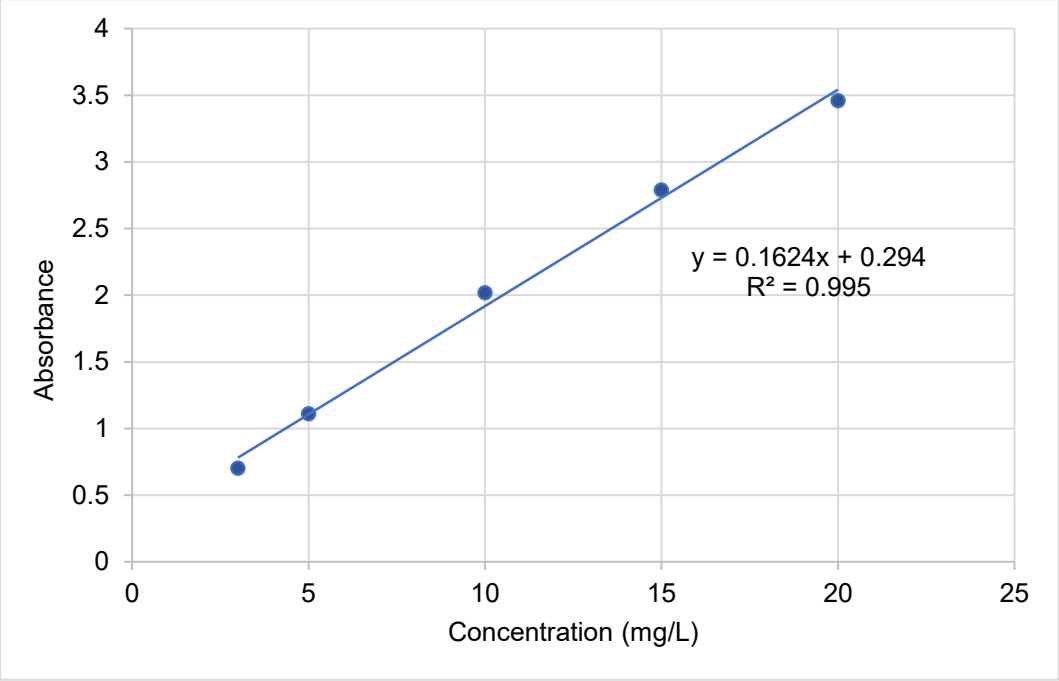

Figure A4. UV-vis calibration curve for methylene blue dye, measured at 664 nm.

Figure A5. Image of solution and biochar sample post-desorption of methyl orange and methylene blue dyes, at pH 8 and pH 2, respectively.

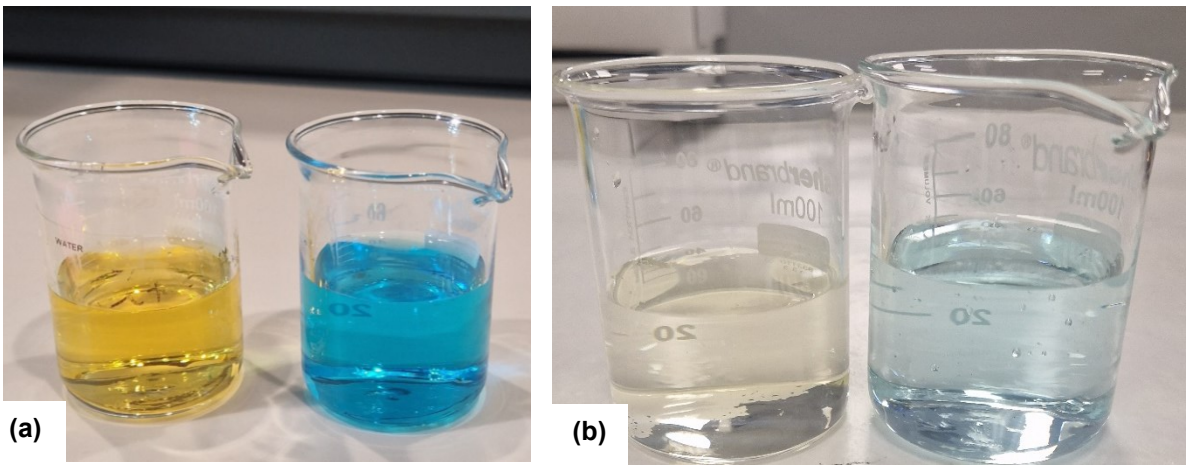

Figure A6. Images of filtered solutions: (a) after 20 minutes of desorption of methyl orange (left) and methylene blue (right), (b) after 1 hour of desorption of methyl orange (left) and methylene blue (right).

Appendix B

A step-by-step Face-centred Central Composite Design (CCD) using Design Expert 13.1.0

- **Step 1**

  Launch the Design Expert software by clicking on its icon on your desktop. A similar interface to the one shown below will appear, depending on the version of the software. On the same interface, click on the "NEW DESIGN" button as identified below in Figure B1.

Figure B1. The initial interface of Design Expert software

- **Step 2**

  After launching the software, a similar interface as the one shown in Figure B2 will appear, showing various design options available in Design Expert. On the same interface, click on the "Response Surface" button as highlighted by the red arrow in Figure B2.

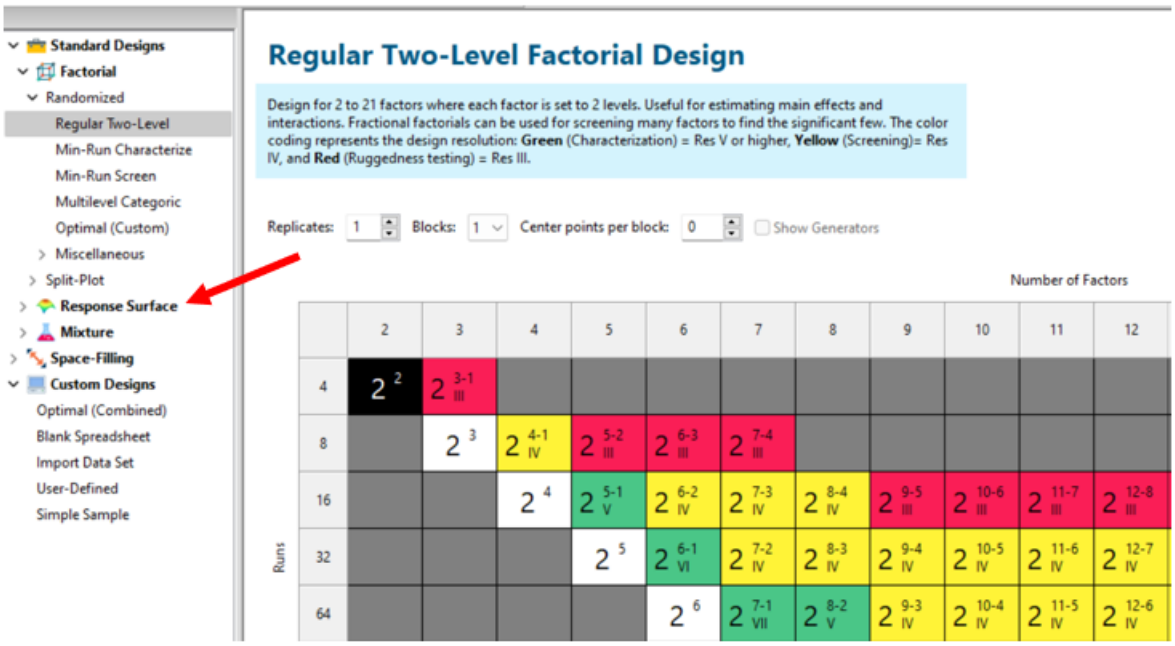

Figure B2. Design Expert interface showing various design options.

- **Step 3**

  The next step is to select the type of design, number of factors and centre points. Click on the "Central Composite" button (see arrow 1) and set the numeric factors to 3 (see red arrow 2), as demonstrated in Figure B3. This corresponds to the three factors considered in the experiment. Click on the "Options" button (see arrow 3) to set other components such as replication, centre points and α value. In this case, the centre point is set to 4 (see arrow 4). According to the National Institute of Standards and Technology [1], and as a rough guide, 3 – 5 centre points are sufficient to estimate experimental errors and the adequacy of the generated model. The value of α is set to 1 for Face-centred CCD (see arrow 5). Figure B3 illustrates the different options for α values, which depend on the experimental objectives and constraints.

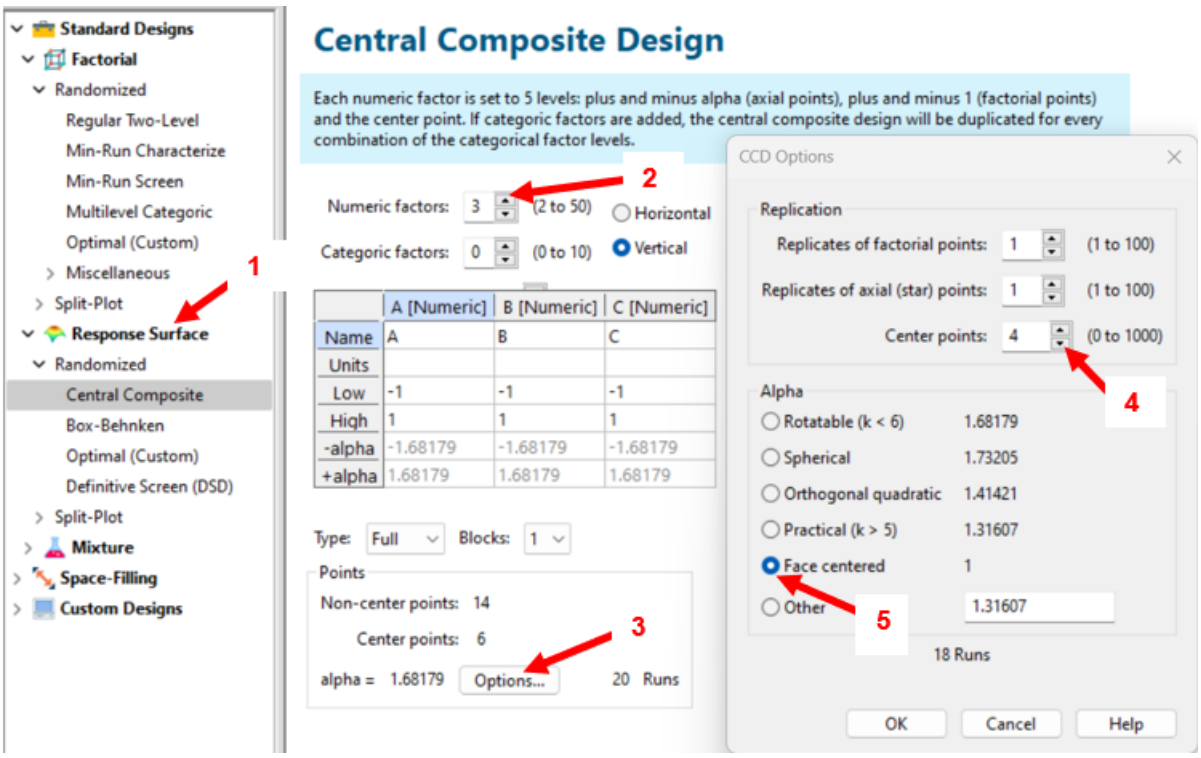

Figure B3. Design Expert interface showing various design options and settings.

- **Step 4**

  The name of the factors and their units are entered (see arrow 1), followed by the levels (low and high) of the factors (see arrow 2), as shown in Figure B4. The axial values are automatically set by the software. The experiment consists of 18 different runs. Click on the "next" button at the bottom right of the interface to proceed.

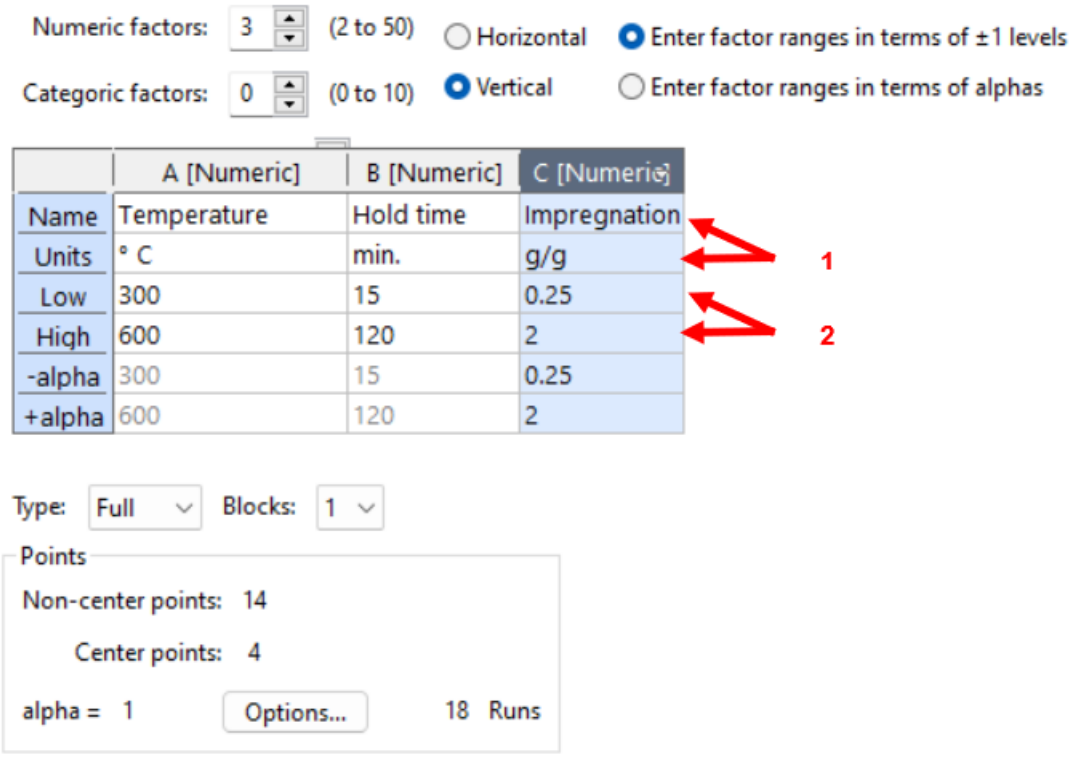

Figure B4. Design Expert interface showing the factors and levels configuration.

- **Step 5**

  Enter the name of the responses and their units, as shown in Figure B5 below. Click on the "finish" button at the bottom right of the interface to generate the design columns.

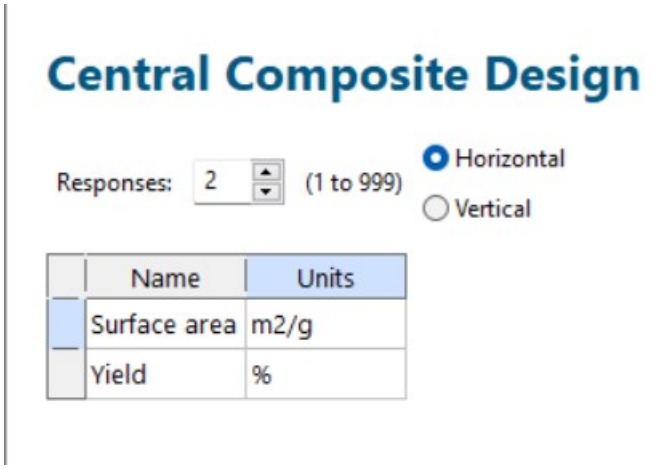

Figure B5. Design Expert interface showing the responses configuration.

- **Step 6**

  After generating the design, the next step is to conduct the experiment according to the generated design and the responses are entered into the columns for analysis. Figure B6 below shows randomised runs that are generated by the software.

Std	Run	Space Type	Factor 1 A:Temperature ° C	Factor 2 B:Hold time min.	Factor 3 C:Impregnation ... g/g	Response 1 Surface area m2/g	Response 2 Yield %
13	1	Axial	450	67.5	0.25		
3	2	Factorial	300	120	0.25		
1	3	Factorial	300	15	0.25		
8	4	Factorial	600	120	2		
16	5	Center	450	67.5	1.125		
10	6	Axial	600	67.5	1.125		
15	7	Center	450	67.5	1.125		
14	8	Axial	450	67.5	2		
9	9	Axial	300	67.5	1.125		
6	10	Factorial	600	15	2		
5	11	Factorial	300	15	2		
2	12	Factorial	600	15	0.25		
4	13	Factorial	600	120	0.25		
11	14	Axial	450	15	1.125		
18	15	Center	450	67.5	1.125		
7	16	Factorial	300	120	2		
12	17	Axial	450	120	1.125		
17	18	Center	450	67.5	1.125		

Figure B6. Design Expert interface showing the generated randomised runs.

- **Step 7**

  The analysis of the results is the next step. Select the response to be analysed from the same interface or pane as in Step 6 (see arrow 1 in pane 1 in Figure B7). Then, pane 2 will appear with the transformation options. The analysis should be first performed without any transformation (see arrow 2 in pane 2). A transformation is only needed when the residuals (errors) depend on the magnitude of the predicted values [2]. To initiate the analysis, click on the "Start Analysis" button after choosing a transformation option (see arrow 3).

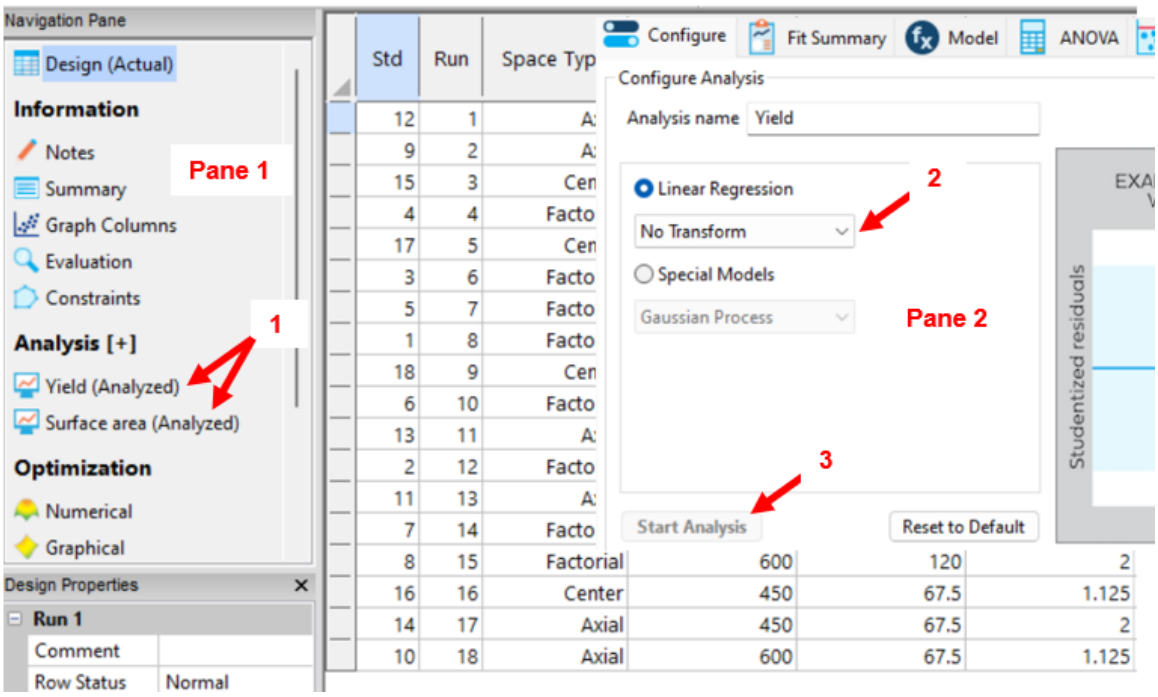

Figure B7. Design Expert interface showing the configuration for result analysis.

- **Step 8**

  The results of the analysis can be accessed from the buttons highlighted in Figure B8 (Fit Summary, ANOVA (Analysis of Variance) and Diagnostics). The detailed interpretation of the results is provided in Chapter 5.

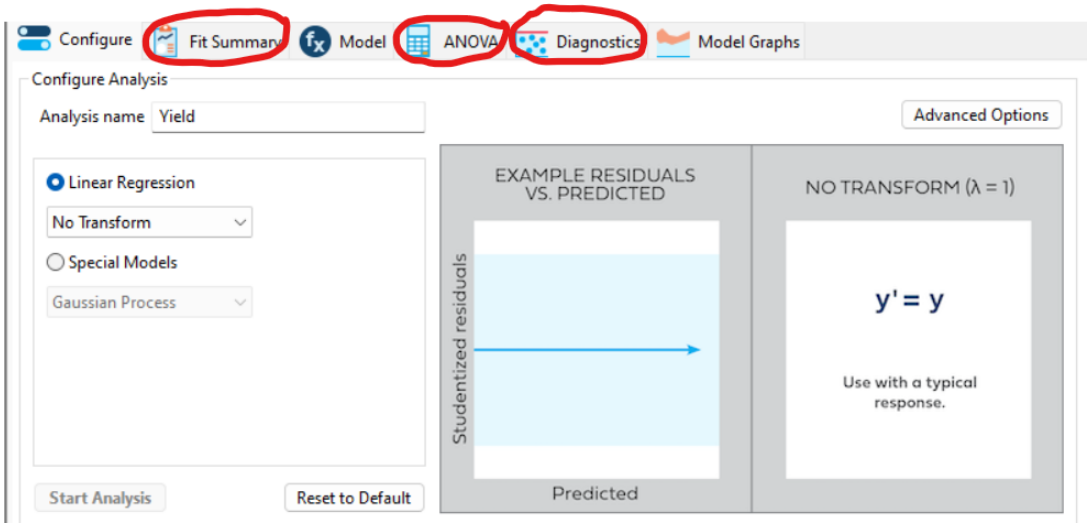

Figure B8. Design Expert interface showing the navigation panes to access the analysis results.

References

[1] N.I.S.T. *Adding centerpoints* [Online]. Available: https://www.itl.nist.gov/div898/handbook/pri/section3/pri337.htm [Accessed 22 June 2021].
[2] Miller, D. M. (1984). Reducing transformation bias in curve fitting. Am Stat 38**:** 124-126. https://doi.org/10.1080/00031305.1984.10483180

Appendix C - Publication

C.1. Production of High Surface Area Activated Carbon from Peanut Shell by Chemical Activation with Zinc Chloride: Optimisation and Characterization.

BioEnergy Research
https://doi.org/10.1007/s12155-023-10683-7

Production of High Surface Area Activated Carbon from Peanut Shell by Chemical Activation with Zinc Chloride: Optimisation and Characterization

Ashleigh Fletcher[1] · Tosin Somorin[1] · Oluwagbemi Aladeokin[1]

Received: 20 July 2023 / Accepted: 21 September 2023

Abstract
The potential of peanut shell as a precursor to produce activated carbon by chemical activation with $ZnCl_2$, and the effect of activation variables were investigated using response surface methodology. Activation variables examined were temperature, hold time and impregnation ratio; among these, impregnation ratio and temperature were found to most affect the final characteristics of the produced activated carbon. The activation process was mapped, using design of experiments, and the optimum activation conditions were found to be a temperature of 485 °C, with a hold time of 15 min and an impregnation ratio of 1.7. Under the optimised conditions, an activated carbon with a relatively high surface area of ~ 1700 m^2/g was produced, at a yield of 47%. Moreover, the carbon exhibited a relatively high density, ranging from 1.455 g/cm^3 to 1.750 g/cm^3, as well as a low ash content below 1% and a high fixed carbon content above 86%. SEM analysis and FTIR characterisation revealed the heterogenous nature of the produced carbon materials. The developed materials, with potential as adsorbents, removed up to 99.8% of a target dye (methyl orange) depending on their available surface area. Hence, through the insights gained, an optimised carbon is produced, demonstrating the potential to tailor activated carbon materials produced from waste biomass.

Keywords Chemical activation · Activated carbon · Peanut shell · Impregnation ratio · Response surface methodology

Introduction

In the last decade, global peanut cultivation has grown due to increased demand, attributed mainly to their perceived health benefits, resulting in a total production of ~ 41.4 MMT in 2019/2020 [1]. Peanut and other nutshells are considered as waste in various parts of the world and are usually used for their fuel value [2]. However, this agricultural by-product can be converted to higher value products, such as activated carbon (AC) [3, 4], which has various commercial applications and is typically produced from different organic precursors such as wood, coconut shell, coal, bones, peat etc. [5, 6]. In addition, various agricultural residues, such as rice husk, corn stalks, apricot stones, almond shells, coffee beans etc., have been explored to produce ACs, due to their comparatively low cost [7, 8]. Researchers have previously reported the production of AC using peanut shell as a precursor [3, 9–13], with surface areas up to 1200 m^2/g reported; however, these studies have lacked a focus on determining the controlling variables to enhance the carbon characteristics.

AC forms a large class of porous solid media, and due to their large porosities, they are widely used as adsorbents in the removal of pollutants and organic compounds from gases, water, wastewater, and air [14]. The textural and structural characteristics of AC depend on factors such as carbon content and solid structure of the precursor, activation method, activating agent and activation conditions. AC can be obtained via two routes: physical and chemical activation. Physical methods involve carbonisation of biomass in an inert environment, followed by partial gasification of the resulting char in oxidising gases such as carbon dioxide, steam, air or a mixture of these gases, using high temperatures, ranging between 700 and 1000 °C, to enhance the pore structure [5, 15, 16]. By contrast, chemical methods require lower temperatures (< 700 °C), using dehydrating

✉ Oluwagbemi Aladeokin
oluwagbemi.aladeokin@strath.ac.uk

[1] Department of Chemical and Process Engineering, University of Strathclyde, Glasgow G1 1XJ, UK

Published online: 03 October 2023

agents such as $ZnCl_2$, phosphoric acid, KOH, etc., to influence carbonisation and inhibit the formation of tar, thus increasing the carbon yield [16]. Such chemical routes are mostly applied for biomass with carbon content above 45%, [17] and peanut shells are reported to have levels at ~ 46% [2], making them ideal candidates for chemical activation. The effectiveness of $ZnCl_2$ in enhancing the porosity of porous carbonaceous materials has been well established in previous studies. $ZnCl_2$ acts as a catalyst that decomposes the biomass structure and facilitates the dehydration process during the carbonisation step, leading to the formation of char, aromatic compounds and pore structure [15, 16, 18]. Therefore, this study employs $ZnCl_2$ as the chemical agent for the preparation of porous carbon materials.

As ACs can be applied in a range of applications, it is essential to tailor the final properties of the AC to the chosen application, to fully understand and optimise the process [19]. Traditional approaches involve varying each experimental parameter, one at a time; however, a more efficient way to reduce the number of experimental runs, while also understanding the interplay between variables, is to apply design of experiment (DoE) [20], which provides the capability to vary factors simultaneously. Response surface methodology or modelling (RSM) is a useful technique used in DoE to study the interactions between parameters, allowing optimisation. It employs various surface visualisation techniques, such as contour plots, surface plots, interaction plots, and so on, to evaluate the influence of the factors on the response and the identification of the optimal factor combination that maximises or minimises the response [21].

Previous studies have investigated the effect of various activation parameters, such as impregnation ratio, temperature, time, and particle size, on the preparation of porous carbon materials from different precursors [15, 22–24]. Among these parameters, impregnation ratio and temperature were found to have a significant influence on the characteristics of the final product. However, studies of peanut shells did not provide sufficient information on how the activation variables influenced the final properties of the produced carbons and the optimisation of the activation variables. Moreover, previous studies of peanut shells employed two stages to carbon production: precursor charring and chemical activation shells [3, 10]. This process is complex and energy-intensive, compared to the one-stage process.

In this work, RSM was used to study the influence of activation variables in a single step chemical activation process, selected to simplify the process for production at scale, while providing economic gain, as energy input is reduced. Through the insights gained, an optimised carbon is produced, demonstrating the potential to tailor AC materials produced from waste biomass.

Materials and Methods

Materials

Raw peanut (enclosed in its shell) was obtained from a commercial source within the UK. Zinc chloride ($ZnCl_2$, > 98%, solid), and 1 M hydrochloric acid (HCl) solution were purchased from Fisher Scientific, UK. Methyl orange ($C_{14}H_{14}N_3NaO_3S$) was purchased from Sigma – Aldrich, UK. All reagents used were of analytical grade and were used without further purification.

Preparation of Activated Carbons

The peanut shells (PNTS) were removed and washed with water to remove any surface dirt before subsequent oven-drying at 100 ± 2 °C overnight. After drying, the shells were ground and screened to a particle size of 2 mm with a sieve shaker. 5 g (W1) of the screened precursor was impregnated with $ZnCl_2$ at various impregnation ratios ($ZnCl_2$ g/ precursor g) of 0.25, 1.13 and 2. In all experiments, the precursor was properly mixed in 25 mL of deionised water containing different weights (W2) of $ZnCl_2$ depending on the impregnation ratio. The mixture was allowed to equilibrate for ~ 24 h under room temperature. After the impregnation process, the sample was oven-dried at 100 ± 2 °C overnight. The oven-dried sample was carbonised in the tube furnace under nitrogen (inert atmosphere, 250 mL/min), at a temperature of 300, 450 or 600 °C using a dwell/hold time (residence time) of either 15, 68 or 120 min at a ramp-rate of 15 °C/min. The carbonised product obtained from the furnace was weighed (W3), before being transferred into a jar containing 200 mL of 0.1 M HCl and agitated for 1 h on a shaker to leach out any remaining activating salt. The product was boiled in hot deionised water for ~ 10 min and washed in room temperature deionised water to completely remove any chloride ions and reduce acidity. The washed product was dried in the oven at 100 ± 2 °C for ~ 24 h, weighed again after drying (W4) and stored for characterisation. The naming of samples for easy identification includes the precursor initials, impregnation ratio (I.R.), activation temperature and hold time.

The yield of the process in percentage was calculated using the following equation:

$$Yield = (W4/W1) \times 100 \quad (1)$$

Also, to take account of the activating reagent recoverable from washing, the following equation is used to calculate the reagent recovery (R.R.) in percentage:

$$R.R = ((W3 - W4)/W2) \times 100 \quad (2)$$

Design of Experiment for Activated Carbon Preparation

In this study, Design Expert (V13.1.0. Stat-Ease Inc., Minneapolis, USA), a statistical software, was used to set the activation variables/factors' values. Face-centred CCD (FCCD) with three factors and levels design was employed to provide maximum information in minimum experimental runs. This design type is used to find best values for a set of factors to give an optimal response [25]. The factors investigated in this design were temperature (A), hold time (B) and I.R. (C), based on preliminary studies and previous reports [22, 23, 26]. Randomised experimental runs were used to minimise the effects of factors that cannot be controlled in the process. The coded values for the activation variables were − 1 for minimum, 0 for centre point and + 1 for maximum point, as shown in Table 1. Yield (Y_1) and surface area (Y_2) are important properties in determining the economic viability and adsorption capability of ACs, respectively. These two properties were considered as the responses in the design.

Materials Characterisation

Proximate Analysis

Proximate analysis of the raw precursor and the activated carbon was carried out using a thermogravimetric technique version of British Standard BS1016. The procedure was carried out using a method similar to that reported by Ottaway [27]. A NETZSCH STA 449 F3 Jupiter system was used for this analysis.

Adsorption Experiment

Adsorption experiments were carried out to evaluate the efficiency of the activated carbon, by agitating 0.05 g sample with 50 mL of methyl orange (MO) solution (100 mg/L), in 500 mL Erlenmeyer flasks. The mixtures were agitated on an orbital shaker operated at 150 rpm, and at room temperature. At predetermined time intervals, the mixtures were separated by centrifugation, and the residual concentrations (C_t) were measured at 465 nm, using a Varian CARY 5000 UV-VIS-NIR spectrophotometer. The percentage removal of MO was calculated using the equation below.

$$Removal\ (\%) = \frac{C_0 - C_t}{C_0} \times 100 \quad (3)$$

Where C_0 and C_t (mg/L) represent the initial concentration and concentration at time t, respectively.

Point of Zero Charge

The determination of point of zero charge (PZC) of the AC was carried out using a salt addition method [28]. Several vials containing an aliquot of 40 mL of 0.1 M $NaNO_3$ each were prepared. 0.1 M HNO_3 or 0.1 M NaOH solutions was used to adjust the pH values from 3 to 11. 0.2 g of AC was added to each of the solutions and the solutions agitated at 150 rpm for ~ 24 h on a VWR STD 3500 shaker. After equilibrium was attained, the mixture was filtered, and the pH reading was recorded. The experiment was performed in triplicate and a mean value recorded.

Fourier Transform Infrared Spectroscopy

AC samples were analysed for various surface functional groups using Fourier transform infrared spectrometry (FTIR). The samples were scanned over a range of 500–4000 cm^{-1} using an MB3000 FT-IR laboratory analyser with Horizon MB™ FTIR software. 449 scans were taken at a resolution of 8 cm^{-1}.

Density

Densities of the AC samples created within this study were determined using helium pycnometry (Micromeritics Accupyc II helium pycnometer with Accupyc II version 3.0 software). A pycnometer sample cup was cleaned and

Table 1 Activation parameters and their coded values for the Face-centred central composite design for chemically activated synthesis of peanut shell derived carbons

Variables (factors)	Units	Variable levels				
		Low (-1)	Mid (0)	High (1)	-α	+α
Temperature (A)	(°C)	300	450	600	300	600
Hold time (B)	(min)	15	68	120	15	120
Impregnation ratio, I.R. (C)	(wt/wt)	0.25	1.13	2	0.25	2
Responses						
Yield (Y_1)	(%)					
Surface area (Y_2)	(m^2/g)					

Table 2 Model summary statistics for analysed variables for chemically activated carbons derived from peanut shells

Response	R^2	Adjusted R^2	Predicted R^2	Std. Dev.	Mean	C.V. %	Adeq. Precision
Yield (%)	0.9932	0.9856	0.9360	0.83	51.26	1.61	33.55
Surface area (m^2/g)	0.9784	0.9541	0.8475	144.34	926.15	15.58	16.54
Reagent recovery (%)	0.9833	0.9645	0.7697	5.00	70.83	7.07	21.70
Micropore area (m^2/g)	0.9793	0.9561	0.8616	69.63	469.49	14.02	16.88
Mesopore area (m^2/g)	0.9694	0.9350	0.7634	99.35	429.82	23.11	15.77

weighed before a small sample of AC was introduced into the sample cup; the weight was taken again to determine the sample mass. The sample cup, with the sample, was transferred into the pycnometer, and sealed within the pycnometer for analysis. The system was purged with helium gas to remove any gas molecules trapped within the system before the analysis.

Textural Analysis

The textural characteristics of the activated carbon were determined using the method of Brunauer et al. [29]. This was achieved using a Micromeritics ASAP 2420 instrument that employs nitrogen adsorption at -195.8 °C. The sample was first degassed before analysis, to remove any contaminant species, via heating under vacuum. Degassing was performed at 250 °C for 4 h, using a ramp rate of 10 °C/min. The specific surface area (S_{BET}) was calculated using Brunauer-Emmett-Teller (BET) method. The micropore area (S_{micro}) and micropore volume (V_{micro}) were obtained the by t-plot method of de Boer et al. [30]. The pore-size distribution was calculated by the Barrett–Joyner–Halenda (BJH) equation [31].

The total pore volume (TPV) was calculated using the equation below.

$$TPV = Q_{sat} * (\frac{\rho_{vap}}{\rho_{lig}}) \quad (4)$$

Where Q_{sat} is maximum nitrogen adsorption (in cm^3/g, usually at relative pressure of 0.97 or above), ρ_{vap} is density of N_2 vapour at STP and ρ_{liq} = density of liquid N_2 at boiling point.

Scanning Electron Microscopy (SEM)

The surface morphology of the raw precursor and the activated carbon was observed, using a JEOL JSM-IT100 scanning electron microscope, at an accelerating voltage of 20 kV. The samples were mounted on aluminum SEM specimen stubs, by double sided carbon adhesive discs. The scanning was performed under high vacuum (HV) and at a magnification of 250x.

Results and Discussion

Fit Summary for the Design of Experiment for AC Preparation

Design Expert was used to analyse the dataset obtained from the surface area analysis, yield of the process, and other dependent variables. The sequential model sum of squares from the statistical software suggested quadratic models for all the dependent variables. The regression equations obtained for each dependent variable from the analyses are shown in Eqs. 5 and 6. The coefficient of determination (R^2) was used to assess how well the regression model fits the data for this study. R^2 values obtained were 0.9932 and 0.9784 for yield and surface area, respectively. These values indicate a good fit of the dataset to the regression models i.e., above 97% of the variability observed in the responses can be explained by the selected model. The model and fit statistics for all analysed variables are summarised in Table 2. The Adjusted R^2 is a measure of the amount of variation around the mean which can be explained by the model and adjusted for the number of terms in the model. Reduced adjusted R^2 values are observed from the model summary statistics; this may be attributed to the presence of some model terms that do not add much value to the model. The predicted R^2 measures the amount of variation in predictions and can be explained by the model.

$$Y_1 = +124.50 - 0.25A - 0.05B - 8.07C + 0.01AC - 0.01BC + 1.00C^2 \quad (5)$$

$$Y_2 = -6429.31 + 29.84A - 2.48B + 367.17C - 0.0039AB + 1.90AC - 0.15BC - 0.0313A^2 + 0.0346B^2 - 380.30C^2 \quad (6)$$

where A = temperature, B = hold time, and C = I.R.

The predicted R^2 values are in reasonable agreement with the adjusted R^2, i.e., they are within 0.2 of the adjusted R^2. Within the Design Expert system, an adequate precision > 4 indicates an adequate model discrimination [32]; in this case, all adequate precision values are well above 4. The coefficient of variation (C.V.) is the standard variation

Table 3 Model summary statistics for responses (after model transformation) for chemically activated carbons derived from peanut shells

Response	R^2	Adjusted R^2	Predicted R^2	Std. Dev.	Mean	C.V. %	Adeq. Precision
Surface area (m^2/g)	0.9937	0.9865	0.9112	1.82	26.34	6.91	30.99
Micropore area (m^2/g)	0.9950	0.9893	0.9158	1.15	19.47	5.92	34.45
Mesopore area (m^2/g)	0.9870	0.9724	0.8781	1.98	17.19	11.53	23.38

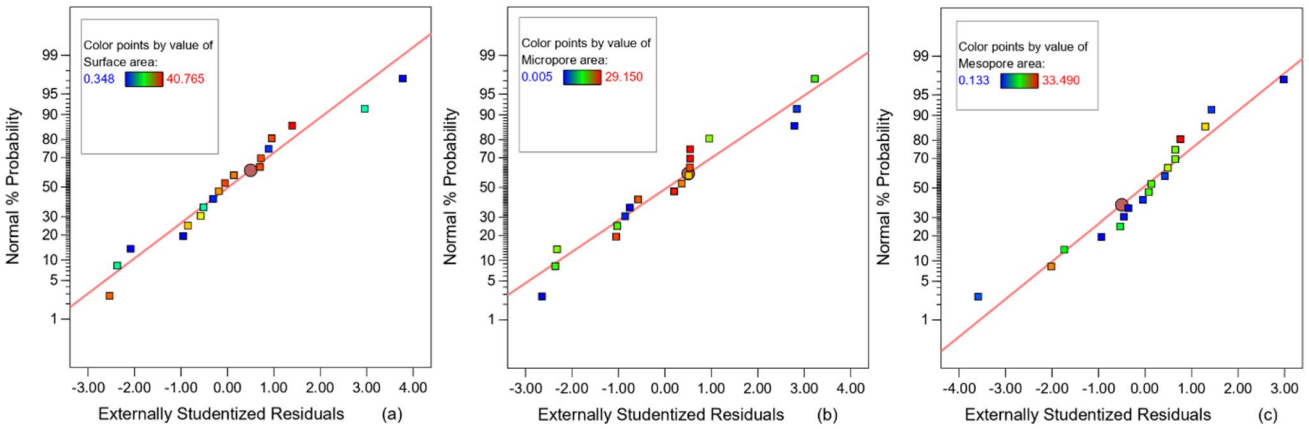

Fig. 1 Normal plots for: **a** surface area (**b**) micropore area (**c**) mesopore area, after model transformation, for chemically activated carbons derived from peanut shells

expressed as a percentage of the mean; this can be used to measure the reproducibility of a model and as a general rule, a model will be reasonably considered reproducible if C.V. is > 10% [33]. As shown in Table 2, C.V. for surface area, micropore and mesopore areas are > 10%. This can be attributed to errors in the measurement of these quantities.

To further assess the adequacy of the models, diagnostic plots, such as the normal plot, residual versus predicted response plot, and predicted versus actual plot, were employed. The diagnostic plots for yield and surface area are presented in (Figs. S1 and S2, see Supplementary Information). The predicted versus actual plot for yield indicates a strong agreement between the predicted and the actual values, as shown by the points aligning with the 45-degree line and the high R^2 value. On the other hand, the surface area shows a weaker agreement. The normal plot for yield demonstrates that the residuals follow a normal distribution, as evidenced by the points conforming to the straight line. However, for surface area, some departure from the line is noticeable – this suggests that a transformation may enhance the model. The residual versus predicted values plot for yield displays a random distribution of the residuals. The plot should exhibit a random distribution (constant variance of residuals throughout the graph) [34]. Conversely, the same plot for surface area exhibits some heteroscedasticity, as the variance of the residuals increases from right to left. This may indicate the need to transform the response. No outlier was found in any of the plots.

As indicated by the adjusted R^2 values for surface area, micro- and mesopore areas, reducing the number of terms in the models might improve the adjusted R^2. Model reduction was performed for the responses by eliminating insignificant terms, after which, the overall models did not show significant improvement (Table S1, see Supplementary Information), possibly because the number of significant terms was higher than that of insignificant terms.

The residual versus predicted values plot indicated that model transformation was necessary. Transformation of responses is an essential aspect of any data analysis. It is required when the residuals (errors) are dependent on the magnitude of the predicted values [35]. Model transformation was carried out by using the recommended transformation, square root transformation, within Design Expert. The square root transformation is the simplest form of transformation; this was employed to enhance the model. The model summary statistics after model transformation are shown in Table 3. The R^2, and adjusted R^2, values increased, and the predicted R^2 remained reasonably consistent with the adjusted R^2 values. This indicates a better fit, reducing the errors between the observed values and the predicted values.

Figure 1 displays the normal plots for the responses. The enhancement of the models, after transforming the responses, is further verified by the increased conformity of the residuals on the normal plots, for all responses.

Equation 7 shows the final regression equation (Table S3, Supplementary Information) for the ANOVA performed for surface area response after transformation.

$$\sqrt{Y_2} = -158.93 + 0.73A + 0.037B + 11.86C - 0.00016AB + 0.022AC + 0.018BC - 0.00072A^2 + 0.00025B^2 - 7.35C^2 \quad (7)$$

Analysis of Variance (ANOVA)

Statistical analysis was carried out on the independent variables (A: Temperature, B: Hold time, C: I.R.) to observe the single and interaction effect of the variables on the responses (Y_1: Yield, Y_2: Surface area) and choose the best model for the system. As presented in Table 3 above, the closeness of R^2 to unity, indicates a good fit of the dataset to the models. However, analysis of variance (ANOVA) was used to further check the adequacy of the selected quadratic models. This was done by comparing the p-values and F-values from the ANOVA table (Table S2, see Supplementary Information). A suitable model will have high F-value, its p-value < 0.05 (significant) and have lack of fit as non-significant (p > 0.05) [36]. The analysis shows that the p-values for the quadratic models selected for yield and surface area are < 0.05. This indicates statistical correctness of the selected models.

It is observed from the table that model terms A, B, C, AC, and A^2 have p-values < 0.05 for yield, i.e., temperature, hold time, I.R., and the interaction of temperature and I.R. affect the yield of the process. Temperature has the greatest impact on yield since it shows the highest F-value, 933.85. The lack of fit is not significant in this case since it shows a p-value > 0.05. It is observed from the ANOVA table that model terms A, C, AC, A^2, and C^2 have p-values < 0.05 for surface area i.e., temperature, I.R, and the interaction of temperature and I.R. are parameters that affect the surface area. Temperature is also observed to have the greatest impact on surface area since it has the highest F-value of 623.98. The lack of fit for this model has p-value > 0.05 i.e., lack of fit is not significant for this model. This indicates that the model fits the dataset and can be used to navigate through the design space.

Influence of Activation Variables

The one factor effect on the yield of the process is shown in (Fig. S3, see Supplementary Information). The yield reduces with increase in temperature to ~ 550 °C and above this temperature, the yield only demonstrates a slight decrease. This can be attributed to the basic structure being already formed at ~ 500 °C, since the distillation of tar occurs ~ 350–500 °C [19]. The hold time has little effect on the yield of the process.

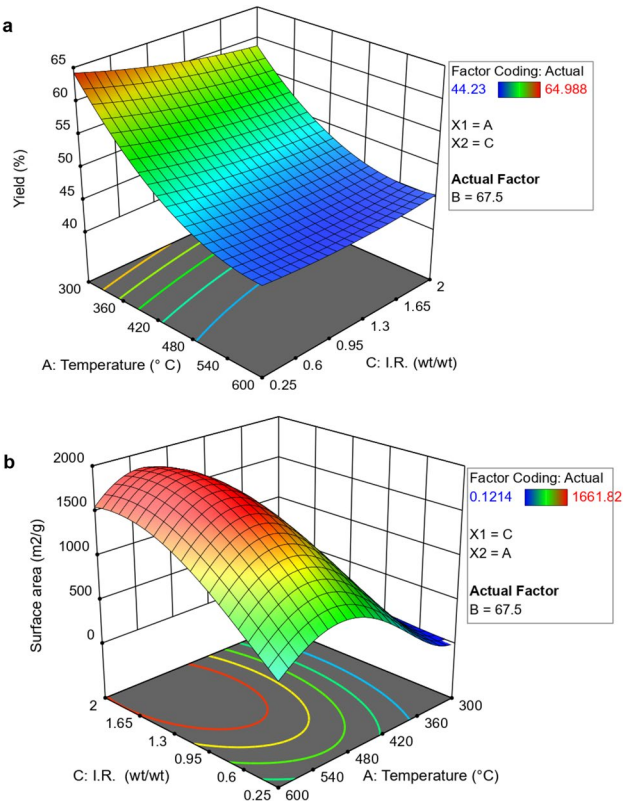

Fig. 2 **a** Interaction effects of temperature and impregnation ratio (I.R.) on process yield; **b** Interaction effects of temperature and impregnation ratio (I.R.) on surface area, for chemically activated carbons derived from peanut shells

The yield demonstrates a gradual reduction as I.R. increases, showing minor changes for I.R. > 1.5. Increase in activating agent may lead to more cracks in the structure, causing deformation of micropores and reducing productivity [37]. An increase in activating agent increases the evolution of volatile matter, which leads to a reduction in yield [5]. The interaction of temperature and I.R. is also an important factor that affects the yield of the process. As shown in Fig. 2a, at temperatures < 350 °C and I.R. < 1.5, the yield of the process is ≥ 60%, however, the surface area stays below 500 m^2/g. The yield remains within the range 50–55% at temperatures of 350–455 °C and is not greatly affected above 480 °C. It is also noted that the surface area increases gradually in this region with increase in temperature; this confirms the significance of temperature in developing the internal porous structure of the carbons. As reported by Hock et al. [17], the formation of pores and channels in the activated carbon matrix is attributed to the release of volatiles from the precursor material due to the dehydrating effect of $ZnCl_2$ at elevated temperature. However, these pores are unstable and tend to collapse or enlarge at higher temperature, thereby reducing the surface area of the activated carbon.

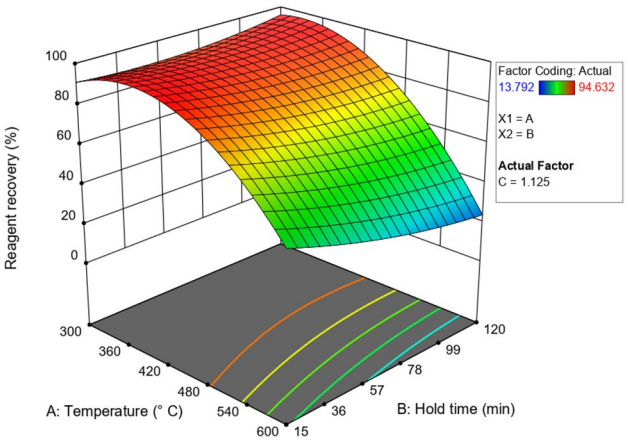

Fig. 3 Interaction effects of temperature and hold time on reagent recovery for chemically activated carbons derived from peanut shells

The one factor effect on the surface area is shown in Fig. S4, see Supplementary Information. The surface area considerably increases with increase in temperature to ~ 520 °C and a decrease in microporosity is noted with further increase in temperature > 520 °C. Microporosity starts to decrease at I.R. > 1. This is associated with widening of the pores with increase in $ZnCl_2$ loading, which leads to increased mesoporosity, as shown in Figs. S5 and S6 (see Supplementary Information). The surface area remains below 500 m^2/g with carbonisation temperature < 375 °C, within the selected range of I.R. However, at I.R. > 1 and carbonisation temperature > 420 °C, the surface area increased considerably above 500 m^2/g.

Increasing porosity with increasing I.R. suggests that porosity is created by the interstices left in the carbon material after washing and, at these temperatures, volatile substances are released from the surface of the carbon material during carbonisation. Figure 2b shows the effect of the interaction of temperature and I.R. on porosity development. The above discussion stated the most significant activation parameters (temperature and I.R.) and the range of temperatures and I.R. for producing activated carbons with diverse properties from peanut shells for various applications, which was lacking from the previous studies using the same precursor.

Reagent recovery (R.R.) from the activation process primarily depends on two factors (temperature and hold time). As shown in Fig. 3, the R.R. demonstrates a significant decrease with carbonisation temperature above 500 °C. This is likely associated with the reagent evaporating from the carbon sample as the temperature increases. It is also noted that R.R. decreases as hold time increases with temperature, ascribed to the fact that more evaporation is expected the longer the activating agent stays at higher temperatures.

Sample densities were observed to increase with an increase in both temperature and I.R. The increase in density with I.R. may be linked to tar inhibition by $ZnCl_2$ resulting from the condensation reaction [22]. As shown in Table S4 (see Supplementary Information), all activated carbon samples show relatively high densities with the minimum being 1.455 g/cm^3 and maximum, 1.750 g/cm^3.

Activation Process Optimisation

It was observed that there is a trade-off between yield and surface area; therefore, the Design Expert desirability function was employed to reach a balance. In the optimisation process, a target was set for the yield while the surface area was maximised. Design of experiments suggests optimisation of the produced carbon, to give a relatively high surface area of 1662 m^2/g and yield of 45.93% with the following activation parameters: a temperature of 600 °C, a hold time of 15 min, and an I.R. of 2. Experimental validation was performed, in triplicate, to ascertain the optimal conditions produced by RSM. Table 4 presents the optimised activation parameters from RSM and the validations obtained via experiment, note these samples (PNTS1.7-485-15) were used for further characterisation with PNTS2-600-15. As shown in Table 4, the optimised sample shows an average surface area of 1687 m^2/g, which is relatively higher than the quantity previously recorded for biochars created using the same precursor.

Table 4 Optimal activation conditions to produce high carbon yield and surface area for chemically activated carbons derived from peanut shells, and experimental validation

Source	Activation parameters			Responses		Desirability	Avg. Pore size, nm
	Temp., °C	Hold time, min	Impregnation ratio, I.R., wt/wt	Yield, %	Surface area, m^2/g		
RSM	485	15	1.7	47.22	1727	1	
Validation experiment 1	485	15	1.7	47.41	1683		3
Validation experiment 2	485	15	1.7	46.88	1696		3
Validation experiment 3	485	15	1.7	46.80	1683		3

Table 5 Textural characteristics of the prepared activated carbon and experimental design with the response variables (yield and surface area) for chemically activated carbons derived from peanut shells

Run	Sample name	A	B	C				Dependent variables	
		Temp., ° C	Hold time, min.	I.R. (wt/wt)	Avg. Pore size, nm	Micropore vol., cm^3/g	Total pore vol., cm^3/g	Yield (Y_1), %	Surface area (Y_2), m^2/g
1	PNTS1.13-450-120	450	120	1.13	3	0.416	0.876	46.63	1562
2	PNTS1.13-300-68	300	68	1.13	6	0.006	0.006	60.20	51
3	PNTS1.13-450-68	450	68	1.13	3	0.431	0.810	48.94	1464
4	PNTS0.25-600-120	600	120	0.25	3	0.247	0.283	45.55	537
5	PNTS1.13-450-68	450	68	1.13	3	0.407	0.787	48.95	1420
6	PNTS0.25-300-120	300	120	0.25	43	Negligible	0.006	64.07	Negligible
7	PNTS2-300-15	300	15	2	8	Negligible	0.001	61.01	1
8	PNTS0.25-300-15	300	15	0.25	25	Negligible	Negligible	64.99	Negligible
9	PNTS1.13-450-68	450	68	1.13	3	0.429	0.857	48.73	1539
10	PNTS2-600-15	600	15	2	3	0.276	1.016	45.93	1662
11	PNTS0.25-450-68	450	68	0.25	3	0.224	0.274	49.87	586
12	PNTS0.25-600-15	600	15	0.25	3	0.248	0.290	46.20	550
13	PNTS1.13-450-15	450	15	1.13	3	0.416	0.746	49.03	1349
14	PNTS2-300-120	300	120	2	3	0.025	0.047	57.33	84
15	PNTS2-600-120	600	120	2	3	0.278	0.861	45.93	1510
16	PNTS1.13-450-68	450	68	1.13	3	0.443	0.854	48.21	1541
17	PNTS2-450-68	450	68	2	3	0.351	0.875	46.90	1551
18	PNTS1.13-600-68	600	68	1.13	2	0.391	0.687	44.23	1262
Optimised	PNTS1.7-485-15	485	15	1.7	3	0.387	0.940	47.41	1683

Characterisation Analysis

Table S4 (see Supplementary Information) and Table 5 present the surface area, average pore size, micropore volume, yield, micropore area, and mesopore area (external surface area) obtained from the textural analysis of all AC samples through N_2 adsorption. The total pore volume was calculated from the N_2 adsorption data using Eq. (3). The N_2 adsorption – desorption isotherms of PNTS2-600-15 and PNTS1.7-485-15 are shown in Fig. S7 (see Supplementary Information); it can be observed that both samples are characterised by a mixture of micro- and mesopores (as seen by the opening of the knee). However, the isotherm of PNTS1.7-485-15 is approaching a horizontal plateau which indicates the presence of uniform wider micropores; by contrast, the plateau of PNTS2-600-15 continues at high relative pressure (P/P_O) and the presence of hysteresis indicates higher mesopore volume. The pore size distribution (PSD), as shown in Fig. S8 (see Supplementary Information), shows that both samples are characterised by pore size < 50 nm. It can be observed that PNTS2-600-15 exhibits a more heterogenous characteristic due to the presence of various pore sizes, as shown in the PSD.

As discussed by Seader et al. [38], the high capacity of a sorbent which helps to minimize the amount of sorbent used in a system is one of the properties that make a sorbent suitable for commercial use.

A relatively high surface area of 1662 m^2/g was achieved from the design of experiment, and the lowest value < 1 m^2/g. The low surface area was a result of low I.R. and activation temperature. It is observed that at high temperature and I.R. of 1.13, more micropore area is produced with the highest being 849 m^2/g. Depending on the adsorbate molecule size, micropore volume has a higher effect than the mesopore volume in liquid adsorption. Micropore volume favours adsorption of micropollutant in a liquid phase adsorption [39]. Thus, these samples with high micropore volume can take advantage in a liquid adsorption, provided the adsorbate molecules are small enough to be accommodated with the micropores. Table 5 shows that all samples have average pore size > 2 nm, and are, therefore, classified as mesoporous [40].

Figure 4 shows the scanning electron micrographs obtained for the parent material and two activated carbon samples. As shown in Fig. 4a, the raw PNTS sample exhibits a rough and irregular cellular structure with no visible openings within

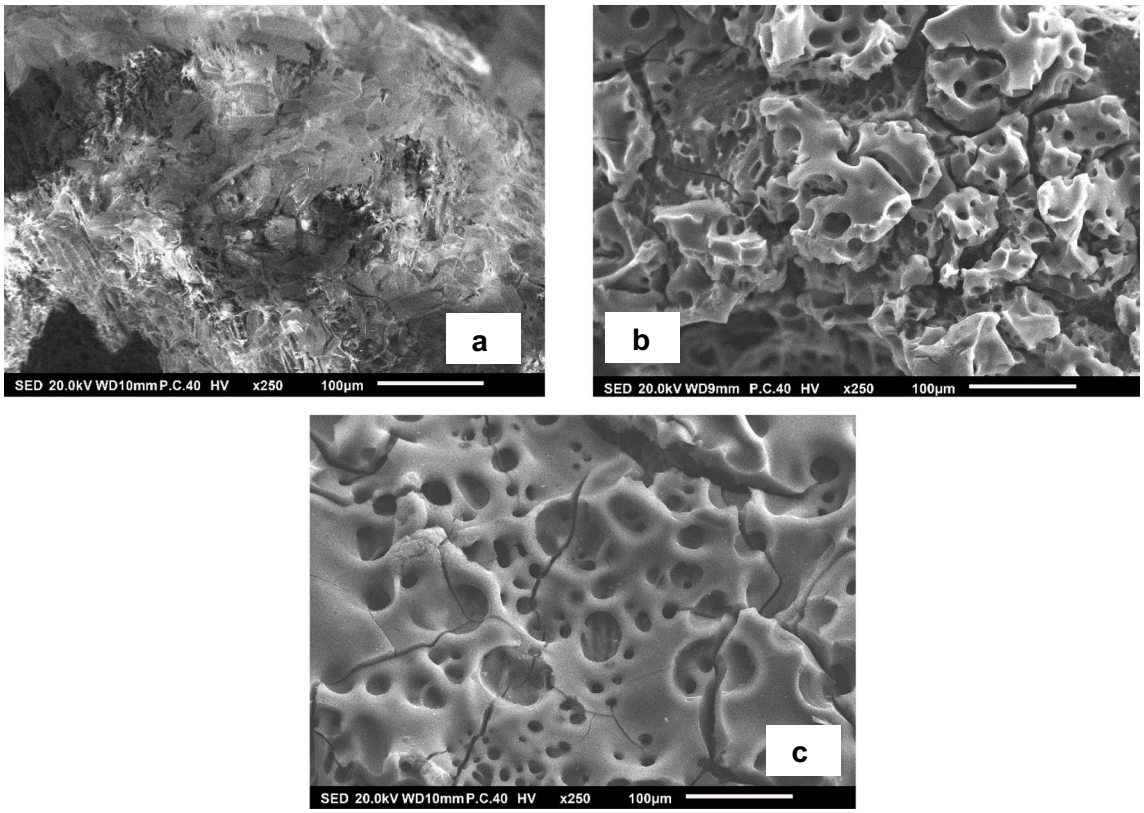

Fig. 4 Scanning electron micrographs of **a** raw peanut shells (PNTS), and for chemically activated carbons derived from peanut shells: **b** PNTS1.7-485-15 and **c** PNTS2-600-15

the structure. However, after activation, at low magnification (250x), clear channels are visible within the structure, as shown in Fig. 4b and c. The images show the geometrical heterogeneity of the activated carbon materials, coupled with the pore characteristics shown in Table 5, this will contribute to the unique sorption properties of the activated carbon materials [41]. The surface of the optimised sample (PNTS1.7-485-15) is comparatively smooth and textural analysis (Table 5) demonstrates the presence of both micro- and mesopores within the carbon. At the same magnification, the surface of run 10 (PNTS2-600-15) appears to be smoother and but with the presence of larger channels, which can be attributed to the widening of the pores, with an increase in $ZnCl_2$ loading, which leads to increased mesopore area (Table 5).

The micropore character for the optimised materials was also visualised using Dubinin-Radushkevich analysis (Figs. S9 and S10, see Supplementary Information), which showed that the microporosity deviates from a Gaussian distribution with more filling at larger pore widths, indicating that the microporosity present is predominantly comprised of supermicropores. In tandem with the micropore contribution to the total pore volume, shown in Table 5, this is likely a key contribution to the small average pore diameters observed for these materials.

Figure 5a shows the PZC plot for the optimal runs PNTS2-600-15 and PNTS1.7-485-15. The PZC was 5.8 for PNTS2-600-15 and 4.58 for the optimised sample. PZC plays a significant role in the selection of adsorbents for an adsorption system. When the pH of a solution ($pH_{solution}$) is lower than the PZC of an adsorbent, the surface of the adsorbent becomes positively charged due to protonation of the acidic groups present on the surface and when $pH_{solution}$ above the PZC of an adsorbent, the surface of the adsorbent becomes negatively charged because of the dissociation or ionisation of the acidic oxygen groups on the surface [42]. This can affect the interaction of the adsorbent surface and charged species, such as ionic dyes.

Surface chemistry was further probed using FTIR analysis. Various peaks in the FTIR spectrum of the precursor (Fig. 5b) indicate the presence of several functional groups in the raw peanut shell. The absorption peaks at 3332 cm^{-1} and 1249 cm^{-1} correspond to the O-H stretching frequency (3600–3200 cm^{-1}) and bending frequency (1410–1260), respectively [43], and this could be associated with the presence of cellulose and water of crystallisation [26, 43]. It is observed that the O-H stretching disappeared in the activated samples, which could be attributed to the dehydrating effects of $ZnCl_2$ and increased activation temperature. The absorption

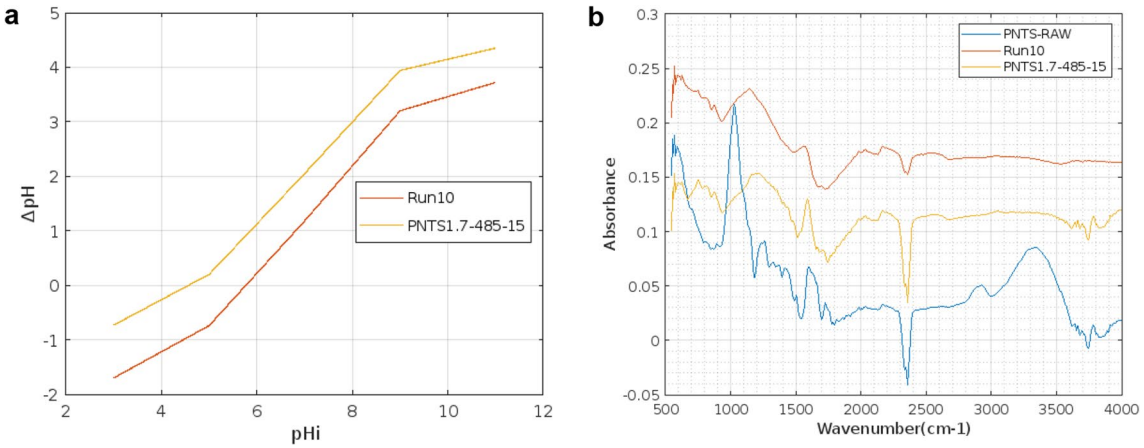

Fig. 5 **a** Point of zero charge plots obtained for chemically activated carbons derived from peanut shells: PNTS2-600-15 and PNTS1.7-485-15; **b** FTIR spectra for raw PNTS, and for chemically activated carbons derived from peanut shells: PNTS2-600-15 and PNTS1.7-485-15

Table 6 Proximate Analysis of raw peanut shells, and for chemically activated carbons derived from peanut shells: PNTS2-600-15 and PNTS1.7-485-15

	RAW PNTS	*P*NTS2-600-15	PNTS1.7-485-15
Volatile matter (%)	69.79	6.53	11.40
Fixed carbon (%)	27.53	91.19	86.42
Moisture content (%)	1.71	1.67	2.03
Ash (%)	< 1	< 1	< 0.5

peaks at 1728 cm^{-1} and 1712 cm^{-1}, for the raw and optimal run samples, indicate the presence of carbonyl (C═O) stretching vibrations of carboxyl groups [26]. N-H bending, which can be associated with amine functional groups (1650–1560 cm^{-1}) is observed to be present in all samples. The bands at 1026 cm^{-1}, 1141 cm^{-1} and 1188 cm^{-1} could be attributed to the C-O contributions from acid anhydride groups. This indicates that the surface of the carbon is heterogeneous in character and would likely enhance adsorption of polar species.

Proximate analysis provides insight into the moisture, volatile, fixed carbon, and ash contents of carbon samples, and the data obtained for the raw PNTS, and optimal runs are shown in Table 6. The moisture and ash contents are < 3% and 1% respectively, for all samples. The low ash content is an indication of quality carbon material, and this makes the AC potentially suitable for the removal of organic pollutant from an aqueous phase due to their hydrophobic nature [44]. Low volatile content is observed in PNTS2-600-15, and this can be attributed to the degree of heat treatment during carbonisation i.e., most volatiles were released from the surface of the carbon during carbonisation.

Adsorption Test

Figure S11 (see Supplementary Information) presents the percentage removal of MO with respect to time, under constant initial concentration, and solution pH. The results indicate that the rate of MO removal increases with contact time. The uptake of MO with Run 10 (PNTS2-600-15) occurs faster; this can be attributed to the fact that run 10

Table 7 Comparison of MO removal efficiency with various adsorbents

Adsorbent	% Removal	Experimental conditions				References
		Adsorbent dose (g/L)	pH	temp. (°C)	time (hr)	
AC from popcorn	48.5	0.25	-	25	12	[45]
AC from waste tire rubber	80.0	0.5	3.60	23	24	[46]
AC from coconut shell	100	10	-	25	0.2	[47]
Mesoporous carbon from Silica material	99.0	2.0	-	25	1	[48]
AC from grape seed	94.0	20	2.0	45	55 min	[49]
AC/$NiFe_2O_4$	99	3.0	3.0	30	30 min	[50]
PNTS2-600-15	99.8	1.0	5.5	22	24	This work

is characterised with larger mesopore area (Table 5), which aids the diffusion of the MO species into the interior sites of the adsorbent. However, after 24 h contact time, both samples attained nearly the same percentage removal. Table 7 lists the MO removal efficiency of some adsorbent materials previously reported [45–50]. It can be seen from the table, in terms of the removal efficiency, that the adsorbent material developed within this study shows excellent performance.

Conclusion

The results presented within this investigation show that the chemical activation method employed was suitable for creating peanut shell based activated carbon, as relatively large surface areas were recorded. The RSM reveals that temperature and impregnation ratio were the most important parameters that influenced the AC properties. The AC samples show heterogenous morphology and functional groups, which may enhance their adsorption capacity for various pollutants. This work suggests that peanut shell is a promising raw material for producing effective adsorbents for wastewater treatment. Future work will focus on the adsorption performance and optimization of the AC samples for the removal of different contaminants.

Supplementary Information The online version contains supplementary material available at https://doi.org/10.1007/s12155-023-10683-7.

Acknowledgements The authors express sincere gratitude to the National Physical Laboratory (NPL) for conducting the density measurements that are presented in this work.

Declarations

Conflict of Interest The authors declare no competing interests.

References

1. INC (2020) Nuts and dried fruits statistical yearbook 2019/2020. International Nut and Dried Fruit Council Spain. Publications - International Nut & Dried Fruit Council https://www.nutfruit.org. Accessed 21 Apr 2023
2. Perea-Moreno M-A, Manzano-Agugliaro F, Hernandez-Escobedo Q, Perea-Moreno A-J (2018) Peanut shell for energy: properties and its potential to respect the environment. Sustainability 10:3254. https://doi.org/10.3390/su10093254
3. Malik R, Ramteke D, Wate S (2006) Physico-chemical and surface characterization of adsorbent prepared from groundnut shell by $ZnCl_2$ activation and its ability to adsorb colour. Indian J Chem Technol 13. http://nopr.niscpr.res.in/handle/123456789/7048. Accessed 03 Mar 2022
4. Titirici M-M, White RJ, Brun N, Budarin VL, Su DS, Del Monte F, Clark JH, Maclachlan MJ (2015) Sustainable carbon materials. Chem Soc Rev 44:250–290. https://doi.org/10.1039/C4CS00232F
5. Heidarinejad Z, Dehghani MH, Heidari M, Javedan G, Ali I, Sillanpää M (2020) Methods for preparation and activation of activated carbon: a review. Environ Chem Lett 18:393–415. https://doi.org/10.1007/s10311-019-00955-0
6. Seader J, Henley EJ, Roper DK (2016) Separation process principles: With applications using process simulators. Wiley, Hoboken
7. Klasson KT, Ledbetter CA, Uchimiya M, Lima IM (2013) Activated biochar removes 100% dibromochloropropane from field well water. Environ Chem Lett 11:271–275. https://doi.org/10.1007/s10311-012-0398-7
8. Dai Y, Sun Q, Wang W, Lu L, Liu M, Li J, Yang S, Sun Y, Zhang K, Xu J (2018) Utilizations of agricultural waste as adsorbent for the removal of contaminants: a review. Chemosphere 211:235–253. https://doi.org/10.1016/j.chemosphere.2018.06.179
9. Kumari G, Soni B, Karmee SK (2020) Synthesis of activated carbon from groundnut shell via chemical activation. J Inst Eng India Ser E 1–8. https://doi.org/10.1007/s40034-020-00176-z
10. Kamaraj M, Umamaheswari P (2017) Preparation and characterization of Groundnut shell activated carbon as an efficient adsorbent for the removal of Methylene blue dye from aqueous solution with microbiostatic activity. J Mater Environ Sci 8:2019–2025
11. Ahmad MA, Yusop MFM, Zakaria R, Karim J, Yahaya NKE, Yusoff MaM, Hashim NHF, Abdullah NS (2021) Adsorption of methylene blue from aqueous solution by peanut shell based activated carbon. Mater Today Proc 47:1246–1251. https://doi.org/10.1016/j.matpr.2021.02.789
12. Garg D, Kumar S, Sharma K, Majumder C (2019) Application of waste peanut shells to form activated carbon and its utilization for the removal of Acid Yellow 36 from wastewater. Groundw Sustain Dev 8:512–519. https://doi.org/10.1016/j.gsd.2019.01.010
13. Malik R, Ramteke DS, Wate SR (2007) Adsorption of malachite green on groundnut shell waste based powdered activated carbon. Waste Manag 27:1129–1138. https://doi.org/10.1016/j.wasman.2006.06.009
14. Sricharoenchaikul V, Pechyen C, Aht-Ong D, Atong D (2008) Preparation and characterization of activated carbon from the pyrolysis of physic nut (Jatropha curcas L.) waste. Energy Fuels 22:31–37. https://doi.org/10.1021/ef700285u
15. Caturla F, Molina-Sabio M, Rodriguez-Reinoso F (1991) Preparation of activated carbon by chemical activation with $ZnCl_2$. Carbon 29:999–1007. https://doi.org/10.1016/0008-6223(91)90179-M
16. Smíšek M, Černý S (1970) Active carbon: manufacture, properties and applications. Elsevier Publishing Company, Amsterdam
17. Hock PE, Zaini MaA (2018) Activated carbons by zinc chloride activation for dye removal – a commentary. Acta Chim Slovaca 11:99–106. https://doi.org/10.2478/acs-2018-0015
18. Anisuzzaman S, Joseph CG, Krishnaiah D, Bono A, Suali E, Abang S, Fai L (2016) Removal of chlorinated phenol from aqueous media by guava seed (Psidium guajava) tailored activated carbon. Water Resour Ind 16:29–36. https://doi.org/10.1016/j.wri.2016.10.001
19. Molina-Sabio M, Rodrıguez-Reinoso F (2004) Role of chemical activation in the development of carbon porosity. Colloids Surf a

Physicochem Eng Asp 241:15–25. https://doi.org/10.1016/j.colsurfa.2004.04.007
20. Jawad AH, Alkarkhi AF, Mubarak NSA (2015) Photocatalytic decolorization of methylene blue by an immobilized TiO2 film under visible light irradiation: optimization using response surface methodology (RSM). Desalin Water Treat 56:161–172. https://doi.org/10.1080/19443994.2014.934736
21. Mehmood T, Ahmed A, Ahmad A, Ahmad MS, Sandhu MA (2018) Optimization of mixed surfactants-based β-carotene nanoemulsions using response surface methodology: an ultrasonic homogenization approach. Food Chem 253:179–184. https://doi.org/10.1016/j.foodchem.2018.01.136
22. Ahmadpour A, Do D (1997) The preparation of activated carbon from macadamia nutshell by chemical activation. Carbon 35:1723–1732. https://doi.org/10.1016/S0008-6223(97)00127-9
23. Ruiz Bevia F, Prats Rico D, Marcilla Gomis A (1984) Activated carbon from almond shells. Chemical activation. 1. Activating reagent selection and variables influence. Ind Eng Chem Prod Res Dev 23:266–269
24. Zhang H, Yan Y, Yang L (2010) Preparation of activated carbon from sawdust by zinc chloride activation. Adsorption 16:161–166. https://doi.org/10.1007/s10450-010-9214-5
25. Pabari RM, Ramtoola Z (2012) Application of face centred central composite design to optimise compression force and tablet diameter for the formulation of mechanically strong and fast disintegrating orodispersible tablets. Int J Pharm 430:18–25. https://doi.org/10.1016/j.ijpharm.2012.03.021
26. Sayğılı H, Güzel F (2016) High surface area mesoporous activated carbon from tomato processing solid waste by zinc chloride activation: process optimization, characterization and dyes adsorption. J Clean Prod 113:995–1004. https://doi.org/10.1016/j.jclepro.2015.12.055
27. Ottaway M (1982) Use of thermogravimetry for proximate analysis of coals and cokes. Fuel 61:713–716. https://doi.org/10.1016/0016-2361(82)90244-7
28. Bakatula EN, Richard D, Neculita CM, Zagury GJ (2018) Determination of point of zero charge of natural organic materials. Environ Sci Pollut Res 25:7823–7833. https://doi.org/10.1007/s11356-017-1115-7
29. Brunauer S, Emmett PH, Teller E (1938) Adsorption of gases in multimolecular layers. J Am Chem Soc 60:309–319. https://doi.org/10.1021/ja01269a023
30. De Boer J, Lippens B, Linsen B, Broekhoff J, Van Den Heuvel A, Osinga TJ (1966) Thet-curve of multimolecular N2-adsorption. J Colloid Interface Sci 21:405–414. https://doi.org/10.1016/0095-8522(66)90006-7
31. Barrett EP, Joyner LG, Halenda PP (1951) The determination of pore volume and area distributions in porous substances. I. computations from nitrogen isotherms. J Am Chem Soc 73:373–380. https://doi.org/10.1021/ja01145a126
32. Noordin MY, Venkatesh V, Sharif S, Elting S, Abdullah A (2004) Application of response surface methodology in describing the performance of coated carbide tools when turning AISI 1045 steel. J Mater Process Technol 145:46–58. https://doi.org/10.1016/S0924-0136(03)00861-6
33. Ahmadi M, Vahabzadeh F, Bonakdarpour B, Mofarrah E, Mehranian M (2005) Application of the central composite design and response surface methodology to the advanced treatment of olive oil processing wastewater using Fenton's peroxidation. J Hazad Mater 123:187–195. https://doi.org/10.1016/j.jhazmat.2005.03.042
34. Vining G (2010) Technical advice: residual plots to check assumptions. Qual Eng 23:105–110. https://doi.org/10.1080/08982112.2011.535696
35. Miller DM (1984) Reducing transformation bias in curve fitting. Am Stat 38:124–126. https://doi.org/10.1080/00031305.1984.10483180
36. El-Masry E, Ibrahim H, Moamen OA, Zaher W (2022) Sorption of some rare earth elements from aqueous solutions using copolymer/activated carbon composite: multivariate optimization approach. Adv Powder Technol 33:103467. https://doi.org/10.1016/j.apt.2022.103467
37. Donald J, Ohtsuka Y, Xu CC (2011) Effects of activation agents and intrinsic minerals on pore development in activated carbons derived from a canadian peat. Mater Lett 65:744–747. https://doi.org/10.1016/j.matlet.2010.11.049
38. Seader JD, Henley EJ, Roper DK (2010) Separation Process Principles, 3rd edn. John Wiley Incorporated, Hoboken
39. Murray A, Örmeci B (2018) Competitive effects of humic acid and wastewater on adsorption of Methylene Blue dye by activated carbon and non-imprinted polymers. J Environ Sci 66:310–317. https://doi.org/10.1016/j.jes.2017.04.029
40. Thommes M, Kaneko K, Neimark AV, Olivier JP, Rodriguez-Reinoso F, Rouquerol J, Sing KS (2015) Physisorption of gases, with special reference to the evaluation of surface area and pore size distribution (IUPAC Technical Report). Pure Appl Chem 87:1051–1069. https://doi.org/10.1515/pac-2014-1117
41. Dąbrowski A, Podkościelny P, Hubicki Z, Barczak M (2005) Adsorption of phenolic compounds by activated carbon—a critical review. Chemosphere 58:1049–1070. https://doi.org/10.1016/j.chemosphere.2004.09.067
42. Tran HN, You S-J, Chao H-P (2016) Effect of pyrolysis temperatures and times on the adsorption of cadmium onto orange peel derived biochar. Waste Manag Res 34:129–138. https://doi.org/10.1177/0734242X15615698
43. Fleming I, Williams DH (1966) Spectroscopic methods in organic chemistry. Springer, Berlin
44. Zuim DR, Carpiné D, Distler GaR, De Paula Scheer A, Igarashi-Mafra L, Mafra MR (2011) Adsorption of two coffee aromas from synthetic aqueous solution onto granular activated carbon derived from coconut husks. J Food Eng 104:284–292. https://doi.org/10.1016/j.jfoodeng.2010.12.019
45. Yu Y, Qiao N, Wang D, Zhu Q, Fu F, Cao R, Wang R, Liu W, Xu B (2019) Fluffy honeycomb-like activated carbon from popcorn with high surface area and well-developed porosity for ultrahigh efficiency adsorption of organic dyes. Bioresour Technol 285:121340. https://doi.org/10.1016/j.biortech.2019.121340
46. Islam MT, Saenz-Arana R, Hernandez C, Guinto T, Ahsan MA, Bragg DT, Wang H, Alvarado-Tenorio B, Noveron JC (2018) Conversion of waste tire rubber into a high-capacity adsorbent for the removal of methylene blue, methyl orange, and tetracycline from water. J Environ Chem Eng 6:3070–3082. https://doi.org/10.1016/j.jece.2018.04.058
47. Islam MS, Ang BC, Gharehkhani S, Afifi ABM (2016) Adsorption capability of activated carbon synthesized from coconut shell. Carbon Lett 20:1–9. https://doi.org/10.5714/CL.2016.20.001
48. Mohammadi N, Khani H, Gupta VK, Amereh E, Agarwal S (2011) Adsorption process of methyl orange dye onto mesoporous carbon material–kinetic and thermodynamic studies. J Colloid Interf Sci 362:457–462. https://doi.org/10.1016/j.jcis.2011.06.067
49. Yönten V, Sanyürek NK, Kivanç MR (2020) A thermodynamic and kinetic approach to adsorption of methyl orange from aqueous solution using a low cost activated carbon prepared from Vitis vinifera L. Surf Interfaces 20:100529. https://doi.org/10.1016/j.surfin.2020.100529
50. Jiang T, Liang Y-D, He Y-J, Wang Q (2015) Activated carbon/NiFe2O4 magnetic composite: a magnetic adsorbent for the adsorption of methyl orange. J Environ Chem Eng 3:1740–1751. https://doi.org/10.1016/j.jece.2015.06.020